

Charakterisierung der Zell-Transistor Kopplung

Dissertation
zur Erlangung des Grades
„Doktor der Naturwissenschaften“



am Fachbereich
Chemie und Pharmazie der
Johannes Gutenberg-Universität Mainz

vorgelegt von
Sven Ingebrandt
geboren in Alzey

Mainz, Mai 2001

Mai, 2001

Characterisation of the Cell-Transistor Coupling

as a thesis
for the degree of
„Doktor der Naturwissenschaften“



submitted to
Fachbereich
Chemie und Pharmazie
Johannes Gutenberg-Universität Mainz

by
Sven Ingebrandt

Mainz, May 2001

Für Corinna

Contents

1. INTRODUCTION	1
2. ELECTRICALLY ACTIVE CELLS	7
2.1 Electrical Aspects of Functional Biomembranes.....	9
2.2 Resting Potential.....	11
2.3 Hodgkin-Huxley Theory.....	11
2.4 Neuronal Cells	16
2.5 Cardiac Muscle Cells	20
3. LOW NOISE SENSORS FOR BIOLOGICAL SIGNAL TRANSDUCTION	23
3.1 Functional Principle of a Field-Effect Transistor	24
3.2 Sensors for Bioelectronic Signal Transduction	34
3.2.1 <i>ION-SENSITIVE FIELD-EFFECT TRANSISTORS</i>	34
3.2.2 <i>16-CHANNEL FET-ARRAYS FOR CELL-TRANSISTOR MEASUREMENTS</i>	37
3.2.3 <i>CHARACTERISATION OF THE FET-CHIPS</i>	38
3.2.4 <i>P-CHANNEL FET-ARRAYS FOR CELL-TRANSISTOR MEASUREMENTS</i>	40
3.2.5 <i>N-CHANNEL FET-ARRAYS FOR CELL-TRANSISTOR MEASUREMENTS</i>	41
3.2.6 <i>BACKSIDE-CONTACTED FIELD-EFFECT TRANSISTORS</i>	44
3.2.7 <i>EXTENDED GATE ELECTRODE ARRAYS</i>	51
3.3 Minimising Noise in the Set-up.....	60
3.3.1 <i>CORRELATION</i>	61
3.3.2 <i>SPECTRAL NOISE DENSITY:</i>	62
3.3.3 <i>AUTOCORRELATION-FUNCTION:</i>	63
3.3.4 <i>PROCEDURE FOR INTERSPERSED NOISE TRACKING</i>	65
3.3.5 <i>NOISE OF THE USED FET-DEVICES</i>	67
3.3.6 <i>MOSFET NOISE</i>	70
3.3.7 <i>NOISE OF THE BACKSIDE-CONTACTED FET-ARRAYS</i>	74
3.3.8 <i>NOISE OF THE EGE-DEVICES</i>	76
3.3.9 <i>JFET NOISE</i>	79

4. EXPERIMENTAL SET-UP	85
4.1 Measurement Set-up	86
4.2 Amplifiers and Set-up for External Cell Measurements	89
4.2.1 <i>EGE PREAMPLIFIER STAGE</i>	89
4.2.2 <i>BACKSIDE-CONTACTED FET PREAMPLIFIER STAGE</i>	92
4.2.3 <i>ADAPTER FOR THE LANGMUIR-BLODGETT FET-CHIPS</i>	93
4.2.4 <i>16-CHANNEL MAIN AMPLIFIER FOR THE FET- AND</i> <i>EGE-SYSTEM</i>	95
4.2.5 <i>64-CHANNEL MAIN AMPLIFIER FOR THE EGE-SYSTEM</i>	96
4.3 The Patch-Clamp Amplifier.....	98
4.3.1 <i>OVERVIEW</i>	98
4.3.2 <i>COMPENSATION PROCEDURES</i>	100
4.3.3 <i>PATCH-CLAMP MEASUREMENTS</i>	106
4.3.4 <i>SOLUTIONS AND PIPETTES FOR PATCH-CLAMP RECORDING</i>	109
5. BIOELECTRONIC COUPLING	111
5.1 Point Contact Model	112
5.2 Cell-Transistor Coupling Measurements	115
5.3 Modelling the Cell-Sensor Coupling using PSPICE	119
5.4 Ionsensitivity of the BioFETs	139
5.4.1 <i>CONCENTRATION CHANGES IN THE CELL-TRANSISTOR CLEFT</i> ..	139
5.4.2 <i>CALIBRATION CURVE: IONSENSITIVITY OF THE BIOFETs</i>	140
5.4.3 <i>IONSENSITIVITY OF TRANSISTORS</i>	144
5.5 Extended Point Contact Model	148
6. CELL-TRANSISTOR COUPLING MEASUREMENTS.....	153
6.1 Sensor Preparation for Cell Cultures	155
6.2 Experiments with Single Neurons 157	
6.2.1 <i>CELL LINES</i>	157
6.2.1.1 <i>NEUROBLASTOMA CELL LINE SH-SY5Y</i>	158
6.2.1.2 <i>NEUROBLASTOMA CELL LINE TR14</i> 164	
6.2.2 <i>PRIMARY CULTURED NEURONS</i>	178
6.2.2.1 <i>DISSOCIATED NEURONS OF THE NEOCORTEX</i>	178
6.2.2.2 <i>DISSOCIATED HIPPOCAMPAL NEURONS</i>	181
6.2.2.3 <i>BRAINSTEM SLICE NEURONS</i>	185
6.3 Primary Cultured Cardiac Myocytes	201
6.3.1 <i>SINGLE CELL EXPERIMENTS WITH CARDIAC MYOCYTES</i>	202
6.3.2 <i>CARDIAC MYOCYTE LAYERS</i>	204
6.3.3 <i>SIGNAL SHAPES OF EXTRACELLULAR RECORDED</i> <i>ACTION POTENTIALS FROM CARDIAC MYOCYTE LAYERS</i>	208

6.3.4 UPSIDE-DOWN MEASUREMENTS	217
6.4 The Cell-Transistor Chip for Pharmacological	
Screening.....	222
6.4.1 PHARMACOLOGY	224
6.4.2 DOSE-RESPONSE CURVES FOR STIMULANTS AND RELAXANTS.....	225
6.4.3 SIGNAL SHAPE CHANGES INDUCED BY DRUGS	228
6.4.4 SIGNAL VELOCITY IN THE CELL LAYER.....	230
7. CONCLUSION AND OUTLOOK	235
8 APPENDIX	241
A Fabrication of the backside-contacted p-channel FETs	241
B Source Code for the Simulation of the Point Contact	
Model using OrCADs PSpice 9.1	249
C Patch-Clamp equipment.....	251
D Equipment for Cell-Transistor Coupling Measurements.....	252
E FET and EGE Encapsulation	253
F Chemicals.....	254
LITERATURE.....	257
ABBREVIATIONS.....	273
Formula signs.....	273
Technical Terms	278
THANK YOU / DANKESCHÖN !!!	279

Chapter 1

Introduction

Mammalian neuronal cells, especially that of humans, have evolved over thousands of years of evolution to become one of the most sophisticated and complex signalling and processing systems in any living organisms. The human brain contains some 10^{11} neuronal cells with 10^{14} functional connections, called synapses. Each cell is capable of forming up to 80,000 connections. This huge network represents the most powerful, and yet the least known, processing system known. Every single cell carries an ingenious detection system with which cells are able to communicate among each other and to detect chemical or electrical stimuli from their environment. This detection system possesses a very high selectivity and sensitivity as in some cases even a single molecule is enough to trigger a reaction of the cell (ligand-gated cell-surface receptors).

To assist a better understanding of the biological signal processing and transduction, the inherently complex system of cellular networks has to be simplified. On a single cell level, the characteristic electrical properties of cells can be observed by impaling the cellular membrane with carefully designed (with a specific tip diameter) glass

microelectrodes. With the use of this technique, action potentials of neuronal cells can be recorded and the presence of voltage-gated ion-channels has been demonstrated (Hodgkin and Huxley, 1952). A further improvement of this method leads to the development of patch-clamp technique (Hamill et al., 1981; Neher and Sakmann, 1976), where the glass electrode is placed close to the cell membrane and a low resistive electrical contact to the cells' interior is established. This so-called *whole-cell* configuration offers the possibility of investigating voltage-gated ion-channels on the cell membrane. The technique has been improved to a point such that even the function of single ion-channels can be studied. This measurement method opened a new field in medical, pharmaceutical and physiological research. Neher and Sakmann, who invented this electrophysiological technique, were awarded a Nobel Prize in physiology and medicine for this achievement in 1991. The intracellular method possesses a very high signal-to-noise ratio, but has also some major disadvantages. The procedures of a patch-clamp system are very complicated. The method is invasive and it invariably destroys the cell after the measurement. It is limited to observing only a few cells at the same time as the measurement heads of a patch-clamp set-up require a lot of space and a maximum of 4 patch-clamp pipettes on one cell substrate is practicable. Long-term measurements are not feasible as the cells are subjected to a high degree of stress during a patch-clamp measurement, which makes an observation over several hours impossible. Furthermore, in some cases, the cells being observed may have 'moved', as most cells are highly motile.

In the past decades, extracellular measurement methods have been developed, which avoided the above-mentioned disadvantages. With the planar technology, it was possible to integrate a number of sensitive spots in a very small area of the microelectrode sensor chips (Gross et al., 1977; Israel et al., 1984; Pickard, 1979; Thomas et al., 1972). With such metal microelectrode systems, the recording and stimulation with electrically active cells cultured on the sensor chips are possible. For these systems, it is crucial that the electrodes have low impedance. Electrode materials like indium tin oxide (ITO), titanium nitride (TiN), gold, or platinum are widely used (Hämmerle et al., 1994; Nisch et al., 1994). For the improvement of the electrode impedance, platinum coatings like platinum black, (Calusaru, 1979; Ibl, 1962; Robinson, 1968), or platinum white, (Thiébaud et al., 1997), are shown to be the most appropriate.

A second approach to these extracellular sensors is based on the use of *metal-oxide-semiconductor field effect transistor* (MOSFET). For the use of such devices in an aqueous surrounding, the sensitive input electrode (gate) is contacted over the electrolyte by a reference electrode (in most cases, Ag/AgCl wire). This so-called electrolyte-oxide semiconductor FET (EOSFET) was developed by Bergveld in 1970 (Bergveld, 1970). First experiments were performed in detecting electrical signals from muscle fibres using EOSFETs (Bergveld et al., 1976). In 1991, the first recording from a

large invertebrate neuron cultured on a FET device was reported (Fromherz et al., 1991). With the help of an additional contact, a capacitive stimulation of the cell was shown to be possible (Fromherz and Stett, 1995) and even a bi-directional interface between cell and transistor had been developed (Stett et al., 1997).

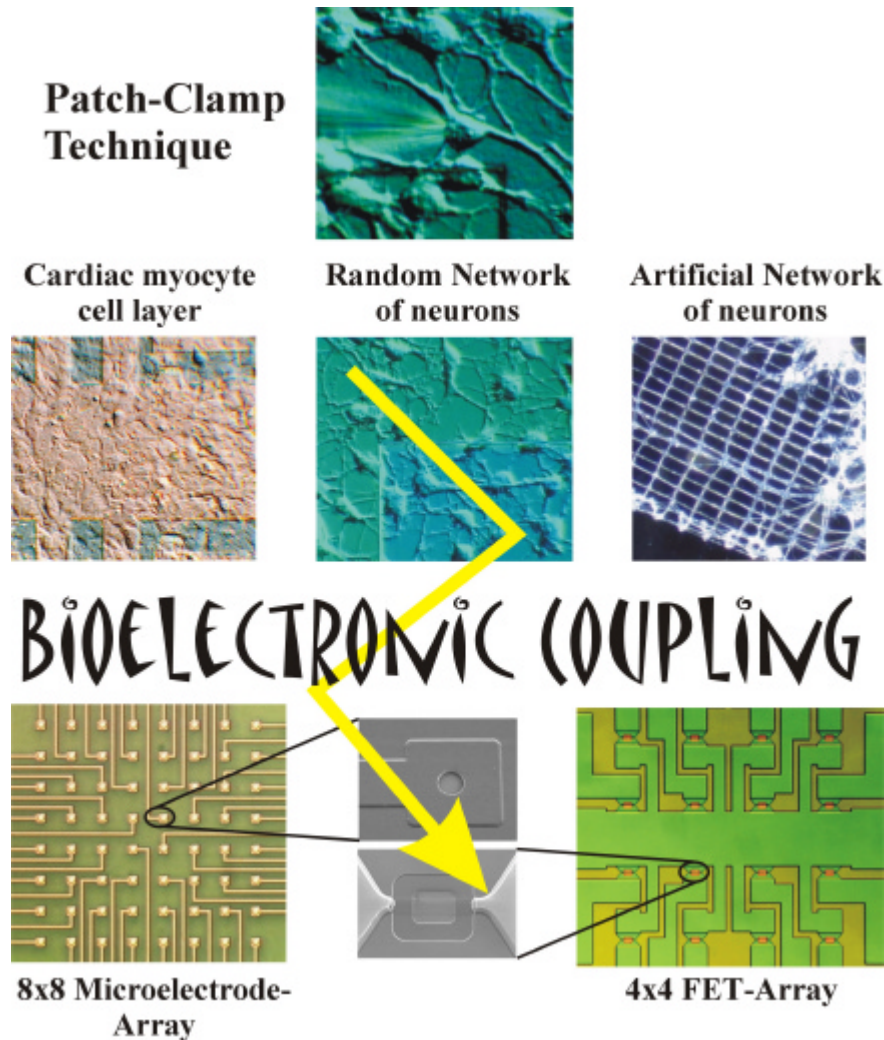


Figure 1-1 Intracellular and extracellular methods for the investigation of cell-sensor communication used in the present study. On top of a classical patch-clamp glass pipette attaches a neuron from the left side. Cellular systems used in this work were cardiac myocyte layers and random networks of neurons. Future project will use artificial networks of neurons on the sensor surfaces. The coupling behaviour of these electrically active cells were investigated with microelectrode arrays and FET-arrays.

The explanation of the recorded extracellular signal shapes was first attempted using an equivalent electrical circuit, the *Point-Contact Model*, which described the cell detector contact (Regehr et al., 1989). The coupling of signals from large invertebrate neurons with FET sensors was described in detail using the equivalent circuit models

and distributed systems as given by the two-dimensional cable theory (Fromherz et al., 1991), (Jenker and Fromherz, 1997; Weis and Fromherz, 1997). In a further stage, the *Point Contact Model* took the contribution of voltage-gated ion-channels in the contact region between cell and transistor into considerations (Fromherz, 1999).

There are a number of fields of application where the extracellular signal recording can be the most invaluable. One of which is in pharmacological studies. The biosensor research aims to produce a revolutionary sensory system by combining physical and electronic converter elements. The concept of a whole-cell sensor, which uses the cellular-microelectronic interface for the detection of drug responses on living cells has been proposed by Parce et al. (1989). These sensors can offer a non-invasive means in cellular research. In other research areas, the use of such sensor systems have been proposed in 1976 for the recovery of partially sighted or blind people (Frueh and Felker, 1976) and other fields of application are currently being considered. Metal electrodes are used for the stimulation of muscle tissues for the support of hemiplegic patients (Prochazka and Davis, 1992). The classical example for stimulation of muscle tissue is the artificial pacemaker (Schechter, 1972). Future projects aim to create a 2-dimensional neuronal networks on such extracellular devices to investigate the cognitive functions on a much reduced scale.

The basic understanding of the recorded signals is crucial to the future application of this system. In the present study, a fundamental goal is to further characterise the cell-transistor coupling.

The present approach is to:

- Continue to improve the existing extracellular sensors and the extracellular recording system previously developed (Krause, 2000; Offenhäusser et al., 1997; Sprössler et al., 1998), and to further improve the signal-to-noise ratio of the set-up.
- Develop new field-effect transistor types with a novel backside contact approach and to make a larger free area for cell cultures.
- Improve the 16-channel microelectrode set-up to 64-channels with a new encapsulation, a new amplifier system, and new recording software, which offers the capability of online sampling of all 64 channels.
- Investigate TR14 *cell line* as a cellular system on the extracellular sensors.
- Introduce brain slice cultures and to examine its values in whole-cell based biosensor system
- Device an improved model for the observed potassium ion-channel accumulation phenomenon (Straub et al., 2001; Vassanelli and Fromherz, 1999) in the cleft between a single cell and a single transistor.

- Investigate the applicability and reliability of the cardiac myocyte layer – FET sensor hybrid system in terms of drug screening.

The format of this thesis is as follows:

- *Chapter 2* will describe the use and functions of *Electrically Active Cells* like neurones and cardiac myocytes. Attempts will be made in explaining how these systems communicate using weak electrical signals.
- *Chapter 3* deals with the *Low Noise Sensors for Biological Signal Transduction*. The basic functions of a FET device in both MOSFET and EOSFET configuration are explained. The sensor chips are electrically characterised and the encapsulation processes are explained. Furthermore, a new backside-contacted FET sensor is introduced. The last part of this chapter deals with the noise sources occurring in the extracellular measurement set-up and with the intrinsic noise of the extracellular sensors itself.
- *Chapter 4* will focus on the *Experimental Set-up* used for the cell-transistor coupling measurements. The electrical circuitries used in a standard patch-clamp amplifier are elucidated and it will be shown how these circuitries are crucial to the basic understanding of the extracellular signal shapes.
- *Chapter 5* will explain the *Bioelectronic Coupling* the classical Point Contact Model and how the cell-transistor assembly is simulated using a standard simulation program for modelling electrical circuits (student version of PSPICE ver. 9.1, OrCAD Inc., USA). Based on the results obtained with this simulation method a new extended Point-Contact Model is proposed, which is taking ion concentration changes in the cleft between the electrically active cells and the ion-sensitive FET device into account.
- *Chapter 6* the *Cell-Transistor Coupling Measurements* and different cellular systems are characterised in terms of their coupling behaviour to the extracellular sensors. The investigation of the applicability of the cardiac myocyte layer – FET sensor hybrid system in terms of drug screening was performed by the application of different cardio-stimulants and relaxants to the cells.
- *Chapter 7* the *Conclusions and Outlook* of the results are provided and possible further developments of the cell-based biosensors are proposed.
- The *Appendix* contains a detailed fabrication process for the backside contacted FET arrays, the precise PSPICE source-code for the simulation of the cell-transistor contact. A list of all chemicals and equipment used in this work will also be provided.

Chapter 2

Electrically Active Cells

In order to integrate live biological cells with standard chip architectures of the miniaturised hybrid cell-transistor chip, understanding the electrical properties of cellular systems is essential. In this chapter, the electrophysiological characteristics of the cells will be addressed. In the present study, we have chosen two different cellular systems: neuronal and cardiac systems.

Neuronal cells from different regions of the mammalian central nervous system are connected in specific ways in order to perform a variety of functions. The controls of specialised functions, the communications between different brain regions and to the remainder of the body are dependent upon strong synaptic contacts. In some cases, signals are transported to the spinal cord and then the brain to be processed (via afferent fibres) and, subsequently, actions by the brain are taken (via the efferent fibres). Most neuronal cells have to be stimulated by another cells (by neurotransmitters) or from an

external impulse to initiate their electrical activity (electrical, chemicals and drugs). However, some cells are spontaneously active e.g. neurons from the respiratory nuclei within the brainstem.

In the second chosen cellular system, cardiac myocytes (heart muscle cells) from embryonic E15-E18 rats were used. Cardiac myocytes are myogenic (i.e. they generate spontaneous action potentials). There are specialised cells from the *sinoatrial node* and the *atrioventricular node* which drive the rest of the myocytes (they are pacemaker cells of the heart which generate action potentials at slight higher rate than the rest of the cells). As such, the signal propagation of heart cells is said to be autorhythmic. This provides us with a completely different system in the study of the coupling between biological cells and the transistor chips.

In Figure 2-2 a typical cell with all its different parts is shown.

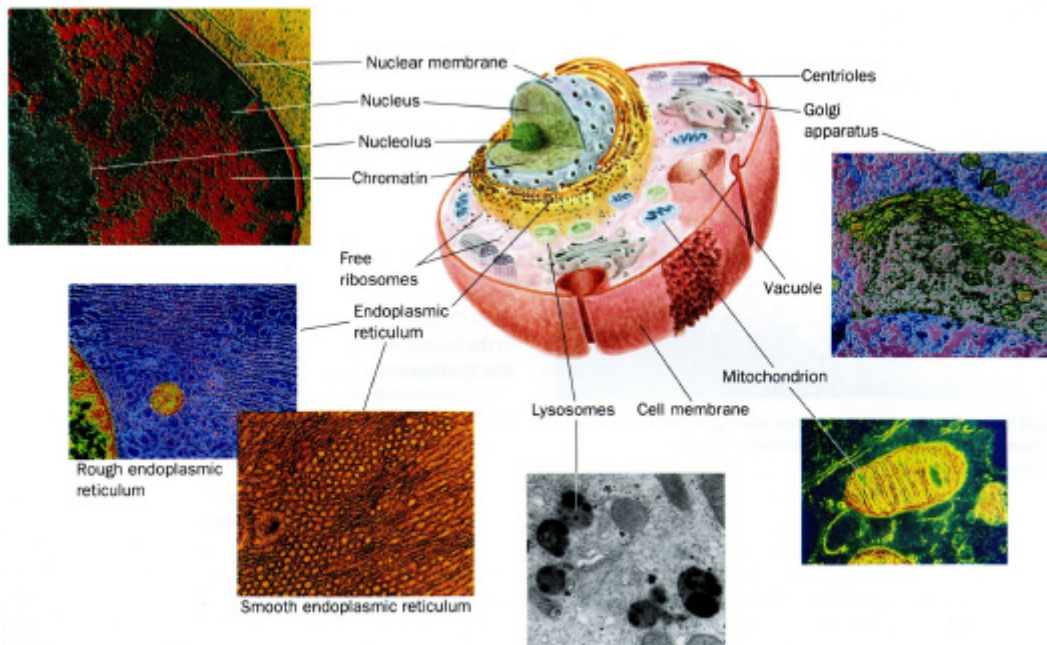


Figure 2-2 Picture showing different parts of a cell. The surrounding pictures are obtained by different methods using staining techniques. The whole figure was adapted from Voet and Voet (1995).

In the first part of this chapter, the structure of such cells will be explained and how these cellular systems can be electrically active. The significance of the resting potential and the understanding of action potentials, which can be monitored by extracellular sensors, will be described. In the third part, a general introduction to the Hodgkin-Huxley Theory (Hodgkin and Huxley, 1952) will be given, which serves the explanation of voltage-gated ion-channels in biomembranes. The main structures of neuronal cells and heart muscle cells will be also illustrated.

2.1 Electrical Aspects of Functional Biomembranes

Every cellular membrane in the body has the same basic phospholipid structure, which cannot be crossed by water-soluble ions. The membranes of different cells differ in the functional transmembrane proteins they contain. These proteins interchange Na^+ -, K^+ -, Ca^{2+} , or Cl^- -ions between the outside (Exterior) and the inside (Cytosol) over the phospholipid membrane (Figure 2-3).

These large molecules can be categorised into: (1) *passive channels*, which allow a passive transport of ions over the membrane; (2) *active ion pumps*, which maintain the different ion concentration of the interior and the exterior part of the cells; and (3) *carrier proteins*, which transport the ions by conformational changes.

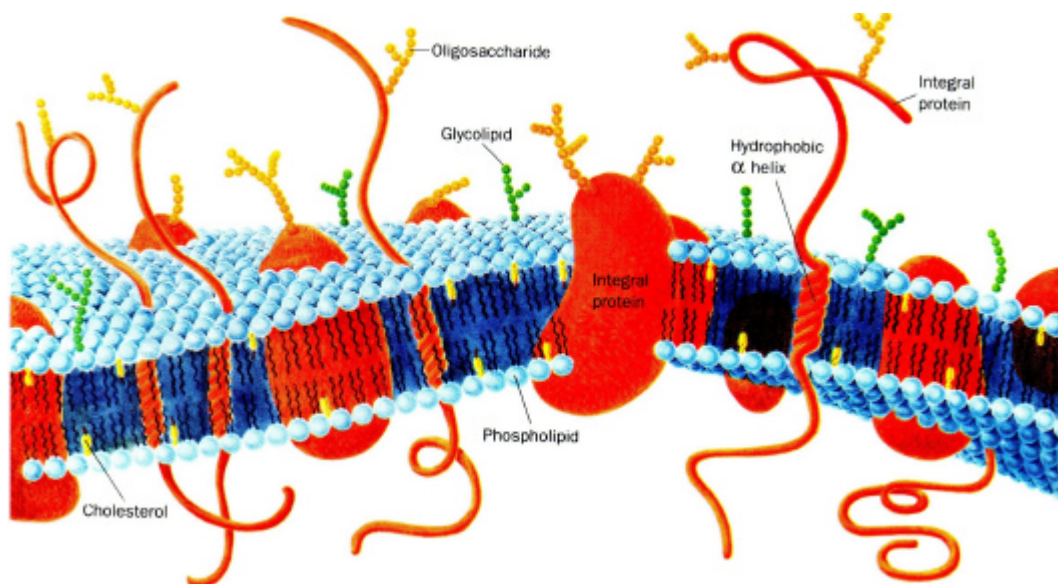


Figure 2-3 Sketch of a typical biological membrane consists of different functional proteins. The figure was adapted from Voet and Voet (1995). ‘It shows a schematic diagram of a plasma membrane. Integral proteins are embedded in a bilayer composed of phospholipids and cholesterol. The carbohydrate components of glycoproteins and glycolipids occur only on the external face of membrane.’

One of the most important ionic pumps is the Na^+/K^+ -pump, which operates by the conversion of ATP. Carrier proteins act by binding ions and transporting them over the membrane. This is mainly done by stoichiometric binding and structural changes. With this means even large insoluble molecules like peptides can be transported.

The most important proteins for the electrical activity of cells are the ion-channels. The exchange of molecules is rapid (up to 10^6 per sec) and is driven by electrochemical

gradients. In Figure 2-4 a sketch of an ion-channel is shown. The complete structure of such macromolecules is still largely unknown, but the existence of the functional parts like selectivity filter, gate and sensor can be deduced from patch-clamp experiments.

The ion-channels can be classified into *ligand-*, *mechanically-* and *voltage-*controlled. The present study focused primarily on the voltage-gated Na^+ , K^+ , and Ca^{2+} -ion-channels. The exchange of these ions in a timely manner produces action potentials, which are the electrical signals in the cellular activity. The specific voltages between the extracellular and the intracellular spaces regulate the opening and closing of these channels. In the next part, an electrically active cell in the resting state will be discussed.

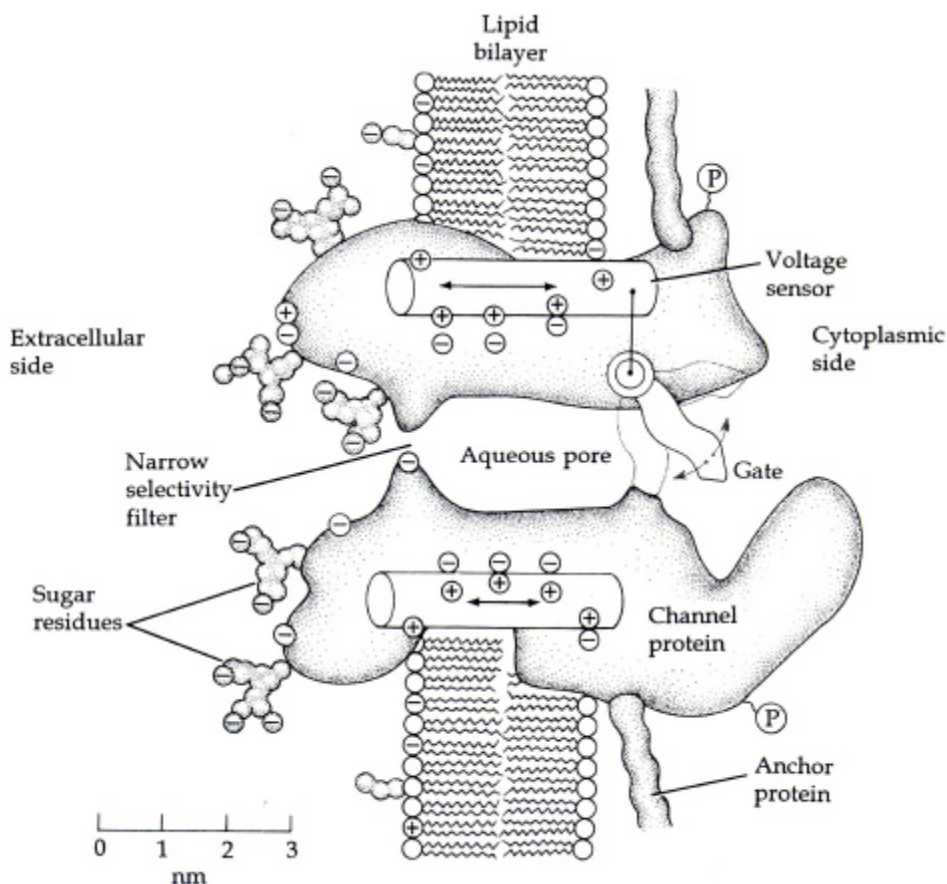


Figure 2-4 Diagram showing an ion-channel with several functional domains. ‘The channel is drawn as a transmembrane macromolecule with a hole through the centre. The external surface of the molecule is glycosylated. The functional regions – selectivity filter, gate, and sensor – are deduced from *voltage-clamp* experiments and are only beginning to be charted by structural studies.’ The figure was adapted from Hille (1992).

2.2 Resting Potential

The resting potential of a cell V_{RP} is the voltage between the internal and the external part. It arises from different ion concentrations, which are maintained from ion pumps incorporated within the membrane. The equilibrium potential E_i of a single ion species i is described by the Nernst-equation and related to the ion concentrations $c_i^{interior,exterior}$, the valency of the ion species i and the temperature T .

$$E_i = E_{interior} - E_{exterior} = \frac{RT}{zF} \ln \frac{c_i^{interior}}{c_i^{exterior}} \quad (2.1)$$

where R is the gas constant, z is the number of electrons, and F is the Faraday constant. The concentration and voltage ratios at a plasma membrane are very complex. Both inorganic ions and all negatively charged carrying molecules in the cytoplasm (e.g. negatively charged proteins, other large anions and Cl^- -ions) play a major role. Inorganic ions for mammalian cells are Na^+ , K^+ , Ca^{2+} , or Cl^- -ions. The potential (V_M in units of voltage) of a plasma membrane is related to concentration differences and permeability coefficients of all ion species. The Goldman-equation serves as good description of the membrane potential (Eq. 2.2):

$$V_M = \frac{RT}{F} \ln \frac{P_{K^+} [K^+]_o + P_{Na^+} [Na^+]_o + P_{Cl^-} [Cl^-]_i}{P_{K^+} [K^+]_i + P_{Na^+} [Na^+]_i + P_{Cl^-} [Cl^-]_o} \quad (2.2)$$

with the permeability constants P_i .

The resting potential of a neuron lies close to the K^+ equilibrium potential and no net membrane current is flowing in the stationary state. The values for resting potentials of electrical active cells are in the range of -30 to -70 mV.

2.3 Hodgkin-Huxley Theory

Electrically active cells can generate action potentials. During such an action potential, the membrane voltage V_M is changing over time. If the membrane voltage is risen to a threshold value, which is characteristic to each cell type, first the *fast* sodium channels open and a positive current is flowing into the cell (depolarisation). The membrane potential is rising up to a maximum value until the positive charge inside the cell is beginning to repel any incoming positive ions.

After a short period (1-3 ms) the sodium channels are closing and the potassium channels are beginning to open. A positive outflow of potassium ions to the extracellular space is lowering the membrane voltage (repolarisation or

hyperpolarisation) in an attempt to restore the resting membrane potential. Sometimes an overshoot in the negative direction can be observed (after hyperpolarisation). In Figure 2-5, a spontaneous action potential of a motorneuron from a brainstem slice culture is shown.

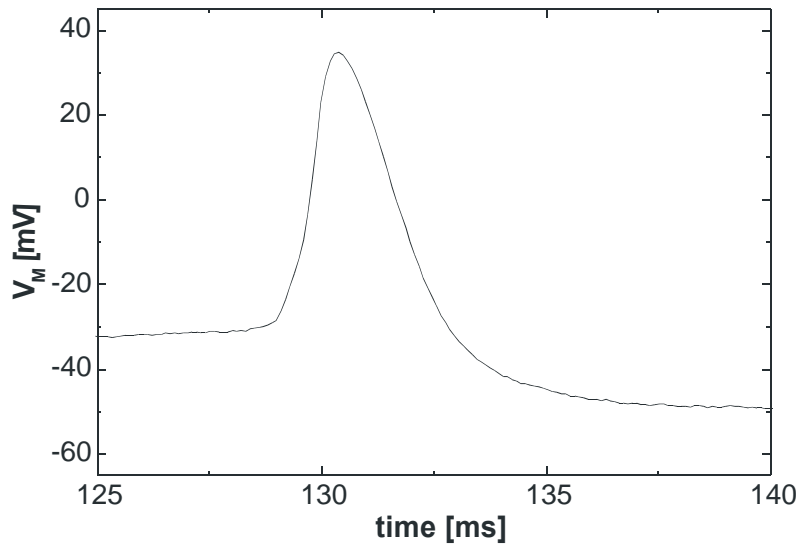


Figure 2-5 Spontaneous action potential of a motorneuron from a brainstem slice. The resting potential of the cell was -55 mV.

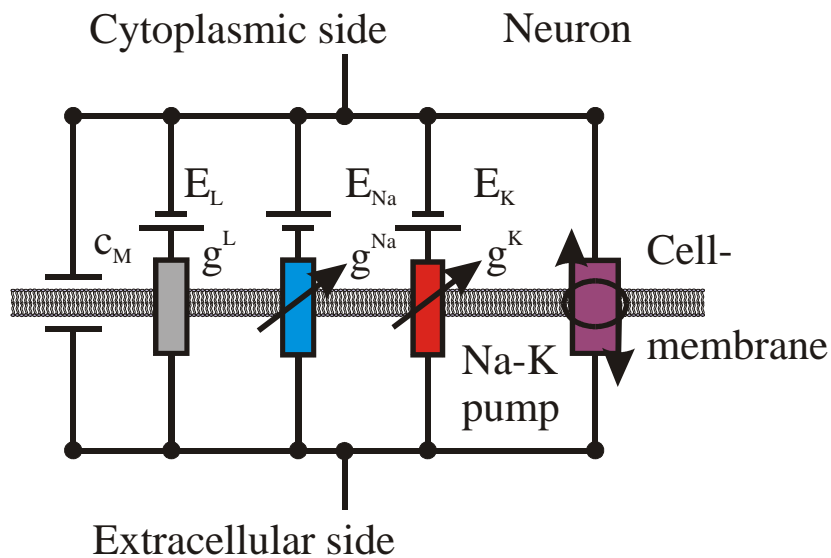


Figure 2-6 Electrical model of a neuronal cell membrane (Hodgkin and Huxley, 1952). The electrical properties of the cell membrane are described with the Nernst potentials E_i of the ions, with the specific ion conductances g^i of the voltage-gated ion-channels, and with the specific membrane capacitance c_M . Currents of other ions and currents caused by leaks in the membrane are summed up to a voltage-dependent leakage conductance g^L . The ion concentration gradient is maintained by the $\text{Na}^+\text{-K}^+$ -ionpump.

The Hodgkin-Huxley Theory (Hodgkin and Huxley, 1952) describes the action of ion-channels in an electrical model (Figure 2-6). The capacitance of the cell membrane is described by the specific capacitance c_M . The specific conductance g^{Na} and g^K for the Na^+ - and K^+ -ions are related to the ion current densities i_M^i , the membrane potential V_M and to the Nernst-potential E_i of the ion species i with $g^i = i_M^i / (V_M - E_i)$.

All other currents over the membrane are summed up to a leakage current and described by a voltage-dependent resistor, a specific conductance g^L and a Nernst-potential E_L . The ion current density is then the sum of all currents in the electrical model:

$$i_M = c_M \frac{dV_M}{dt} + g_{Na}(t)(V_M - E_{Na}) + g_K(t)(V_M - E_K) + g_L(t)(V_M - E_L) \quad (2.3)$$

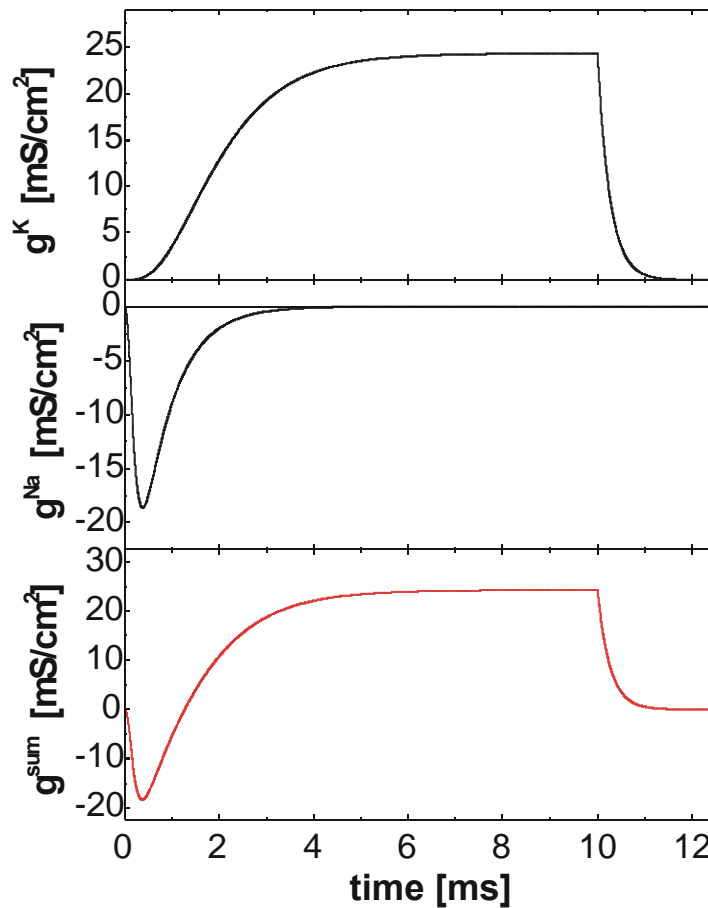


Figure 2-7 The specific conductances of K^+ - and Na^+ -ions of a neuronal cell. The membrane potential of the cell was modelled to $V_M = 9$ mV (situation during a stimulation pulse in a voltage-clamp experiment). The graphs are plotted using the Hodgkin-Huxley model. In the lower plot the sum of both conductances is plotted. It would reflect the current signal measured with the patch-pipette.

The first element is the capacitive current over the membrane, which can be caused by the quick rising of the membrane potential. The other parts are the voltage-dependent ion currents for a certain ion type or the leakage current. The ion conductance of a real cell is time dependent. The equations in the Hodgkin-Huxley Theory are using empirical values for these conductances (Hille, 1992).

The Hodgkin-Huxley equations are describing the time- and voltage-dependent changes in the specific conductance g^i of the single ion species over the cell membrane. In Figure 2-7 the graph for the specific conductance of a neuronal cell after a stimulation pulse up to the membrane potential of 9 mV is shown.

The characteristic shape for the Na^+ - and K^+ -ion current densities are described by following equation:

$$i_M = c_M \frac{dV_M}{dt} + \bar{g}_K n^4 (V_M - E_K) + \bar{g}_{Na} m^3 h (V_M - E_{Na}) + \bar{g}_L (V_M - E_L) \quad (2.4)$$

With the dimensionless parameters n , m and h in the Hodgkin-Huxley Theory (Hille, 1992).

For the modelling of action potentials of cardiac myocytes one has to take an additional influence of the Ca^{2+} -ion current Figure 2-9.

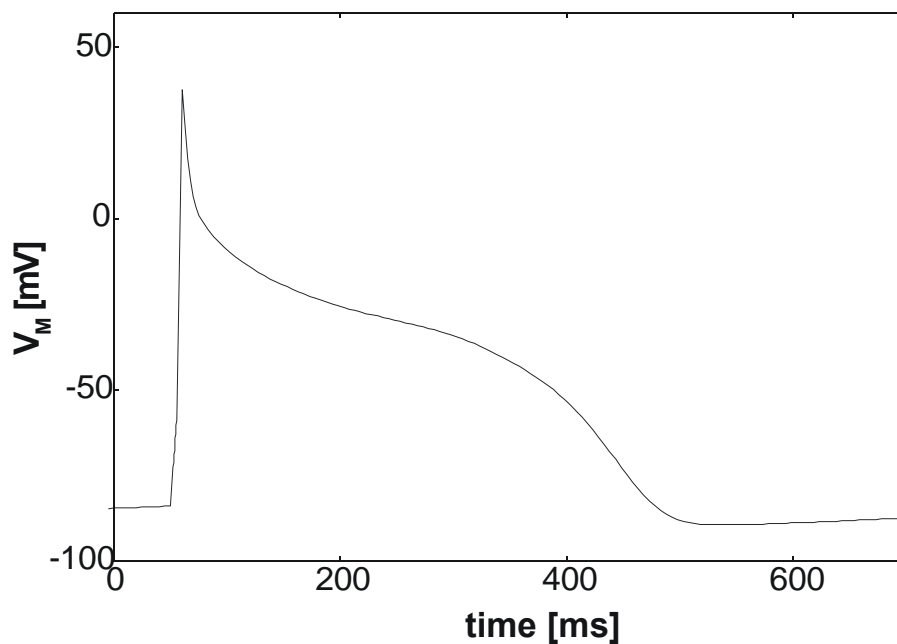


Figure 2-8. Action potential of a cardiac myocyte (Purkinje fibre) modelled with the Hodgkin-Huxley equations. The long plateau at -30 mV is caused by an Ca^{2+} influx into the cell.

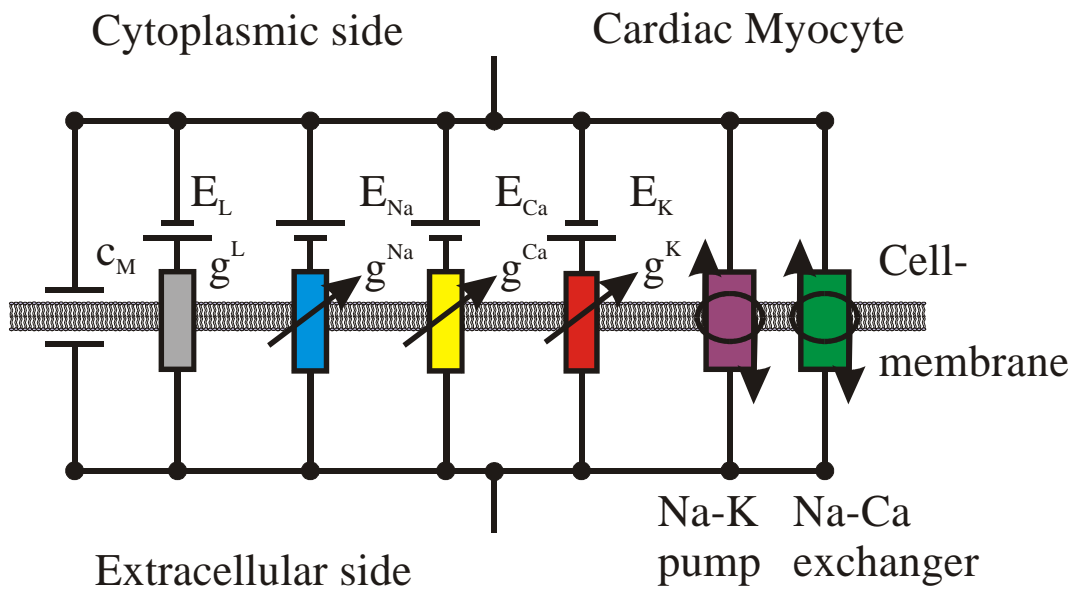


Figure 2-9 Electrical model of a cardiac myocyte (Purkinje fibre). In addition to neuronal cells in Figure 2-6 one has to take the Ca^{2+} influence into account. This is done by the Nernst potential E_{Ca} , the specific ion conductance for calcium g^{Ca} , and by adding the Na-Ca exchanger pump into the model.

In the electrical model of a cardiac myocyte (Purkinje fibre), the Ca^{2+} influence plays a major role. In Figure 2-9 the Nernst potential E_{Ca} , the specific ion conductance for calcium g^{Ca} , and the Na-Ca exchanger pump are added into the model. The specific conductance for Ca^{2+} -ions was described by Shrier and Clay (1986). The Ca^{2+} -ion current is causing the plateau phase (transient current) during an action potential. An inward Ca^{2+} current compensates the repolarisation driven by the outflow of potassium ions for a certain time. The Ca^{2+} -ion current is delaying the repolarisation of the cell and causing the characteristic shape of a cardiac myocyte action potential.

2.4 Neuronal Cells

Neuronal cells have many different functions in the body. Not only are neurons of the brain morphologically and physiologically different in different parts of the brain, they also perform different tasks. Some of them innervate muscle cells and can stimulate muscle cells to contract or to cause relaxation. Some of them are used in receiving and sending signals from sensory organs.

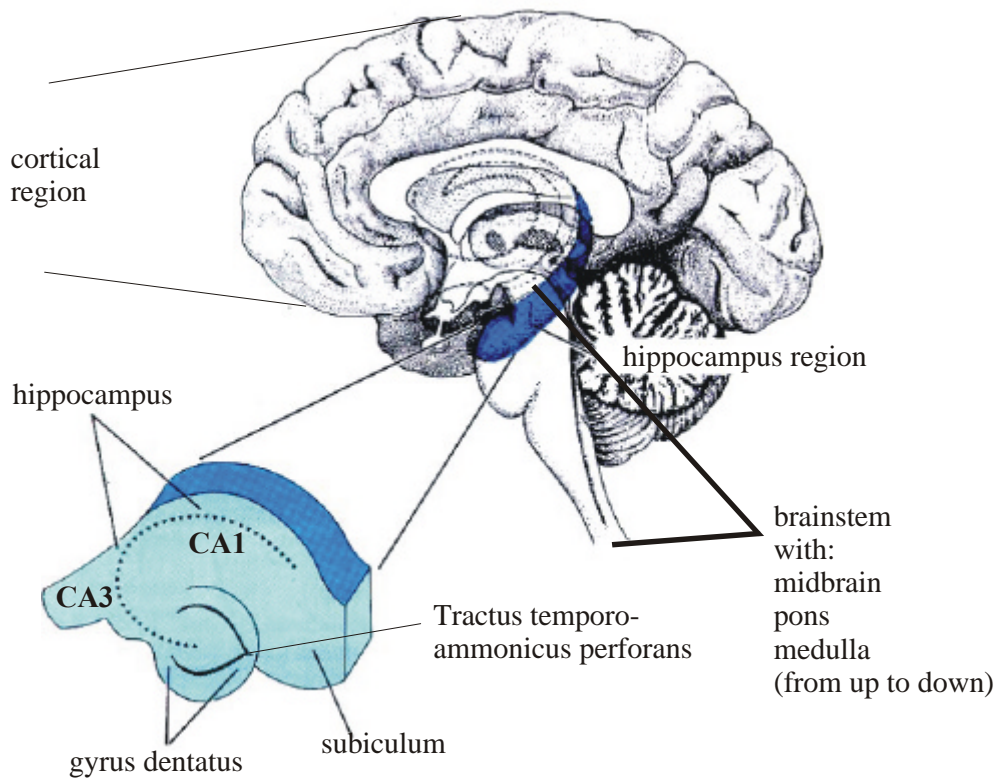


Figure 2-10 Different regions of the brain as they were used in preparation for the culturing of neuronal cells in this work. The figure shows the medial section of a human brain. It was adapted from Nicholls et al. (1995) and was subsequently modified. The cortical neuronal culture was the most straightforward and had the best yield. Much more complicated was the culturing of dissociated hippocampal neurons as the hippocampi from embryonic rats are very small. The brainstems were coronally sliced. Therefore, the slices contain a number of groups of neurons across the whole plane on the brainstem.

The present study utilised primary cultures of neurones from different brain areas: dissociated brain cells from the neocortical region, dissociated brain cells from the hippocampal region, which are known to form synapses in culture and are important in long term memory formation, and cells from brainstem slices. The slice cultures reflect a more ‘natural and complete’ environment for the growth of neurons as the cells are:

- Not chemically digested with trypsin
- Not mechanically broken down by trituration
- Contain glial cells/astrocytes, which are essential for healthy neuronal development

Different regions of the brain from which the cells were obtained are shown in Figure 2-10.

Cells are determined by their difference in morphologies and are subsequently chosen in patch-clamp experiments. In Figure 2-11 the schematic shapes of different neurones are shown. The motoneurons of the brainstem were the most interesting cells for this study. This is because cells from some regions of the brainstem are known to produce action potentials without external stimulation.

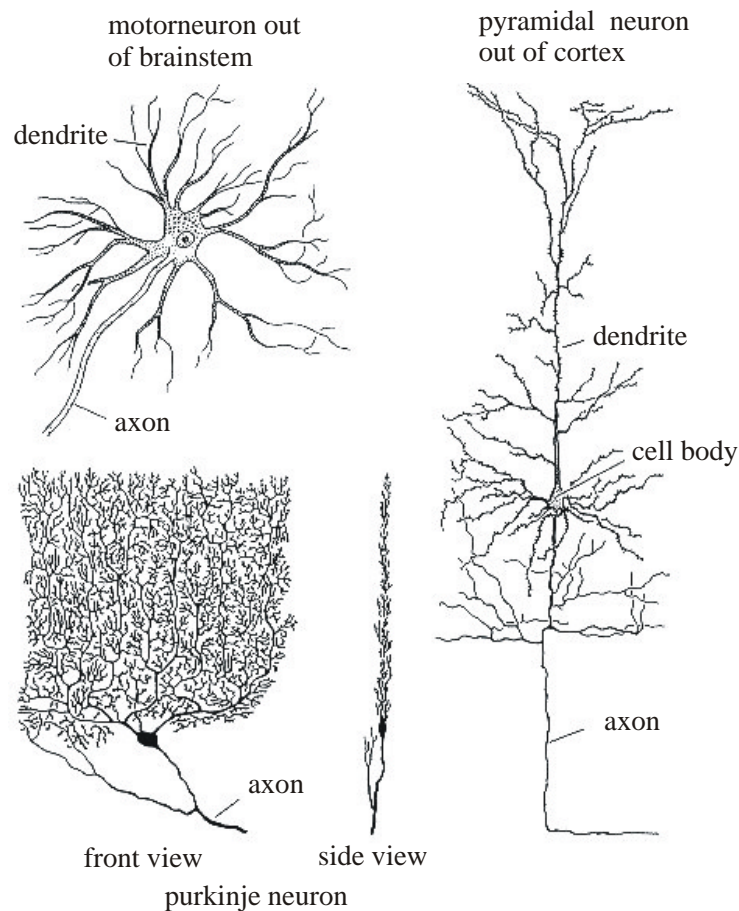


Figure 2-11 A schematic of different neuronal shapes. The figure was adapted from Nicholls et al. (1995). Motoneurons of the brainstem are known to produce action potentials without external stimulation. The Purkinje and pyramidal neurons can both be found in the cortical region and in the hippocampus.

In Figure 2-12 a picture of a motoneuron on a FET surface together with a schematic sketch describing different parts of cell body, axon, and dendrites is shown.

The cell body contains the nucleus, Golgi apparatus, mitochondria, endoplasmic reticulum, and other small structures, which are separated from the exterior by a phospholipid bilayer. In the photograph, it is surrounded by a round shaped dendritic region, which can receive signals from other cells via chemical synapses (axo-dendritic or dendro-dendritic connection). In the human body, a single massive axon can be several meters long. It is used for sending signals to the telodendria, which form presynaptic gates with other cells or are innervating muscle cells for stimulation.

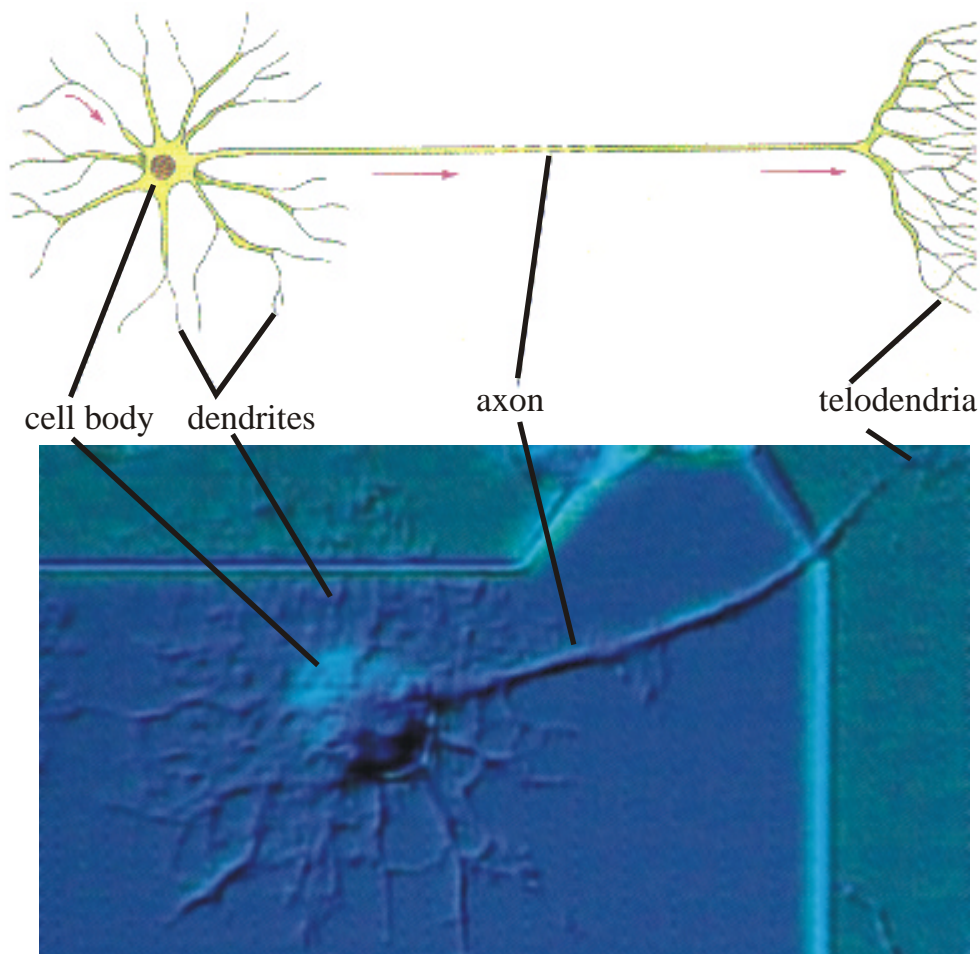


Figure 2-12 Motoneuron on FET surface. The corresponding parts of a motoneuron on the FET is compared to a diagram by Alberts et al. (1995). The cell body with a round shaped dendric region, one massive axon and some telodendria at the ending terminal of the axon. Unfortunately the cell was not located on a sensitive spot of the FET array.

The most important cell-cell contacts for the neurons are chemical synapses. The term synapse was first described by C. Sherrington in 1897. R.Y. Cajal obtained the first

morphological evidence for the existence of such cell-cell contacts in 1911. Synapses are contact regions between cells where signal propagation/transduction occur. There are two major differences in synapse types. First the chemical synapses, where a chemical coupling mechanism transmits an action potential. The distance in the synaptic cleft is about 50 nm. The presynaptic membrane contains many synaptic vesicles (about 50 up to several thousand) with a diameter of 50 nm, which store neurotransmitters at high concentrations. At present, many important neurotransmitters (e.g. acetylcholine, glutamate, serotonin, glycine, GABA, dopamine, norepinephrine) are known but their complete profiles are yet to be determined.

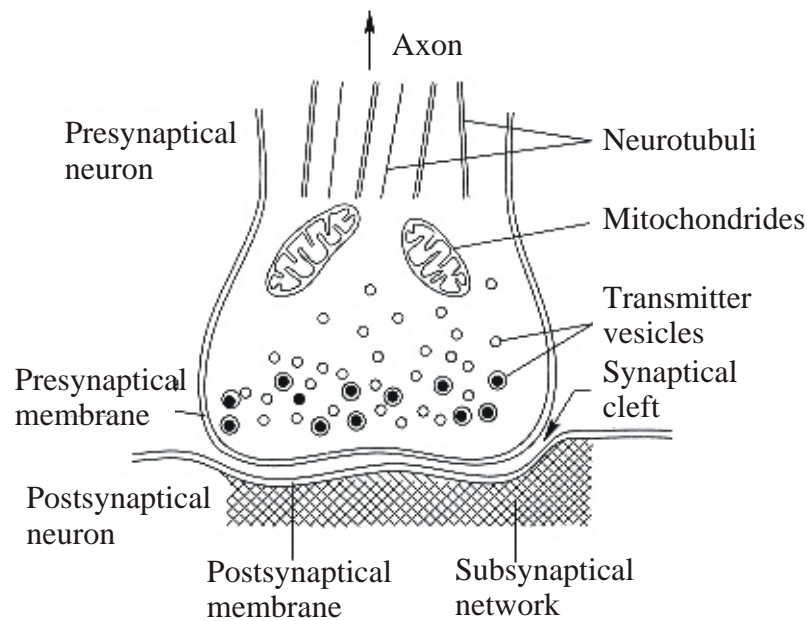


Figure 2-13 Schematical view of a chemical synapse. The cells are separated by a narrow cleft of about 50 nm. The neurotransmitter molecules are concentrated and stored inside the transmitter vesicles. When an action potential arrives at the presynaptic terminal, the neurotransmitters are released (exocytosis) into the cleft and activate the appropriate receptor molecules. The figure was adapted and modified from Hofmann (1996).

2.5 Cardiac Muscle Cells

All muscle cells contract by using mechanisms that convert energy derived from chemical reactions into mechanical energy. The major functions of muscles are to produce movements inside (cardiac muscles in propelling blood around the body) or outside the body (whole body movement).

There are three types of muscles: *skeletal*, *smooth* and *cardiac* cells. Each skeletal muscle fibre is a single cylindrical cell containing several peripherally located nuclei, whereas both cardiac and smooth muscles have a single, centrally located nucleus. They vary in size (length · diameter): skeletal (1-40 mm · 10-100 μm), smooth muscle cells (100-500 μm · 2-6 μm) and cardiac myocytes (50-100 μm · 10-20 μm). Cardiac muscle cells have a horizontal structure as shown in Figure 2-14. Once seeded, these cells form close contact to the fibronectin pretreated substrate surface.

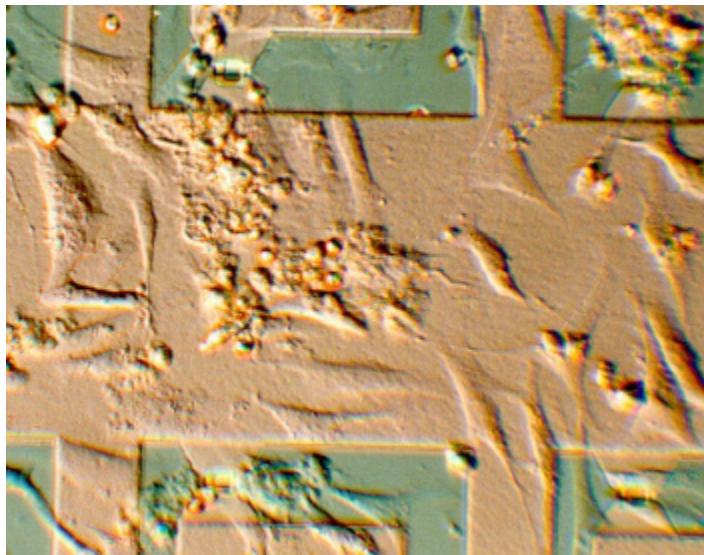


Figure 2-14 Cardiac myocytes cultured in a low density on a FET surface. The cell shape is elongated and the cells are attached to the substrate by a fibronectin coating. In this photograph (DIC-mode) the cells were cultured for one day on the surface.

In skeletal muscle fibres, *actin* and *myosin* myofilaments are organised to form sarcomeres, which when joined end to end form the myofibrils. Each sarcomere extends from one Z-line to an adjacent Z-line, which is a filamentous network of protein forming a structure for the attachment of actin myofilaments. The arrangement of the actin myofilaments and myosin myofilaments gives the myofibril a striated appearance when viewed longitudinally. Each light band (isotropic, I-band) includes a Z-line and the actin myofilaments. Each dark band (anisotropic, A-band) extends the length of the myofilaments within a sarcomere. The actin and myosin overlap for some distance at

both ends of the A-band. In the centre of the A-band is a smaller band called the H-zone where actin and myosin myofilaments do not overlap and only myosin myofilaments are present. M-line is in the middle of the H-zone and consists of delicate filaments that attach to the centre of the myosin myofilaments and hold them in place. During contraction of muscle fibres, actin and myosin filaments glide past each other without shortening.

Cardiac muscle tissue is striated like skeletal muscle but usually contains one centrally located nucleus. In Figure 2-15, the structure of a single cardiac myocyte of a rat is shown. Adjacent cells join together to form branching fibres by specialised cell-to-cell attachments called intercalated disks, which have gap junctions (form with connexin Cx43 proteins, Figure 2-16) that allow action potentials to pass from cell to cell.

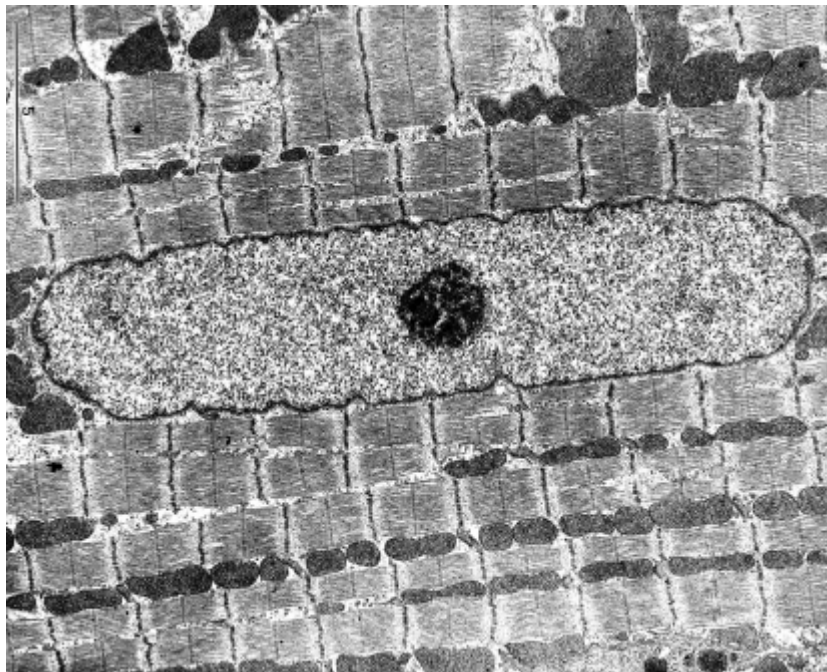


Figure 2-15 Structure of a rat cardiac myocyte. In the middle part, the nucleus can be seen. The myofibrills are seperated by mitochondria. In the sarcomeres, the darker Z-line and the lighter M-line can be seen. The actin and myosin filaments are mainly overlapping. The cell was in contracted condition. The figure was adapted from Kleinig and Sitte (1999).

This connection allows a very fast and synchronised transport of the pacemaker signal from the sinodal knot over the whole organ. In cultures, the cardiac myocytes formed a cell layer on the sensor surfaces. After a few days in culture, the dissociated cells are organised to form a tightly packed monolayer and connected by electrical junctions (see above) and are behaving like a ‘model heart’. In a culture such as this, cells from the sinoatrial and atrioventricular nodes are present (one chip contains 5000-

8000 cells). After 2-3 days, some of the cardiac myocytes become pacemaker cells and 'drive' the contractile rhythm of the entire monolayer over the sensor surface. The sealing properties of such a cell layer over the recording spot increase the overall amplitude of the extracellular signals. In chapter 6, the ability of such cellular-transistor hybrid systems in terms of biosensor application will be shown.

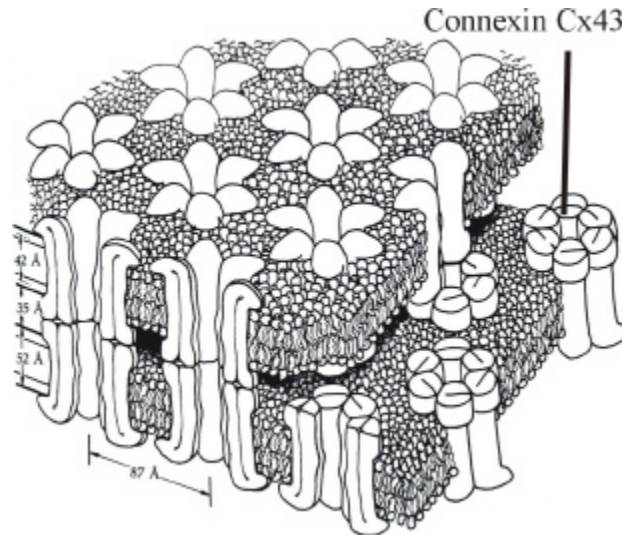


Figure 2-16 Schematic view of electrical synapses. Six subunits of the transmembrane connexin Cx43 proteins are joining and forming wide aqueous pores which can be passed by ionic currents. The figure was reconstructed from electron micrograph and x-ray diffraction images. It was adapted from Hille (1992).

Chapter 3

Low Noise Sensors for Biological Signal Transduction

In this chapter, the construction of extracellular sensors and the basic procedures developed for minimising the noise in our set-up will be described. In order to record extracellular signals in a voltage range of 10-100 μV , the external noise sources must be minimised.

First the transistor arrays will be discussed. The transistor gates are arranged in a 4x4 matrix on a single-crystalline silicon chip and have non-metallised gates like ion-sensitive (ISFET (Bergveld, 1970)) sensors. Three different types of FETs have been constructed: First *p*-channel FET-arrays, which are our standard devices and were the first transistors used in our group (Krause, 2000; Offenhäusser et al., 1997; Sprössler et al., 1998). Second type of devices are the *n*-channel FET-arrays, which showed better signal-to-noise ratios because the channel was partly buried using special process steps (Krause, 2000). The third type of device is backside-contacted *p*-channel FET-arrays,

which were developed during the present study. The backside contact offers a larger free area on the frontside of the sensor chip. With this special kind of device, it is now possible to adapt microflow systems, to culture larger slices on the FET chips and to develop sensors for Langmuir-Blodgett transfer of model membranes onto the sensor surface.

The second extracellular sensor type used in this study are metal electrodes made from gold and titanium (Krause et al., 2000). They only need one contact to the sensor spot, which makes an array of 8x8 channels on one chip possible. The measurement principle used at present is essentially the same as that in the FET set-up. During this work it became apparent that much lower noise levels can be achieved by using the gates of commercially available low-noise *junction field-effect transistors* (JFETs) adapted to the metal electrodes. Our electrode chips are thus called *extended gate electrode devices* (EGEs). Here the electrode channels are directly connected to the gate input of the JFETs, which performs an I-V conversion with very high impedance at the input stage. Using this concept, it was possible to work with much lower signal amplification at the input stage of the amplification circuit, which offers a wider frequency range and a lower noise level of this amplification stage.

In the first part of this chapter, the basic function of a field-effect transistor and the concept of biochemical sensing using non-metallised gates will be described. The sensors used in the present study (p-channel FETs, n-channel FETs, and EGEs), and the backside-contacted FET arrays will be discussed. The detailed processing steps for the production of the backside-contacted devices are shown in the appendix. At the end of this chapter, the basic procedures for tracking noise sources used in this work will be shown and how the noise level was minimised. A basic description of intrinsic noise comparing metal oxide FETs (MOSFETs) and JFETs will be given in the last part.

3.1 Functional Principle of a Field-Effect Transistor

For the basic understanding of the working principle of a field-effect transistor, the control of the electrical properties of semiconductors by external fields has to be elucidated.

The metal-oxide-semiconductor (MOS)-interface

In Figure 3-1 a MOS-structure with p-doped silicon as substrate (several 100 μm thick) is shown. The substrate is at the bottom contacted by a metal electrode B ('body' or 'bulk'), to which the potential of the counter electrode V_g is related. On the topside of the substrate an isolating layer of silicon oxide is formed by dry oxidation (thickness

$d_{ox} = 3\text{--}100\text{ nm}$), which is called gateoxide and is used in isolating the gate contact from the semiconductor bulk.

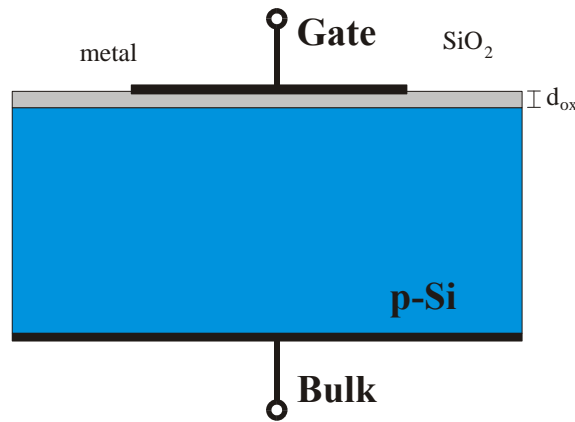


Figure 3-1 Cross-section of a metal-oxide-semiconductor (MOS) interface. The figure was adapted from Schlachetzki (1990).

As gate metal Al, Mo, W, Au, or highly doped polycrystalline silicon are in use. In this lateral structure, dimensional effects can be ignored. In the band model, such structures are described by the work function for electrons F_i from different materials into the vacuum region. For simplification the work function of the metal and the semiconductor are assumed to be equal (e.g. polysilicon gate). In addition, charged interface states in the Si/SiO₂ interface region or charges in the oxide film are ignored. The band model is thus without external voltage between G and B shown in Figure 3-2.

The Fermilevel W_F lies because of the p -doping of the semiconductor close to the valence band W_V . From W_F to the vacuum-level, the work functions F_M for the metal and F_{SC} for the semiconductor are plotted. Both materials are isolated from each other by a thin isolating layer with thickness d_{ox} . In the case of SiO₂, as isolating layer the band gap would be 9 eV. In Figure 3-2 a) the flatband situation is shown, where the bands of the semiconductor are horizontally touching the isolator layer. Applying a negative voltage V_g to the gate is attracting hole carriers from the semiconductor bulk to the interface region and is, in equilibrium condition, building up a positive charge under the isolating layer, which equalises the negative charge at the interface metal/isolator (Figure 3-2 b)).

If the gate is positive charged, which means V_g positive, depletion will take place (Figure 3-2 c)). The hole-carriers are repelled in the stationary state to the inner part of the semiconductor bulk. The uncompensated acceptor atoms (e.g. Boron) are bound in the silicon lattice, which leads to negative charges in a layer with thickness w . The band bending W_s is extended more and more into the semiconductor bulk with increasing V_g . The maximum band bending for depletion W_m is reached, when the distance between

W_C and W_F in the interface region is equal to the distance between the W_V and W_F in the semiconductor bulk.

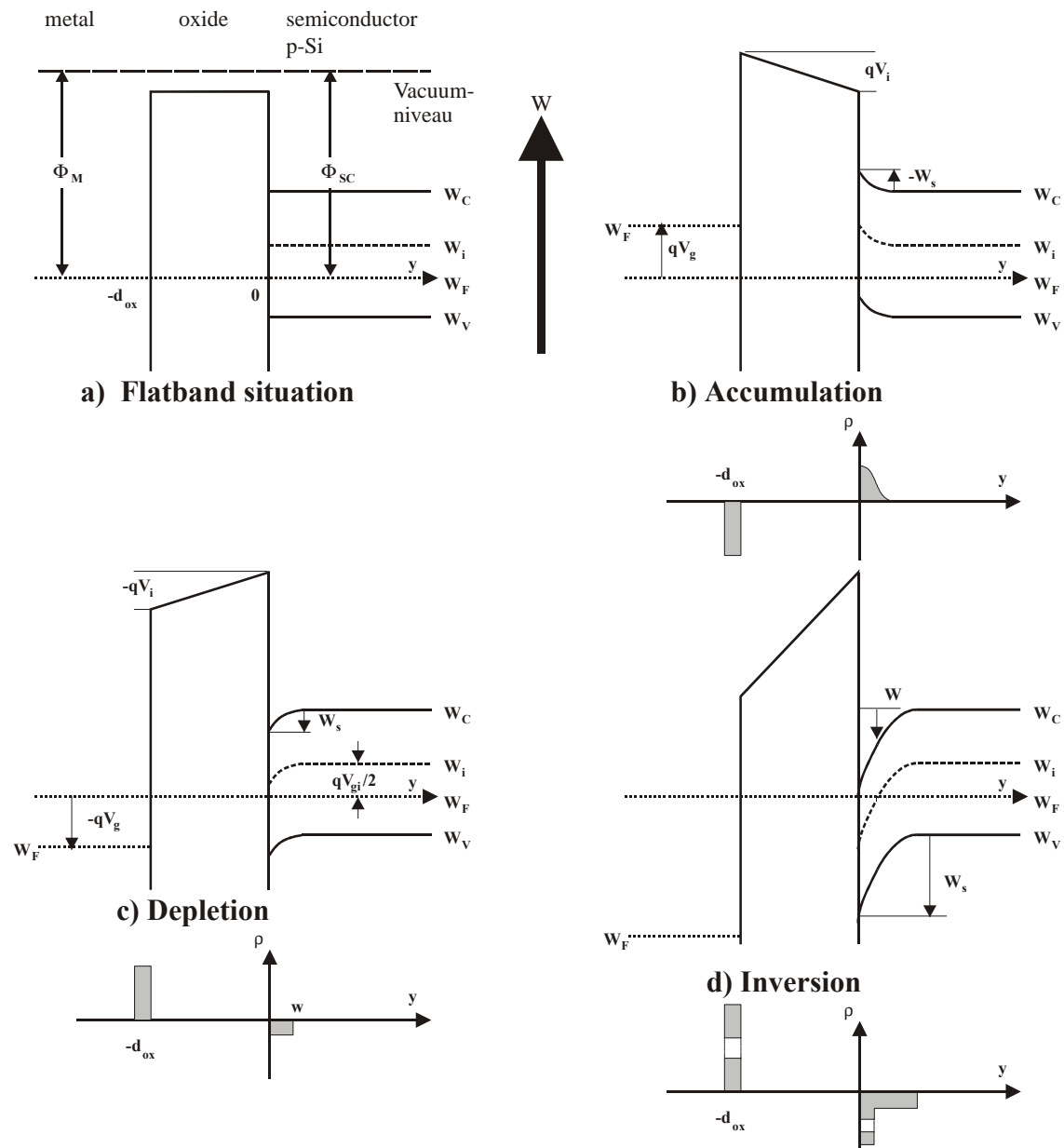


Figure 3-2 Band model of the metal oxide interface. An external voltage between G and B can shift the MOS-structure in the different modes of enhancement, depletion, and inversion. The figure was adapted from Schlachetzki (1990).

Because of the large carrier density in the metal, the negative charge on the gate is located at $y = -d_{ox}$. At the interface region of the semiconductor, the distance between the energy of the valence band and the Fermi level is reduced because of the higher hole-carrier density. This effect is called band-bending W_s , which is also present in the conducting W_C and in the intrinsic energy bands W_i . The electrical field is overlapping

the isolating layer, which leads to a voltage drop V_i inside of the semiconductor. The case where the gate is negatively charged with respect to the semiconductor bulk is called accumulation (p-doped silicon).

If V_g exceeds this value, the energy level W_C approximately equals to W_F such that the semiconductor interface region takes over an n-characteristic. This means it is now possible that n-carriers are accumulating at a very high concentration underneath the isolating layer and are shielding the electrical field between the gate and the semiconductor bulk. This situation is called inversion (Figure 3-2 d)) and the inversion region is called the channel of the MOS-structure.

In real substrates, the simplification of the same work functions for semiconductor and gate metal is clearly not valid. Even if no external voltage is applied, there are carriers flowing through the external contacts until the Fermilevels become equal. This leads to a potential difference between the gate metal and the semiconductor, which is called the contact potential F_{MS} .

$$q\Phi_{MS} = qV_i + qW_s = \Phi_M - \Phi_{SC} = \Phi_M - \left(W_c + \frac{1}{2}W_G + q\Phi_F \right) \quad (3.1)$$

The contact potential drops at the oxide with V_i and inside of the semiconductor with the band bending W_s . It is equal to the difference of the work functions F_M and F_{SC} per charge. The work function of the semiconductor is given by the electron affinity W_c , half of the band gap of the semiconductor W_G and the Fermilevel qF_F inside of the semiconductor bulk. Additional to the contact potential interface states Q_I in the oxide and the semiconductor/isolator interface are leading to a band bending. They are the main noise sources in the audio frequency range, which will be discussed later. The external voltage, which have to be applied in order to compensate these two effects, is called flatband voltage V_{FB} .

$$V_{FB} = \Phi_{MS} - \frac{Q_I}{C_I} \quad (3.2)$$

Here C_I is the capacitance of the interface. In Figure 3-2 this effect was ignored for simplification.

N-channel MOSFET

A field-effect transistor is a device that is highly sensitive to voltage changes at the gate input. A slight change in gate potential is coupled by an electrical field change over the thin gateoxide layer to a current, which is flowing directly below the thin gateoxide in the inversion channel.

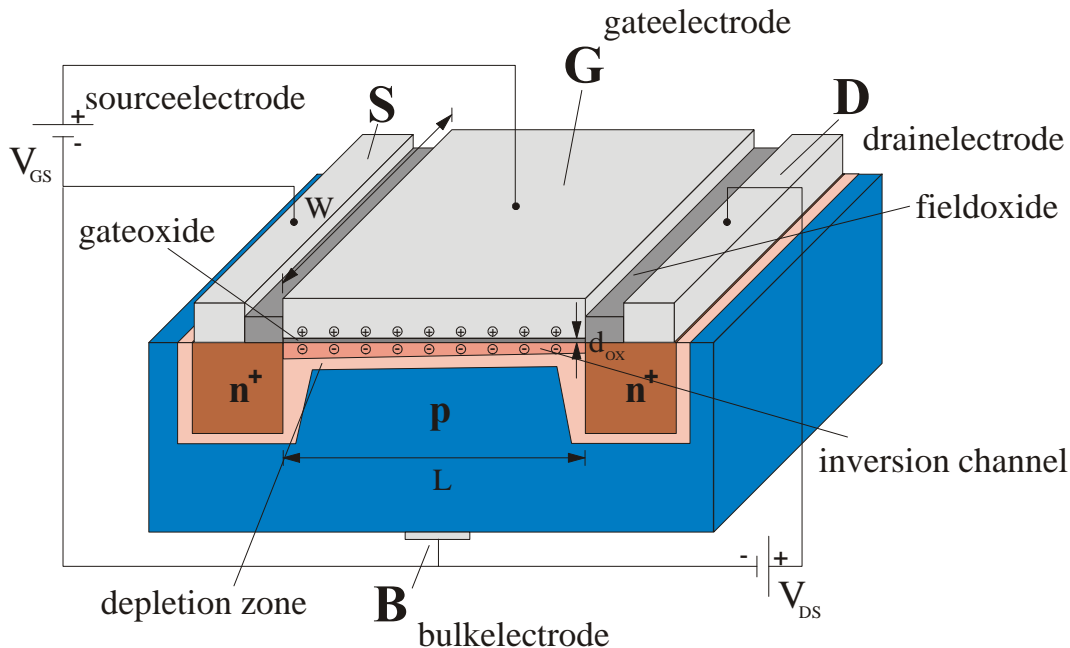


Figure 3-3 Schematical view of the structure and electrical contacts to the n-channel FETs used in this work. A slightly p-doped silicon chip having n-doped source and drain contacts. The gate metal is isolated from the channel with a thin (8-12 nm) silicon dioxide layer. With an appropriate gate-source voltage, an inversion channel is opening and a current is flowing between source and drain. This current is highly sensitive to potential changes at the gate input.

The inversion channel has metal contacts on both sides, which are called *source* and *drain* (the particular carriers for the respective device types are transported from source to drain). The current which is flowing is called drain-source current I_{DS} . The thickness of our non-metallised gateoxides is $d_{ox} = 8-12$ nm for the work in electrolyte solution. The industrial standard for metallised MOSFETs is 3-4 nm (Cho et al., 1998; Cho et al., 1999); Hattori et al., 1999; Lucovsky et al., 1997).

In Figure 3-3, a schematically view of an n-channel MOSFET is shown. In a slightly p-doped single crystalline silicon chip, the source and drain contacts are implanted with n-impurities in a very high density. The function of the transistor will now be discussed for the case of an enhancement mode n-channel FET.

Figure 3-4 is used for calculation of the drain-source current of the MOSFET. It is necessary to assume that the MOSFET structure contains enough mobile carriers, which can be injected from the source contact, after an inversion layer is formed by applying a sufficient gate-source voltage V_{GS} .

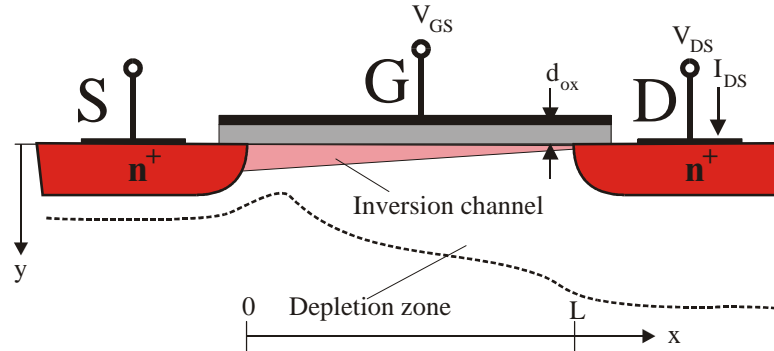


Figure 3-4 Schematical figure for the calculation of the drain-source current of the n-channel enhancement-mode MOSFET. The figure was adapted from Schlachetzki (1990).

All voltages are referred to the source electrode, which is normally connected to the bulk potential. The specific charge at a certain position x of the channel with length L is given by:

$$Q = c_{ox} \left(\frac{W_S}{q} - V_{GS} \right) \quad (3.3)$$

where the specific oxide capacitance is given with $c_{ox} = \epsilon_{ox}/d_{ox}$.

Both the charge Q and the band bending W_S are dependent on the position x in the channel. The total charge is the sum of the charge Q_B of the pinned acceptor atoms in the depletion zone and the charge of the mobile carriers Q_n (electrons) in the inversion channel. Therefore, the previous equation becomes:

$$Q_n(x) = Q - Q_B = c_{ox} \left(\frac{W_S(x)}{q} - V_{GS} \right) - Q_B(x) \quad (3.4)$$

Assuming the interface potential $W_S(x)/q$ to be given with V_{gi} (case for strong inversion) and with the voltage $V(x)$, which dropped because of the current I_{DS} at position x against source. The charge Q_B of the pinned acceptor atoms in the depletion zone can be calculated from the thickness $w(x)$ of the depletion zone with applied voltage $V(x) + V_{gi}$:

$$Q_B(x) = -qN_A w(x) = -\sqrt{2e \cdot qN_A (V(x) + V_{gi})} \quad (3.5)$$

This makes with Eq. 3.4 to become:

$$Q_n(x) = c_{ox}(V(x) + V_{gi} - V_{GS}) + \sqrt{2\mathbf{e} \cdot qN_A(V(x) + V_{gi})} \quad (3.6)$$

The drain-source current is given by the charge in the channel, its width and with the local field density $-dV/dx$:

$$I_{DS} = -Q_n(x)\mathbf{m}_nW \frac{dV}{dx} \quad (3.7)$$

Here W is the width of the channel and μ_n is the mobility of the carriers. It is for silicon at room temperature and small electrical fields: $\mu_p = 500 \text{ cm}^2/\text{Vs}$ and $\mu_n = 1450 \text{ cm}^2/\text{Vs}$ (Schlachetzki, 1990). Integrating this equation along the channel length L using V_{DS} at the drain-end and assuming a constant current I_{DS} in the whole channel leads to the source-drain characteristic of the n-channel MOSFET:

$$I_{DS} = c_{ox}\mathbf{m}_n \frac{W}{L} \left(\left(V_{GS} - V_{gi} - \frac{V_{DS}}{2} \right) V_{DS} - \frac{2}{3} \frac{\sqrt{2\mathbf{e} \cdot qN_A}}{c_{ox}} \left((V_{DS} + V_{gi})^{\frac{3}{2}} - V_{gi}^{\frac{3}{2}} \right) \right) \quad (3.8)$$

The threshold voltage V_{th} , at which the channel is open, is given by:

$$V_{th} = V_{gi} + \frac{1}{c_{ox}} \sqrt{2\mathbf{e} \cdot qN_A} V_{gi} \quad (3.9)$$

This value is strongly dependent on the technological and design properties, like doping density, dimensions, gate dielectric, and oxide thickness.

In Eq. 3.8, the linear characteristic in the low voltage region of the transistor characteristic is described. The curves are bending at a certain values into the saturation region. In this region, the curves are nearly parallel and there is always an inverted region between source and drain. To reach this, the gate-source voltage V_{GS} should always be higher than the drain-source voltage with:

$$V_{GS} - V_{th} > V_{DS} \geq 0 \quad (3.10)$$

The saturation region with its horizontal characteristic curves is reached, if the inversion channel at the drain-end of the channel is pinched off, which means the charge $Q_n(L)$ in the channel (Eq. 3.6) disappears. The pinch-off voltage V_{DS}^p is then calculated with:

$$V_{DS}^p = V_{DS} - V_{gi} + \frac{\mathbf{e} \cdot qN_A}{c_{ox}^2} \left(1 - \sqrt{1 + \frac{2c_{ox}^2 V_{GS}}{\mathbf{e} \cdot qN_A}} \right) \quad (3.11)$$

The respective saturation current I_{DS} can be calculated using Eq. 3.8. In good approximation for practical transistors the often-used formula for transistor design is:

$$I_{DS} \approx c_{ox}\mathbf{m}_n \frac{W}{2L} (V_{DS} - V_{th})^2 \quad (3.12)$$

Depletion-mode transistor:

The working principles of an n-channel depletion-mode device are as follows. The gate area at the initial stage is slightly n-doped and a current is already able to flow between source and drain only if a drain-source voltage V_{DS} is applied. Application of a negative voltage on the gate of the MOS capacitor will deplete the n-type channel region. An applied gate-source voltage V_{GS} modulates the conductivity of the channel. The width of the depletion region $w(x)$ is determined by the doping concentration N_D and the oxide thickness d_{ox} using following equation:

$$-V_{GS} = V_{Si} + V_{ox} = \left(\frac{qN_D}{2e_{Si}} \right) w^2(x) + \left(\frac{qN_D d_{ox}}{e_{ox}} \right) w(x) \quad (3.13)$$

The depletion width x_d increases as V_{GS} is made more negative. If the semiconductor substrate is thin enough, the entire substrate can be depleted before the surface inversion condition is reached (pinch-off voltage V_{DS}^p). The voltage V_{DS}^p can be calculated by substitution of the thickness of the semiconductor region D for $w(x)$ in the previous equation:

$$-V_{DS}^p = \left(\frac{qN_D}{2e_{Si}} \right) D^2 + \left(\frac{qN_D d_{ox}}{e_{ox}} \right) D \quad (3.14)$$

In analogy to the enhancement-mode transistor, conditions are needed such that the drain current I_{DS} will saturate when V_{DS} becomes sufficient large. Therefore, the gate and drain voltages must act together to reduce the thickness of the conducting channel at the drain end below the value it has at the source end (pinch-off at the drain end at $V_{DS} = (V_{GS} - V_{DS}^p)$). By neglecting the voltage drop across the depleted semiconductor region the drain-source current I_{DS} can be described by:

$$I_{DS} = \frac{\mathbf{s} \cdot \mathbf{W}}{L} \left(V_{DS} + \frac{V_{DS}^2}{V_{DS}^p} \right) \quad (3.15)$$

with the channel conductivity \mathbf{s} .

Real Transistors:

For real transistors, some modifications to the above discussed transistor characteristics have to be made. First a more than one-dimensional field in the gate area has to be considered, which reduces the mobility of the carriers close to the surface. The electrical field E_x perpendicular to the gateoxide layer is accelerating the carriers into the oxide/semiconductor interface region. Here, a scattering process is taking place, which reduces the average mobility of the carriers. The reduced effective mobility μ_{eff} is given by

$$\mathbf{m}_{eff}^* = \frac{\mathbf{m}_0}{1 - \mathbf{q}(V_{GS} - V_{th})} \quad (3.16)$$

with the surface scattering factor \mathbf{q} . In addition a high electrical field E_y parallel to the surface leads to velocity saturation. A good approximation to this effect is done by further correcting the effective mobility with:

$$\mathbf{m}_{eff} = \frac{\mathbf{m}_{eff}^*}{1 + \frac{V_{GS}}{LE_c}} \quad (3.17)$$

The correction field E_c is dependent on the parameter and the type of semiconductor. Typical values, E_c , for holes are between 2-10 V/ μm .

For $|V_{DS}| > |V_{DS}^p|$ the pinch-off point is shifted towards the source region and the inversion channel length is reduced. This results in a 2-dimensional electrical field in the drain region. A simple model is able to describe these effects with a correction term for the drain-source current (Paul, 1994):

$$I_{DS}^{\max} = I_{DS}^{\max*} \left(1 - \frac{V_{DS} - V_{DS}^p}{V_A} \right) \quad (3.18)$$

The extrapolation of the linear part in the saturation region leads to the so-called Early-voltage V_A .

The resistances of the drain and source connections are usually ignored in the theoretical description. They are playing a major role in our FET device performance. Because of the special design of the transistor arrays used in this study (especially for the backside-contacted devices) the source and drain lanes are several 100 μm long. For the determination of the resulting drain-source current, this behaves like a reduced mobility, although the mechanism is completely different. Together with the correction discussed before it leads to the following corrections for I_{DS} :

$$I_{DS}^* = \frac{1}{1 - (\mathbf{q} + \mathbf{a})(V_{GS} - V_{th})} \cdot \frac{1}{1 + \frac{V_{DS}}{LE_c}} I_{DS} \quad (3.19)$$

With the correction \mathbf{a} caused by the source R_S and drain resistance R_D defined as follow:

$$\mathbf{a} = \mathbf{m}_p \cdot \frac{W}{L} c_{ox} (R_S + R_D) \quad (3.20)$$

which aggravates the transistor's performance.

Small-signal model:

In addition to the transfer and output characteristics, the dynamic properties of the transistor are important. For a standard source circuit, small signal parameters can be determined by partial differentiation:

$$g_m = \left. \frac{\partial I_{DS}}{\partial V_{GS}} \right|_{V_{BS}, V_{DS}} \quad g_{mb} = \left. \frac{\partial I_{DS}}{\partial V_{BS}} \right|_{V_{GS}, V_{DS}} \quad g_d = \left. \frac{\partial I_{DS}}{\partial V_{DS}} \right|_{V_{GS}, V_{BS}} \quad (3.21)$$

The most important parameter is the transconductance g_m , which is in the active region independent of the gate-source voltage V_{GS} for the ideal transistor (for the range $-V_{DS} \sim -V_{DS}^p$):

$$g_m = -m_p c_{ox} \cdot \frac{W}{L} V_{DS} \quad (3.22)$$

Using the corrections introduced before (Eq. 3.17), the transconductance is reduced with increasing gate voltage. In the saturation region, the transconductance g_m depends on the drain-source current for $-V_{DS} \sim -V_{DS}^p$:

$$g_m = \frac{2I_{DS}^{\max}}{V_{GS} - V_{th}} \quad (3.23)$$

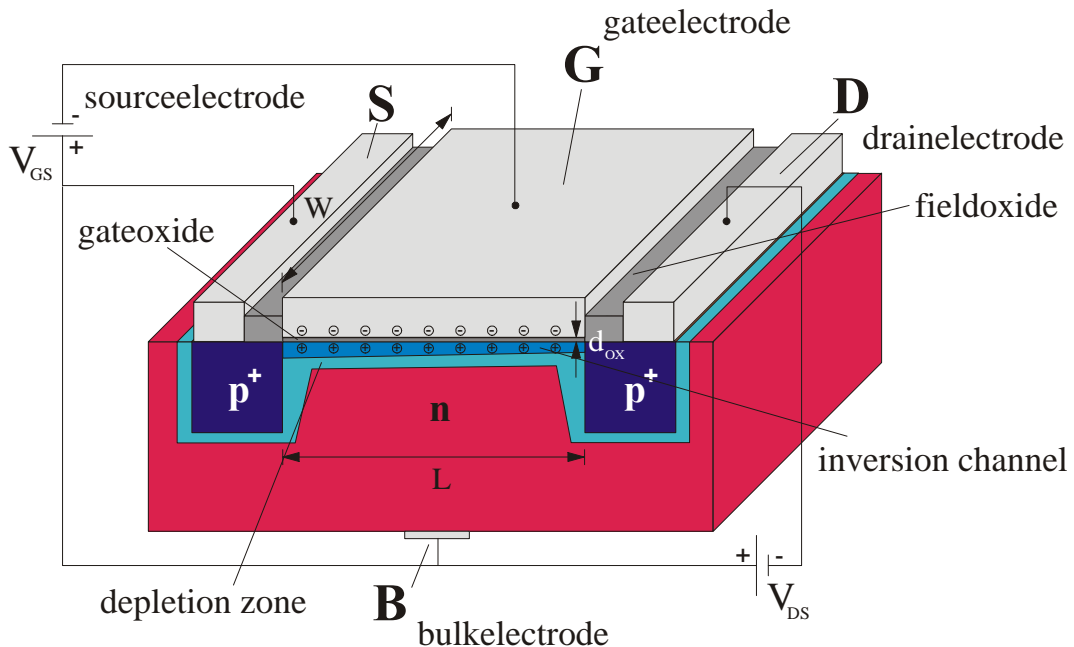
P-channel MOSFET

Figure 3-5 Schematical view of the structure and electrical contacts to the p-channel FETs used in the present study.

The structure of a p-channel FET is shown in Figure 3-5. In slightly n-doped single crystalline silicon, the source and drain contacts are highly implanted with p-impurities. All voltages applied to the transistor are counted as negative and the characteristic curves are located in the third quadrant.

3.2 Sensors for Bioelectronic Signal Transduction

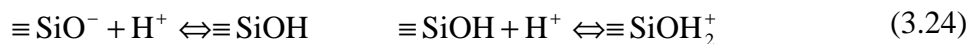
In the following section, the sensor devices used in this work will be described. First the concept of the ion sensitive field-effect transistor (ISFET), which were first invented by Bergveld (1970), will be explained. The layout, encapsulation, operation modes, and characteristics of the 16-channel p- and n-channel FET devices will be shown. In the next part, the backside-contacted FET arrays will be introduced. After this the metal electrode layouts developed by Krause (2000) will be shown. A new encapsulation and the concept of combining standard metal microelectrodes with low noise junction field effect transistors that were developed during this work and will be shown at the end of this paragraph.

3.2.1 Ion-sensitive Field-Effect Transistors

The electrolyte-oxide-semiconductor (EOS)-interface

In the MOS-system, the gate voltage is applied to the metal or polysilicon gate contact and the voltage drops over the gateoxide and inside the semiconductor bulk. In an ion sensitive field effect transistor, the gate is not metallised and is in contact with the electrolyte solution and a reference electrode (in most cases an Ag/AgCl reference (Figure 3-6)). The voltage drop happens in this electrolyte–oxide–semiconductor system. Yates et al. (1974) have described this system theoretically with the Site-Binding model for thermal oxidised silicon (SiO₂) (Yates et al., 1974).

Having contacted the aqueous electrolyte hydrolyses the SiO₂-surface and silanol groups (SiOH) are being built. These groups are pH-dependent with:



The surface groups may be negative, neutral, or positive charged. In an equilibrium reaction these charged groups are attracting counter ions from the electrolyte solution. The pH-value, where the surface is neutral is called the *Point of Zero Charge* (pH_{pzc}) and is for SiO₂-surfaces 2...2.5 (Bousse, 1982).

Together with the absorbed counter ions, the charged surface is building a Helmholtz double layer. In the Stern-model, this double layer is followed by a diffuse Gouy-Chapman-layer. The potential drop Ψ_d and the thickness L_d of the diffuse layer in the

electrolyte is dependent on the carrier concentration based on the Poisson-Boltzmann equation. By using high ionic concentration of 0.2 M, the Gouy-Chapman-layer is fused with the Helmholtz layer and L_d is within the range of the molecular distances (Wedler, 1987).

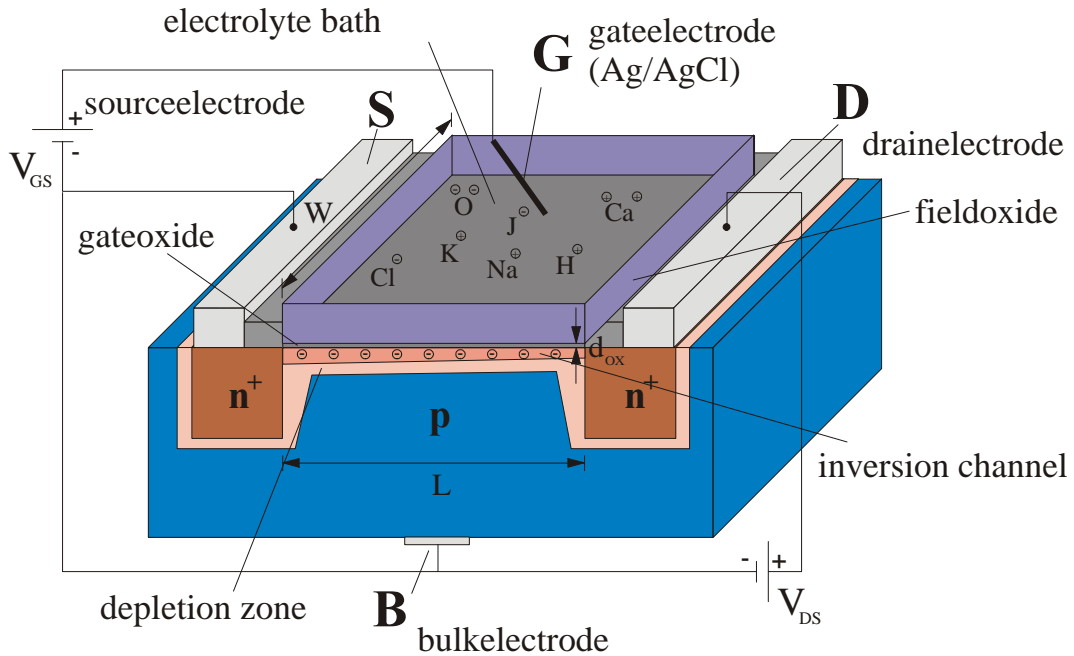


Figure 3-6 Schematical view of an n-channel ISFET. The metal gate is replaced by an electrolyte bath chamber contacted with an Ag/AgCl reference electrode.

Similar to the MOS-system (Eq. 3.2), the flatband voltage V_{FB}^E for the electrolyte system is defined by the work function (Bousse, 1982):

$$V_{FB}^E = V_{ref} - \frac{1}{q} \Phi_{SC} - \Psi_E - \frac{Q_I}{C_I} + c^E + dc \quad (3.25)$$

The work function of the metal in this equation is replaced with the potential of the reference electrode V_{ref} relative to the vacuum level. The vacuum level can be calculated with the electrode potential relative to the normal hydrogen electrode (NHE) plus the value of the Fermilevel relative to the vacuum state ($V_{NHE} = 4.7$ V (Bousse et al., 1983)). For the Ag/AgCl-electrode a value of $V_{ref} = 4.9$ V is calculated.

The surface potential c^E cannot be directly measured. However, in the literature, a value of $c^E \approx 0.03$ V for the ion concentrations used is stated (Madden et al., 1977). The value of the potential dc caused by the contact to the electrolyte is not known but measurements with other electrodes show only very small differences and therefore this value is negligible (Frumkin et al., 1974). The potential drop at the electrolyte surface Ψ_E is in accordance to the *Site-Binding-model* related to the pH-value of the electrolyte (Bousse et al., 1983; Siu and Cobbold, 1979), which is used by the ion-sensitive field-

effect transistors. The experimental value for the pH-dependent potential drop in the electrolyte is $Y_E = 37 \text{ mV/pH}$. With the point of zero charge value of $\text{pH}_{pzc} = 2.2$ (Bousse et al., 1983) the potential drop in the cell culture electrolyte ($\text{pH} = 7.4$) is thus calculated to be $Y_E \approx 0.19 \text{ V}$. In the MOS-system, the contact potential with aluminium as gate material lies at $F_{MS} = -0.25 \text{ V}$, whereas the value for the EOS-system is $F_{ES} = 0.44 \text{ V}$. Values for the work function for aluminium and n-doped silicon are $F_M = 4.1 \text{ V}$ and $F_{SC} = 4.3 \text{ V}$, respectively (Ruge and Mader, 1991). These results with unchanged oxide charge as starting condition in a change of the contact potential of $\Delta V_{FB} = 0.69 \text{ V}$.

In the work of Bousse et al. (1983) the flatband voltages for the MOS- and EOS-systems were obtained with capacitance measurements. For n-doped silicon and an ion concentration of 0.1 M for the electrolyte solution ($\text{pH} = 2.2$), a change in flatband voltage of $\Delta V_{FB} \approx 0.86 \text{ V}$ was measured (Bousse, 1982). With the potential drop over the electrolyte at a pH-value of $\text{pH} = 7.4$ The total change in the flatband voltage is $\Delta V_{FB} \approx 0.88 \text{ V}$.

The flatband voltage of an EOSFET is shifted with this constant value compared to a classical MOSFET with aluminium as the gate material. The potential drop in the electrolyte is in an ideal situation only dependent to the pH-value of the electrolyte. An additionally applied voltage, V , drops only at the gateoxide and inside of the semiconductor bulk material. Because of the much larger capacitance of the electrolyte/solid interface ($c_d \approx 20 \mu\text{Fcm}^{-2}$) compared to the gateoxide capacitance ($c_l \approx 0.5 \mu\text{Fcm}^{-2}$) it has only little influence.

3.2.2 16-channel FET-Arrays for Cell-Transistor Measurements

The standard devices used in this work were developed and had been previously characterised by Krause (2000). The FET array consists of 4x4 equal transistor gates arranged in a square on a 5x5 mm² silicon chip. The gate distances are 100 and 200 μm as indicated in Figure 3-7 and Figure 3-8, respectively.

The fabrication process and the variation of the gate sizes from 4x2 μm² up to 16x4 μm² are described by Krause (2000). The FET devices with gates spacing of 200 μm were primarily used in the present study. The layout of the gate area and the structure of a single gate are shown in Figure 3-8.

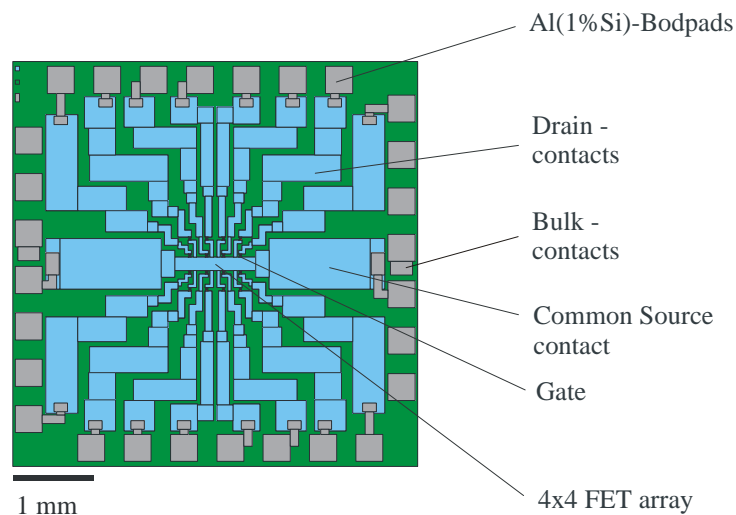


Figure 3-7 Layout of the 16-channel FET-arrays.

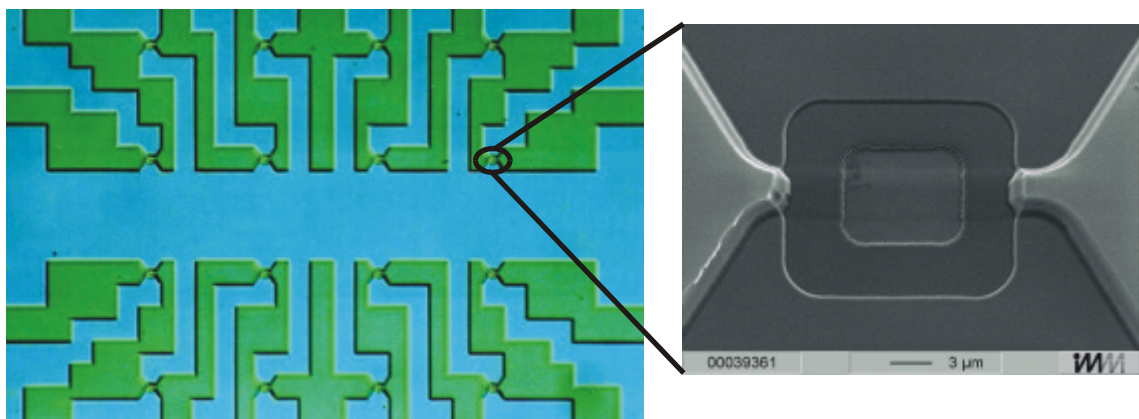


Figure 3-8 Layout of the used FET-arrays in the gate area (left side) (DIC-microscope picture). On the right side the detailed view of a single gate structure is shown (SEM-microscope).

The chips were encapsulated as previously described (Krause, 2000; Offenhusser et al., 1997; Sprossler, 1997). The $5 \times 5 \text{ mm}^2$ FET chips were cleaned in an ultrasonic ethanol/acetone bath to remove photolithography varnish residues. The chips were then glued with two-component glue (EPO-TEK H20E-175, Epoxy Technology Inc., USA) onto a 28pin DIL-ceramic socket holder. The contacts from chip to socket were done by wirebonding with a $25 \mu\text{m}$ aluminium wire (Al/1% Si) using ultrasonic bonding (Westbond, USA). The area for cell culture was provided by gluing a glass ring (d=16 mm, h=3 mm) onto the DIL socket and a small funnel onto the silicon chip. The funnel was made by mould technique using PDMS (SYLGARD 182, Dow Corning, Germany).

The resulting funnel provides a free area of $A \approx 7 \text{ mm}^2$ (3 mm diameter) for culturing cells on the chip. The free volume between glass ring and funnel was filled with isolating PDMS glue (SYLGARD 96-083, Dow Corning, Germany) to prevent shortcuts between bondwires and electrolyte bath. The total bath volume was about $400 \mu\text{l}$. The fully encapsulated FET chip is shown in Figure 3-9.

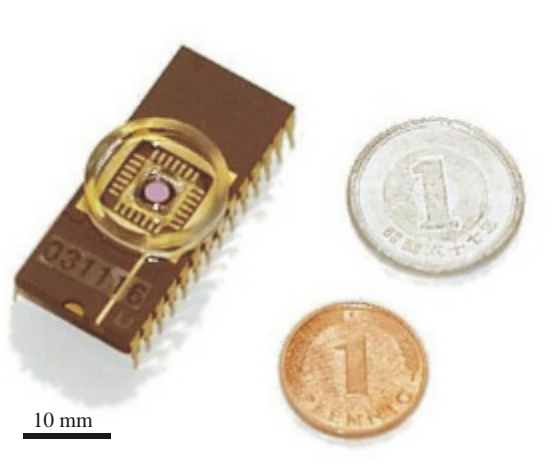


Figure 3-9 16-channel FET chip in standard encapsulation. The chip was glued onto a 28pin DIL socket and a little bath chamber for cell culturing was formed by a glass ring and a little funnel glued onto the chip.

3.2.3 Characterisation of the FET-Chips

The characterisation of the FET chips was done by measuring the output characteristics $I_{DS}(V_{DS})$ at constant V_{GS} and the transfer characteristics $I_{DS}(V_{GS})$ at constant V_{DS} . The amplification was then determined by differentiating the transfer curve and calculating g_m for the steepest working point. The electrical contacts are slightly modified compared to the classical FET set-up, because the electrolyte – which is the gate electrode – should be held at ground potential for using the chips together with a patch-clamp probe. On the frontside of the main amplifiers, the variable

potentials 'AP' and 'FET' are shown, which define the source, drain, and gate potentials. Because of the restrictions posed by the amplifier set-up, the current range for I_{DS} can only operate between -1mA and $+1\text{mA}$. The potentials are defined as following:

$$\begin{aligned} AP &= -V_{GS} \\ FET &= -V_{GS} + V_{DS} \end{aligned} \quad (3.26)$$

In Figure 3-10 the electrical set-up for the FET chips is shown.

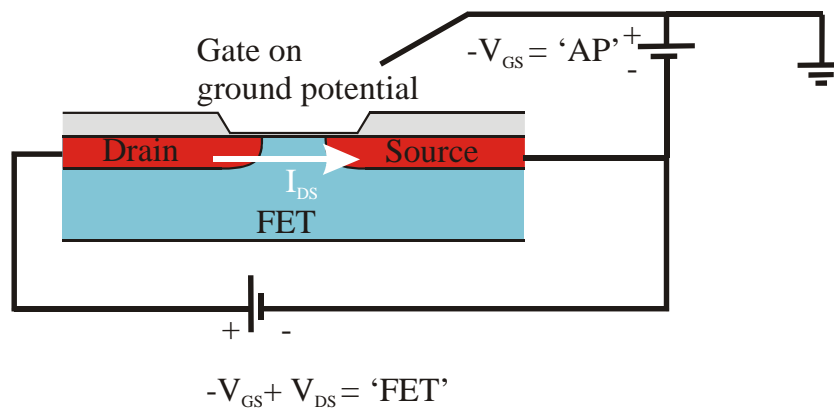


Figure 3-10 Electrical contacts to the transistor. The electrolyte, which corresponds to the gateelectrode, should be held on ground potential for working with patch-clamp probes in addition. The definitions for the two potentials 'AP' and 'FET' shown on the frontside of the main amplifiers are indicated in the figure.

3.2.4 p-channel FET-Arrays for Cell-Transistor Measurements

Figure 3-11 shows the characteristics for a p-channel FET array with gate dimensions of $3 \times 16 \mu\text{m}$ and a gateoxide thickness of 12 nm. The characteristic curves are in the third quadrant by convention and all voltages are counted to be negative. The top graph shows the output characteristics $I_{DS}(V_{DS})$ in a range of $V_{DS} = 0 \dots -3 \text{ V}$ at constant V_{GS} from $0 \dots -2.4 \text{ V}$.

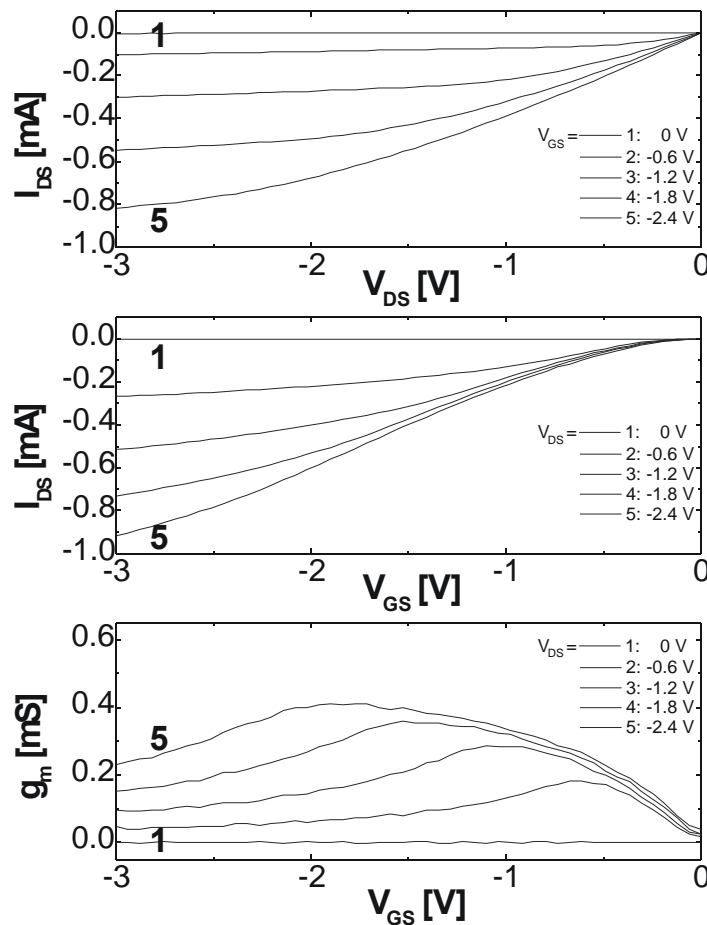


Figure 3-11 Characterisation of a p-channel transistor. In the top traces the output characteristics is shown with $I_{DS}(V_{DS})$. In the middle part the transfer characteristics $I_{DS}(V_{GS})$ and in the bottom graph the transconductance $g_m(V_{GS})$ is shown.

The plot shows an enhancement mode transistor, as a gate-source voltage has to be applied to open the channel between source and drain. The middle graph shows the transfer characteristics $I_{DS}(V_{GS})$ in a range of $V_{DS} = 0 \dots -3 \text{ V}$ at constant gate-source voltage V_{GS} from $0 \dots -2.4 \text{ V}$. The bottom graph is the numerical derivative of the middle graph and is called the transconductance of the transistor. An ideal working point for this device would thus be: $V_{DS} = -2.4 \text{ V}$ and $V_{GS} = -2 \text{ V}$ with $g_m = 0.4 \text{ mS}$. In the bottom

plot, it can be seen that the transistor has a threshold voltage ($V_{th} = -0.1$ V) very close to 0 V. For the different gate sizes and different gateoxide thickness of the p-channel arrays, the transconductance values are in the range of $g_m = 0.2 \dots 0.6$ mS.

3.2.5 n-channel FET-Arrays for Cell-Transistor Measurements

Figure 3-12 shows the characteristic curves for an n-channel FET array with gate dimensions of $3 \times 16 \mu\text{m}$ and a gateoxide thickness of 12 nm. The characteristic curves are located in the first quadrant by convention and all voltages are considered to be positive. The top graph shows the output characteristics $I_{DS}(V_{DS})$ in a range of $V_{DS} = 0 \dots 3$ V at constant V_{GS} from $0 \dots 2.4$ V.

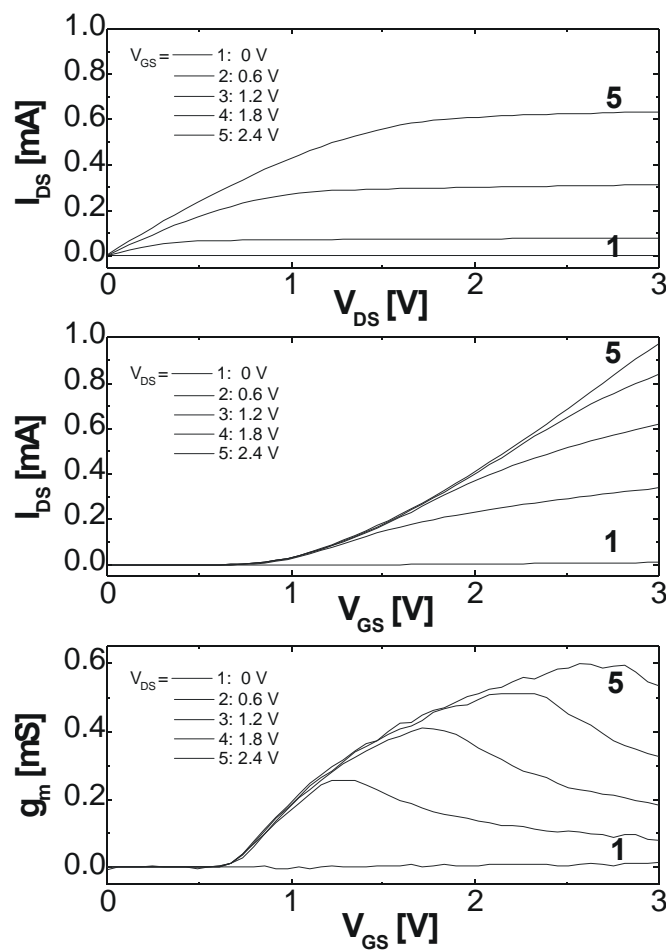


Figure 3-12 Characterisation of a n-channel transistor. In the top traces the output characteristics is shown with $I_{DS}(V_{DS})$. In the middle part the transfer characteristics $I_{DS}(V_{GS})$ was measured and numerically derived in the bottom plot.

The plot shows an enhancement-mode transistor, as a positive gate-source voltage has to be applied to open the channel between source and drain. The middle graph

shows the transfer characteristics $I_{DS}(V_{DS})$ in a range of $V_{DS} = 0 \dots 3$ V at constant V_{GS} from $0 \dots 2.4$ V. The point at $V_{DS} = 2.4$ V and $V_{GS} = 2.7$ V with $g_m = 0.6$ mS is a good working point for this device, which is higher than for a p-channel FET with same gate dimensions. In the bottom plot it can be seen that the transistor has a threshold of $V_{th} = 0.6$ V.

For different gate sizes and different gateoxide thickness of the n-channel arrays, the transconductance values are lying in the range of $g_m = 0.4 \dots 1.5$ mS. The values for the n-channel FET arrays are higher because of the following reasons:

For an ideal transistor, the transconductance g_m is only dependent on the gateoxide thickness, the channel dimensions length L and width W , and on the carrier mobility in the channel μ . In the linear region, which is shown in the top graph of Figure 3-12 with the range $V_{DS} = 0 \dots 0.5$ V, the transconductance is independent on the drain-source current I_{DS} with:

$$g_m = m_{n/p} \frac{e_{ox}}{d_{ox}} \frac{W}{L} V_{DS} \quad (3.27)$$

In the saturation region the transconductance is dependent on the square route of I_{DS} :

$$g_m = \frac{\sqrt{2m_{n/p} e_{ox} I_{DS}}}{W d_{ox}} \quad (3.28)$$

As discussed before electrons have about three times higher mobility in a single crystalline silicon than holes. This is the reason for higher transconductance values of the n-channel transistor arrays. The evaluation of all available gate dimensions and oxide thickness have shown that the highest transconductance for the transistor arrays could be obtained with the shortest length of $L = 2$ μm , the widest channel $W = 16$ μm , and the thinnest gateoxides of $d_{ox} = 8$ nm.

Our n-channel FET chips have advantageous in terms of the noise level, because the channel was partly buried by special processing steps (see below) and in terms of amplification properties due to higher transconductance. The main disadvantage is caused by the positive gate-source voltage, which has to be applied for an n-channel enhancement-mode transistor. This voltage is causing problems, because positive ions are being attracted to the gateoxide and are accumulating inside the amorphous oxide layer. This results in a high DC-drift in the normally constant drain-source current and subsequently creating conducting pathways through the isolating SiO_2 . Once these pathways are established, the gateoxide of the transistor is partly destroyed, which renders the device useless. The present work focused on the use of n-channel chips for cell-transistor coupling measurements, because the voltages are only being applied to the chips for a short period (1-2 min). For the experiments with the cardiac myocyte cell layers (up to 20 min) they were very rarely used, because of the very weak long-term

stability. To overcome this problem, an additional gate implant was tested at the end of the fabrication process of the n-channel wafers in order to shift the threshold voltage V_{th} to values that are more negative.

Gate implant for the n-channel FET arrays

With an additional gate implant at the end of the production process, it was possible to shift the transfer characteristics of the n-channel FETs to values that are more negative.

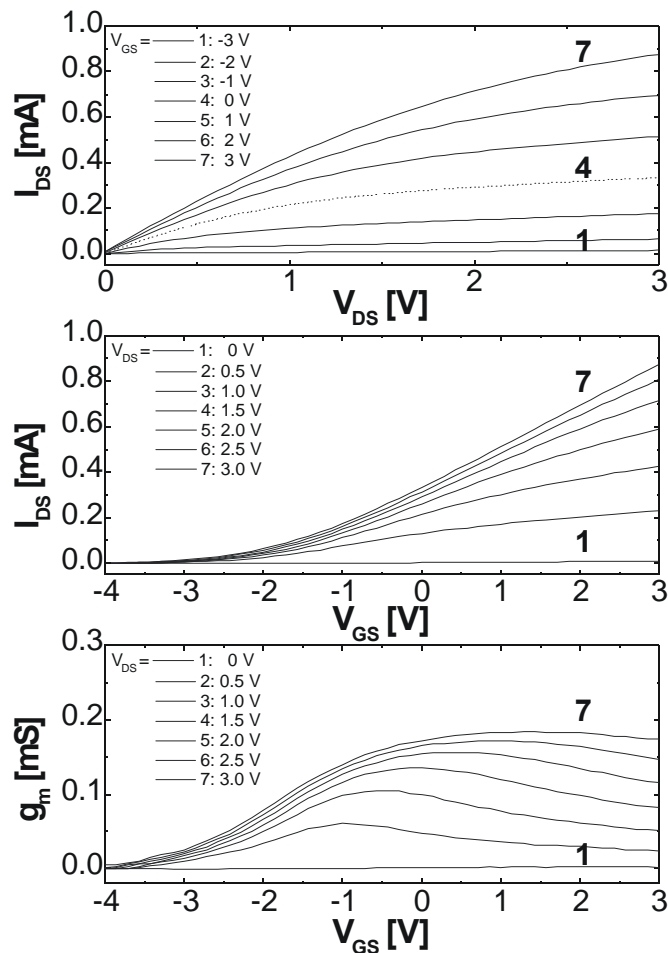


Figure 3-13 Gate-implant to the enhancement mode n-channel FETs. In the upper trace it can be seen that the chip can be operated in both, enhancement- and depletion-mode as the zero voltage curve (dotted) had already a transistor-like characteristics. The threshold voltage was shifted to $V_{th} = -4.1$ V, which can be seen in the lower plots.

The ions were implanted through the existing gate windows with a very low dose of $1 \cdot 10^{12}$ ions/cm² and a very low acceleration voltage of $V_{acc} = 30$ keV. With this procedure, the transfer characteristic shifted and the transistors were transformed in a

bi-mode type. Figure 3-13 illustrates how the transistor can be driven in both, enhancement- and depletion-mode.

The main disadvantage of the gate implant was that the noise level of these devices became too high (about factor of 2 to 3 higher). This may be caused by trapped ions inside of the gateoxide or the number of interfacial states increased because of a damaged structure. This always results in a higher generation-recombination noise (see below). In addition, this process was very un-reliable, because only a fraction of the chips on one wafer was shifted in the optimal way. Many of the transistors showed only resistor-like characteristics as the channel path became completely conducting.

3.2.6 Backside-contacted Field-Effect Transistors

A special chip design of backside contacts to the transistor arrays was developed in the present study. The main advantage is that no wirebonding to the chips was necessary. The contacts were established with the flip-chip technique (Lau, 1995). The mask design of the $6 \times 6 \text{ mm}^2$ chips was adapted to the dimensions of a special 22pin DIL chip carrier (KD-77261-B-JMI, Spectrum Semiconductor Materials Inc., San Jose, USA) and the chips are being glued on top of the gold-plated bond pads of the chip carrier.

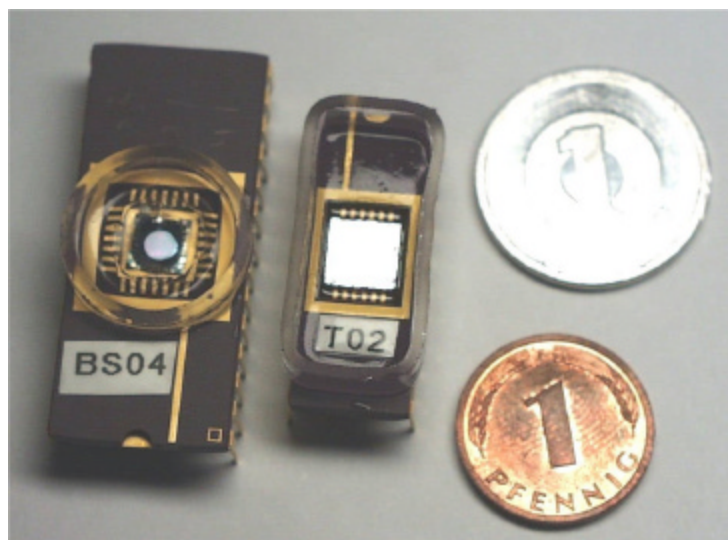


Figure 3-14 Encapsulated backside-contacted FET chip (middle). On the left side the standard FET device is shown for size comparison. The reflecting area in the middle of each device is the free space available for cell culturing.

The chip encapsulation was performed after gluing a rectangular glass ring on top of the chip carrier and using an isolating epoxy underfill to prevent shortcuts between the flip-chip bumps and filling up the bath chamber with PDMS glue (SYLGARD 96-083, Dow Corning, Germany) (Figure 3-14).

A much wider free space for cell culturing is available with this device (standard device: 7 mm², backside-contacted device: 36 mm²). The bath chamber carries 700 µl of culture medium, which is almost twice the amount of medium in the standard devices. The topology of the device is almost flat, which is important for cell density control when cells are being plated on the surface. In the standard FET-chips, cells tended to accumulate at the edge of the funnel. The flip-chip process was done with the combination of screen-printer and fineplacer set-up arranged by Krause (2000) (Figure 3-15) and the use of a two-component flip-chip epoxy glue (EPO-TEK H20E-PFC, Epoxy Technology Inc., USA). The optical controlled fineplacer unit (FINEPLACER-145 "PICO", FINTECH electronic, Germany) offers a very high xy-accuracy, which made the alignment of laminin-grids using a microcontact printing process on the sensor surfaces possible (Lauer et al., 2001).

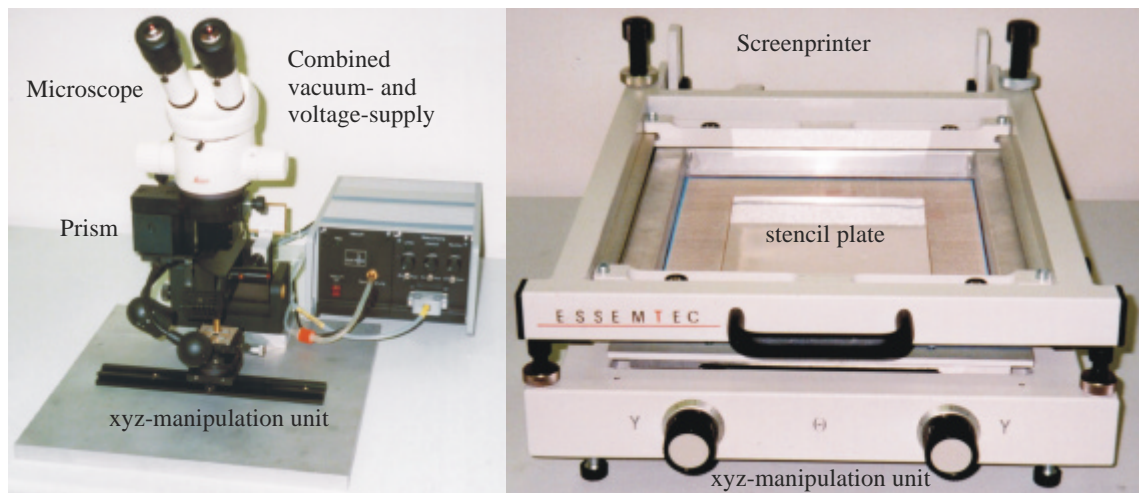


Figure 3-15 Set-up for flip-chip contacting the backside-contacted FET arrays and the EGE-chips. The whole set-up was arranged by Krause (2000). On the right side the screenprinter (ESSEMTEC SP-002, ESSEMTEC AG, Schweiz) can be seen, with which the epoxy bumps are made on the chip contacts. With the fineplacer unit (FINEPLACER-145 "PICO", FINTECH electronic, Germany) on the left side the chip and the PCB or the chip socket can be aligned and glued together.

The fabrication process for the design of the backside contacts was much more complicated than the standard chip processes. During fabrication the chips had to be handled with much more care, because if one of the thin membranes covering the holes breaks, the chips are not usable any more. The holes through the wafer were etched with a plasma etching process, which stops at a SiO₂-layer. The remaining membrane thickness was calculated to compensate negative and positive stress caused by the thin silicon nitride and silicon dioxide layers. This was accomplished by thin membranes consisting of 1 µm thick SiO₂ and 0.6 µm thick Si₃N₄. The membrane was stable in a certain range but can be very easily broken during the standard cleaning protocols for

cell culturing. Therefore, it was crucial to use the underfill epoxy glue (Underfill U300, Epoxy Technology Inc., USA) after the flip-chip process, which has a very high viscosity. Capillary forces are dragging it into the holes and it stabilises the membrane after being cured. The detailed process for the production of the backside-contacted FET arrays is described in the appendix. Because of the more complicated process, only p-channel devices were developed.

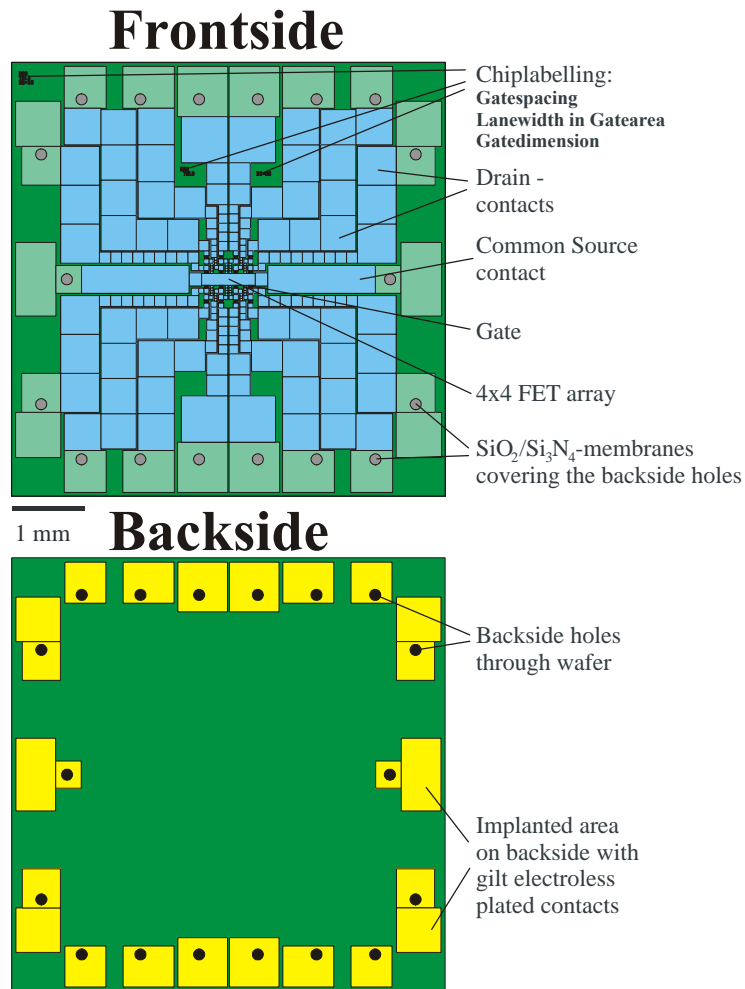


Figure 3-16 Chiplayout of the backside-contacted FET-arrays. The design of the lanes was adapted to largest lane area, because every backside contact introduced an additional series resistance of about 300 W, which aggravates the transistor performance (paragraph 3.1). The lanes are arranged together with the same number of squares, which guarantees similar series resistance and thus same transconductance for each of the 16 transistors. The holes through the wafer were doped in a gas phase process using BN-Wafers. The SiO₂/Si₃N₄-membranes are 1.6 μm thick and stable to the electrolyte solution. The backside contacts were implanted and plated with an electroless galvanic process with zink as seed metal (Simon and Reichl, 1990) for the use in a flip-chip encapsulation process.

The main differences to the standard FET-arrays were the design of the backside holes with the remaining membranes on the frontside, the gas-phase doping of the holes using BN-Wafers inside of the diffusion oven, and the gold contacts on the backside of the chips using an electroless galvanisation process (Simon and Reichl, 1990). These gold contacts were found to be essential for good flip-chip contacts. In Figure 3-16 the chip layouts on the frontside and on the backside of the FET-arrays are shown.

The design of the lanes was adapted to larger lane areas compared to the standard FET arrays. With this modification it was possible to partly compensate the additional series resistances of about 300Ω introduced by every backside contact and to prevent aggravation of the transistor performance. The lanes were arranged together with the same number of squares, which ensured similar series resistance and thus same transconductance for each of the 16 transistors. In Figure 3-17 the gate area of a transistor chip together with a scanning electron microscopic picture of a single gate is shown.

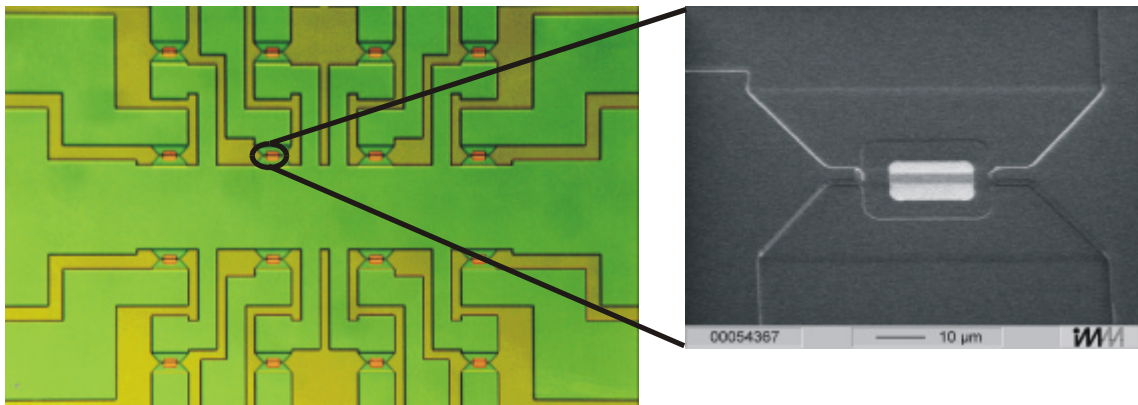


Figure 3-17 Layout of the backside FET-arrays in the gate area (left side) with the detailed view of a single gate structure (right side). The area of the drain and source lanes is much larger compared to the standard FET layout (Figure 3-8).

In Figure 3-18 a scanning electron image shows a hole through the wafer from the front- and the backside. In order to get a good contrast, the membrane on the frontside was removed by scratching before taking the picture. The aspect ratio of the plasma etching process is very high. Therefore, holes from the backside with radius of $150 \mu\text{m}$ on the photolithographic mask will result in about $160\text{-}170 \mu\text{m}$ membrane radius on the frontside. In Table 3.1, the various gate sizes with their labelling and their amount on the wafer are shown. The gate window sizes were varied in a very wide range ($8 \times 10 \mu\text{m}$ up to $38 \times 68 \mu\text{m}$) and different gate designs were used. We tried to evaluate the difference between rectangular (normal type) and tapered (indicated by L) source and drain designs. In addition to double-gate transistors (indicated by D), triple gate transistors (indicated by DD) were also produced. It became apparent that the triple gate

transistors were the most suitable for cell measurement even when the cells were much smaller than the gate dimensions. In principle, it should be possible to construct ‘multi’-gates with a very large area and thereby increasing the probability of individual cells localising on the transistor gates. In Figure 3-19 a single neuron out of a brainstem slice is cultured on a very large gate chip (32x38 μm triple gate). Despite the cell not covering the gate, it was possible to detect signals.

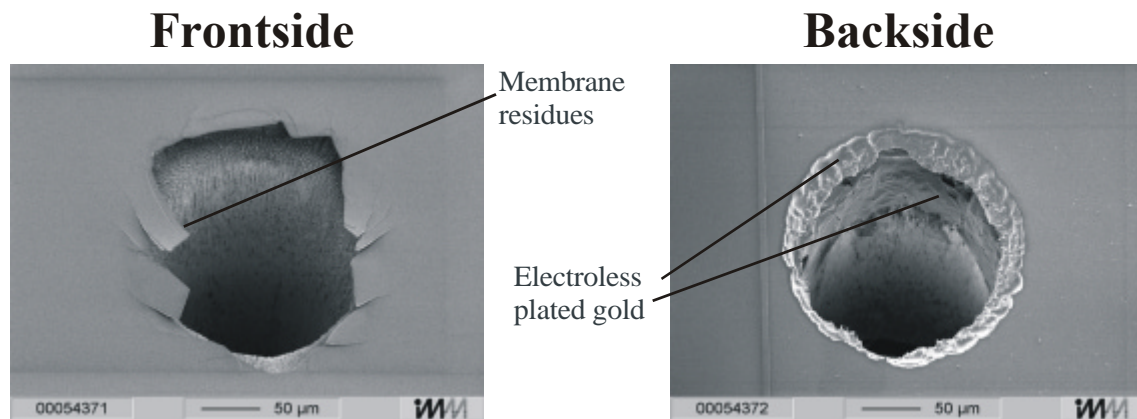


Figure 3-18 Electron micrograph images of a hole through the wafer. In order to get a good contrast the membrane on the frontside was destroyed by scratching before taking the picture. On the backside image the electroless plated gold even deposited to the inside of the hole can be seen. A comparison of the hole diameters shows the very high aspect ratio of the plasma etching process.

20μm x 100μm – Array (2x3):			200μm x 200μm – Array (4x4):		
20	180x30	48	70	38x20	8
100μm x 100μm – Array (4x4):			70	18x20	8
20	8x10	2	70	38x32	8
20	8x20	2	70	68x20	2
20	18x20	6	70	68x32	2
20	18x32	2	70L	18x20	4
20L	8x10	2	70L	38x20	4
20L	8x20	4	70LD	18x20	2
20D	8x10	2	70LD	38x20	2
20D	18x20	8	70LD	38x32	2
20D	18x32	2	70D	38x20	8
20DD	18x32	6	70D	38x32	8
			70D	18x20	8
			70D	68x20	2
			70D	68x32	2
			70DD	68x32	6

Table 3-1: Different gate sizes for the backside FET arrays and their amount on the wafer.

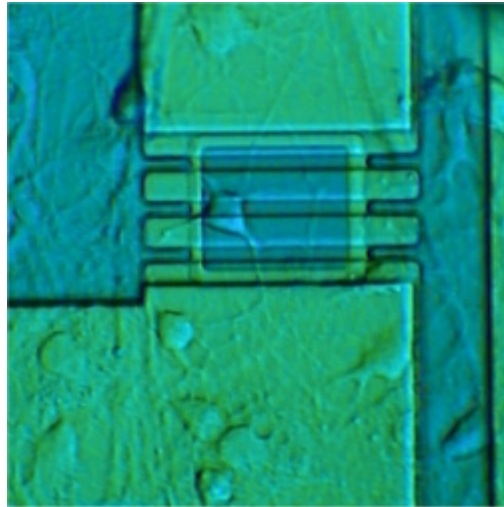


Figure 3-19 Single neuronal cell on a large triple gate structure ($32 \times 38 \mu\text{m}$). Despite the fact that the cell was not at all covering the gate, it was possible to measure signals in such cases.

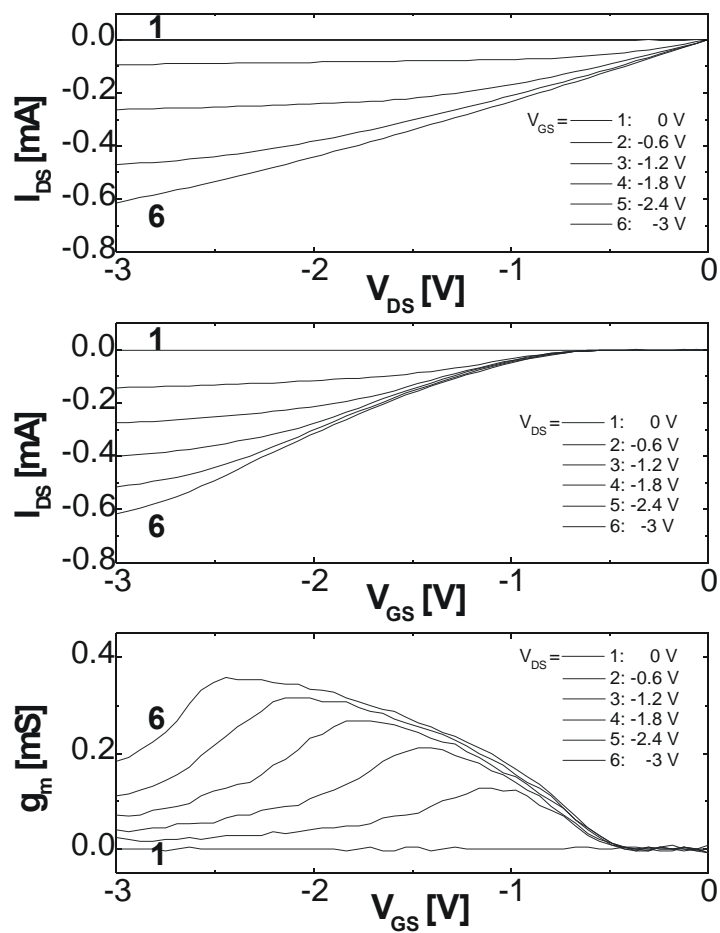


Figure 3-20 Characteristics of a p-channel triple gate backside-contacted transistor ($68 \times 32 \mu\text{m}^2$ gatesize).

In Figure 3-20, the characteristics of a triple gate backside-contacted transistor are shown. The p-channel FET showed nearly the same characteristics compared to the standard p-channel FET arrays. The transconductance of such transistors is reduced because of the higher series resistances from the backside contacts as can be calculated using Eqs. 3.19, 3.20 to a transconductance value of 0.35 mS at a working point of $V_{DS} = -3\text{V}$, $V_{GS} = -2.5\text{V}$. The threshold voltage V_{th} is -0.5V .

The concept of the backside contacts offers a wide variation of encapsulation methods for the chips. In principle, it would be possible to construct an 'upside-down' device, where the transistor is manoeuvred onto a preestablished culture of cells.

For the use of the backside-contacted chip together with Langmuir-Blodgett model membranes, a special chip adapter was developed. As a result of space limitations of the contact lanes on the chip adapter, only 12 FET gates are contacted. The full encapsulation was done using the flip-chip technique and 6x12 mm silicon pieces for framing the chip. (Figure 3-21).

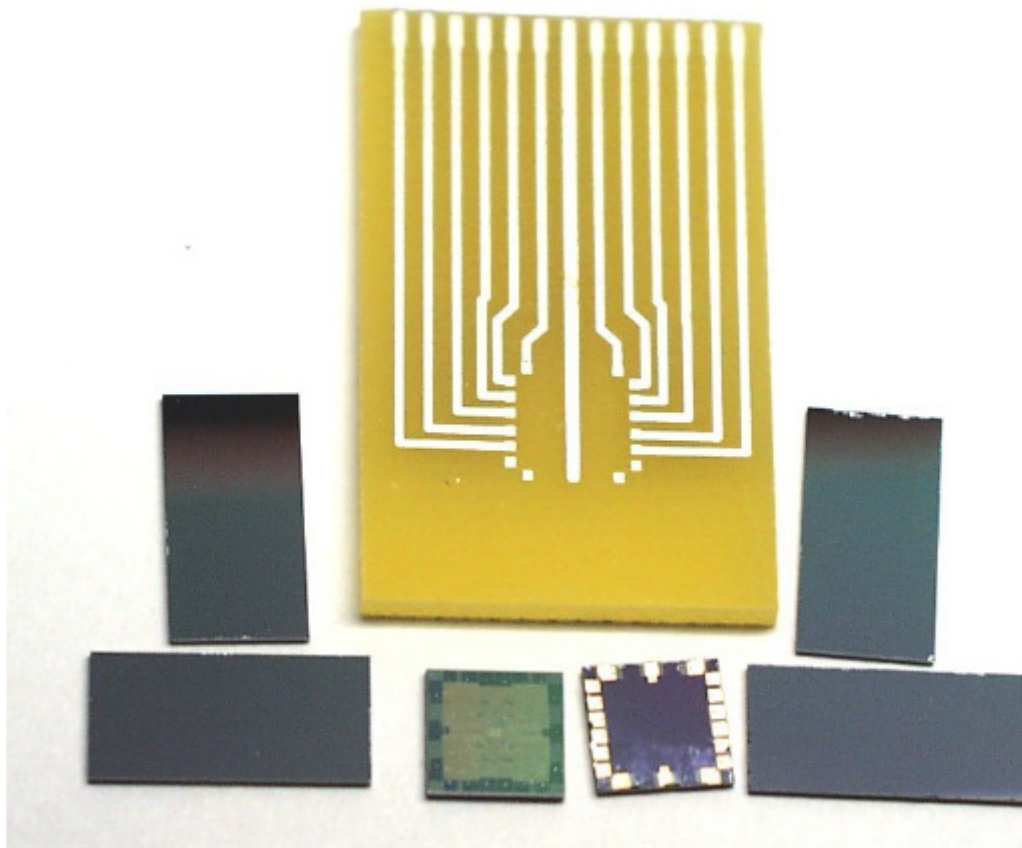


Figure 3-21 Un-encapsulated device for the Langmuir-Blodgett transfer of model membranes onto the chip surface. In the middle part two backside FET chips are shown. In the flip-chip process the chip is glued with its gold contacts onto the printed circuit board (PCB, MPIP Electronic Lab., 2000) and framed by four 6x12 mm dummy silicon pieces.

Experiments using model membranes on top of the transistor gates were performed using these kinds of devices and the standard p- and n-channel transistors. The rationale is that the membrane is shielding the transistor gate from the electrolyte solution and the pH-dependency of the gate voltage V_g is lowered. Functional proteins like Annexin V (building pores) or Nitrate Reductase (supposed to convert Nitrate into Nitrite and to pump 2 H^+ -ions for each converted Nitrate molecule through the membrane) was incorporated in model membranes. The Nitrate Reductase, isolated from the bacterium “*Pseudomonas stutzeri*”, was kindly provided by P. Steinrücke (Institute of Molecular Biotechnology, Jena, Germany). Annexin V is a member of the Annexin protein family and binds to negatively charged phospholipid membranes in a calcium dependent manner. They also show ion channel activity under certain conditions (Demange et al., 1994; Hofmann et al., 1997; Liemann et al., 1996). More likely a pore is formed into the bilayer membranes and ions are able to bridge the external bath region to the cleft between transistor and membrane. In this case the pH-dependency is brought up again. In the case of Nitrate Reductase the protein was pumping H^+ -ions through the membrane. This resulted in a local pH-change in the cleft between membrane and transistor surface, which was monitored by the ion-sensitive transistor. The results are discussed in detail in (Baumgart, 2001).

3.2.7 Extended Gate Electrode Arrays

For the EGE arrays (Krause et al., 2000) a new 64-channel amplifier set-up was developed during this work. Therefore, a new kind of encapsulation for the chips had to be established. The theoretical aspects of using metal electrodes as bioelectronic transducers will be first considered. The design of the electrodes and the new encapsulation method will also be shown. This section also discusses the surface modification using platinum white galvanisation process (Thiébaud et al., 1997) and the influence to the electrode impedance.

Electrode-electrolyte interfaces:

When a metal object is placed into an ionic solution a space charge layer builds up at the metal-electrolyte interface (Bard and Faulkner, 1980). A chemical reaction (Eq. 3.35) leading to a space charge layer introduces a capacitance as electrical circuit element.



with electron donor D , electron acceptor A , and the charge z of the ion.

In Figure 3-22, an illustration of the nanostructure of the space charge layer at an aqueous electrode is shown. The Helmholtz-Perrin model assumes that the charge in the solution is essentially 2-dimensional and located at the outer Helmholtz plane (OHP). In

this case the parallel-plate capacitor model $C = \epsilon_0 \epsilon_r A/d$ is not totally valid. It would yield a value of $c_H \approx 0.11 \text{ F/m}^2$ for the Helmholtz capacitance assuming a distance of 0.5 nm between electrode surface and OHP (ϵ_0 dielectrical constant of the vacuum, ϵ_r relative dielectrical constant of the medium between the plates ($\epsilon_r = 78.54$ for water @ 25°C), A denotes the surface area of the plates, and d is the distance of the plates.

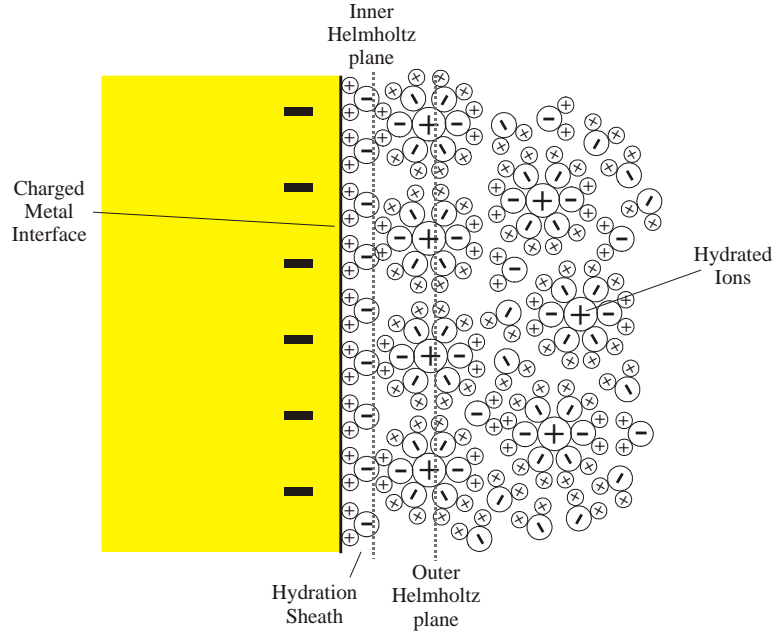


Figure 3-22 Structure of the space charge layer at an aqueous metal-electrode, showing the hydration sheath, a monolayer of oriented water molecules at the metal surface, and the next layer of hydrated cations. The figure was adapted from the Southamton Electrochemistry group (1985).

The Gouy-Chapman model of diffuse charges assumes neither a layer of hydrated ions stuck at the OHP, nor a linear voltage drop across the dielectric layer. The capacitance of the diffuse space charge can be derived with:

$$C_D = \frac{\epsilon_0 \epsilon_r A}{L_D} \cosh\left(\frac{zV_0}{2V_t}\right)$$

$$L_D = \sqrt{\frac{\epsilon_0 \epsilon_r V_t}{2n^0 z^2 q}} \tag{3.30}$$

with the potential at the electrode V_0 (Ag/AgCl pseudo reference electrode), T absolute temperature, q the charge of an electron, the voltage $V_t = kT/q$, the bulk concentration of the appropriate ion, and the Debye length L_D described by Bard and Faulkner (1980). The Stern model combines these two models, with following equation for the interfacial capacitance C_I of the metal-electrolyte interface:

$$\frac{1}{C_I} = \frac{1}{C_H} + \frac{1}{C_D} = \frac{1}{\epsilon_0 \epsilon_r A} \left[d_{OHP} + \frac{L_D}{\cosh\left(\frac{zV_0}{2V_t}\right)} \right] \quad (3.31)$$

Extended-gate electrode arrays:

The microelectrodes developed by Krause (2000) were designed for the use of single cell cultures and organised neuronal networks. This limited the range of available microelectrode diameters (6-100 μm with 10 μm as typical value) and spacing between the electrodes (100, 200 μm respectively). The main advantages of the electrode chips are easier fabrication processes, the possibility to create an 8x8 array in contrast to the 4x4 arrays of the transistor chips, and the possibility of microstructured surface design like plateaus and tips. The layout of the EGE chips is shown in Figure 3-23.

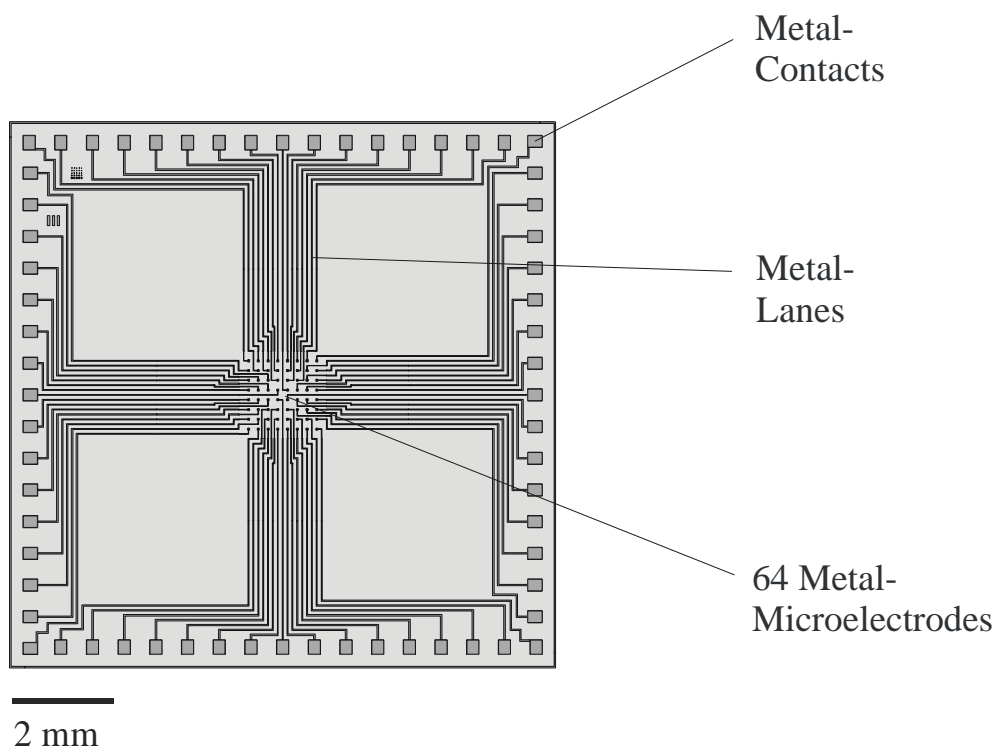


Figure 3-23 Layout of the EGE metal-electrode chips (Krause, 2000).

The fabrication processes for all metal-electrode wafers consist of mainly three steps. First, the evaporation of the electrode material like titanium or gold ($d = 300 \text{ nm}$), followed by the isolator sandwich layer of $\text{SiO}_2/\text{Si}_3\text{N}_4/\text{SiO}_2$ ($d_i = 500/500/100 \text{ nm}$), and finally by etching of the electrode and outer contacts. Figure 3-24 shows a closer view of the inner part of the chip showing the 8x8-electrode array and a SEM image of a

single electrode. It can be clearly seen that the etching process on the electrode resulted in a $1.1\ \mu\text{m}$ deep hole through the isolating layer. Therefore, the cell distance to the sensor spot is increased, especially in the case of cell layers, which can very likely span over the hole. To overcome this problem, certain topographical modifications to the electrodes were made with the aims to decrease the cell-sensor distance d and to improve the sealing properties of cell layers.

An additional processing step for the design of the topology was done by isotropic etching of Si_3N_4 layers of different thickness. Depending on the thickness of the initial layer, the diameter of the etched electrode areas and the etching time, different topologies such as tips, plateaus with different heights and diameters have been achieved (Figure 3-25).

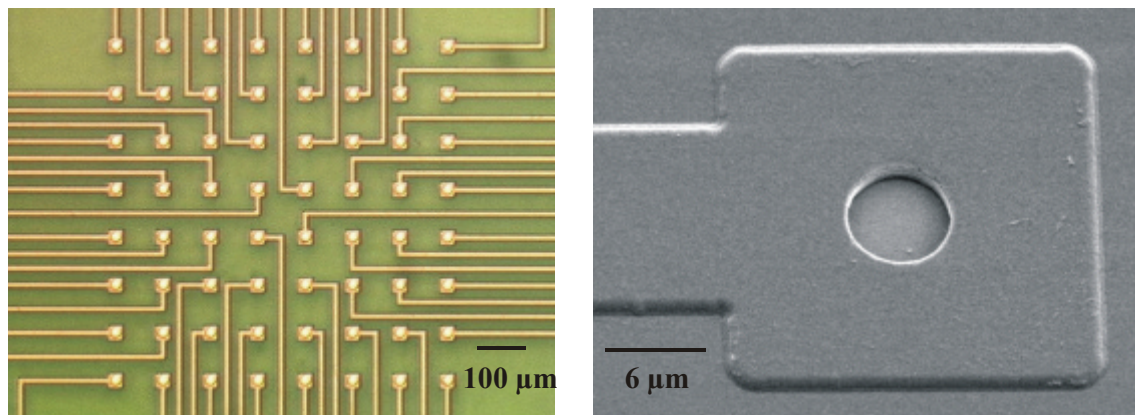


Figure 3-24 Closer view to the 8x8 extended-gate electrode array (left side). On the right side a scanning electron micrograph (SEM) picture of a single, planar electrode is shown ($d = 6\ \mu\text{m}$).

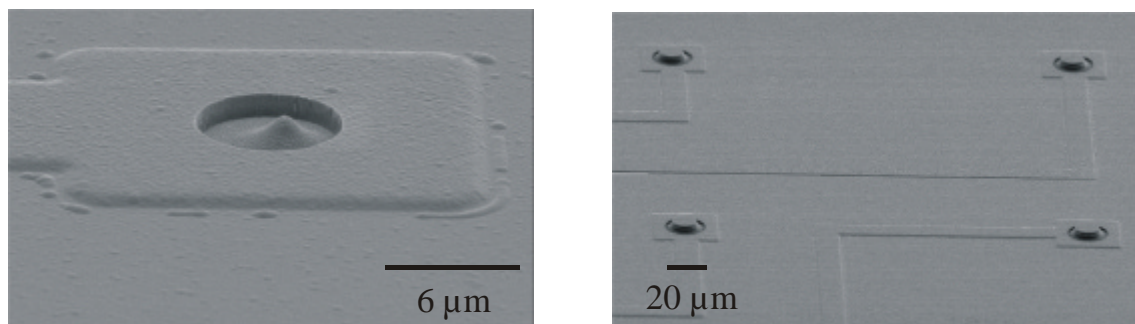


Figure 3-25 Metal-microelectrodes with different topology like tips (left side) and plateaus (right side) were designed by anisotropic etching of an initial Si_3N_4 layer before designing the metal electrodes (Krause, 2000).

Encapsulation of the electrode chips:

For the use of the electrode chips in the new 64-channel amplifier system, a new encapsulation method was developed. In contrast to the encapsulation method used by Krause et al. (2000) the PCB board on which the chips were glued had a smaller size (24x24 mm²). The 64 gold jacks for plug-in of the stimulation pulses to each single electrode were initially soldered onto the PCBs of the EGE-chips. These contacts were transformed into the new amplifier head (Chapter 4). This made the encapsulation of a single device much easier and less time consuming to produce.

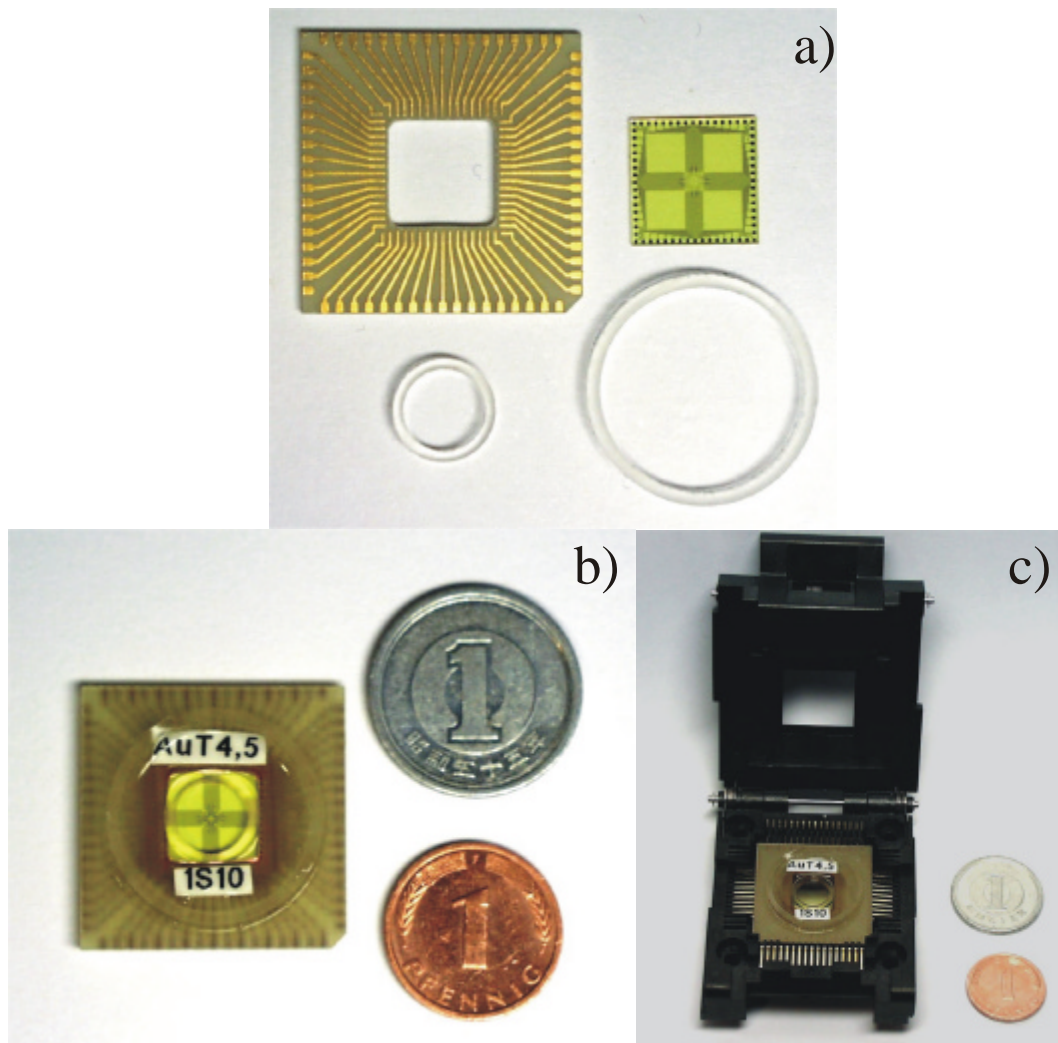


Figure 3-26 Encapsulation of the EGE chips. In picture a) the un-encapsulated device, the PCB and the two glass rings for building the cell culture dish are shown. In picture b) the fully encapsulated device can be seen. The PCB was designed to fit into a 68-channel test socket with spring contacts (PLCC68 IC51, Yamaichi Electronics Inc., Germany). This test socket was intergrated in to the amplifier head (chapter 4) using a modified top cover, which carries the Ag/AgCl reference electrode.

The electrode dyes (11x11 mm²) were cleaned using ethanol and acetone in an ultrasonic bath to rid of photoresist residues prior to the encapsulation. The chips were then glued onto the PCB using the polymer flip-chip technology (Lau, 1995). The method was similar to the previously described process for encapsulation of the backside-contacted FET chips (see above).

In the first step, the polymer bumps of the two component polymer glue were printed onto the 300x300 μm² contacts of the PCBs using the screen printer. The previously used metal foil containing the 64 laser-cut holes was replaced by a transparent polymer foil containing the contacts for the EGE chips and the backside FET chips (ELASER Inc., Germany). This made the alignment of the PCBs and the mask using the x,y-placer unit much easier. A fineplacer unit was used to perform the optical controlled gluing of the dyes onto the PCB. After curing the conducting flip-chip polymer glue at 150°C, the underfill glue was used on the backside of the PCB to prevent shortcuts between the single contacts. The PCBs had a hole 9x9 mm² in the middle part and a thickness of 1 mm. By gluing a glass ring (7 mm diameter, 1 mm thickness and 1 mm height) onto the frontside of the electrode chip and a second glass ring (16 mm diameter, 1 mm thickness and 1.5 mm height) onto the frontside of the PCB, a cell culture dish is formed. The final step is to fill the area between the two glass rings with PDMS glue. The free area for cell culture was 38.5 mm² and the chip was able to carry 600 μl of cell culture medium. In Figure 3-26 b), the encapsulated EGE chip (2nd generation) is shown.

Thin-film microelectrode performance:

The optimum design of microelectrodes for extracellular signal recordings of single cells should ideally be very small (2-10 μm diameter) with minimum electrode impedance. However, electrode size is inversely proportional to the impedance. The impedance $Z(t)$ of a gold microelectrode is frequency dependent as follows:

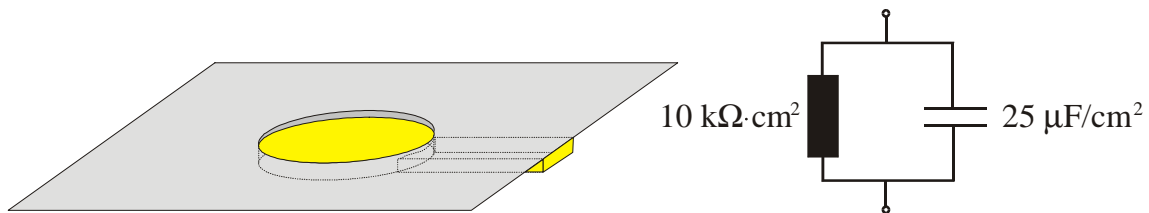


Figure 3-27 RC-element for a planar gold electrode with typical values for the specific resistance and capacitance.

The impedance $Z(t)$ of the electrode is defined with:

$$Z(t) = |Z|e^{i\phi} = Z' + iZ'' \tag{3.32}$$

with the phase shift f the real part Z' and the imaginary part Z'' of the impedance. The electrical properties of planar gold electrodes can be described with RC-elements (Figure 3-27).

For a microelectrode with diameter of $d = 10 \mu\text{m}$ the electrode area can be calculated to $A = 7.85 \cdot 10^{-7} \text{ cm}^2$. The resistance would then be $R = 12.73 \text{ G}\Omega$ and the capacitance $C = 19.6 \text{ pF}$. The total voltage drop V at the parallel RC-element is the sum of the reciprocal single voltage drops V_C, V_R at both elements:

$$\frac{1}{V} = \frac{1}{V_R} + \frac{1}{V_C} \quad (3.33)$$

The admittance Y is defined with its real part and its imaginary part:

$$Y = Y' + iY'' = \frac{1}{R} + i\omega C \quad (3.34)$$

This leads to the impedance of the element:

$$Z = \frac{1}{Y} = \frac{1}{\frac{1}{R} + i\omega C} = \frac{1}{\frac{1}{R}(1 + i\omega RC)} = \frac{R}{1 + i\omega t} \quad (3.35)$$

with the time constant $t = R \cdot C$. It is with the above specific values for planar gold (Figure 3-27) $t = 0.25 \text{ s}$. The '1' in Eq. 3.35 represents the real part and $i\omega t$ the imaginary part of the impedance. For the frequencies of interest in the ms-range ($f = 1 \text{ kHz}$) only the imaginary part contributes to the total impedance and its value drops with higher frequencies.

$$Z \cong \frac{R}{i\omega t} = \frac{1}{i\omega C} \quad (3.36)$$

It shows that the impedance is lowered with increasing electrode area as the capacitance C is proportional to the electrode area A . Nonplanar microstructures (sizes 10-0.5 μm), surface roughening (RMS values of 10 nm up to 2 μm , and chemical modifications (films with thickness of 100 nm down to monolayers $< 1 \text{ nm}$) are the three techniques by which microelectrode performance can be optimised. For the above values, the impedance of a planar gold electrode with diameter of 10 μm can be calculated to 8 $\text{M}\Omega$ at 1 kHz. In Figure 3-28 a schematically view of the planar metal electrode structure is shown.

For the fabrication of planar microelectrodes many different materials have been used. Substrate silicon, glass, and sapphire are all standard materials. Thin film microelectrodes have also been fabricated on flexible polyimide substrates by White et al. (1983). An overview to different microelectrode array types have been given by Pickard (1979).

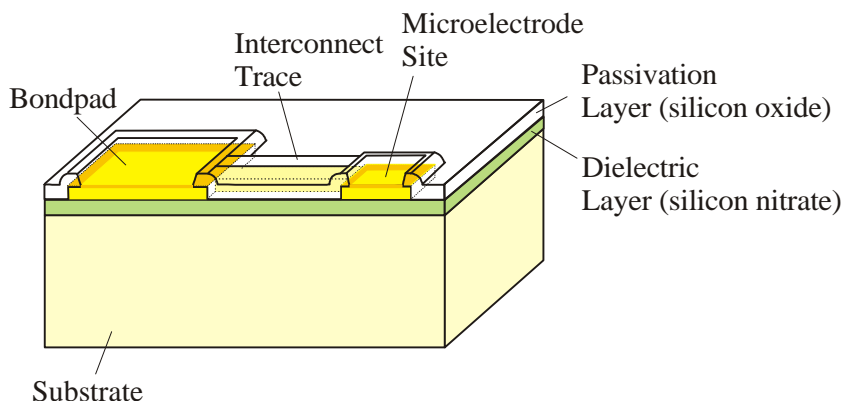


Figure 3-28 Schematical view of the structure of planar thin-film microelectrodes. The conductive traces, microelectrode sites, and bond pads are photolithographically defined on the substrate. The passivation layer protects the interconnect traces towards the electrolyte. At the bondpads and the microelectrode sites holes are etched through the passivation layer.

Non-planar microelectrode structures:

There are different etching methods available to create non-planar microelectrode structures. By selective etching of the substrate prior to defining the metal electrode sites, ‘pillars’ or ‘needles’ can be fabricated (Figure 3-25). If the structures are large, a drastically drop of the electrode impedance can be reached as a result of Eq. 3.36. In addition, the distance d of the cells to the sensor spot will be decreased, which results in higher signal amplitudes (Chapter 5).

Another technique for increasing the effective surface area of the electrode site is to alter the surface by either roughening existing surfaces or depositing materials that are inherently coarse.

In neuroscience, the traditional approach to altering microelectrode nanostructure is the electroplating of platinum powder (platinum black coating, (Robinson, 1968)). In addition, the electrode site is elevated, which results in a distance decrease to the cell culture. On the other hand, the elevated platinum ‘sponges’ are very unstable in standard cleaning processes. The method of the metal powder deposition process is described in detail by Calusaru (1979) and Ibl (1962). The etching methods are also increasing the effective surface by chemical, electrolytic, or plasma etching of the metal, which preferentially attacks certain areas to produce pits or pores. Here, the structures are not elevated, which result in a better long-term stability of the structures. We have used the platinum white electroplating process (Thiébaud et al., 1997) to test the influence of the coating to the electrode performance. In Figure 3-29 a SEM-image of the platinum white coating can be seen.

impedance. We interpret the slightly higher signal amplitudes obtained with coated electrodes in our set-up with the elevation of the structure and hence better seal resistances.

3.3 Minimising Noise in the Set-up

If a signal A carries noise at the output, the time-dependence of this signal $A(t)$ is not predictable (e.g. the voltage at the output of our amplifier circuit). For a noise-rich signal, the time-dependence cannot be precisely measured. However, one can make probability estimates by using the probability density function $P(A)$ and the time-average:

$$\bar{A} = \lim_{T \rightarrow \infty} \frac{1}{2T} \int_{-T}^{+T} A(t) dt \quad (3.37)$$

This linear average value would be shown by a very slow instrument and is equivalent to the ‘DC-value’ of $A(t)$. The information about the deviation of $A(t)$ from this value is given by:

$$a(t) = A(t) - \bar{A} \quad (3.38)$$

The time-average value of this function is zero by definition.

$$\overline{a(t)} = 0 \quad (3.39)$$

A degree for the power coupled to the fluctuation of this function $a(t)$ is given by the square value of $\overline{a^2}$, which is the standard function in noise theory. This square value (often called variance \mathbf{s}^2), is defined as time-average of the function $a(t)^2$:

$$\mathbf{s}^2 = \overline{a(t)^2} = \lim_{T \rightarrow \infty} \frac{1}{2T} \int_{-T}^{+T} [a(t)]^2 dt \quad (3.40)$$

The value $\mathbf{s} = \sqrt{\overline{a^2}}$ is called effective value of the noise function $a(t)$ (rms-value: root mean square-value). The variance can be expressed with $A(t)$ and using Eq. 3.38:

$$\mathbf{s}^2 = \overline{a^2} = \overline{(A - \bar{A})^2} = \overline{A^2 - 2A\bar{A} + \bar{A}^2} = \overline{A^2} - 2\bar{A}^2 + \bar{A}^2 = \overline{A^2} - \bar{A}^2 \quad (3.41)$$

The value \mathbf{s}^2 is expressing the noise power, $\overline{A^2}$ is a unit for the total power, and \bar{A}^2 is a unit for the DC-power. This means the total noise power is given by adding DC- and AC-noise power.

3.3.1 Correlation

If two or more noise functions are present, they may be coupled to some extent. This means the information in the first signal contains also some information about the second value. The squared deviation of the two existing noise functions a_1 and a_2 is defined with:

$$\overline{(a_1 + a_2)^2} = \overline{a_1^2} + \overline{a_2^2} + \overline{2a_1a_2} = \mathbf{s}_1^2 + \mathbf{s}_2^2 + 2c_{12}\mathbf{s}_1\mathbf{s}_2 \quad (3.42)$$

with \mathbf{s}_1^2 , \mathbf{s}_2^2 the variances of the single noise functions and the correlation coefficient c_{12} defined with:

$$c_{12} = \frac{\overline{a_1a_2}}{\sqrt{\overline{a_1^2}\overline{a_2^2}}} = \frac{1}{\mathbf{s}_1\mathbf{s}_2} \lim_{T \rightarrow \infty} \frac{1}{2T} \int_{-T}^{+T} a_1(t)a_2(t)dt \quad (3.43)$$

The correlation coefficient is proportional to the time-average of $a_1(t) \cdot a_2(t)$. For un-correlated noise functions this value is zero.

$$\overline{a_1(t)a_2(t)} = 0 \quad (3.44)$$

The same arguments can be used for the general noise functions $A_1(t)$ and $A_2(t)$. If they are not correlated then:

$$\overline{A_1(t)A_2(t)} = \overline{A_1} \overline{A_2} \quad (3.45)$$

For un-correlated events the correlation coefficient c_{12} is zero. With Eq. 3.42 the total squared deviation is then equal to the sum of the single squared deviations:

$$\overline{(a_1 + a_2)^2} = \overline{a_1^2} + \overline{a_2^2} \quad (3.46)$$

if a_1 and a_2 are not correlated. As a consequence, this means that the noise power of two un-correlated noise events have to be added up. This is the case when interspersed noise sources coming from outside and contributing to the total noise of the amplifier circuit (e.g. the thermal noise of a resistor in series, an operational amplifier in series...). The interspersed noise sources are occurring in most cases at a certain frequency.

The correlation coefficient defined in Eq. 3.43 is a measure for the correlation of two noise functions and determines the addition of these with Eq. 3.42. The two noise functions are correlated, if $c_{12} \neq 0$ (e.g. for the voltage drop of a noisy current at two resistors in series $c_{12} = 1$). There are special cases, where $c_{12} = 0$, although the two noise functions have the same reasons and should be fully correlated. For the voltage drop of a nearly sinodal noise-current (e.g. interspersed carrying a certain frequency, $f(t) = f_0 \sin(\omega t)$), which takes place when a resistor and capacitor are in series, it is

$c_{12} \approx 0$. This is caused by the orthogonal phase-shift of the current at the two elements, although the interspersed noise was highly correlated.

The most common measure for the correlation of two noise functions is the correlation function r_{12} . It is the average value of the product of the two functions, but one of the functions is shifted with the variable period of time t .

$$r_{12}(t) = \overline{a_1(t)a_2(t+t)} = \lim_{T \rightarrow \infty} \frac{1}{2T} \int_{-T}^{+T} a_1(t)a_2(t+t)dt \quad (3.47)$$

The correlation coefficient c_{12} in Eq. 3.49 is a special case of the correlation function $r_{12}(t)$, as it reflects the normalised value of the correlation function $r_{12}(0)$:

$$c_{12} = \frac{r_{12}(0)}{s_1 s_2} \quad (3.48)$$

It is now clear that obtaining $c_{12} = 0$ is not enough for the determination of un-correlated events. If $r_{12}(t) = 0$ for all values of t , then the events are un-correlated:

$$r_{12} \equiv 0 \quad (3.49)$$

$\Rightarrow a_1$ and a_2 are un-correlated

3.3.2 Spectral Noise Density:

For a noise event, a frequency spectrum can be plotted. In doing so, the spectral noise density $W(f)$ can be defined, which reflects the ‘power’ in a frequency range with band width $df = 1$ Hz at a certain frequency f . In Figure 3-30 a typical noise spectrum is shown, which can be divided into three characteristic regions.

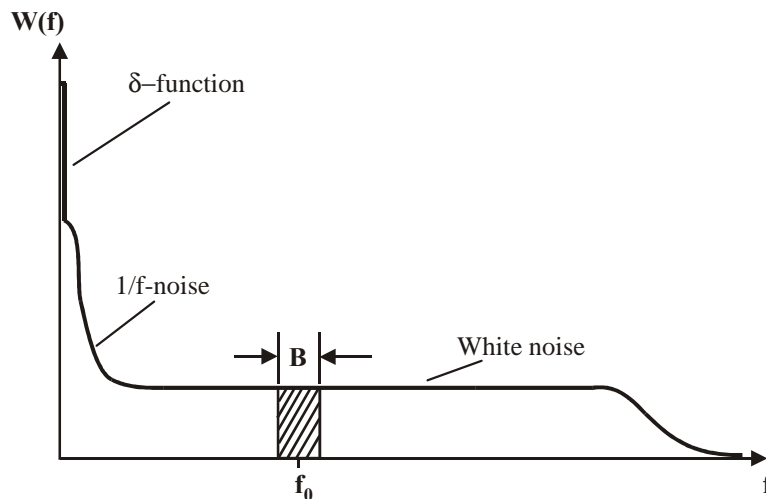


Figure 3-30 Typical noise spectrum $W(f)$ with the different regions. The figure concept was adapted from Müller (1990).

At low frequency, the noise power is inversely proportional to frequency. This region is called $1/f$ -noise. There is a region at higher frequencies, where the spectral noise density, which is the noise power per frequency unit, is independent on the frequency. This region is called ‘white noise’. The total noise power $\overline{a^2}$ of the noise event is the integral over the whole noise density with:

$$\int_0^{\infty} W(f)df = \overline{a^2} \quad (3.50)$$

This value is because of physical reasons finite, this means the spectral noise density drops at a certain border frequency to zero. The Eq. 3.50 refers to pure noise functions. A DC-part of the noise would be reflected in the noise spectrum (Figure 3-30) with a δ -function at $f=0$, and it is:

$$\int_0^{\infty} W(f)df = \overline{A^2} \quad (3.51)$$

In actual recordings, the noise is always measured in a certain frequency range B (Figure 3-30). In many cases, the noise is independent to the frequency and it is in this narrow frequency range the integral is:

$$\overline{a^2} \Big|_B = \int_B W(f)df = W(f_0)B \quad (3.52)$$

This noise function is then called ‘narrow-band-noise’ and can be treated as equivalent to a real signal. For a noise function $a(t)$, the unit of $\overline{a^2}$ in Eq. 3.50 is V^2 and $W(f)$ has the unit of V^2/Hz . By analogy to this, the dimension of $W(f)$ for current noise is A^2/Hz , for frequency fluctuations Hz^2/Hz , or $1/Hz$ for phase fluctuations. In all cases the function $W(f)$ is called the noise density.

3.3.3 Autocorrelation-Function:

The autocorrelation-function is a special case of the correlation function Eq. 3.47 for $a_1 = a_2 = a$. It gives an estimate if the value of $a(t_1)$ and the value of $a(t_1 + \mathbf{t})$ are correlated. This is the case if a noise source introduces an interspersed noise portion at a certain frequency. The autocorrelation-function is defined as:

$$\mathbf{r}(\mathbf{t}) = \overline{a(t)a(t + \mathbf{t})} = \lim_{T \rightarrow \infty} \frac{1}{2T} \int_{-T}^{+T} a(t)a(t + \mathbf{t})dt \quad (3.53)$$

The absolute value of a Fourier transformed time-event reflects the spectrum of the amplitude of this event. For noise events this time-function is unknown. One can calculate the Fourier transformed autocorrelation-function and receives the noise spectrum.

The Fourier transformed autocorrelation-function $w(f)$ is defined as follows:

$$\begin{aligned}
 w(f) &= \int_{-\infty}^{+\infty} \mathbf{r}(t) \exp(-2\pi i f t) dt \\
 \mathbf{r}(t) &= \int_{-\infty}^{+\infty} w(f) \exp(2\pi i f t) df
 \end{aligned}
 \tag{3.54}$$

With $t = 0$ this leads to:

$$\mathbf{r}(0) = \int_{-\infty}^{+\infty} w(f) df
 \tag{3.55}$$

Because of $\mathbf{r}(0) = \overline{a^2}$ the function $w(f)$ has to be a spectral power density. The reason for this is that the integral over the whole frequency range $-\infty$ to $+\infty$ is equal to the total noise power itself. The spectral power density $w(f)$ is because of $\mathbf{r}(t) = \mathbf{r}(-t)$ a real and even function ($w(f) = w(-f)$). With Eq. 3.50, only positive frequencies are relevant and by defining $W(f) = 2w(f)$, the so-called *Wiener-Khintchine Equations*, resulting:

$$\begin{aligned}
 W(f) &= 2 \int_{-\infty}^{+\infty} \mathbf{r}(t) \exp(-2\pi i f t) dt \\
 \mathbf{r}(t) &= \int_0^{\infty} W(f) \cos(2\pi f t) df \\
 \mathbf{r}(0) &= \int_0^{\infty} W(f) df = \overline{a^2}
 \end{aligned}
 \tag{3.56}$$

Because of the symmetry of $\mathbf{r}(t)$ the spectrum $w(f)$ is real and a real set of equations is enough to describe the transformation. By changing the borders of the integration for $\mathbf{r}(t)$ these equations become:

$$\begin{aligned}
 W(f) &= 4 \int_0^{\infty} \mathbf{r}(t) \cos(2\pi f t) dt \\
 \mathbf{r}(t) &= \int_0^{\infty} W(f) \cos(2\pi f t) df
 \end{aligned}
 \tag{3.57}$$

One starting condition for this Fourier Transformation is the finite size of the total noise power, which is always given for physical reasons. The *Wiener-Khintchine Equations* are valid for all noise functions $A(t)$. A DC-part \overline{A} leads to a constant value, which has to be summed up to the autocorrelation-function. A Fourier Transformation of this leads to a δ -function in the spectrum at $f = 0$.

3.3.4 Procedure for Interspersed Noise Tracking

We have used the previous considerations for tracking interspersed noise in our set-up and for discrimination of different noise sources. The procedure was as described above. A noise measurement of the EGE set-up is shown in Figure 3-31, which reflects the basic procedures. The signal output was measured for 5 seconds at a sampling rate of 10 kHz. The difference of the two measurements was the power supply. The power supply used in the first system introduced a noise source at a frequency of 100 Hz. By using a battery power supply in the newer amplifier systems, which were fully decoupled from the main voltage supply, this noise source was eliminated.

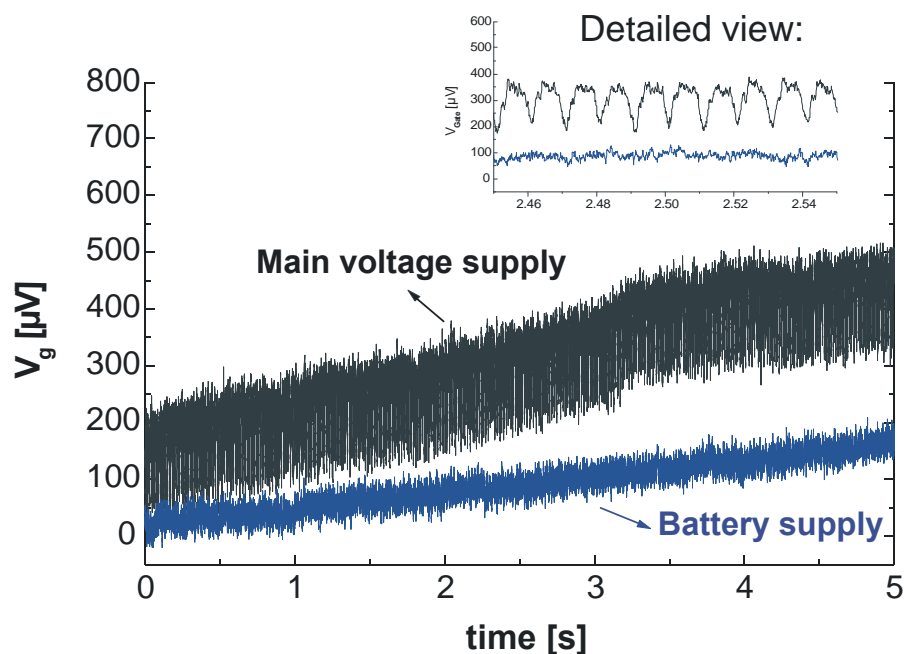


Figure 3-31 Noise rawdata of the EGE set-up with and without battery supply. The power supply, which was used in the first systems, introduced a noise at a frequency of 100 Hz (detailed view). The lower trace represents the same set-up provided with a battery power supply, fully decoupled from the main voltage supply.

In Figure 3-32, the autocorrelation-functions $r(t)$ (V^2) of the two different raw data traces were calculated based on Eq. 3.53. By performing the Fast Fourier Transformation of these two traces, the respective noise power spectra can be calculated by using Eqs. 3.56. The results are shown in Figure 3-33. It can be clearly seen, that the noise spectrum of the standard power supply carried a strong 100 Hz interspersed noise with its higher harmonics (200, 300,...Hz). This noise source was totally eliminated by using the battery power supply.

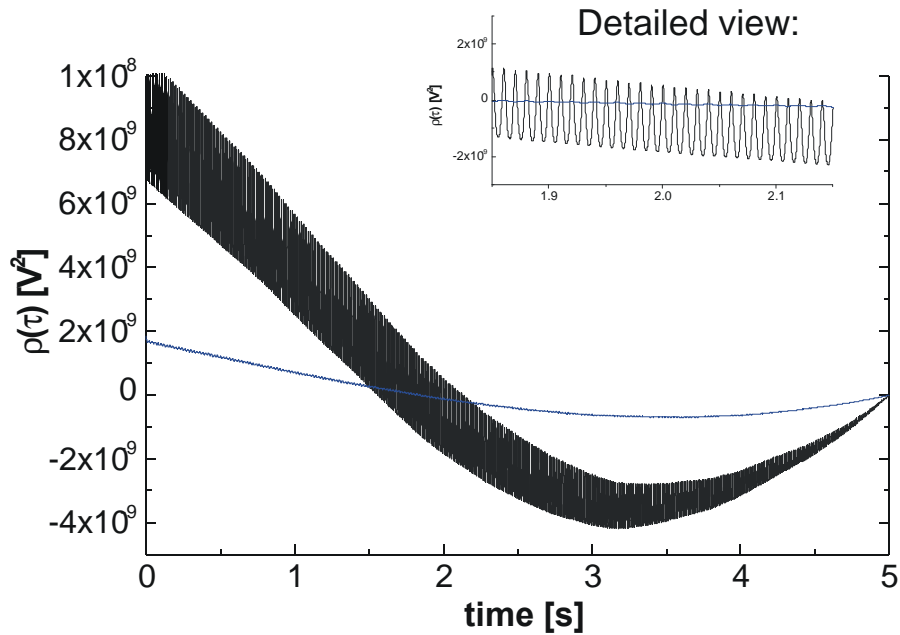


Figure 3-32 Autocorrelation-functions of the two noise rawdata traces. The noise trace, which carried the 100 Hz noise, has much higher values for $r(t)$.

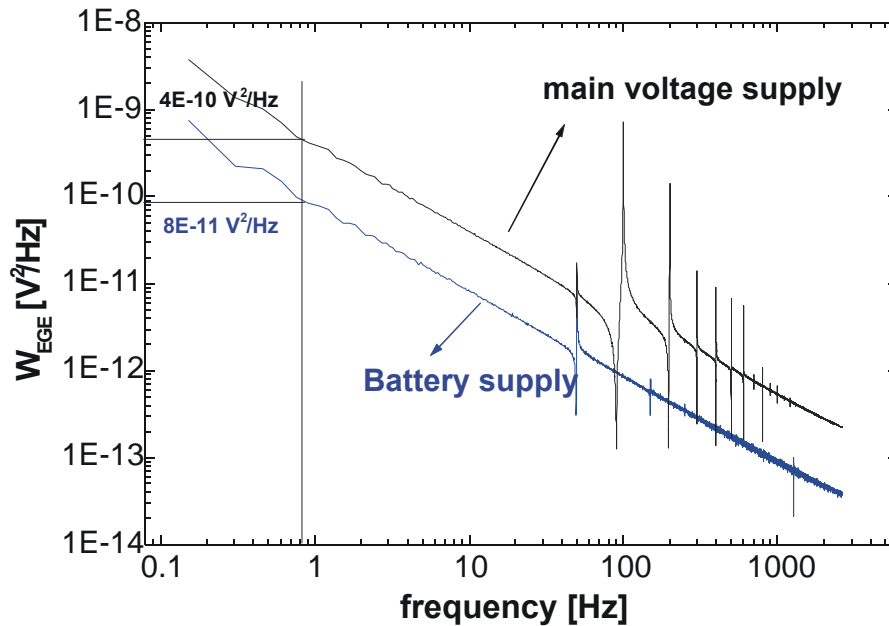


Figure 3-33 Noise power spectra of the two noise measurements shown in Figure 3-31. It can be clearly seen, that the noise spectrum in the upper trace carries a strong 100 Hz interspersed noise and its higher harmonics (200, 300,...Hz). This noise source was totally extinguished by using the battery power supply.

The above procedure was always used for minimising the noise in the amplifier output. The influence of the 50 Hz frequency was always present. We attempted to

shield the whole set-up with a Faraday cage, but realised that this noise was picked up at the input stage, which is the transistor gate. This remaining interspersed noise source represented only a few percent of the total noise. The noise introduced by the amplifier circuitry was about 10 times lower than the total noise (Krause, 2000; Krause et al., 2000; Sprössler, 1997). These measurements were performed using a 10 k Ω resistor instead of the transistor at the gate input. It became cleared that the intrinsic noise of the transistor contributed to the main part of the total noise of the measurement signal at the amplifier output.

3.3.5 Noise of the used FET-Devices

The following procedures for analysing the noise at the amplifier output were the same as described in the previous paragraph. Noise measurements were performed for 5 s with a sampling rate of 10 kHz. This results in a noise spectrum from 0.2 to 5000 Hz, which falls within the range that is required for the measurement of bioelectronic signals. In this very un-usual frequency range for MOSFETs - they are normally driven at MHz frequencies - the total noise of the set-up is dominated by the 1/f-noise of the transistor gate.

It is difficult to compare the noise of different devices because the transistors are different in gate dimensions, in gate-oxide thickness, and are driven at different working points. Many measurements were performed with n-, p-channel FET arrays of different generations and with various gate designs. In the following only some examples are shown reflecting the trends obtained from many noise measurements. In Figure 3-34, the raw data traces are shown. The upper trace shows a noise measurement of a p-channel device of the 2nd generation developed by Krause (2000). The transistor had a gate area of $A_{gate} = 3 \times 16 \mu\text{m}^2$ and a gateoxide thickness of $d_{ox} = 12 \text{ nm}$. The working point was driven at $V_{GS} = -1.8 \text{ V}$ and $V_{DS} = -2.5 \text{ V}$ and revealed a transconductance of $g_m = 0.5 \text{ mS}$, which was a high value for the p-channel devices. From the raw data, a peak-to-peak noise of 350 μV can be estimated. It is compared with the noise of a p-channel device of the 1st generation developed by Offenhäusser et al. (1998). This device had a gate area of $A_{gate} = 6 \times 24 \mu\text{m}^2$ and a gateoxide thickness of $d_{ox} = 14 \text{ nm}$. The working point was driven at $V_{GS} = -3 \text{ V}$ and $V_{DS} = -3 \text{ V}$ and revealed a transconductance of $g_m = 0.42 \text{ mS}$. The noise of this device was slightly lower than the noise of the p-channel FET - 2nd generation. In the lower trace, a noise measurement of an n-channel device developed by Krause (2000) is shown. The transistor had a similar gate area of $A_{gate} = 3 \times 16 \mu\text{m}^2$ compared to the p-channel device and a gateoxide thickness of $d_{ox} = 12 \text{ nm}$. According to the theory, n-channel devices should carry a higher 1/f-noise (see below), but the channels of our n-channel devices were partly buried in additional processing steps. This resulted in a much lower transistor noise compared to the p-channel devices. Its noise measurement is shown in Figure 3-34.

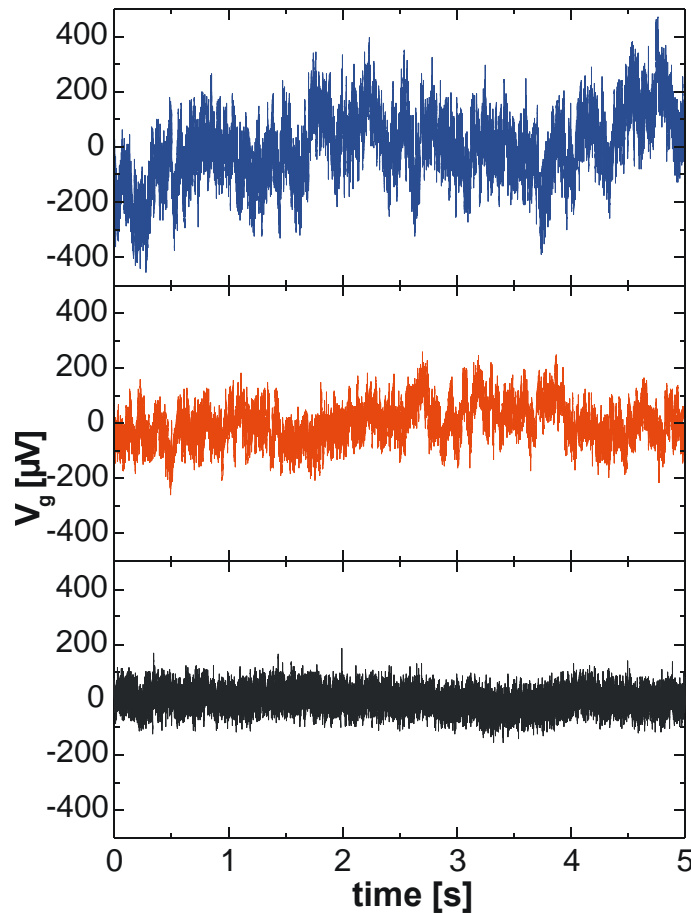


Figure 3-34 Noise measurements of three different FET devices. In the upper trace the noise measurement of a p-channel device out of the 2nd generation is shown. Its noise is a little bit higher than the noise of the 1st generation p-channel device (middle trace). The lowest noise reveals the n-channel device, because of a partly buried channel. All noise traces are calculated with the respective transconductances to their corresponding gate voltage.

It can be clearly seen that the n-channel device had the lowest noise level with a peak-to-peak amplitude of $V_{gate} = 160 \mu\text{V}$. The device was driven at a working point of $V_{GS} = 3 \text{ V}$, $V_{DS} = 3 \text{ V}$ and revealed a transconductance of $g_m = 0.88 \text{ mS}$, which was a typical value for the used n-channel devices. In Figure 3-35, the autocorrelation-functions of these three measurements are shown. The values for $r(0)$ are reflecting the uncompensated DC-part of the noise. The DC-parts were:

- upper trace: $r_{p-2}^{nd}(0) = 1.54 \cdot 10^{-8} \text{ V}^2$
- middle trace: $r_{p-1}^{st}(0) = 0.47 \cdot 10^{-8} \text{ V}^2$
- lower trace: $r_{n-1}^{st}(0) = 0.11 \cdot 10^{-8} \text{ V}^2$

The trace for the n-channel autocorrelation-function in Figure 3-35 is plotted with a 0.1x scaling of the y-axis. Based on these autocorrelation-functions, it can be seen that

the raw data traces carried almost no interspersed noise, which would occur as periodical modulation in the autocorrelation-function.

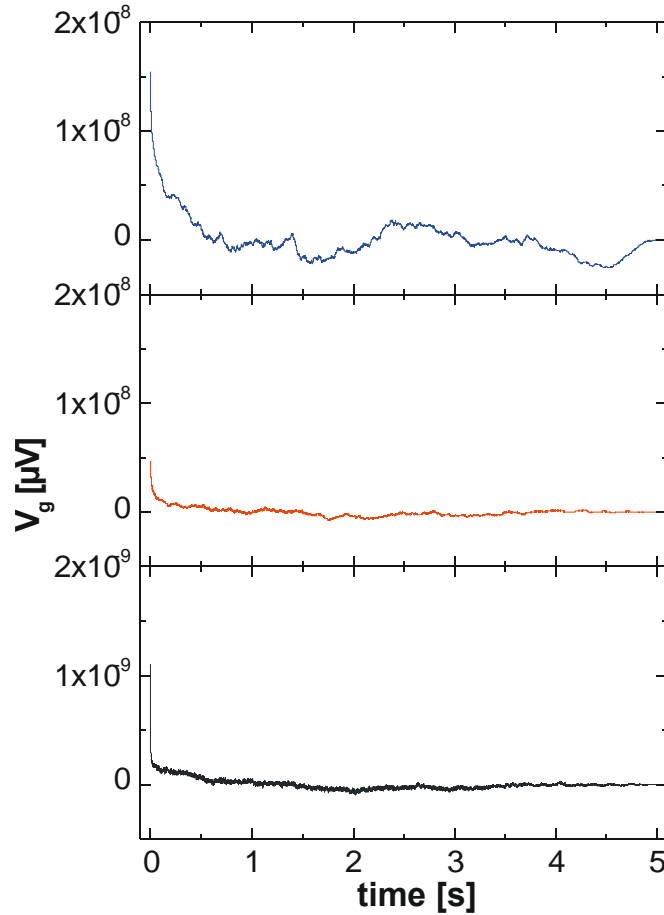


Figure 3-35 Autocorrelation-functions for the three noise measurements shown in Figure 3-34. The un-compensated DC-parts of the devices were $r_{p-2}^{nd}(0) = 1.54 \cdot 10^{-8} \text{ V}^2$, $r_{p-1}^{st}(0) = 0.47 \cdot 10^{-8} \text{ V}^2$, and $r_{n-1}^{st}(0) = 0.11 \cdot 10^{-8} \text{ V}^2$. The lower trace for the n-channel autocorrelation-function is plotted with a 0.1x scaling of the y-axis.

In Figure 3-36, the spectral noise density $W_{FET}(f)$ (V^2/Hz) of the three devices are plotted between 0.2 and 5000 Hz. By fitting the resulting traces with a $1/f^a$ -law the noise was identified as a $1/f$ -noise. The rules here are that if the parameter lies between $0.8 < a < 1.2$, the noise is called ‘ $1/f$ -noise’. The values based on the fits were: $a(n) = 0.8$, $a(p-1^{st}) = 0.88$, and $a(p-2^{nd}) = 0.9$. For comparing to different devices, the values at 1 Hz are often used in the literature. They are:

- $W_{n-FET}(1 \text{ Hz}) = 8 \cdot 10^{-12} \text{ V}^2/\text{Hz}$
- $W_{p1st-FET}(1 \text{ Hz}) = 7 \cdot 10^{-11} \text{ V}^2/\text{Hz}$
- $W_{p2nd-FET}(1 \text{ Hz}) = 5 \cdot 10^{-10} \text{ V}^2/\text{Hz}$

This confirms the previous observation at the raw data traces that the n-channel device carries the lowest noise. In the following section a theoretical treatment of the MOSFET noise will be given.

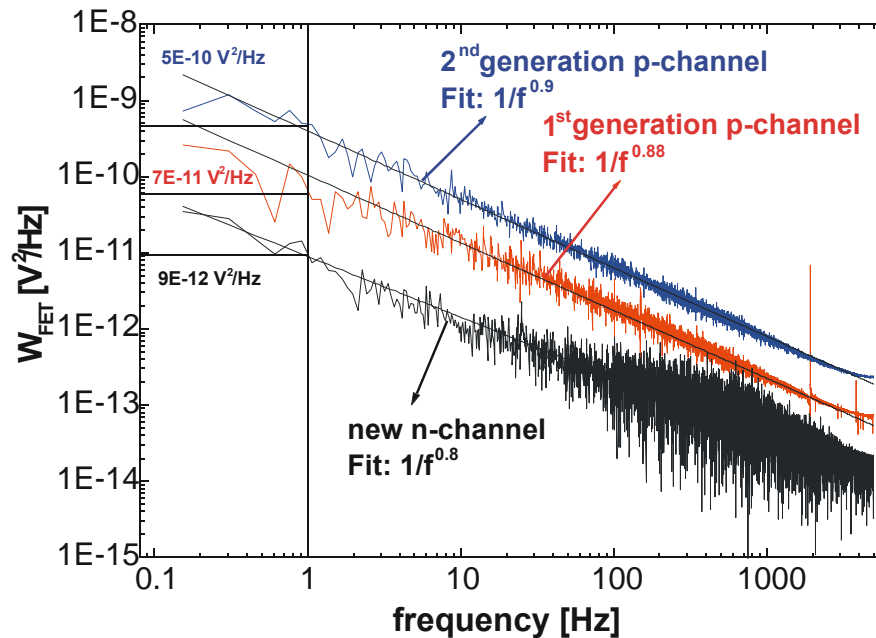


Figure 3-36 Spectral noise density $W_{FET}(f)$ (V^2/Hz) of the three devices plotted between 0.2 and 5000 Hz. The data traces were fitted with a $1/f^a$ -law and $a(n) = 0.8$, $a(p-1^{st}) = 0.88$, and $a(p-2^{nd}) = 0.9$. Therefore in this frequency range the $1/f$ -noise is dominating the overall noise (for '1/f-noise' a should be between 0.8 and 1.2 (Müller, 1990)). For comparison of different devices in the literature the values at 1 Hz are often used.

3.3.6 MOSFET Noise

There are many different noise types, which contribute to the total noise of a MOSFET device (Jordan and Jordan, 1964). The white noise is coupled to the mobility of the carriers in the channel and in the conductor paths. Here the scattering processes in between the carriers and at the scattering centres (e.g. enclosed metal atoms in the silicon lattice) are taking place. The amount of the white noise is proportional to the temperature (because higher temperature leads to more scattering caused by a higher carrier-mobility) and proportional to the resistance of the source and drain contacts. This is the reason for the higher noise level of the backside-contacted FET-arrays (see below). With wider contact lanes and higher doping of the source and drain connections, we were able to partly compensate the series resistance introduced by the backside contacts (about 300 Ω for each contact through the wafer).

Another noise source is the so-called shot noise (or popcorn noise). It occurs at reversed biased p/n-junctions and is caused by the finite size of the charges. The carriers are tunnelling through the p/n-junction with a certain rate. The processes are normally distributed and modulate a current flowing nearby. This noise type plays a minor role in the MOSFET devices (Das, 1972). Its rate is much higher for the junction FETs (Lauritzen, 1965).

In our frequency range of interest (0.1 – 5000 Hz) the main noise source is the frequency dependent $1/f$ -noise (or: generation-recombination noise, flicker noise, pink noise) as identified in the previous paragraph. Its theoretical description was first discussed by McWhorter (1957).

McWhorter-Model:

The McWhorter-Model is the most common theoretical description for the $1/f$ -noise in field-effect transistor devices. It is a physical model dealing with tunnelling processes. A short summary about the basic concepts will be given and how the amount of $1/f$ -noise in our BioFETs may be minimised.

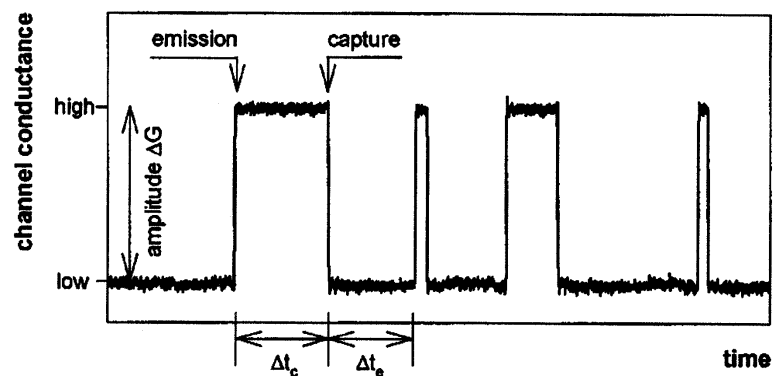


Figure 3-37 Channel conductance modulated by different emission- and capture-processes modulate the channel conductance in time. The figure was adapted from Mueller and Schulz (1998).

The $1/f$ -frequency dependency is energetically the best concept to span over a wide frequency range with the lowest energy consumption. The total $1/f$ -spectrum is a superposition of many single spectra with different frequencies (Müller, 1990). The concept of this model is that the channel conductance is modulated by capture and emission processes of major carriers. It is assumed that locally distributed traps for the carriers at the oxide-semiconductor interface and inside of the gateoxide are catching carriers and releasing them after a certain period of time. The tunnelling process leads to a distribution of time constants as the tunnelling process depends on the tunnelling distance. These fluctuations of the charges in the channel are modulating the transistor

current (Jordan and Jordan, 1964). Figure 3-37 shows different emission- and capture-processes modulate the channel conductance verses time.

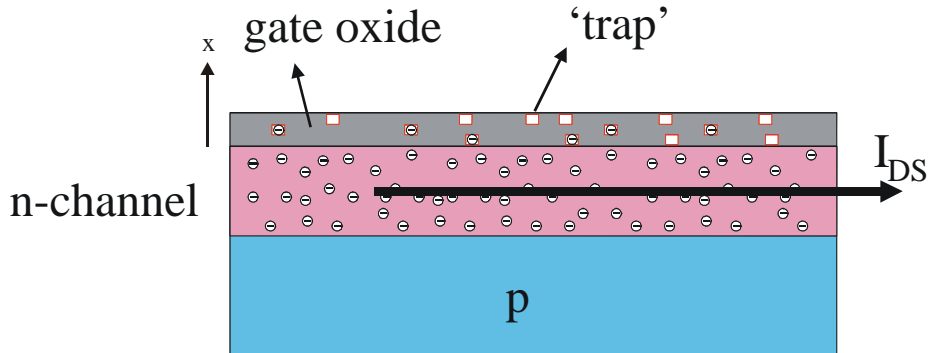


Figure 3-38 MOS-structure with traps in the oxide-semiconductor interface region. The number of oxide traps caused by enclosed impurities and/or imperfect lattice are enhancing the emission- and capture-processes (Müller, 1990).

In Figure 3-38, a MOS-structure with traps in the oxide-semiconductor interface region is shown. It is assumed that these defects in the oxide are evenly distributed in distance. With the hypothesis that these traps are being occupied by carriers from the inversion layer via tunnelling processes. The distribution of the time constants results as follows:

$$t(x) = t(0) \exp\left(\frac{x}{x_0}\right) \tag{3.58}$$

The tunnelling probability depends exponentially on the distance of the trap from the interface and is the reciprocal value of the timeconstant $t(x)$ (Eq. 3.58). The distribution of the time constants reaches from the lowest value $t_{min} = t(0)$, which is given by the traps at exactly the interface region between oxide and silicon up to a maximum value for the distant traps. The number of carriers in the inversion layer is assumed to be infinite. The carrier fluctuations per volume unit $\overline{\Delta N^2} / V = \overline{\Delta n^2}$ are given for every x-interval with (Müller, 1990):

$$\frac{W_N^*(x)}{V} = 4\overline{\Delta n^2} \frac{t(x)}{1 + w^2 t^2} \tag{3.59}$$

The spectrum for the whole process, which is a superposition of the single processes with different time constants, is given by integration over all x-values:

$$W = \int_0^{d_{ox}} \frac{W_N^*(x)}{V} dx \tag{3.60}$$

The spectrum W , which is the power spectrum of the carrier fluctuations per area unit, has the dimension ($\text{m}^{-2}\text{Hz}^{-1}$). With $dx = (x_0/t)$ (Eq. 3.58) and by assuming $\overline{\Delta n^2}$ to be constant it is:

$$W(\omega) = 4\overline{\Delta n^2} x_0 \int_{t_{\min}}^{t_{\max}} \frac{1}{1 + \omega^2 t^2} dt = 4\overline{\Delta n^2} x_0 \frac{1}{\omega} (\arctan \omega t_{\max} - \arctan \omega t_{\min}) \quad (3.61)$$

With the borders $\arctan g = g$ for $g \ll 1$ and $\arctan g = \pi/2$ for $g \gg 1$ the spectrum gives for the range $\omega t_{\min} \ll 1 \ll \omega t_{\max}$:

$$W(\omega) = \frac{4\overline{\Delta n^2} x_0}{\omega} \quad (3.62)$$

In practice, chip designers are dealing with empirical formula, in which the carrier fluctuations per volume unit are expressed with the transistor dimensions (Jakobson et al. 1998).

$$W_{V_{\text{Gate}}}(f) \approx \frac{q^2 k T N_t}{C_{\text{ox}}^2 W L} \cdot \frac{\bar{x}}{f} \quad (3.63)$$

where q is the charge of a single carrier, kT the thermal activation energy, C_{ox}^2 the gateoxide capacitance, W the width, and L the length of the channel. The former distance x_0 of the inversion region and semiconductor/oxide interface is replaced by an average tunnelling distance \bar{x} (~ 0.1 nm) and N_t is the total number of traps at the interface. This value has to be estimated from empirical results and is strongly dependent on clean fabrication processes. In the literature, several attempts have been reported to decrease the oxide defects by additional annealing processes (Cho et al., 1998; Cho et al., 1999; Hattori et al. 1999; Lucovsky et al., 1997) and by loading the oxide with NO_2 gas during the dry oxide deposition on the gate (Masson et al., 1999; Ren et al., 1999). In Eq. 3.63, it shows that the noise can be lowered with lower temperature. It is very restricted, because the cells need to have at least 33°C to maintain their biological function (e.g. the contraction of cardiac myocytes ceases below a certain temperature). In the frequency range we are also restricted as cellular electrical signals occur in the ms-range. With our n-channel devices, the distance \bar{x} from the inversion channel to the interface of the device was increased, which decreases the probability of the tunnelling processes. With the parallel plate capacitor equation $C = \epsilon_0 \epsilon_r W L / d$ this noise source is strongly dependent on the gate size to the power of two. This is the reason why the p-channel FET of the 1st generation revealed a lower noise than the p-channel transistor of the 2nd generation. Other gate materials with higher dielectric constants such as $(\text{Ba}, \text{Sr})\text{TiO}_3$ or ZrO_2 (ϵ_r for these perovskites can be in thin film higher than 200 at room temperature (Schwan, 1996)) may increase the transistor performance. The number of oxide traps N_t can be influenced by special

annealing processes, which may have an influence in the design of new BioFET generations.

Jakobson and Nemirovsky (1999) and Jakobson et al. (2000) have shown that the electrolyte-gateoxide interface is barely contributing to the total noise of ion sensitive devices. The top design of the transistor gate will not change the noise properties of new chip generations.

3.3.7 Noise of the Backside-contacted FET-Arrays

The noise of the backside-contacted FET arrays was found to be slightly higher than the noise of the standard FET arrays. The reason for this is a higher white noise baseline caused by the thermal noise of the higher contact lane resistances. In addition, the transconductance of the transistor is lowered as a result of lower drain source currents I_{DS} (Eqs. 3.19, 3.20). A second problem was the more open encapsulation (especially for the Langmuir-Blodgett device, Figure 3-21), which offered a wider area for interspersed noise sources. In Figure 3-39, the comparison of a noise measurement of the backside FET array 27DD38x32, which is a triple-gate FET device (Figure 3-19), is shown. The gate-structure of the device had a width of 38 μm , a length of 3x2 μm (2 μm for each gate in the triple structure), and a gateoxide thickness of 10 nm. The working point of this transistor was $V_{DS} = -3\text{V}$ and $V_{GS} = -2\text{V}$, which resulted in a transconductance of $g_m = 0.33 \text{ mS}$.

In Figure 3-43, the calculated autocorrelation-functions of the two devices are compared. In the lower trace for the backside-contacted device it can clearly be seen that some interspersed noise frequencies were present.

The noise power spectrum of the backside-contacted FET array lies somewhat higher than the noise power spectrum of the standard device (Figure 3-41). In addition, the trace carries strong frequencies of 50 and 150 Hz, which are shifting the noise level to higher values. The values at 1 Hz are:

- $W_{p2nd-FET}(1 \text{ Hz}) = 5 \cdot 10^{-10} \text{ V}^2/\text{Hz}$
- $W_{backside-FET}(1 \text{ Hz}) = 1.5 \cdot 10^{-9} \text{ V}^2/\text{Hz}$

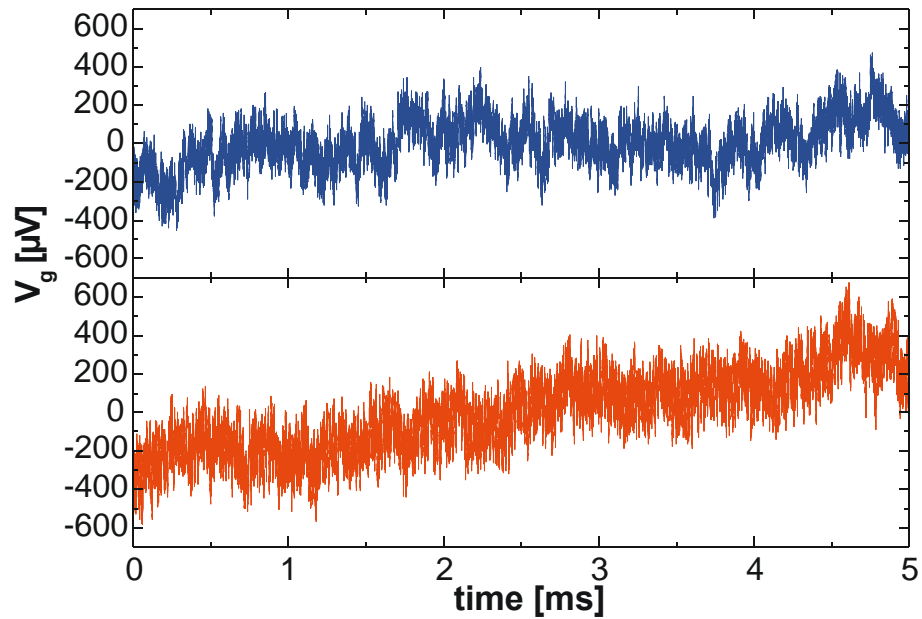


Figure 3-39 Comparison of the noise level of a standard p-channel FET array of the 2nd generation with the noise level of the triple-gate p-channel FET array 27DD38x32 (lower trace).

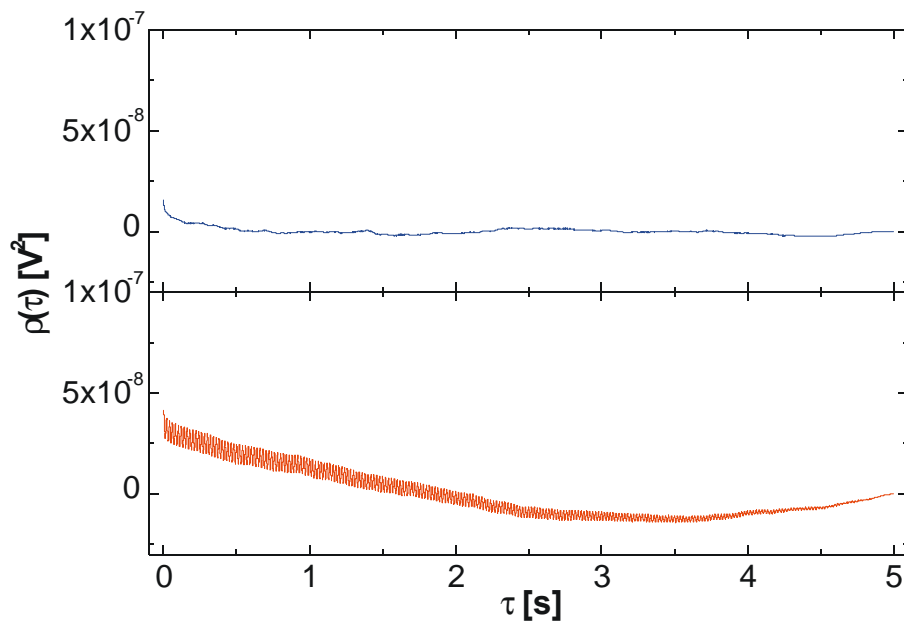


Figure 3-40 Comparison of the calculated autocorrelation-functions of the two devices. In the lower trace for the backside-contacted device it can clearly be seen that some interspersed noise frequencies are present.

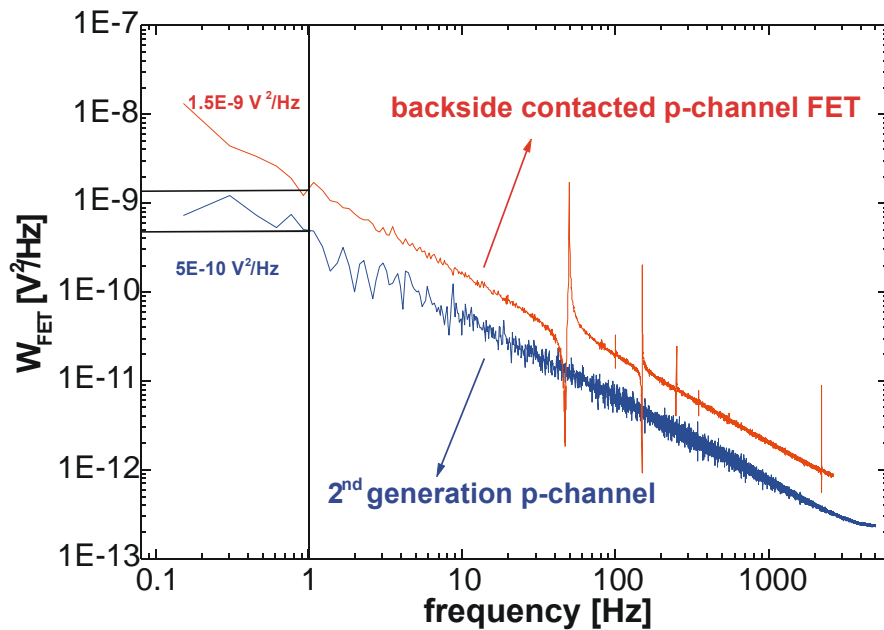


Figure 3-41 Comparison of the noise power spectra of the standard p-channel FET array of the 2nd generation and the triple-gate p-channel FET array 27DD38x32 (upper trace). The trace for the backside-contacted array carries strong frequencies of 50 and 150 Hz, which are shifting the noise level to higher values. The values at 1 Hz are indicated in the figure.

3.3.8 Noise of the EGE-Devices

The noise of the EGE-Devices was minimised by using the electrodes coupled to the gates of low-noise JFETs (see below). In the earlier set-ups, we tried to measure the signals coupled to the electrode with standard current-amplification circuits. This always resulted in a noise level higher than 1 mV caused by the high input impedance. For the coupling of single cells to the electrode it was not desirable to build up platinum coatings in order to decrease the impedance. In the following, the system electrode-JFET-amplification circuit was characterised with respect to noise amplitudes. In Figure 3-42, the raw data traces are shown.

In the upper trace of Figure 3-42, the contribution of the amplifier circuit can be seen. The input stage was bridged with a 10 k Ω resistor, which was biased by a voltage of $V_{Bias} = 0.4$ V. The middle trace shows the noise of the amplifier circuit plus the noise of the JFET (BF510, Philips Semiconductors, Netherlands) with its gate grounded. The working point of the FET here was $V_{DS} = 1$ V and $V_{GS} = 0.05$ V, which revealed a transconductance of $g_m = 2.88$ mS. In trace C, the total noise of the combination of electrode-JFET-amplification unit with a FET working point of $V_{DS} = 1.2$ V and $V_{GS} = 0$ V, which revealed a transconductance of $g_m = 2.58$ mS. The JFET gate was grounded via the electrode-electrolyte-Ag/AgCl bridge.

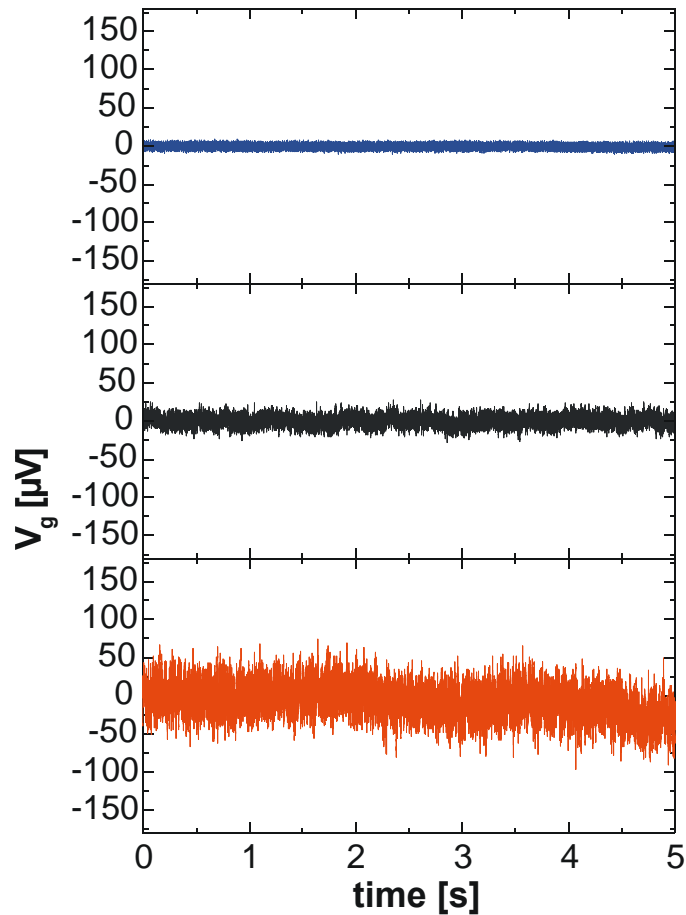


Figure 3-42 Rawdata traces of the EGE set-up. The noise was recalibrated with the respective transconductances to equivalent gate voltage. In the upper trace the input was bridged with a 10 kW resistor, which was biased by a voltage of $V_{Bias} = 0.4$ V. In the second trace the JFET was mounted into the input stage with grounded gate. In the lower trace the electrode chip was mounted into the headstage and the JFET gate was then grounded via the electrode-electrolyte-Ag/AgCl bridge.

In the case of the resistor at the input stage, a peak-to-peak noise amplitude of $V_{gate} = 14$ μ V can be estimated. In the second case, with the directly grounded JFET at the input stage, the peak-to-peak amplitude was $V_{gate} = 35$ μ V. If the electrodes are mounted and connected to the gate input they are acting as antennas and the peak-to-peak amplitude of the total noise increases to $V_{gate} = 100$ μ V.

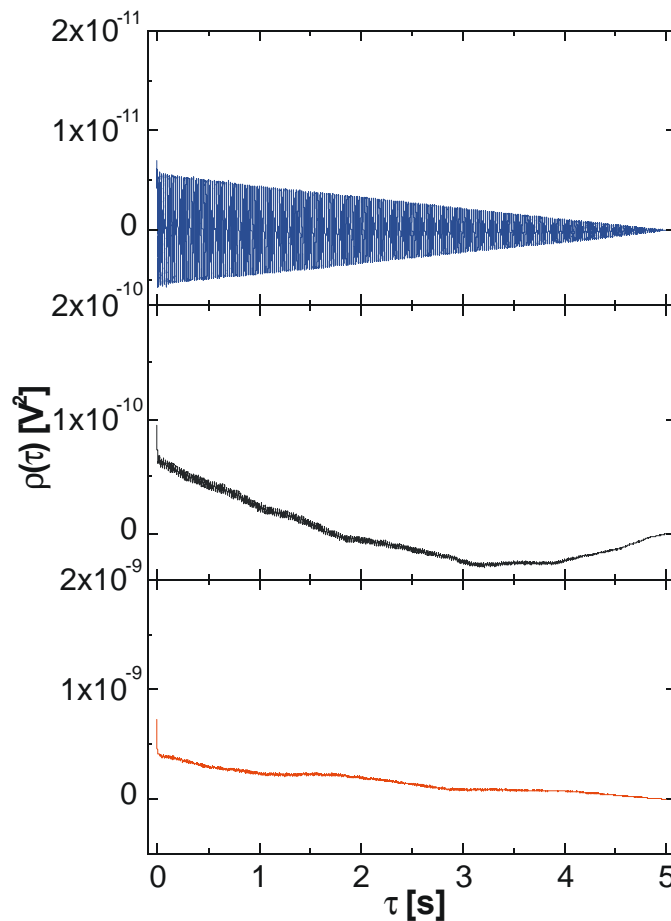


Figure 3-43 Autocorrelation-functions calculated from the rawdata traces of Figure 3-42. The different plots have different scalings: 1x (lower), 0.1x (middle), and 0.01x (upper).

In Figure 3-43 the autocorrelation-functions, which were calculated from the raw data traces, can be seen. The y-axis had to be scaled in aid of comparison.

The spectral noise density $W_{EGE}(f)$ (V^2/Hz) (Figure 3-44) of the three different measurements are plotted in a frequency range of $0.2 Hz < f < 5000 Hz$. For the purpose of comparison, the values at 1 Hz are indicated in the figure. The values are:

- $W_{10kW}(1Hz) = 7 \cdot 10^{-15} V^2/Hz$
- $W_{JFET}(1Hz) = 3 \cdot 10^{-12} V^2/Hz$
- $W_{EGE}(1Hz) = 2 \cdot 10^{-11} V^2/Hz$.

This means the low frequency noise level is one fold higher than the electrode chip connected at the inputs. The noise level of the amplifier circuit can be ignored. It may be possible that by using shorter lanes on the electrode chips (i.e. smaller chips) or shielding the backsides of the electrode dyes by an evaporated conducting layer could lower the antenna effect.

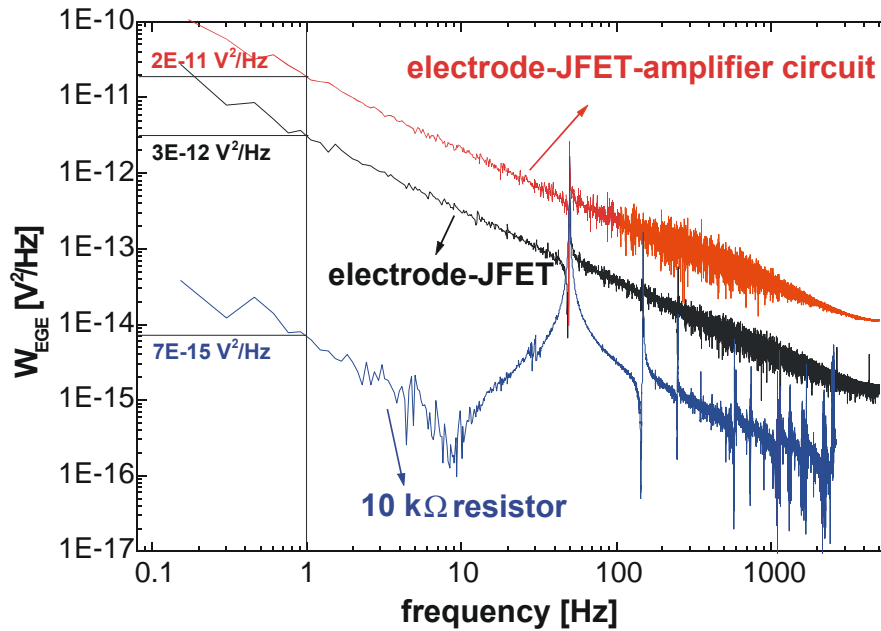


Figure 3-44 The spectral noise density $W_{EGE}(f)$ (V^2/Hz) of the three different measurements in a frequency range of $0.2 \text{ Hz} < f < 5000 \text{ Hz}$. For comparison the values at 1 Hz are indicated in the figure.

3.3.9 JFET Noise

In this section, the noise mechanisms occurring in JFET devices will not be discussed in detail. The basic function, the difference in design, and the intrinsic noise sources will be compared to the previously described treatments of the MOSFET structure.

In the JFET structure a gateoxide layer does not isolate the gate-input of the device. A reversed biased p^+n -junction (for an n-channel JFET) ensures that no current is flowing over the gate structure. The channel is built up under this p^+ -doped gate area and the gate potential influences its conductance. In Figure 3-45, a schematic of a JFET device is shown. For the fabrication of planar JFETs, silicon wafers with epitaxially grown and already doped layers are widely used (Baturitsky, 1996; Fazzi and Rehak, 1996 a; Fazzi and Rehak, 1996 b; Matsuura and Nishida, 1998). Typical values (for an n-channel device) are:

- Bulk material p-doped with $5 \cdot 10^{17} \text{ 1/cm}^3$ impurities.
- Epitaxially layer n-doped with $1 \cdot 10^{17} \text{ 1/cm}^3$ impurities and $\sim 1 \mu\text{m}$ thickness.
- Strongly doped gatearea ($1 \cdot 10^{19} \text{ 1/cm}^3$ impurities) with length L and width W and depth a (typically $0.5 \mu\text{m}$).

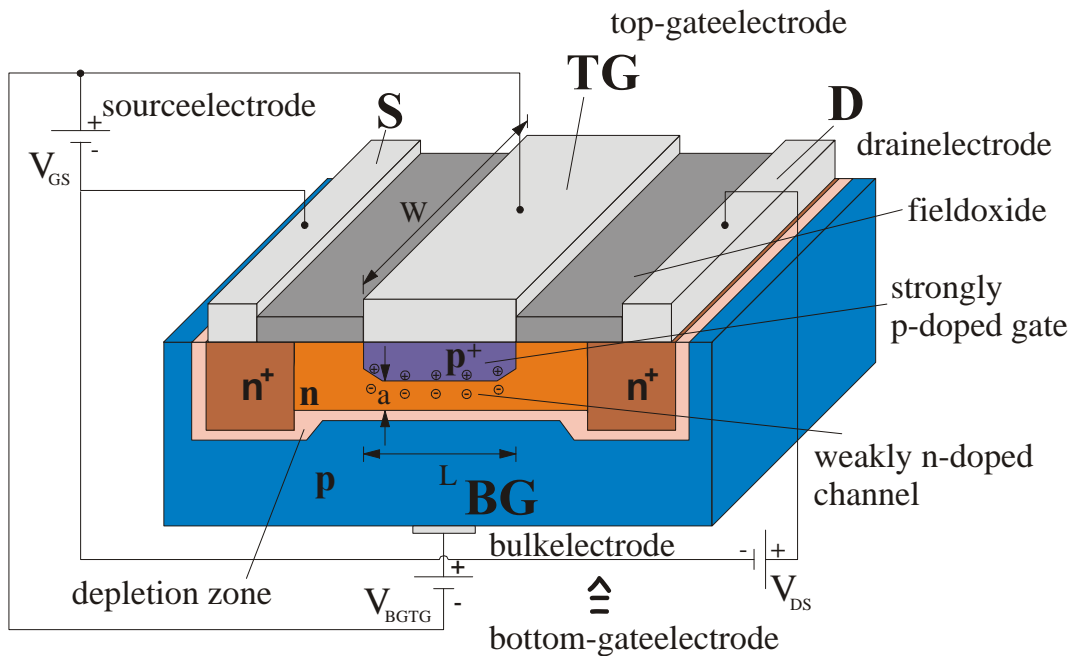


Figure 3-45 Schematical view to the design of a JFET gate structure. The gate area is strongly p-doped and the current is flowing underneath this doped area through the weakly n-doped channel with remaining thickness a . The JFET offers the possibility to influence the drain-source current from the bulk contact in addition. If this contact is connected to the top gate the JFET is called 3-terminal device, if it is individually addressable the JFET is called 4-terminal device.

The JFET is a depletion mode device (see paragraph 3.1), which means a drain-source current I_{DS} is already flowing if a voltage V_{DS} is applied from source to drain contact. Applying an appropriate gate-source voltage V_{GS} can pinch off this current (Müller, 1990):

$$V_p = \frac{qN_D a^2}{2\epsilon_{Si}} - V_D \quad (3.64)$$

V_D is the diffusion voltage, which is normally very small and can be ignored, N_D the total number of electron donators, q the carrier charge, ϵ_{Si} the dielectric constant of silicon, and a the thickness of the channel (thickness of the epitaxially layer minus the diffused gate depth).

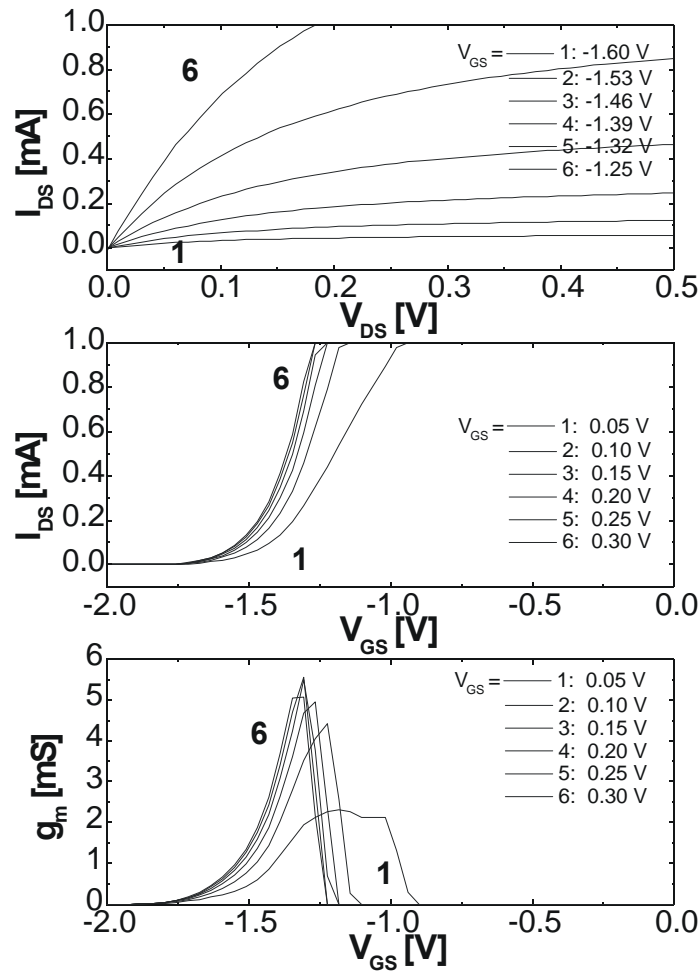


Figure 3-46 Characteristics of the 4-terminal JFET MX16B from MOXTEK Inc., USA. Because of our limited drain-source current of $I_{DS(max)} = 1$ mA the device was driven in a very low working range. Even in this range it had a transconductance of $g_m \gg 5$ mS (at $I_{DS} = 2.5$ mA a value of 16 mS is stated by Lund et al. (1996)).

In Figure 3-45, it can be seen that the JFET offers the possibility to influence the drain-source current from the bulk contact in addition (Fazzi and Rehak, 1996a), (Fazzi and Rehak, 1996b). Therefore, the bulk contact of a JFET device is often called ‘bottom-gate’, BG. If this contact is connected with the top-gate, the JFET is called a 3-terminal device. If it is individually addressable, the JFET is called a 4-terminal device. Similar treatment of the charge in the channel region as in paragraph 3.1 (p-channel MOSFET) leads to the drain-source characteristic of the n-channel JFET (Schlachetzki, (1990):

$$I_{DS} = \frac{qN_D m_n a W}{L} \left(V_{DS} - \frac{2}{3\sqrt{V_p + V_D}} \left((V_D + V_{GS} + V_{DS})^{\frac{3}{2}} - (V_D - V_{GS})^{\frac{3}{2}} \right) \right) \quad (3.65)$$

The characteristics (I_{DS} vs. V_{DS} and I_{DS} vs. V_{GS}) are similar to MOSFET characteristics. The only difference to the MOSFET device in the drain-source characteristic is that it is possible to send current pulses through the gateelectrode without damaging the gate structure. With higher drain-source voltages V_{DS} an avalanche breakdown of the p^+n -junction at the gate occurs with strong drain current I_{DS} . In the case of the 4-terminal device, it is even possible to send current pulses from the bottom-gate to the top-gate (Fazzi and Rehak, 1996a), (Fazzi and Rehak, 1996b). This provides an opportunity to stimulate and record from neuronal cells using the same device.

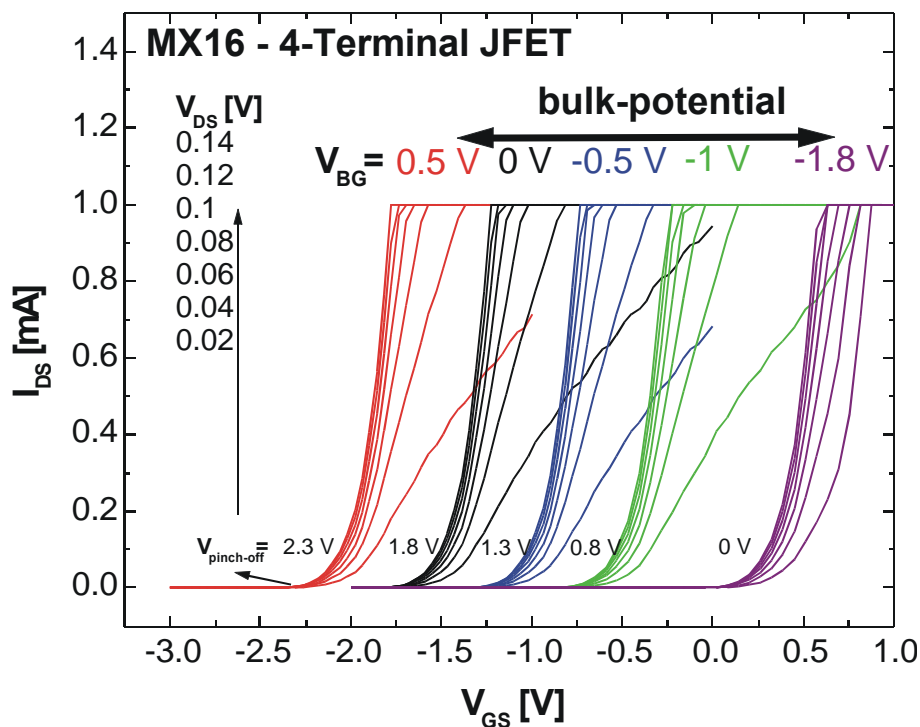


Figure 3-47 Reaction of the gate-source characteristics of the JFET MX16B to different bulk potentials. The pinch-off voltage can be shifted in a wide range.

During this work, some ‘ultra-low-noise’ JFET devices kindly provided from MOXTEK Inc., USA (MX10, MX12, MX16B) were tested. In Figure 3-46, the drain-source characteristic of a 4-terminal MX16B device is shown.

With such devices, it would be possible to influence the transistor from the bottom-gate and to send pulses from the bottom-gate to the top-gate. In Figure 3-47, the influence of the bottom-gate can be seen as different bulk-potentials are shifting the whole characteristic curve. The development of such devices for the use as BioFETs may offer new perspectives in cell-transistor coupling.

From the structure of the JFET device (Figure 3-45), it is clear that this transistor reveals a much lower noise level in the low frequency range. The probability for the tunnelling process, which leads to the generation-recombination noise, is decreased by more than 3 orders of magnitude at 1 Hz, because the carriers are forced to flow about $0.5\ \mu\text{m}$ underneath the interface (Lauritzen, 1964; Santiard and Faccio, 1996). The popcorn noise source introduced by the p^+n -junction is much lower in amplitude. This leads to a reduced total noise level of the JFET devices in the low frequency range. In Figure 3-48 the noise levels of the MX16B JFET is compared with the noise level of the n-channel FET. The JFET was mounted inside a standard chip carrier and the gate was grounded with two Ag/AgCl electrodes bridged over a standard electrolyte bath. The transistor revealed a transconductance of $g_m = 4.85\ \text{mS}$ at a working point of $V_{DS} = 0.5\ \text{V}$, $V_{GS} = -0.95\ \text{V}$. The peak-to-peak noise level can be estimated to $V_{gate} = 30\ \mu\text{V}$, which is about 5 times lower than the noise level of the n-channel device ($V_{gate} = 160\ \mu\text{V}$).

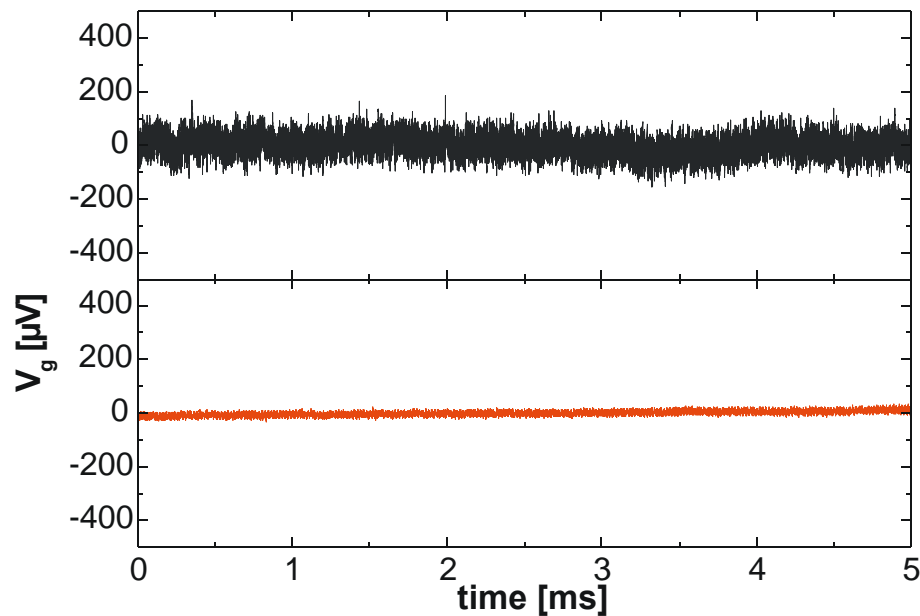


Figure 3-48 Comparison of the noise levels of the n-channel FET (paragraph 3.5) in the upper trace and the ultra-low-noise JFET (MX16B from MOXTEK Inc., USA) in the lower trace. The peak-to-peak noise levels can be estimated to $V_{gate} = 30\ \mu\text{V}$ for the JFET and $V_{gate} = 160\ \mu\text{V}$ for the n-channel device.

Chapter 4

Experimental Set-up

The measurement set-up that is required to produce signal amplification and data acquisition will be first explained. This chapter will also provide accounts of the amplifier systems for the external sensors that utilised different headstage amplifiers for the FET- (16 channels) and EGE-devices (64 channels) and the common 16-channel main amplifier and the 64 channel EGE main amplifier. During the present study, a novel, self-compensating, amplifier circuitry was developed, which automatically subtracts the DC parts of the signals that arise from the constant current in the working point of the transistor. In order to achieve this aim, a very slow feedback loop in their circuitry is used in the new main amplifier. This is followed by a detailed look at the most common measurement tool in electrophysiology - the patch-clamp amplifier. This method is well established for measuring signals from single cells (Hamill et al., 1981; Neher and Sakmann, 1976; Sakmann and Neher, 1995). Finally, the procedures for a standard patch-clamp measurement are explained and the conditions that are necessary

for obtaining good patch-clamp recordings will also be discussed. With the knowledge of the compensation principle, it is easy to interpret the capacitive transient that we observe in the external signals in a voltage-clamp coupling experiment.

4.1 Measurement Set-up

The set up used in the present study has been previously described (Krause, 2000; Offenhäusser et al. 1997; Sprössler, 1997). It is divided in different functional subunits, which are depicted in the schematic Figure 2-3. During this work, two new headstage amplifiers have been developed. One for the backside contacted 16 channel FET arrays and one for the new chipboard carrying the EGE chips, with which 64 channels at 10 kHz can be recorded simultaneously. The FET or the EGE chips, that have established cultured cells, are mounted onto these preamplifiers.

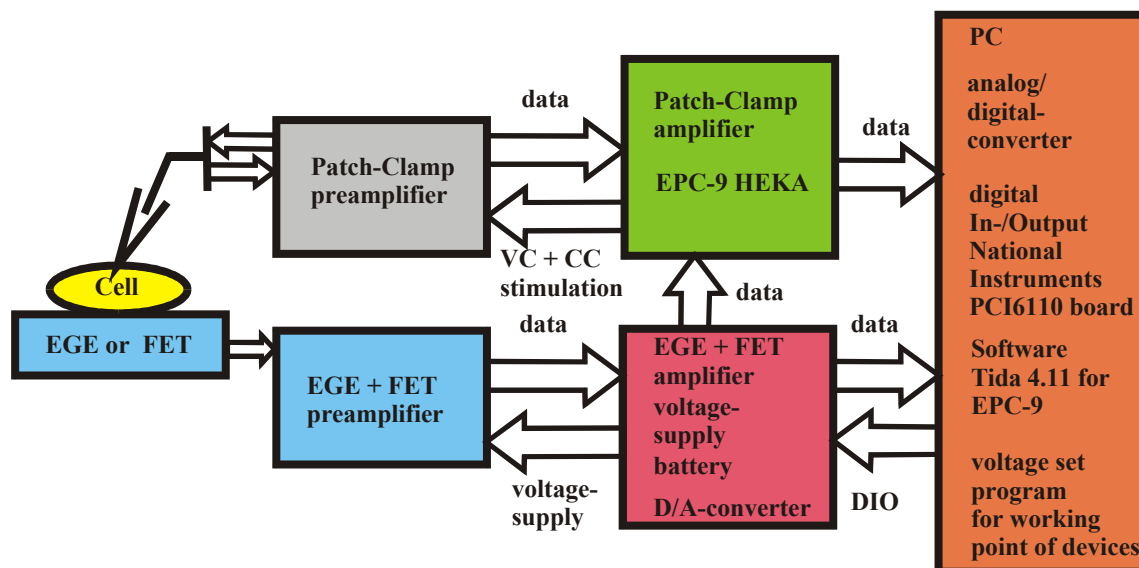


Figure 4-1 Schematic showing the set-up for single cell coupling measurements with EGE or FET chips. Here the second version of the main amplifier available in our group is shown. The data acquisition is mainly performed by the Tida 4.11 software for the EPC-9 patch-clamp amplifier.

The preamplifiers are designed to fit under the incident light differential interference contrast microscope (AxioTech Vario DIC, Zeiss, Germany). They contain the first amplification stage, with current to voltage conversion as well as a 10 times preamplification of the signals. We have currently three versions of main amplifiers. The first FET model, presented by Offenhäusser et al. (1997), also possessed the capability of pH measurements. In this model, DC parts of the signals are compensated by computer controlled DA-converters and it is able to perform a real-time DC measurement. The second model is a 16-channel amplifier for cardiac myocyte

measurements and single-cell coupling measurements. This system can be used with both types of FETs and EGEs using the EPC-9 patch-clamp amplifier operated by the Tida 4.11 software. The third main amplifier, a 64-channel tool, was developed for sensor application with cardiac myocytes cultured on the 64 channel metal electrodes. The pH measurement set-up uses the software routines implemented by Sprössler (1997). For the single cell coupling measurements, the second version of the main amplifier was used.

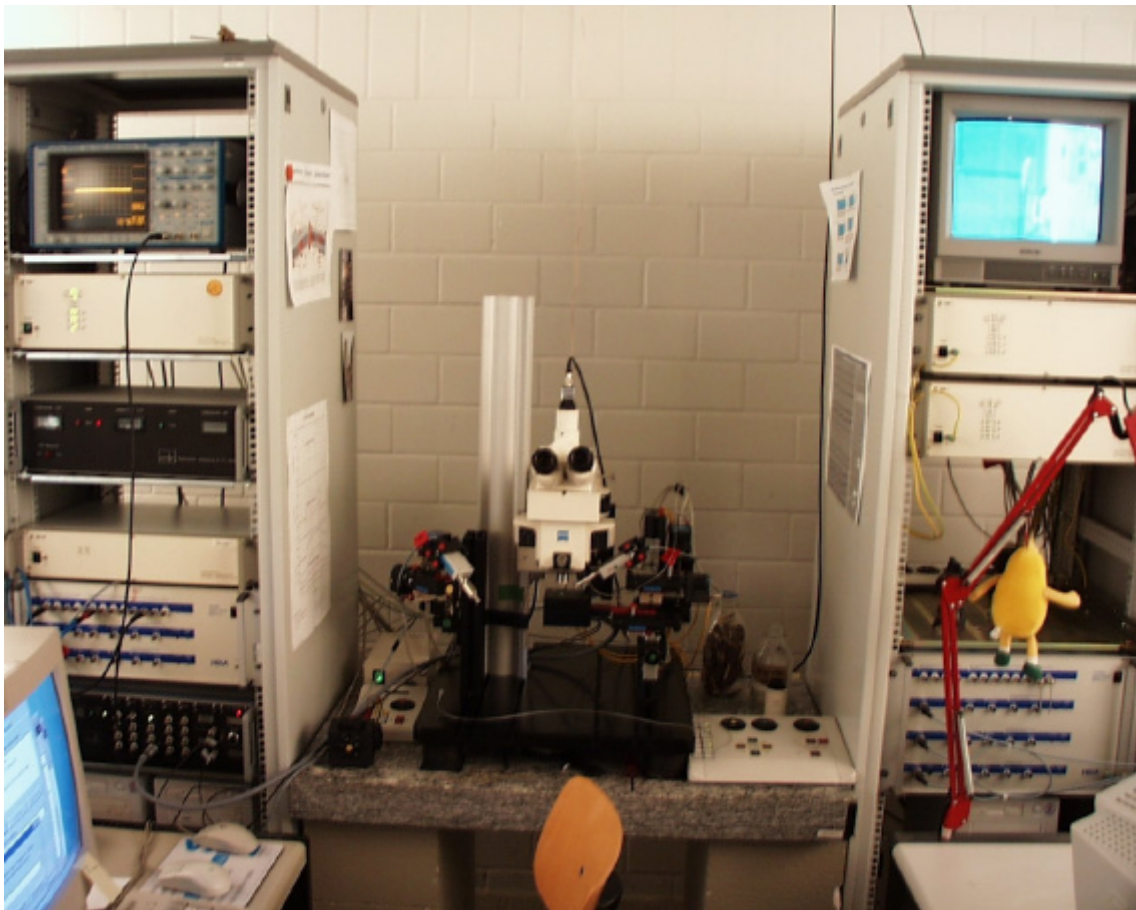


Figure 4-2 Experimental set-up for the cell transistor coupling measurements. The rack on the left side contains an oscilloscope, the control unit for the micromanipulators, the 16-channel main amplifier with its battery power unit, and the EPC-9 patch-clamp amplifier. In the middle part the upright microscope, the mounted preamplifier for the sensor chips, and the two preamplifier arms of the patch-clamp set-up can be seen. In the rack of the second electrophysiology set-up the video monitor is placed. A little CCD-camera, adapted to the upper part of the microscope, is operated by a video card installed in a second PC.

For data acquisition, the TIDA 4.11 software for the EPC-9 system was used. The subsequently amplified signal of the desired transistor gate, where the patch-attached cell was located, can be fed into the external input of the EPC-9 by using a BNC-cable

attached to the front plug for this channel (on the frontside of the main amplifier 16 plugs are provided, one for each channel). With this method, it is possible to make use of the signal averaging routine provided by the TIDA software. The main amplifier contains the power source for all operational amplifiers in headstage, main amplifier and the working point of the FET devices. The subsequent amplified signal was amplified 100 times more in the main amplifier stage. The power supply to the amplifier stages was completely switched to that of a battery. This reduced the interspersed noise in the amplifier output signal significantly (see Chapter 3).

The manipulation of the glass pipettes in the μm range was done with a manipulation unit of Luigs & Neumann GmbH, Germany. These systems contain 3 micromotors for movements in the x-, y- and z-direction controlled by a touchpad. A fourth motor was used to manipulate the microscope in the z-direction. The power supply to the micromanipulation unit, the patch-clamp amplifier and the main amplifier for the extracellular devices are located inside a rack (Figure 4-2).

The micromotors for the manipulation of the two patch-clamp pipettes, the preamplifier for the extracellular sensors and the microscope were mounted on a vibration-free, air buffered platform. An axiotech microscope from Zeiss offers the possibility of mounting a camera for the observation of cells during measurements. A CCD-camera (Sony XC-333 P, Sony International Europe GmbH, Stuttgart), operated with the PC and a video card (Matrox Meteor II, Matrox Imaging GmbH, Germany), was used to follow the gradual movements of the pipette to the cell visualised on a colour monitor (Sony Trinitron, SSM-14N5E). This allowed a very precise movement of the glass pipette onto the cell membrane. It was a much more successful procedure than the 'electrical method' by means of observing the pipette current signal in the TIDA screen with the PC. During the initial pipette manipulation in a cell-transistor coupling measurement, a total of the 100 \times magnification was adequate. However, once the pipette was immersed into the bathing solution, a 200 \times magnification would be more appropriate in order to view the structures of the glass tip and the cell membrane more clearly. The images were captured by optical control via the CCD-camera and displayed onto the video screen. The advantage of using an immersed lens was that the image errors caused by light reflection and scattering as light enters from air to liquid are no longer present and no vibrations at the liquid surface affected the image of the cell. These circumstances resulted in a much better optical control during a coupling measurement.

4.2 Amplifiers and Set-up for External Cell Measurements

The extracellular signals monitored by the FET- or EGE-sensors are amplified in two stages. The first stage is located inside the head of different preamplifiers, which can be mounted under the microscope. They are connected with a special shielded cable to the main amplifier stage, which is located in the rack beside of the microscope platform. In the following part the different electronic components are described.

4.2.1 EGE Preamplifier Stage

The second version of the EGE preamplifier headstage was developed based on the knowledge gained from the first version (Krause et al., 2000). The housing is made of aluminium, which was black anodised to prevent from further oxidation.

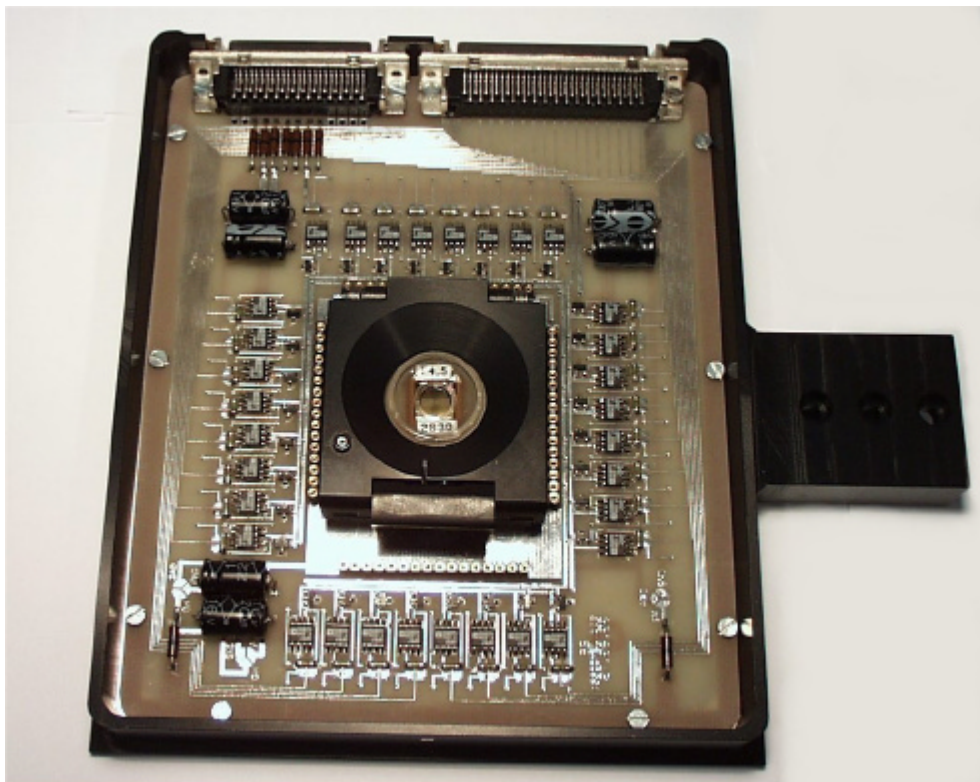


Figure 4-3 Housing of the EGE preamplifier-stage with the electronic circuit board. It contains the first amplification unit for all 64 channels. In the middle part the test socket with the gilt spring contacts can be seen. The large 68 D Sub connector contains all separate data lines and the 50 D Sub connector is used for voltage supply of OPs, FETs and heating.

It consists of a ground plate and a cover with a hole in the middle of the upper lid. The housing is designed for the use with an inverted microscope (transmission mode with standard phase contrast, when glass is used as chip material) or for mounting under the microscope (reflection mode with differential interference contrast mode (DIC)). In the ground plate the electronic printed circuit board (PCB) with all electronic components in surface mount technique (SMD) is fixed (Figure 4-3). An (OP-97F Analog Devices inc., USA) operational amplifier (OP) is used for the I-V conversion.

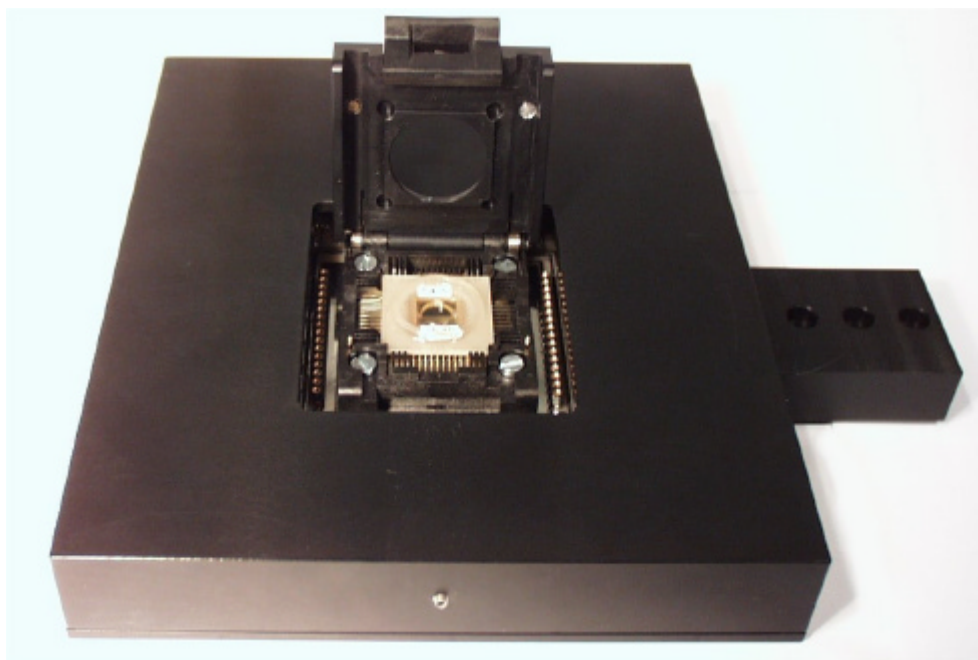


Figure 4-4 EGE preamplifier head with inserted EGE chip and closed covers. The Ag/AgCl electrode is directly integrated in the cover of the test socket. On the frontside the two connectors can be seen and on the left side the holder for the mounting under the hanging microscope is located.

On this board, a modified test socket (PLCC68 T+B IC51, YAMAICHI Inc., Munich) is fixed. This provides 68 gilt spring contacts. The top cover of this test socket has been re-designed in black anodised aluminium. This cover acts as an additional shield (connected to ‘head ground’) and holds the isolated Ag/AgCl electrode (connected to ‘bath ground’). This socket provides a quick and reliable exchange of the EGE-chips. By using such a test socket, an unlimited number of exchanges are possible without contact problems. This is the main advantage to the previous version of EGE-head, where we always had contact problems by using a Pentium socket. At the back of the EGE headstage two connectors are placed. One connector (68 Sub D) contains the data lines and one connector (50 Sub D) is used for the voltage supply of the OPs, the FETs and the heating. Essential elements of the first amplification circuit are the low noise junction FETs (JFET PMBF5484 from Philips Semiconductors, USA).

These transistors exhibit in the relevant frequency range (0.1 Hz to 10 kHz) a very good signal-to-noise ratio with a very low amount of inherent noise. The metal electrodes of the EGE array are directly connected to the gates of these JFETs. The bath solution is grounded with the Ag/AgCl electrode at the socket cover, which acts as ground potential when the gate-source and the drain-source voltages are applied to the JFETs. The voltage supply for the JFETs is located inside of the main amplifier stage.

The drain contacts of the JFETs are connected to the negative inputs of the operational amplifiers. The capacitive or active current at the gate in a coupling measurement is converted at the JFET into a current signal I_{DS} . The OPs are used as I-V converters with $V = 5 \text{ k}\Omega \cdot I$. The converted current inputs are guided through the data lines as preamplified voltage signals. Therefore, the data lines don't have to be particularly shielded.

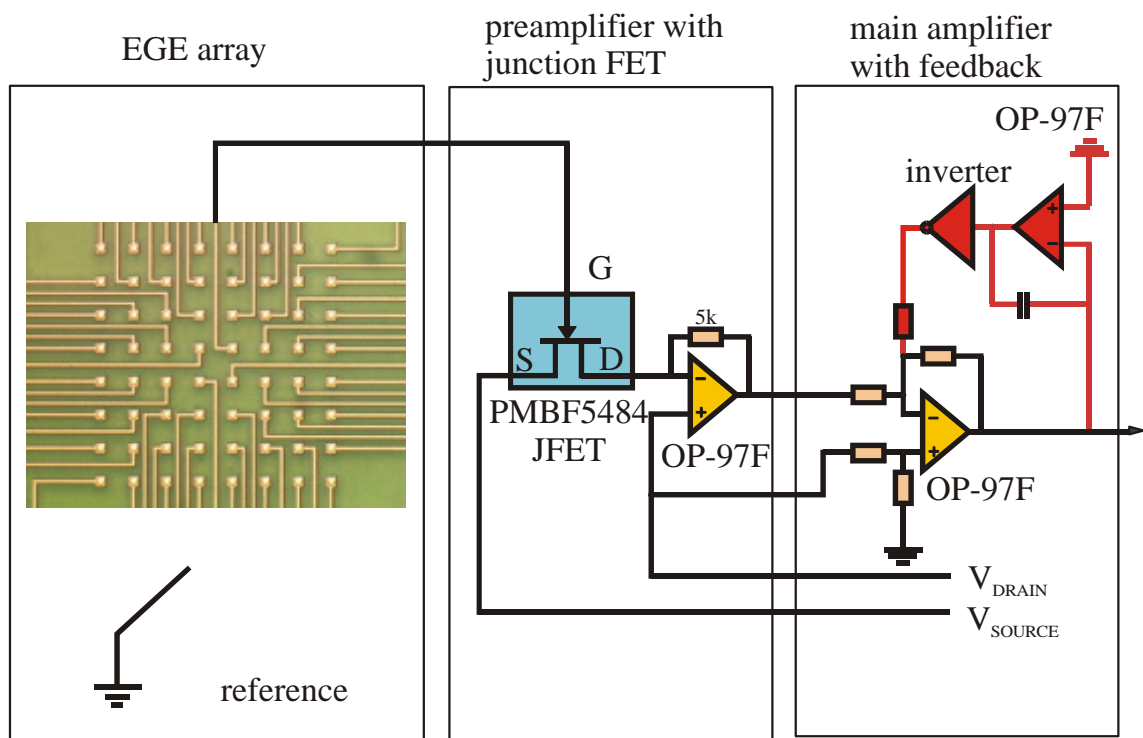


Figure 4-5 Schematic of the first and second amplification unit of the EGE set-up. The main amplifier stage at the right side can be used in the FET set-up as well.

In the predefined working point, high working currents of the JFETs superimpose the measurement signals I_{signal} . The nearly constant DC part of the signals is compensated by a feedback loop, which sets the output of the whole system to baseline.

4.2.2 Backside-contacted FET Preamplifier Stage

The set-up for our standard FET devices was described in detail by Offenhusser et al. (1997) and Krause (2000). The present study introduced a second FET preamplifier, which has been developed for the backside contacted FET devices. The housing of the FET headstage (Figure 4-6) contains a similar preamplifier circuit as the first system. A 22 pin zero force holder for installation of the device into the headstage is used.



Figure 4-6 Preamplifier headstage for the backside contacted FET devices. The size of the housing and the principle of the amplification circuitry is similar to the standard FET preamplifier developed by Offenhusser et al. (1997), Sprosler et al. (1998) and Krause (2000).

The compensation and amplification circuit are nearly the same as those found in the EGE system. Only the electrodes and the commercial JFETs are replaced by our custom-made, FET transistors. In Figure 4-7 the measurement principle for the FET circuit is shown. In this circuitry, the OPs are used as I-V converters with $V = 10 \text{ k}\Omega \cdot I$. The *current* inputs are preamplified and converted to *voltage* signals through the data lines as in the EGE set-up described before. The main advantage of both set-ups is that the signal recording can be done with the same software (MED64 conductor from Panasonic, Japan).

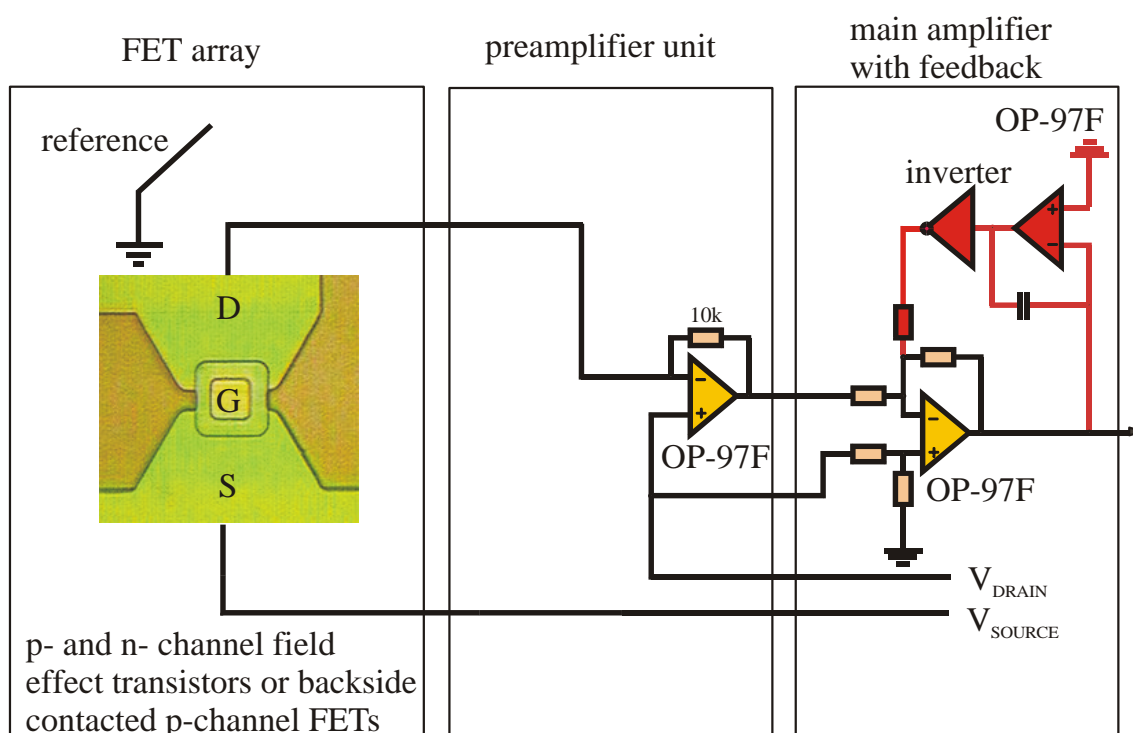


Figure 4-7 Schematic of the first and second amplification unit of the FET set-ups. The electrodes and the commercial JFETs in Figure 4-5 are replaced by our self made FET transistors.

4.2.3 Adapter for the Langmuir-Blodgett FET-chips

For the Langmuir-Blodgett FET chips introduced in chapter 3, an adapter to the standard FET preamplifiers has been developed. With the connector to the chip, the system reads out 12 channels independently (Figure 4-8). The idea behind this measurement set-up was to make use of the pH-sensitivity of the FET chips. It is possible to construct a model membrane with the Langmuir-Blodgett method on the chip with incorporated functional proteins. If the proteins act as proton pumps the H^+ concentration at the gate of the FETs increases rapidly, because the active reservoir is very small (gate area 5×5 up to $7 \times 20 \mu m^2$ and distance of the membrane $0.5-2 \text{ nm}$ (Ottenbacher et al., 1993) gives a volumina $V \approx 0.02 - 0.14 \text{ fl}$).

The principle of the signal amplification for the headstage is similar to the previously described circuitry (Figure 4-7). In this instant, the old version of the main amplifier unit (Sprössler, 1997), where the DC part of the FET signal is not compensated automatically, was used

For the pH-dependent measurements, a real time DC-procedure was used, which was implemented in the TestPoint™ language (Keithley Instruments GmbH, Germany) for the first FET main amplifier. It works together with an ADWin-4 SVIO data acquisition

card (Jäger GmbH, Lorsch) and a 48 channel digital in- and output card (PIO I/O card, Conrad Electronic GmbH, Hirschau). For this kind of measurement no post-amplification (100x) was used, because the signals are much larger than the single cell signals. The higher noise of this assembly as a result of a non-shielded FET chip and longer connections for each channel remains uncritical for such measurements.

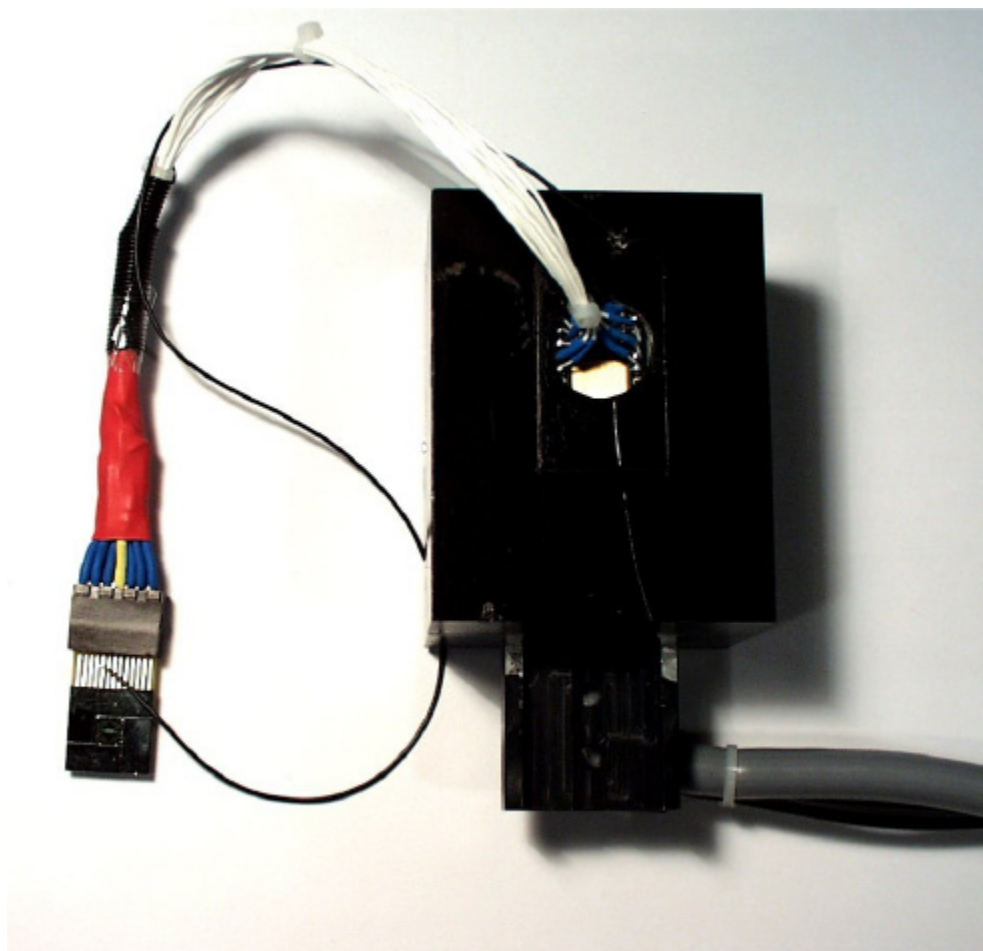


Figure 4-8 For the use of the Langmuir-Blodgett chips a simple adapter with 12 shielded cables and a wrap connector was developed. The single black cable has to be used for the grounding of the electrolyte solution.

For the use of solution during the measurements with incorporated proteins in membranes, a flow-through Teflon cell (Figure 4-9) was developed. Using a peristaltic pump, it can deliver a variety of solutions through this cell for the activation of functional proteins (Baumgart, 2001).

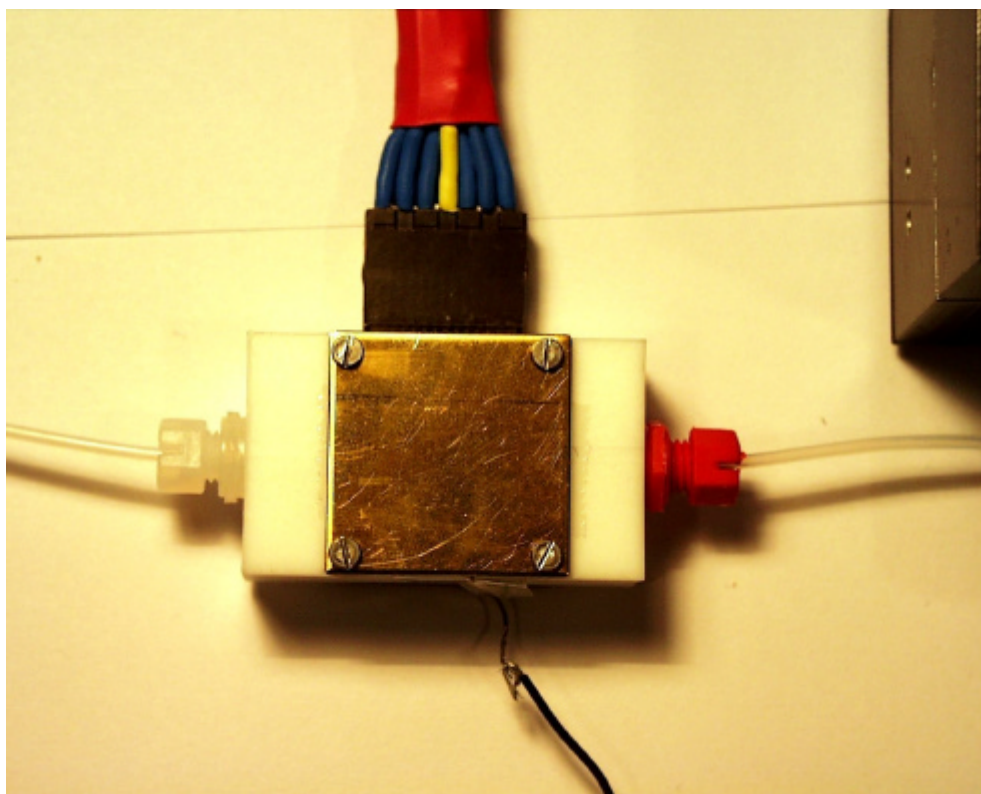


Figure 4-9 Flow-through cell for the Langmuir-Blodgett chip. On top the wrap connector for the chip is shown. On the bottom the ground contact to the electrolyte is realised with an Ag/AgCl wire.

4.2.4 16-channel Main Amplifier for the FET- and EGE-System

The new generation of the 16-channel FET- and EGE-main amplifiers use a new circuitry for the compensation of the DC-part of the recorded signal, which arises from the drain-source current of the FETs at the input. The compensation is done by a feedback loop, which subtracts the output signal to baseline. The time constant of the feedback loop is very low and the 3 dB point of the set-up lies at 1.82 Hz. Therefore, the set-up is no longer a real-time DC measurement set-up, but it leaves the shape of the slowest heart beat signals (up to 300 ms) unchanged. The advantages being that it compensates the very slow DC drifts of the FET and EGE devices caused by temperature changes and ion penetration of the gate oxide. As described in chapter 3 the new set-up uses a battery voltage supply for all electronic components. In the original FET-system, the power consumption was much higher because it used 16 bit D/A converters (DAC707JP, Burr-Brown, USA) to perform the compensation of each channel. The battery had to be mounted in a second box. In the present system, the power consumption is much smaller by using the automatic feedback loop, which has lower power consumption than the previously used DA-converters. Therefore, the

battery could be mounted inside of the FET main amplifier together with the heating plug-in unit (Figure 4-10).



Figure 4-10 16-channel FET- and EGE-main amplifier unit. On the left side the plug-in unit for the battery supply can be seen. The middle part offers the possibility to connect a BNC-cable to each channel for external observation. Here the postamplified signals as they are read with the PCI 6110 data acquisition card (plug at the backside) can be observed. On the right side the heating unit can be seen.

The system is completely controlled with a standard PC (minimum requirements: PII with 400 MHz and a fast 10 GB hard disc), a PCI 6110 data acquisition card from National Instruments, USA, and a 24-channel digital in- and output card (PIO-24 I/O card, BMC Inc., Germany).

4.2.5 64-channel Main Amplifier for the EGE-System

A new 64-channel amplifier for the EGE-system has been developed in the present study. It can be controlled by the same computer, data acquisition card and software as the 16-channel system. It works with the new EGE-headstage preamplifier described above and the second generation of the EGE-chips. The amplification unit is separated from the power and heating unit because of space limitation in the amplifier box. The frontside again provides 64 plugs for additional control of the amplified signals with an oscilloscope (Figure 4-11).



Figure 4-11. 64-channel main amplifier unit. On the frontside the 64 plugs for additional observation of the post-amplified signals can be seen.

4.3 The Patch-Clamp Amplifier

In this paragraph, a short introduction is given about the working principle of a patch-clamp amplifier. The two different operation modes of such an electrophysiological tool and the principles of compensating undesired resistance and capacitance in cell experiments are described. For the understanding of the coupling behaviour of cells attached to both an external sensor chip and the pipette of a commercially available patch-clamp amplifier, it is crucial to clarify the working principle of the patch-clamp amplifier. For modelling the external signal shape in cell-transistor coupling measurements, the capacitance transients over the cell membrane in the attached area was used. They are caused by the steep jump of the potential, when a step change of the membrane potential in *voltage-clamp mode* is selected. The external sensors described in chapter 3 monitor these capacitive transients and their amplitudes allowing an estimation of the specific conductance g_J of the cleft between cell and transistor gate.

4.3.1 Overview

A patch-clamp amplifier is mainly used as an instrument for characterising the electrophysiological properties of a cell. An EPC-9/2 double patch-clamp amplifier operated with the TIDA 4.11 software was used (both from HEKA GmbH, Germany). It contains a current-to-voltage (I-V) converter circuitry to convert the currents to an analog voltage, which is then made available at the current monitor outputs for display or recording at the same time, that pipette currents are being recorded. The potential must be specified, and the various operating modes of the patch-clamp amplifier correspond to mainly different ways of controlling that potential.

Voltage-Clamp Mode:

This is the basic patch-clamp mode, and is implemented by the circuitry shown in Figure 4-12. The pipette potential is derived from the signal applied to Stim.In with a variable offset added from the V-membrane control. The sum of these two sources is displayed and monitored as the V-mon signal. Before the voltage is being applied to the pipette a further variable offset is added from V_0 (which the user can set after entering the bath chamber with the pipette). The *voltage-clamp* method allows the internal voltage of the cell V_M to be constant over the measurement time, which leads in addition to a much easier characterisation of the cell-transistor coupling.

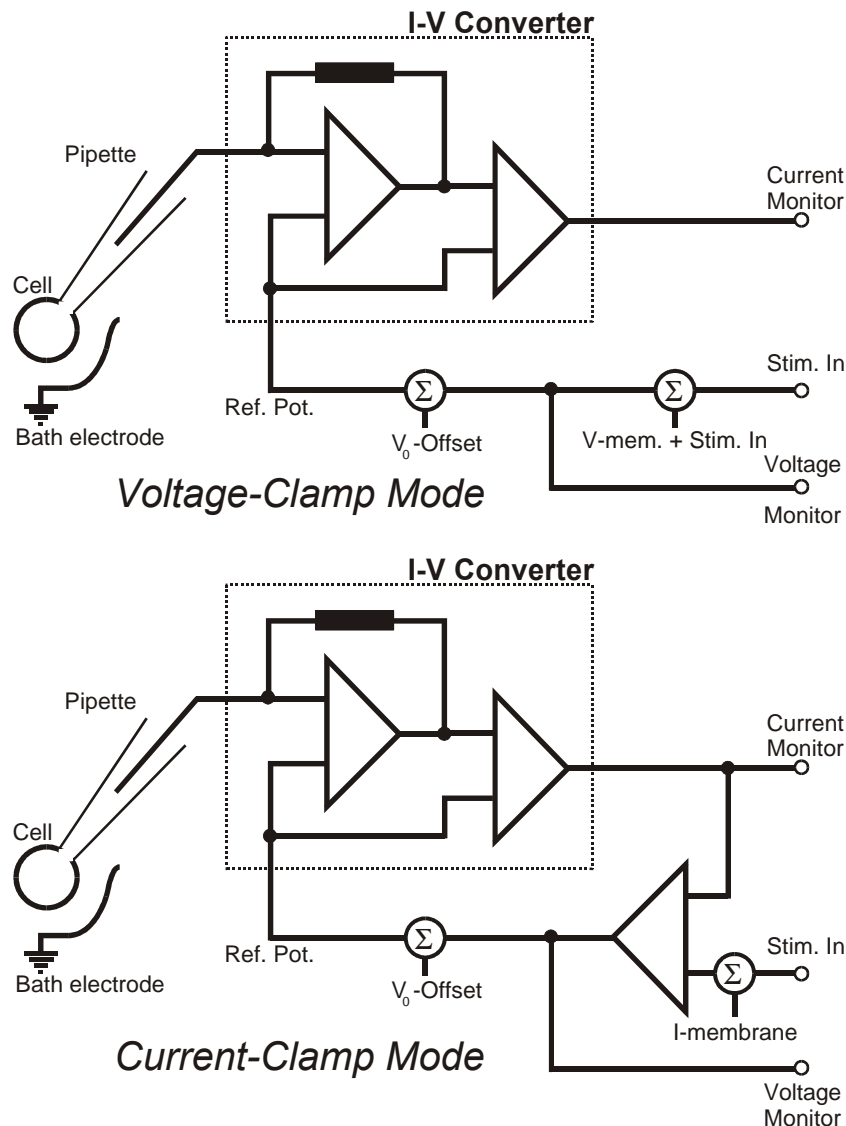


Figure 4-12 Electrical circuitry of the patch-clamp amplifier EPC-9 for the two different operation modes *voltage-clamp* (the membrane voltage V_M is kept constant) and *current-clamp* (a feedback is employed between the current monitor signal and the pipette potential, which keeps the current at zero by varying the pipette potential). The figure was adapted from the user manual of the EPC-9, from HEKA, Germany.

Current-Clamp Mode:

In the *current-clamp mode*, a feedback is employed between the current monitor signal and the pipette potential (Figure 4-12). The feedback acts rapidly (with a time constant of about $30 \mu\text{s}$) to keep the current at zero by varying the pipette potential appropriately; in this way, a high-impedance voltage follower is created, with the output voltage available at the V-mon output.

The original V-membrane viewport becomes an I-membrane display and may be used to inject a steady command current through the action of the feedback amplifier. One can use the *current-clamp mode* to measure the resting potential or spontaneous action potentials in a whole-cell recording. A commanded current can be injected while the pipette potential is measured. The commanded current is determined by the sum of voltages from the Stim.In signal and the I-membrane control. The scaling is internally fixed at 1 pA/mV, i.e., a command from the Pulse Generator or from the I-membrane control that gives rise to 1 mV in the *voltage-clamp mode* would instead give rise to 1 pA in the *current-clamp mode*. This relationship holds regardless of the Gain setting. The polarity is the usual one, in which positive stimuli result in currents flowing out of the pipette.

When switching from *voltage-clamp* to *current-clamp mode*, I-membrane will be set to whatever is appropriate in order to keep the membrane voltage at the value that was commanded in the *voltage-clamp mode* before. Likewise, upon returning to *voltage-clamp*, V-membrane will be maintained. The EPC-9 allows the functions of C-fast and R_S -comp to be active when entering *current-clamp mode*. C-fast then becomes a “negative capacitance” adjustment and R_S -comp becomes a “bridge” adjustment.

4.3.2 Compensation Procedures

Series Resistance Compensation

In whole-cell *voltage-clamp* recording, the membrane potential of the cell is controlled by the potential applied to the pipette electrode. This control of potential is not complete, but depends on the size of the access resistance between the pipette and the cell interior, and on the size of the currents that must flow through this resistance (Figure 4-13.).

The access resistance is called the series resistance (R_S) because it constitutes a resistance in series with the pipette electrode. Part of the series resistance arises from the pipette itself. However, the major part normally arises from the residual resistance of the broken patch membrane, which provides the electrical access to the cell interior. In practice, one can observe that the series resistance usually cannot be reduced below a value about two times the resistance of the pipette alone.

Series resistance has two detrimental effects in practical recording situations. First, it slows the charging of the cell membrane capacitance because it impedes the flow of the capacitive charging currents when a voltage step is applied to the pipette electrode. The time constant for the charging is given by $t_c = R_S \times C_M$, where C_M is the membrane capacitance. For typical values of $R_S = 5 \text{ M}\Omega$ and $C_M = 20 \text{ pF}$ the time constant is $100 \mu\text{s}$. This time constant is excessively long for studying rapid, voltage-activated

currents such as Na^+ currents in neurones, especially since several time constants are required for the membrane potential to settle at its new value after a step change. The second detrimental effect of series resistance is that it yields errors in membrane potential when there is a large membrane current flow. In the case of $R_S = 5 \text{ M}\Omega$, a current of 2 nA will give rise to a voltage error of 10 mV. For studying voltage-activated currents, errors need to be kept to $\sim 2 \text{ mV}$ at most. In the voltage-clamp coupling measurements (see below) we observe that the external signals capacitive transients were caused by the commanded voltage jumps in *voltage-clamp mode*. With the knowledge of the time constant t_c that slows down the membrane charging the capacitive transients can be treated as differentiated voltage steps slowed down by an exponential law (paragraph 5.1).

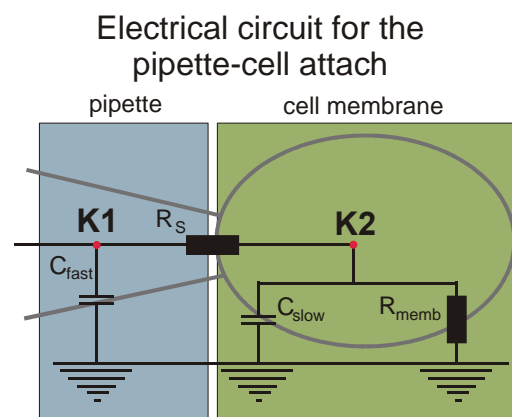


Figure 4-13. Electrical circuitry for the pipette-cell attach. Currents commanded from the patch-clamp amplifier must flow through the series resistance. Voltage steps are loading the cell membrane with the time constant $t_c = R_S \times C_M$ (C_{slow}).

Electronic compensation for series resistance in *voltage-clamp* systems has been in common use since 1952 (Hodgkin and Huxley, 1952). The principle of the compensation in the case of a patch-clamp is that a fraction of the current monitor signal is scaled and added to the command potential (correction pathway in Figure 4-14). When a large current flows in the pipette, the pipette potential is altered in a way that compensates for the potential drop in the series resistance. This arrangement constitutes positive feedback, and can become unstable when overcompensation occurs.

The EPC-9 incorporates additional circuitry to allow capacitance transient cancellation to occur while R_S -compensation is in use (Sigworth et al., 1995). This is shown as a prediction pathway in Figure 4-14, and it accelerates the charging of the membrane capacitance by imposing large transient voltages on the pipette when step changes are commanded (this is sometimes called “supercharging”).

Theoretically, it is desirable to compensate as much of the series resistance as possible. In practice, however, a degree of compensation above 90 % can involve considerable technical problems, and in some situations a value of 90 % is preferable. To illustrate one technical problem, the case, when a 100 mV potential change is commanded and 90 % compensation is in use, is considered.

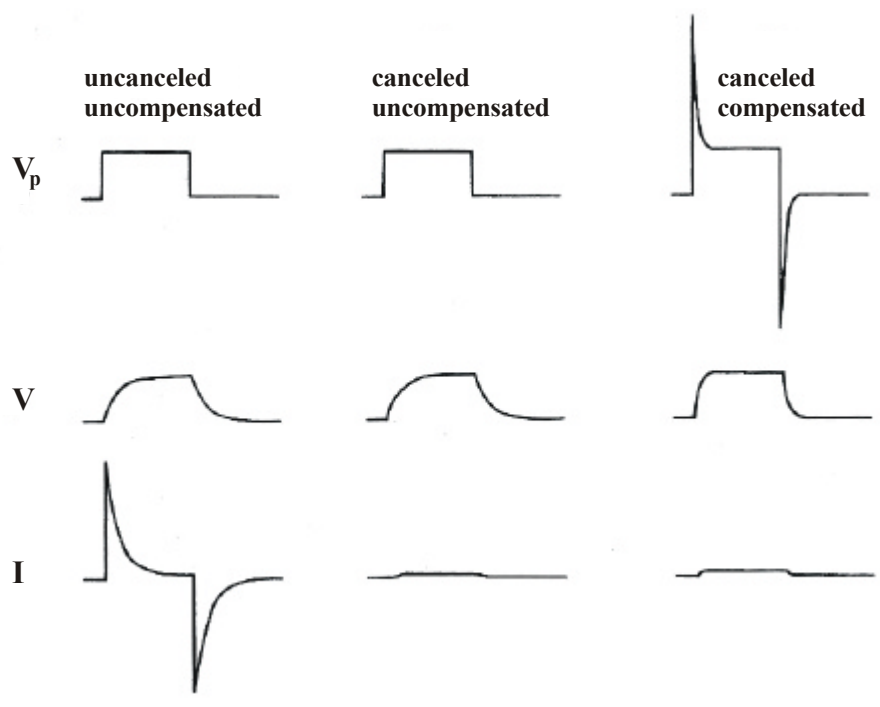


Figure 4-15. Pipette and cell potential during capacitance cancellation and series resistance compensation. In the uncanceled, uncompensated situation (left column), V_p (pipette potential) is rectangular, while V and I (membrane) are exponential functions of time with the same time constant $t = R_S \cdot C_{slow}$. Cancellation of the cell capacitive current does not change the time course of V (middle column). After series resistance compensation V reaches more quickly its state (right column). This is achieved by adding an overshooting component to V_p . The figure was adapted from Marty and Neher (1995).

This degree of compensation means that the cell membrane capacitance will be charged 10 times faster than it normal would. The rapid charging is accomplished in the compensation circuitry by forcing the pipette potential to (very transiently) reach a potential of 1 V. The resulting large current causes the membrane capacitance to charge quickly to its final value of 100 mV. In general, when a voltage step of size DV is commanded, the pipette potential actually receives an initial transient of size $DV/(1-a)$ as a result of the compensation effect. The technical problem comes from the fact that the maximum pipette potential excursion in the EPC-9 is about ± 1.2 V, implying that 90 % compensation can be used for steps only to about 120 mV in amplitude.

Capacitive Compensation

The EPC-9 provides the automatic procedures for both fast and slow capacitance subtractions. In both cases, the ongoing pulse protocols are suspended and short trains of square-wave pulses are applied. The resulting capacitive transients are averaged, leak-subtracted, and then used to calculate the required corrections to the components of the compensation network. The procedure used for the estimation of capacities was first described by Sigworth et al. (1995). The procedure for C-fast compensation, which corresponds to the pipette and stray capacitance, is concerned mainly with the very initial portion of the transient (the first 10-30 μ s). The procedure for the C-slow compensation, which is the whole-cell capacitance attached to the pipette, regards a somewhat later time window.

The relationship between the values of the compensation network (C-slow and R-series) and those of the pipette-cell assembly (C_M and R_S) is straightforward if the membrane conductance is negligible. In this case, a perfect compensation will leave no residual current and C-slow will be equal to C_M . However, if there is a finite membrane conductance, some ambiguity exists because a two-component compensation network is approximating a three-component network. The compensation procedure will then determine the residual current (some filtered version of the command waveform) and C_M is likely to be underestimated. The Auto C-slow procedure of the EPC-9 is designed to provide unbiased estimates of the actual membrane capacitance and series resistance (Sigworth et al., 1995).

Offset Compensation

In all patch-clamp configurations, a number of offsets have to be taken into account. These include amplifier offsets (± 30 mV), electrode potentials (± 200 mV, depending on Cl^- concentration of the pipette and the reference electrode), liquid junction potentials, and potentials of membrane(s) in series with the membrane under study. Some of these offsets are fixed during an experiment (like amplifier and electrode offsets) some are variable.

It is standard practice to control the fixed offsets by performing a reference measurement at the beginning of an experiment. As such, an adjustable amplifier offset is set for zero pipette current. Thereafter the command potential of the amplifier will be equal in magnitude to the membrane potential if there is no change in the offset potential. The polarity of the command potential will be that of the membrane for whole-cell and outside-out configurations but will be inverted in the cell-attached and inside-out configurations. In cell-attached configuration, an additional offset is present caused by the resting potential of the cell under study. Liquid-junction potentials may appear or disappear during the measurement when solution changes are performed or in

the case where the pipette solution is different from the bath solution (Barry and Lynch, 1991), (Neher, 1992), (Neher, 1995).

The EPC-9 software provides an Auto- V_0 button. By using this procedure V_0 is varied systematically for zero pipette current. Before doing so the user can set the L_J variable to an appropriate value to compensate the sum of all “variable offsets”.

In order for the variable L_J to actually represent the various offsets, and to correct for these, three conditions have to be met:

- The user has to calculate L_J correctly, according to the rules outlined below. This value should then be entered in the L_J control.
- An Auto- V_0 operation has to be performed at the start of an experiment. The software will then set V-membrane to $-L_J$ (for Out-Out and Whole-Cell mode) or $+L_J$ (for On Cell and In Out mode) at the start of an Auto- V_0 operation.
- During experiments, V_0 has to be changed in parallel with user-induced changes in L_J . This is done automatically by the Tida software.

An analysis of the underlying offset problem and justification for the procedures was described by Neher (1995).

<i>Solution</i>	L_J
<i>145 K-glutamate, 8 NaCl, 1 MgCl₂, 0.5 ATP, 10 NaOH-HEPES</i>	<i>10 mV</i>
<i>145 KCl, 8 NaCl, 1 MgCl₂, 0.5 ATP, 10 NaOH-HEPES</i>	<i>3 mV</i>
<i>60 Cs-citrate, 10 CsCl, 8 NaCl, 1 MgCl₂, 0.5 ATP, 20 CsOH-HEPES</i>	<i>12 mV</i>
<i>32 NaCl, 108 Tris-Cl, 2.8 KCl, 2 MgCl₂, 1 CaCl₂, 10 NaOH-HEPES</i>	<i>-3 mV</i>
<i>70 Na₂SO₄, 70 sorbitol, 2.8 KCl, 2 MgCl₂, 1 CaCl₂, 10 NaOH-HEPES</i>	<i>6 mV</i>

Table 4.2: Liquid junction offsets for different internal patch-clamp solutions compared to external solution containing 140 mM NaCl as main salt. Out of (EPC-9, 1999).

The rule for calculating the Offset Sum (L_J) is to form the sum of all changes in offset, which occur between the reference measurement and the test measurement. The polarity of a given offset voltage should be taken as viewed from the amplifier input (positive, if positive side of the voltage source is closer to the input). A sign inversion has to be applied if the offset under consideration disappears. A procedure of how to

measure liquid junction potentials is described by Neher (1992). Ion mobilities for calculation of liquid junction potentials are reported by Barry and Lynch (1991). The Table 4.2 lists the values for some typical solutions.

In each case, a liquid junction potential between the given solution and extracellular solution (main salt in the extracellular medium: 140 mM NaCl) is listed. Polarity is that of physiological saline with respect to the given solution (according to the convention of Barry & Lynch (1991)).

In our measurements we used a normal KCl-based internal solution in the pipette (see below: Solutions and pipettes for patch-clamp recording). For a whole cell measurement in this case L_J should be set to +3 mV (sol. 2 in Table 4.2). This compensates for the liquid junction potential between the KCl containing pipette and the NaCl-based bathing solution.

4.3.3 Patch-Clamp Measurements

In the following paragraph a brief description of the procedure for establishing a gigaseal and recording from a single cell in whole-cell recording with the patch-clamp technique is given.

Forming a Seal

Initial Set-up

The EPC-9 automatically applies voltage pulses to the pipette and observes the *Current Monitor* signal and calculates the pipette resistance. For optimal patch-clamp measurements, the pipette resistance should be in the range of 3 to 10 M Ω . The gradual approach to the cell and the contact to the cell membrane cause the pipette resistance to increase by reducing the current through the pipette opening. Before the pipette is inserted into the bath, the current trace should be flat, except for very small capacitive pulses caused by the stray capacitance of the pipette and holder.

Entering the bath

The surface of the bath may be contaminated with dust particles. For this reason it is important to apply a small amount of positive pressure to the pipette before the tip is moved into the bath. One should also avoid going through the air-water interface more than once before forming a seal. After entering the bath the offset potential V_0 can be cancelled by selecting the Auto- V_0 button. From the size of the current response to the test pulses (1-2 mV pulses provided by the EPC-9 in this mode) the TIDA software calculates the pipette resistance automatically (trace 'a' in Figure 4-16). No change in the current trace upon entering the bath could have following reasons:

- bubble(s) in the pipette
- faulty connection to the probe input
- bath electrode not connected

Forming a Gigaseal

When the pipette is pushed against a cell, the current pulses will become slightly smaller to reflect the increasing seal resistance. When the positive pressure is released, the resistance usually increases further. Some cells require more ‘push’ from the pipette than others, but an increase in resistance of 1.5 (i.e., a reduction of the current pulses by this factor) is typical.

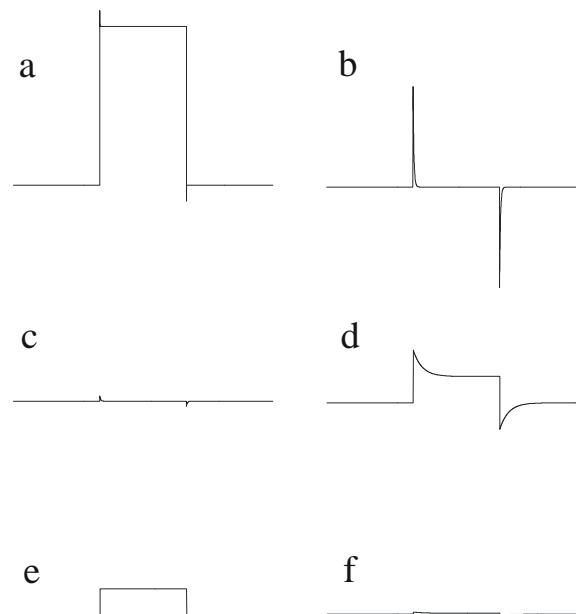


Figure 4-16. Current traces for the different steps for a whole-cell patch-clamp recording. Trace a shows the current response caused by the voltage test pulse of the EPC-9, which reflects the pipette resistance after entering the bath chamber. Trace b describes the situation, when a gigaseal is formed. The peaks are caused by the stray capacities of the pipette and can be compensated by adjusting the C_{fast} compensation circuit (trace c). Trace d reflects the membrane capacitance and the resistance caused by leakage currents over the cell membrane after breaking the patch by light suction at the pipette. The traces e and f are showing the resulting signals after subsequent compensation of C_{slow} (trace e) and leakcomp (trace f). Now a good electrical contact to the inner part of the cell is established and the patch-clamp measurement can start.

Application of gentle suction should increase the resistance further, and result (sometimes gradually, over maybe 30 s, sometimes suddenly) in the formation of a

gigaseal (trace 'b' in Figure 4-16). It is characterised by the current trace becoming essentially flat except for capacitive spikes at the start and end of the voltage test pulse, reflecting the stray resistance of the pipette. These spikes can be cancelled by adjusting the C_{fast} -cancellation circuit (trace 'c' in Figure 4-16).

Breaking the patch

After a gigaseal is formed, the patch membrane can be broken by additional suction or, in some cells, by high voltage pulses (600-800 mV for 10-500 μ s, (Marty and Neher, 1995)). Electrical access to the cell's interior is indicated by a sudden increase in the capacitive transients from the test pulse and, depending on the cell's input resistance, a shift in the current level (trace 'd' in Figure 4-16). Additional suction sometimes lowers the access resistance, causing the capacitive transients to become larger in amplitude but shorter. Low values of the access resistance R_S are desirable (<40 M Ω) and it is important that the resistance is stable while a measurement is taking place. A high level of Ca^{2+} buffering capacity in the pipette solution (e.g., with 10 mM EGTA) helps prevent spontaneous increase in the access resistance caused by partial resealing of the patch membrane.

Capacitive Transient Cancellation

If the fast capacitance cancellation was adjusted (as described above) before breaking the patch, all additional capacitive transients will be caused by the cell capacitance. Cancelling this transient using the C_{slow} and R_S controls will then give estimates of the membrane capacitance C_M of the cell and the series resistance of the patch access to the cell's interior (traces 'e' and 'f' in Figure 4-16). In the case with the EPC-9 patch-clamp amplifier, some improvements of the overall compensation may be achieved by alternating the cycles of *Auto* C_{fast} and *Auto* C_{slow} .

Series Resistance Compensation

Series resistance (R_S) compensation is important when the membrane capacitance is large or when the ionic currents are large enough to introduce voltage errors. To use the R_S -compensation circuit of the EPC-9, the transient-cancellation controls (including C_{fast} and t_{fast} if necessary) has to be adjusted to provide the best cancellation. The *%-comp* control has to be increased in order to provide the desired degree of compensation. In the cell-transistor coupling measurements the capacitive transients of the stimulation pulse were used to estimate the seal conductance g_J in the cleft between cell and sensor. Unfortunately, the EPC-9 hides the strength of the overshooting component, which is internally added to the pipette potential, inside of its circuitry. Therefore, it was decided not to use the series resistance compensation of the EPC-9 for the coupling

measurements. The capacitive transient in the external signals fully reflects the cell membrane loading slowed down by $t_c = R_S \times C_{slow}$.

4.3.4 Solutions and Pipettes for Patch-Clamp Recording

For intracellular recording, the devices were connected to a preamplifier mounted under the microscope. Following solutions and pipette properties were used:

- The culture medium was exchanged by an extracellular recording solution: (5 mM KCl, 150 mM NaCl, 1 mM MgCl₂, 10 mM HEPES, 2.5 mM CaCl₂, 10 mM Glucose, 11 mM EGTA (pH 7.38 at 24°C, adjusted with 1 N NaOH, osmolarity was at 300 mOs/kg)
- The electrodes were pulled from 1.5 mm outer diameter, 1.2 mm inner diameter capillary glass with filament (Hilgenberg, Germany) using a model P-97 Flaming/Brown micropipette puller (Sutter, USA).
- The intracellular recording solution was: (125 mM C₆H₁₁O₇K, 20 mM KCl, 0.5 mM CaCl₂, 2 mM MgCl₂, 10 mM HEPES, 5 mM HEPES (pH 7.36 at 24°C, adjusted with 1 N KOH, osmolarity was at 310 mOs/kg)
- The electrode impedances in the recording solution were between 4 and 15 MΩ.
- Tight seals of at least 1 GΩ were obtained and applying light under-pressure to the electrode tips opened the cell membranes. This led to an increased electrode series resistance and capacitance, which were further compensated. We started the recordings only if the series resistances R_S , which indicated good contacts to the intracellular part, fell under 40 MΩ.

Chapter 5

Bioelectronic Coupling

In this chapter the bioelectronic coupling model is discussed. In the first part the ‘classical’ *Point Contact Model* developed by Regehr et al. (1989) is introduced. Here, the cell transistor assembly is described by an electrical model circuitry taking all possible currents at a point inside the cleft between cell and transistor into considerations. In the second part of this chapter this electrical model is simulated using a student version of the PSPICE simulation program for electrical circuits (PSPICE ver. 9.1, OrCAD Inc., USA). In this paragraph the routines for the simulation are shown and the results discussed. The complete source-code of the simulation circuitry will be shown in the appendix. Previous works (Krause, 2000; Sprössler et al., 1999; Vassanelli and Fromherz, 1999) demonstrated that the extracellular signal shapes of the current in the cleft between cell and transistor had to be scaled by certain factors. This was justified by assuming additional effects like ‘*accumulation or depletion of ion-channels*’ (Straub et al., 2001; Vassanelli and Fromherz, 1999) or ‘*self-gating of ion-channels*’ in the cleft between cell and transistor occur (Fromherz, 1997). In the third part of this

chapter estimations for the ion concentration changes in the cleft during a cellular signal are given. This estimation suggested that ionic concentration changes at the sensor spot might have major influence in the extracellular signal shape and amplitude. Therefore, the sensitivity of our transistors to changes in salt concentration in the electrolyte was calibrated by using test solutions with different salt concentrations (KCl, NaCl, and CaCl₂). In the last part of this chapter the extended *Point Contact Model* for the cell transistor coupling, which takes the ionic changes into account, is introduced.

5.1 Point Contact Model

For the modelling of the extracellular signals in cell-transistor coupling experiments a simple equivalent circuit (*Point Contact Model*) is applied (Fromherz et al., 1991; Pancrazio, 1999; Regehr et al., 1989; Schätzthauer and Fromherz, 1998; Sprössler et al., 1999). For the description of extracellular signal shapes this very simple model turned out to be sufficient. In Figure 5-1 a schematic view of the electrical model circuitry for the cell-transistor-patch pipette assembly during a typical coupling experiment is shown.

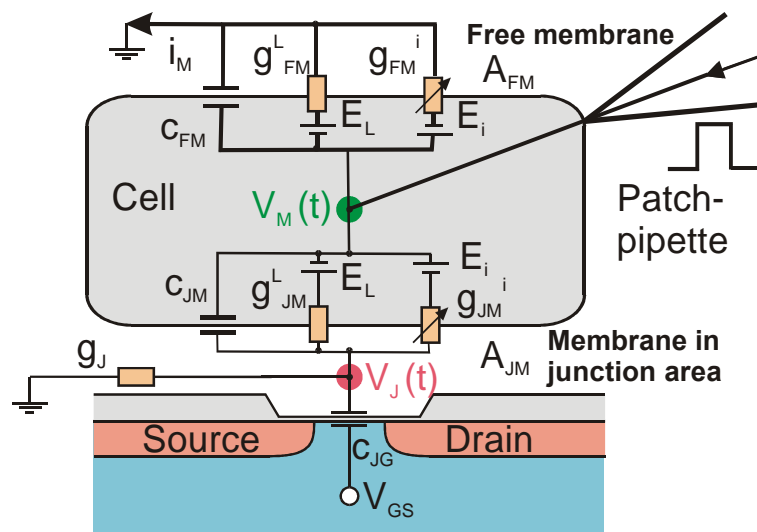


Figure 5-1 Schematic view of a typical cell-transistor coupling experiment. A patch pipette (right side) attaches the cell and after compensation of all parasitic and series resistive and capacitive components the voltage $V_M(t)$ of its inner part is controlled by the patch-clamp amplifier. If the cell is in addition attached to the gate of a FET sensor one can measure the electrical signals of the cell with both sensors simultaneously. If the seal conductance g_J , which describes the contact to the sensor, is low one could obtain the highest signals of the cell contact point $V_J(t)$. For complete description of the extracellular signal shapes the attached and the free part of the membrane have to be distinguished.

If a patch pipette attaches the cell, the voltage $V_M(t)$ of its inner part can be controlled by the patch-clamp amplifier. For having a complete control all parasitic and series resistive and capacitive components have to be compensated by using the standard routines of the patch-clamp amplifier circuitry (chapter 4). If the cell is in addition attached to the gate of a FET sensor, the electrical signals of both sensors can be measured simultaneously and the resulting signal shapes can be compared. The separation of the cell membrane and the gate results in an extended cleft of electrolyte, which can be described by a specific conductance g_J , defined as global seal conductance per junction area A_{JM} . The membrane area of the cell is divided into free part and attached part, whereas for the respective capacitances c_{JM} and c_{FM} the typical specific membrane capacitance $c_M = 1 \mu\text{F}/\text{cm}^2$ is used. The membrane contains various channels (*i*-type) with time- and voltage-dependent and independent specific ionic conductances g^i and with electrochemical driving forces E^i . In the *Point Contact Model* these Na^+ , K^+ , Ca^{2+} - and leakage-currents are modelled by Hodgkin-Huxley elements (Hodgkin and Huxley, 1952).

The ion-channels in the contact region may have different opening properties or different densities indicated by $g_{JM}^i = X^i g^i$ with X^i used as scaling factors. The specific capacitance of the gate is c_{JG} . Kirchhoff's law determines the extracellular voltage V_J with the current through the attached membrane, through the gate oxide and along the seal (Figure 5-1).

$$c_{JG} \frac{dV_J}{dt} + g_J V_J = c_M \frac{d(V_M - V_J)}{dt} + \sum_i g_{JM}^i (V_M - V_J - E_{J0}^i) \quad (5.1)$$

Three approximation are made:

- The capacitive current $c_{JG} \cdot dV_J / dt$ through the gate can be neglected.
- The voltage across the attached membrane is similar to the intracellular voltage with $V_M - V_J \gg V_M$ or $V_J \ll V_M$.
- It can be assumed that the ion concentrations in the cleft are not changing with respect to the bulk electrolyte, implying unchanged reversal voltages E_0^i .

This will result in the following equations:

$$\begin{aligned} V_J &= \frac{1}{g_J} \left(c_M \frac{dV_M}{dt} + \sum_i g_{JM}^i (V_M - E_0^i) \right) \\ &= \frac{1}{g_J} \left(c_M \frac{dV_M}{dt} + \sum_i X^i g^i (V_M - E_0^i) \right) \end{aligned} \quad (5.2)$$

Assuming proper compensation of the parasitic parameters the whole-cell current density i_M is described by:

$$i_M = \sum_i i_M^i = \sum_i g^i (V_M - E_0^i) \quad (5.3)$$

Therefore, Eq. 5.2 can be written as:

$$V_J = \frac{1}{g_J} \left(c_M \frac{dV_M}{dt} + \sum_i X^i i_M^i \right) \quad (5.4)$$

A simultaneous measurement of V_J and i_M with known specific seal conductance g_J allows the determination of differences between the conductance of the average cell membrane and the attached cell membrane.

It is possible to measure the specific seal conductance g_J by frequency-dependent impedance analysis (Fromherz et al., 1993). We have derived g_J from the capacitive responses to the voltage step pulses in voltage-clamp mode (chapter 4). The resulting capacitive transients in the extracellular signal were used to estimate g_J from:

$$g_J = \frac{1}{V_J^0} \left(c_M \frac{dV_M}{dt} \right) \quad (5.5)$$

with the tip height of the capacitive transients, V_J^0 . For the derivative of the pulse inside of the cell dV_M/dt the loading of the access resistance R_S and the compensated capacitance of the cell-pipette compound C_{Slow} have to be taken into account (Marty and Neher, 1995). The loading of this capacitance is reducing the steepness of the stimulation pulse V_M inside of the cell by an exponential law:

A: Positive pulse step

$$V_M = V_{Step} \cdot \left(1 - \exp\left(\frac{-t}{R_S \cdot C_{Slow}}\right) \right) \quad (5.6)$$

hence

$$\frac{dV_M}{dt} = V_{Step} \cdot \frac{1}{R_S \cdot C_{Slow}} \cdot \exp\left(\frac{-t}{R_S \cdot C_{Slow}}\right) \quad (5.7)$$

B: Negative pulse step

$$V_M = V_{Step} \cdot \exp\left(\frac{-t}{R_S \cdot C_{Slow}}\right) \quad (5.8)$$

hence

$$\frac{dV_M}{dt} = -V_{Step} \cdot \frac{1}{R_S \cdot C_{Slow}} \cdot \exp\left(\frac{-t}{R_S \cdot C_{Slow}}\right) \quad (5.9)$$

This predicts the resulting capacitive coupled peaks at the beginning and the end of the stimulation pulse. The first peak is in positive and the second peak in negative direction.

5.2 Cell-Transistor Coupling Measurements

In the cell-transistor coupling measurements the two different modes of a patch-clamp experiment with single cells – *voltage-clamp mode* and *current-clamp mode* – can be used. We focussed in this work mainly on the *voltage-clamp mode* for following reasons:

- During the stimulation pulses in *voltage-clamp mode* the membrane voltage V_M can be treated as constant. The formulas in the Point Contact Model are thus much easier to handle.
- The active cell currents i_M (Eq. 5.3) in *voltage-clamp mode* can be forced up to ten times higher (Figure 5-2) than they typically occur during an action potential.
- The duration of the potassium current signals from neuronal cells can be chosen about ten to twenty times longer than the duration during an action potential.

With some cells extracellular signals in *current-clamp mode* have been obtained, which will be shown in chapter 6. The difference between the two modes is shown in Figure 5-2.

In *voltage-clamp mode* it is possible to force the cell to currents, which would not flow during an action potential. In addition by varying the step height of the voltage pulses only a certain current type (Na^+ , K^+ , Ca^{2+}) can be chosen and recorded several times. This was sometimes necessary in order to overcome the weak signal-to-noise ratios in the cell-transistor coupling of single cells. A repetitive stimulation to the same step height with accompanied transistor recording was used. Afterwards it was possible to diminish the statistical transistor noise (chapter 3) by using an averaging procedure provided by the Tida 4.11 software of the patch-clamp amplifier. Here the *voltage-clamp mode* was also superior to the *current-clamp mode*, because the starting time of the cellular signal is fixed in contrast to the action potential in *current-clamp mode*. The beginning of an action potential stimulated in *current-clamp mode* is variable, because the depolarisation of the cell membrane is not directly commanded by a voltage step but caused by the loading of the membrane capacitance as reaction to a current pulse into the cell. This indirect way of depolarising a cell is not always happening with the same

time-constant (caused by slightly different C_M or slightly different R_S over the measurement time), that causes a variable starting time for the next action potential. This makes an averaging of the signals in current-clamp mode very difficult and an additional software routine would be desirable.

The strongest argument for the *voltage-clamp mode* was the capacitive transients of the voltage steps in the extracellular signal. They were used for estimating the leak conductance g_J as described above.

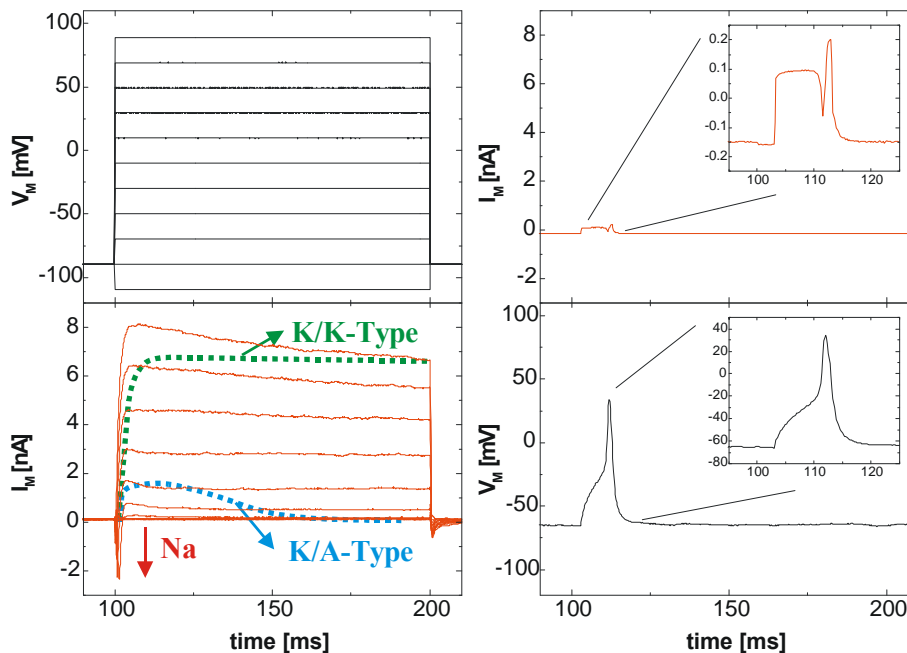


Figure 5-2 Difference between a patch-clamp experiment in *voltage-clamp mode* (left side) and in *current-clamp mode* (right side). For the two measurements the same neuronal cell out of a brainstem slice on a laminin pretreated FET surface (11 DIV) was used. The respective rectangular stimulus pulses (voltage step in *voltage-clamp mode* and current step in *current-clamp mode*) are shown in the upper traces. The resulting cellular signal is shown in the lower plots. The bars of the plots have the same scaling for comparison.

Voltage-Clamp mode (Figure 5-2 left side):

In the *voltage-clamp* experiments the cell is after successful pipette attachment and compensation of all parasitic electrical elements clamped to a holding potential V_{hold} of -90 mV. In the figure an 11-step experiment is shown. The delay between the steps is 200 ms (100 ms before and after) with a duration of 100 ms for each step. This means the total duration of each experiment is less than 4 s. The first step is in the negative direction to -110 mV (hyperpolarisation), which brings the voltage-gated ion channels in a defined closed conformation. The pulse height is then raised in the positive direction to $+20$ mV ($+10$ for a 21-step experiment) for each following step. At -30 mV

the sodium channels are opening and Na^+ -ions are flowing into the cell, which leads to a negative current signal. The sodium channels are ‘self-gating’, which means they are closing automatically after a short period (< 5 ms). By stimulation of the cell to higher potentials the potassium channels are opening and the sodium current are getting weaker. The K^+ current signal is in positive direction and ions are flowing out from the cell interior. The potassium signal is a superposition of potassium A-type and potassium K-type current (Figure 5-2 lower left plot) (Ficker and Heinemann, 1992; Klee et al., 1997).

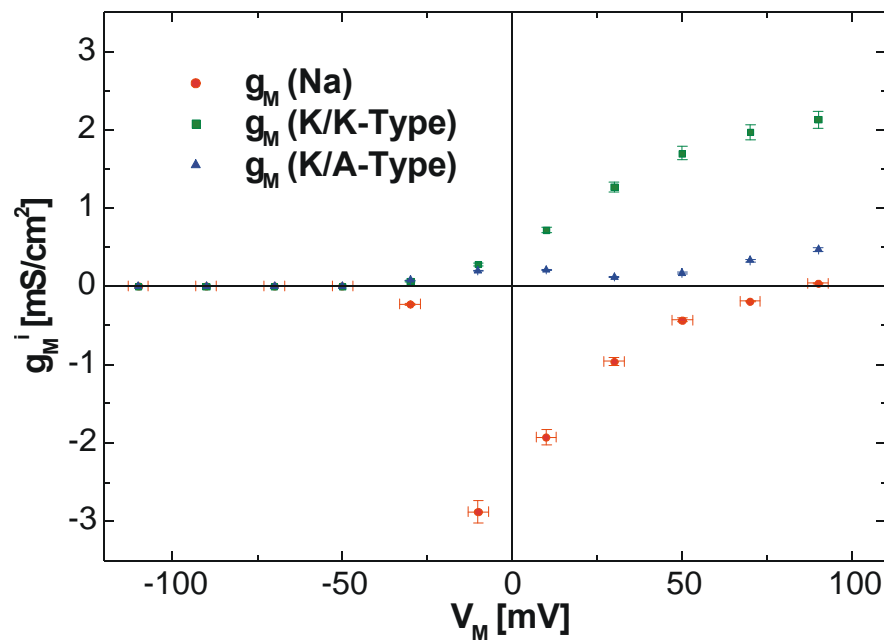


Figure 5-3 Specific ion conductances of the cell membrane out of the voltage-clamp experiment in Figure 5-2. The specific ion conductance is scaled with the membrane surface area (see below), the membrane potential V_M , and with the reversal voltages of the respective ion species using Eq. 5.3.

The A-type ion-channels are causing the initial overshoot of the signal and are also a ‘self-closing’ after a certain period (< 100 ms). The influence of this A-type current is very pronounced in the hippocampal neurons and can be switched off by special voltage-clamp protocols (see below). The potassium K-type channel remains in an open conformation until the stimulation pulse is finished and the holding potential is reached again. The data received out of a voltage-clamp experiment can be plotted as membrane conductance of a certain ion species g_M^i against the membrane potential V_M (Figure 5-3).

Current-Clamp mode (Figure 5-2 right side):

In this mode the patch-clamp amplifier is feeding a constant holding current (here $I_{hold} = 160$ pA) into the cell to hold the membrane potential at the chosen value resting potential of -70 mV. A positive current pulse of 0.25 nA is loading the cell membrane and the membrane potential rises. If the membrane voltage reached -30 mV the sodium channels are opening (see *voltage-clamp mode*) and positive Na^+ -ions are flowing into the cell. The cell elicits an action potential (chapter 3), where the counteracting potassium effluxes get the cell to the holding potential again (repolarisation).

The *current-clamp mode* reflects the ‘natural’ cellular signal and it would be favourable to couple these action potentials into the sensor. Action potentials will also occur in cellular networks, when neuronal cells communicate among each other. During an action potential the active membrane current is much lower as it can be stimulated in the *voltage-clamp mode*. In Figure 5-2 (upper inset) the rectangular current pulse commanded by the patch-clamp amplifier is distorted. In this case, the amplifier circuitry is trying to compensate the active cell current and to keep the commanded step height.

The rapid change of the membrane potential during an action potential (Figure 5-2 lower inset) also cause capacitive transients over the cell membrane into the contact region (Fromherz, 1999). But here the steepness of the rise and fall is also not as high as it can be forced in *voltage-clamp mode*.

5.3 Modelling the Cell-Sensor Coupling using PSPICE

The electrical coupling of single cells can be modelled by the PSPICE simulation program for electrical circuits (student version of PSPICE ver. 9.1 from OrCAD Inc., USA). The complete source-code of the program will be shown in the appendix.

Simulation circuit for the patch-clamp coupling

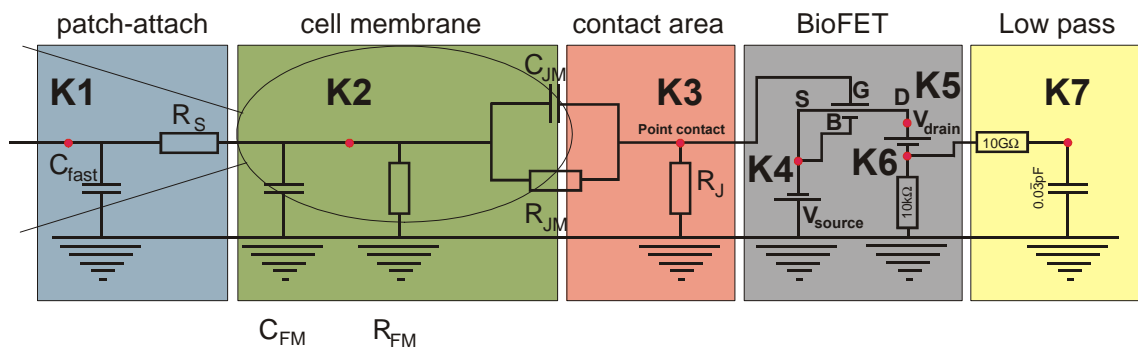


Figure 5-4 Simulation model for PSPICE. The values for the first two passive elements (C_{fast} , R_s) are provided by the patch-clamp amplifier. The values for capacitance and resistance of the attached and the free membrane can be calculated from C_{slow} and R_M . The fitting results are independent to the amount of attached membrane area. The stimulation pulse of the voltage-clamp measurement was provided as voltage source at node 1. The active cell current was provided at node 2 to node 3 into the contact area. The resulting voltage at node 3 is monitored with the simulated BioFET (Figure 5-6). The signal of the BioFET had to be low pass filtered @3kHz according to our amplifier electronics. The voltage at node 7 was the resulting simulation of the cell transistor contact.

As input the data from the patch-clamp coupling measurements were used (stimulation pulse from the voltage-clamp experiment V_{step} and the measured current over the membrane i_M). In Figure 5-4 a sketch of the simulation circuit is shown.

Simulation procedure:

Values resulting from the patch-clamp measurement

The patch-clamp amplifier provides all values for the cell-pipette assembly like:

R_M : Resistance of the cell membrane

i_M^L : Leak-current of the cell at the holding potential of -90 mV

C_{fast} : Compensated value for the stray capacitance cancellation of the patch-pipette

G_L : Leakage conductance of the cell plus the pipette-cell contact

R_S : Series resistance of the cell-pipette contact

C_{slow} : Capacitance of the cell membrane, if the cell-pipette contact is good.

The C_{fast} and the R_S values are directly fed into the PSPICE simulation circuit. For the used pipettes a value of $6 \text{ pF} < C_{fast} < 8 \text{ pF}$ was typical. A good electrical contact to the cell interior is indicated with R_S values lower than $80 \text{ M}\Omega$. The radius of the cell membrane can be derived using the C_{slow} value with:

$$r_{cell} = \sqrt{\frac{C_{slow}}{4\mathbf{p} \cdot c_M}} \quad (5.10)$$

A typical capacitance value for a neuronal cell in a voltage-clamp experiment was $C_{slow} = 6 \text{ pF}$, hence with the specific membrane capacitance $c_M = 1 \text{ }\mu\text{F}/\text{cm}^2$ the radius of the cell would be about $6.9 \text{ }\mu\text{m}$, which can be observed by microscopic analysis (Figure 5-5). Out of this value assuming a bowl surface derived the total membrane surface:

$$A_M = 4\mathbf{p}r_{cell}^2 \quad (5.11)$$

For the respective membrane capacitance and resistance of the attached and free membrane parts (R_{JM} , C_{JM} , R_{FM} , C_{FM}) a certain percentage of attached membrane had to be assumed. Then the values can be derived with (parallel circuit):

$$\begin{aligned} C_{slow} &= C_{FM} + C_{JM} \\ \frac{1}{R_M} &= \frac{1}{R_{FM}} + \frac{1}{R_{JM}} \end{aligned} \quad (5.12)$$

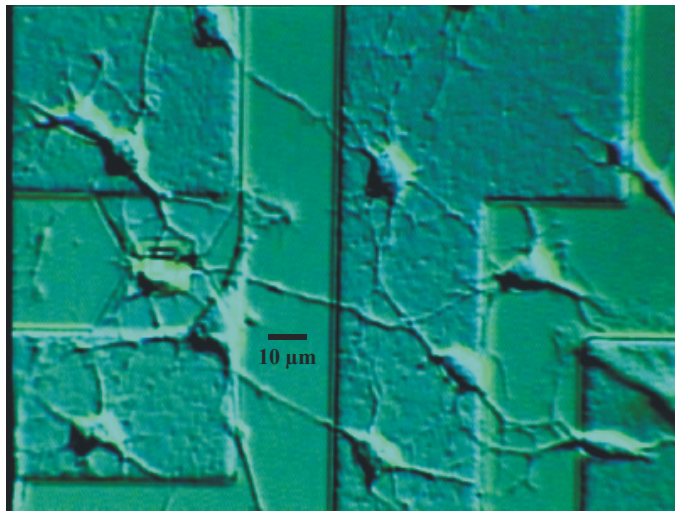


Figure 5-5 Neurons out of a brainstem culture (5 DIV) cultured on a field-effect transistor surface. On the left side a neuron is covering a gate structure. The scale bar indicates the size of the cells.

Low Pass filter:

The amplification unit for the extracellular recording is limited in its frequency range. The low frequency limit is 0.1 Hz for the self-compensating systems and ‘DC’ for the pH-measurement set-up, which can be used for cell measurements as well. The upper frequency is limited by the amplification stages of the amplifier cascade. It has a 3 dB point at the frequency of 3 kHz. This filter cuts off the peaks of the capacitive responses. It is modelled in the PSPICE circuitry with a 10 G Ω resistor and a 0.03 pF capacitor.

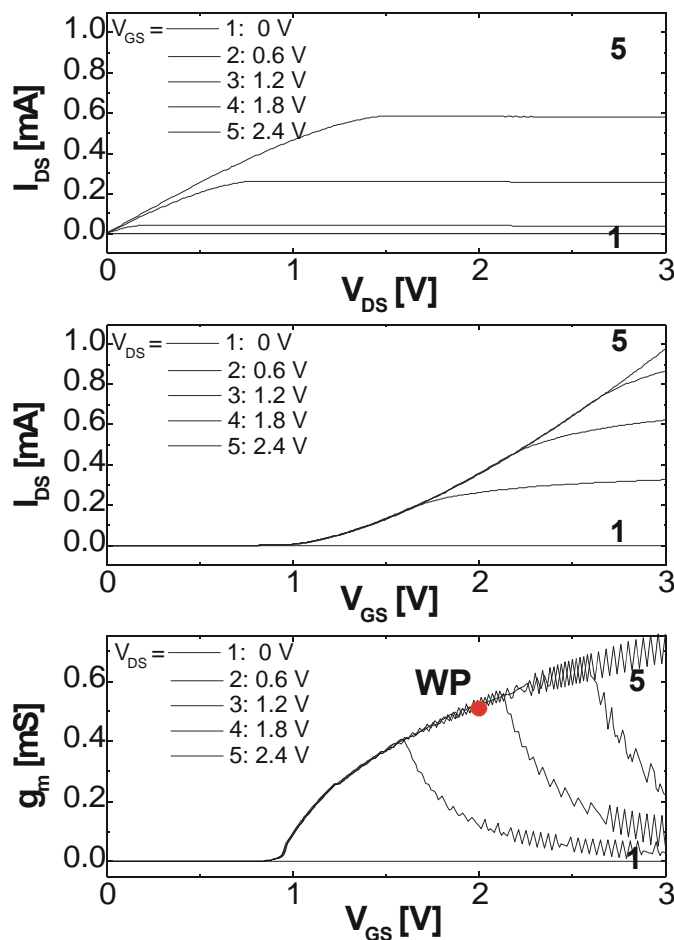


Figure 5-6 Characteristics of the BioFET device, which was simulated according to the dimensions, process parameters, and measured characteristics of our FET devices. The BioFET was simulated according to the characteristics of the real n-channel device shown in paragraph 3.2.5.

The BioFET

The BioFET was adapted to the circuit to make sure that the capacitance of the gateoxide does not change the simulated signal shape. PSPICE provides standard

routines for the modelling of semiconductor devices (Antognetti et al., 1987). The characteristics of the simulated n-channel BioFET are shown in Figure 5-6.

The n-channel BioFET was driven at $V_{DS} = 2.4$ V and $V_{GS} = 2$ V. At this working point it had a transconductance of $g_m = 0.518$ mS, which was a typical value for our transistors. The characteristics of the standard BioFET were simulated according to the dimensions, process parameters, and measured characteristics of our FET devices (Figure 5-6).

The source voltage for the simulated FET is provided at node 4. The bulk contact of the device is connected to source. The drain voltage is provided at node 5. The drain source current I_{DS} is flowing over a 10 k Ω resistor to ground. The voltage drop at this resistor is monitored at node 6 with the low pass. The simulated signal for the cell transistor contact corresponds to the voltage at node 7. For the final scaling of the resulting signal another calibration measurement with defined testpulses was done. This procedure was also done in the 'real' cell-transistor measurements with the respective devices.

Voltage input

The stimulation pulse of the voltage-clamp measurement was provided as voltage source at node 1. PSPICE offers the possibility of creating an input current or voltage source with a list of raw data. For the stimulation pulse the patch-clamp data of the respective stimulation step was fed as voltage source at node 1 into the circuit. The steepness of this pulse is weakened as a result of the loading of the membrane capacitance (Eq. 5.12) by an exponential law (Eqs. 5.6, 5.8). The derivative of this pulse into the contact area (Eqs. 5.7, 5.9) is simulated by the PSPICE circuitry.

Current input

The active cellular current i_{JM} , which is caused by the cell into the contact area, is fed from node 2 to node 3 into the circuitry. This current resulting from the patch-clamp experiment has to be scaled by the standard scaling factor (see below). The leakage current contribution, which is normally compensated by the Tida 4.11 software of the amplifier, has to be taken into account:

Leak current over the attached membrane:

Another important value, the patch-clamp software provides, is the leak current i_M^L for the whole cell flowing over the membrane at the holding potential V_{hold} . The output current of the patch-clamp amplifier is corrected by this value. The leak current is dependent on the value of the holding potential. At the rectangular voltage step the direction of the leak current may change. The correction of this leak contribution is given in Eq. 5.13:

$$i_M = i_M^{corr} - \frac{V_M}{V_{hold}} \cdot i_M^L \quad (5.13)$$

In this equation i_M^{corr} is corrected output current of the patch-clamp amplifier and i_M^L is the leak current at the initial holding potential.

This leakage current reflects the current caused by the rectangular voltage step. The patch-clamp amplifier is automatically compensating this effect by subtracting the leakage current from the output current signal. This results in a current output, which reflects the pure active cell current (for details see Chapter 4). Therefore the current output of the patch-clamp amplifier is not reflecting the ‘real’ situation happening at the cell contact.

Junction resistance R_J :

This value is the main value, which has to be scaled for the resulting amplitude of the extracellular signal. It is calculated using the total junction conductance with $R_J = 1/G_J$.

Total junction conductance G_J :

First the specific conductance of the cell-transistor contact is derived with the following procedure: The specific seal conductance is defined with Eq. 5.5 and with the total conductance $G_J = g_J A_{JM}$ it is:

$$G_J = \frac{1}{V_J^0} \cdot \left(\frac{dV_M}{dt} \right) \cdot c_M A_{JM} \quad (5.14)$$

In this equation V_J^0 is the extracellular tip height of the capacitive response to the stimulation pulse. This leads with $dV_M/dt = V_{step}/(R_S \cdot C_{slow})$ for $t=0$ (Eq. 5.7) to the junction resistance derived with:

$$R_J = V_J^0 \frac{V_{step}}{R_S \cdot C_{slow}} \cdot \frac{1}{c_M A_{JM}} \quad (5.15)$$

For the simulation with PSPICE the value V_J^0 is adjusted such, that the amplitude of the capacitive responses of the simulated and the recorded data are matching in the initial voltage step at 100 ms.

Scaling of the cell-transistor contact:

Out of the above discussion it is apparent that the respective circuit values for the simulation are strongly dependent on the amount of attached membrane. By assuming an attached membrane area of 10 % (Vassanelli and Fromherz, 1999) the input data are scaling with:

Resistance of the free cell membrane: $1/R_{FM} = 1/(0.9 \cdot R_M)$

Resistance of the attached cell membrane: $1/R_{JM} = 1/(0.1 \cdot R_M)$

Capacitance of the free cell membrane: $C_{FM} = 0.9 \cdot C_{slow}$

Capacitance of the attached cell membrane: $C_{JM} = 0.1 \cdot C_{slow}$

The value for the junction resistance is also scaling with (Eq. 5.15):

$$R_J = V_J^0 \frac{V_{step}}{R_S \cdot C_{slow}} \cdot \frac{1}{c_M A_M \cdot 0.1} \quad (5.16)$$

The leak-corrected active cell current, which is fed from node 2 to node 3, is also scaling with:

$$i_{JM} = (i_M + i_M^L) \cdot 0.1 \quad (5.17)$$

During the simulations it was apparent that the simulated signal is independent on the amount of attached membrane area. The different scaling of the input data were compensating each other and the resulting simulated signal response at node 7 is equal (see below). The 10 % value was then chosen for all simulations of the extracellular response.

For the first simulations in this chapter extracellular signals that didn't required to be averaged were mainly used. The cell-transistor contact was very strong and such high cellular currents effectively overcame the weak signal-to-noise ratios.

Examples for the signal modelling using PSPICE:

A: Sodium current of a single cardiac myocyte coupled to a p-channel FET

In the first example a strong sodium current of a single cardiac myocyte was modelled using PSPICE. The transistor surface was pre-treated with fibronectin and the single cell covered the transistor gate (Figure 5-7). In Figure 5-8 the voltage-clamp coupling measurement is shown. Two coupling measurements with this single cardiac myocyte cell (1 DIV) were performed. Trace A shows the two stimulation pulses from the holding potential of -90 mV to -30 mV and 0 mV.

This procedure releases sodium currents of different heights. In Figure 5-8 (trace B) the membrane currents caused by the strong sodium influxes into the cell are shown. The coupled extracellular signal of the FET is an overlaid signal of the capacitive coupled current as a result of the stimulation pulse and the coupled sodium current of the cell into the transistor. For obtaining a better signal-to-noise ratio the signals were averaged 135 times. The dotted traces in C were simulated results using the *Point Contact Model*. The fitting parameters were fixed to the response with higher

stimulation pulse but lower sodium current. The corresponding values used for these fitting procedures are given in Table 5.1.

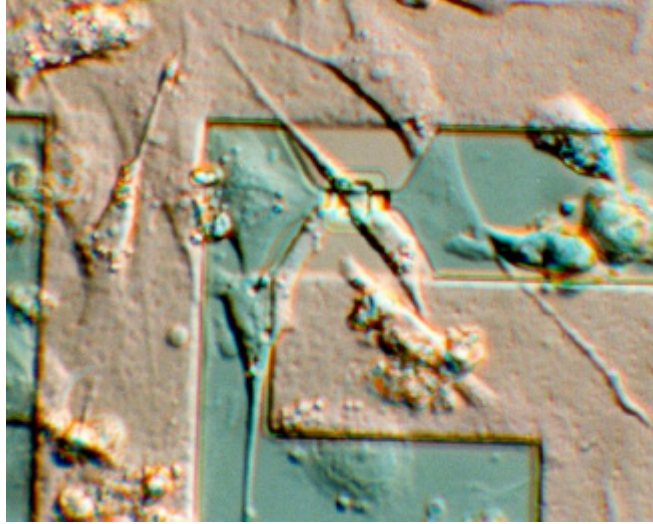


Figure 5-7 Single cardiac myocyte cell covering the gate structure of the p-channel FET 584232 (gate area $3 \times 8 \mu\text{m}^2$, $g_m = 0.33 \text{ mS}$). The following coupling measurements were performed with this cell.

<i>Voltage-clamp coupling</i>	Patch-Clamp input	Step 1	Step 2
Chip: p-channel 584232 ($V_{DS} = -3\text{V}$, $V_{GS} = -1.8\text{V}$) $g_m = 0.33 \text{ mS}$; Gatesize: $3 \times 8 \mu\text{m}^2$ Fibronectin coated	$V_{rest} = -36 \text{ mV}$ $G_L = 2.48 \text{ nS}$ $C_{slow} = 9.02 \text{ pF}$	$V_{step} = 60 \text{ mV}$ $R_M = 1.36 \text{ G}\Omega$ $i_M^L = 140.6 \text{ pA}$	$V_{step} = 90 \text{ mV}$ $R_M = 1.62 \text{ G}\Omega$ $i_M^L = 138.2 \text{ pA}$
Date: 06.01.00 Files: Si000601.003 – 005 (averaged 135x)	$R_S = 19.1 \text{ M}\Omega$; $C_{fast} = 7.14 \text{ pF}$	$R_J = 1103555.6 \Omega$	$R_J = 1103555.6 \Omega$
10 % of membrane attached Cell: Cardiac Myocyte (1 DIV)	$A_M = 9.1 \cdot 10^{-10} \text{ m}^2$ $r_{cell} = 8.5 \mu\text{m}$	$g_J = 0.998 \text{ S/cm}^2$	$g_J = 0.998 \text{ S/cm}^2$

Table 5.1: Values for the simulation the voltage-clamp coupling experiment using a single cardiac myocyte (1 DIV).

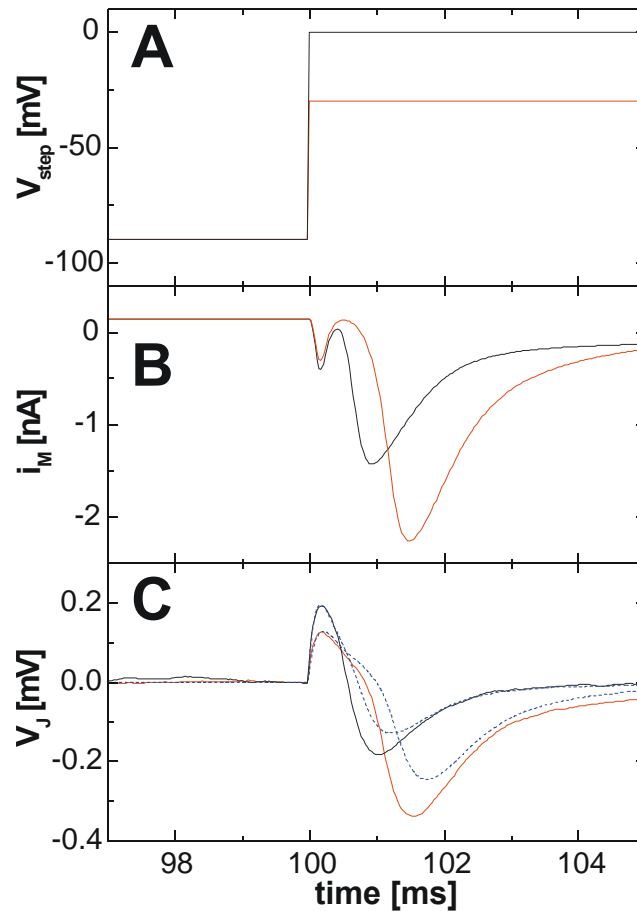


Figure 5-8 Two voltage-clamp coupling measurements of a single cardiac myocyte (1 DIV). The transistor (p-channel array FET 584232; gate area $3 \times 8 \mu\text{m}^2$, $g_m = 0.33 \text{ mS}$) surface was pretreated with fibronectin. Trace A shows the two stimulation pulses. Trace B shows the membrane current caused by a strong sodium influx into the cell. Trace C shows the coupled extracellular signal of the FET, which is an overlaid signal of the capacitive coupled current as a result of the stimulation pulse and the coupled sodium current of the cell monitored by the transistor (averaged 135 times). The simulations obtained with the *Point Contact Model* using PSPICE are overlaid to the extracellular responses (dotted lines).

As described above the fitted extracellular responses are independent on the scaling factor of the cell-transistor contact. In Figure 5-9, two simulations to the second step of the previous experiment are shown. Both simulated traces are matching perfectly.

The simulation is only dependent on the value of the extracellular monitored tip height V_j^0 of the capacitive transient. The strong influence can be seen in the next plot (Figure 5-10).

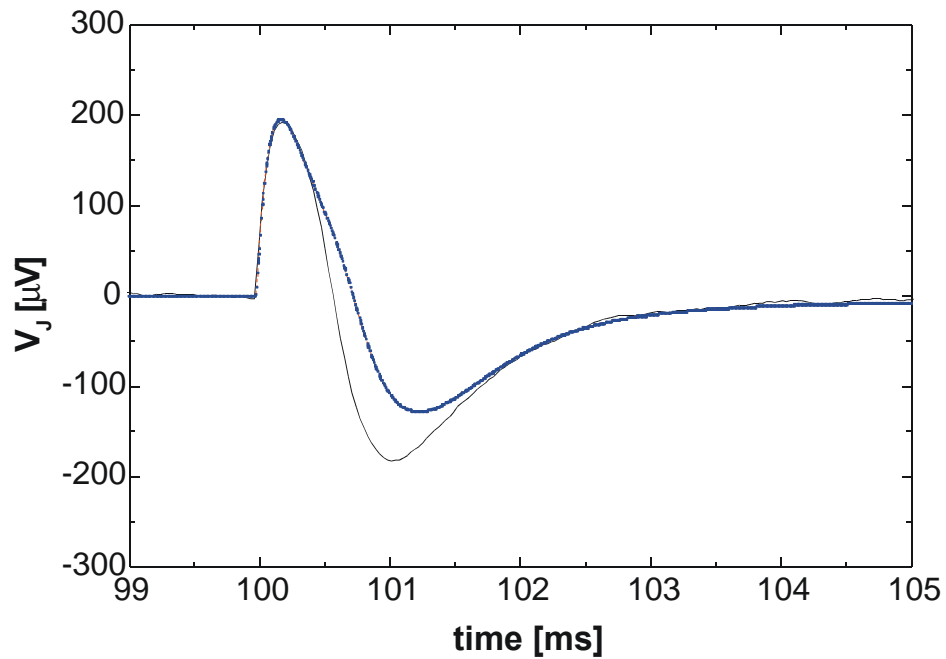


Figure 5-9 Simulated traces to the second response of the previous experiment. Both simulated traces (dotted) are lying above each other. For the first simulation 10 % and for the second simulation 20 % attached membrane area was used.

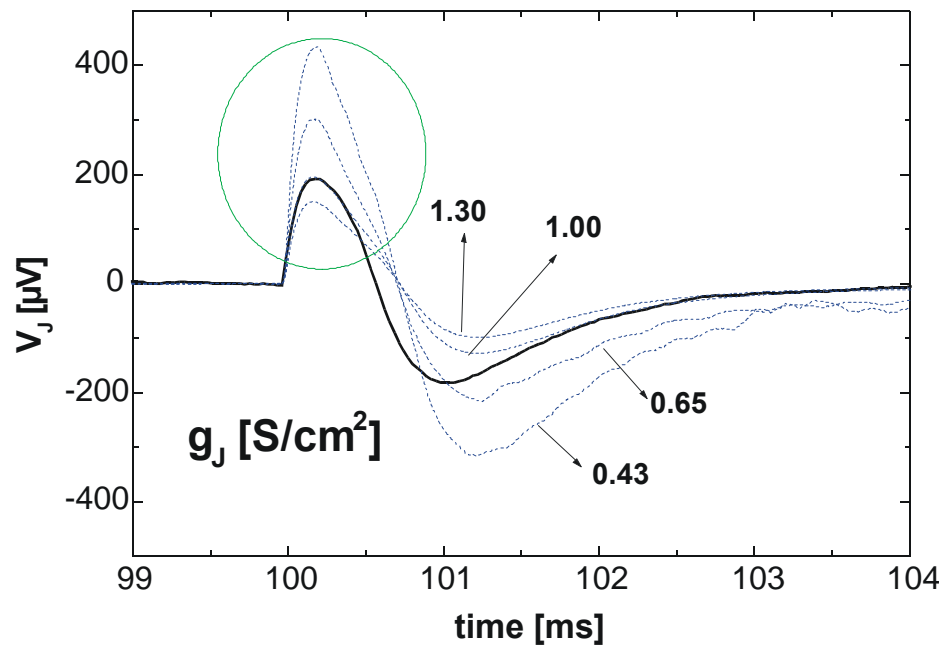


Figure 5-10 Procedure for finding the right scaling value for the sealing conductance g_J in the cleft between cell and transistor. The traces simulated with PSPICE are dotted and the respective sealing conductance for each simulation is given in the figure. The simulated responses are strongly dependent on the g_J values.

From the fitting procedure in Figure 5-10 a sealing conductance of $g_J = 0.998 \text{ S/cm}^2$ was used for modelling the second response of the second voltage-clamp experiment. It suggested that the sodium current was underestimated. In order to obtain the right amount of extracellular recorded sodium current the current source provided into the attached area would have to be scaled by a factor of $X^i = 1.40 \pm 0.05$. To estimate the error introduced by the averaging procedures the single responses were also simulated.

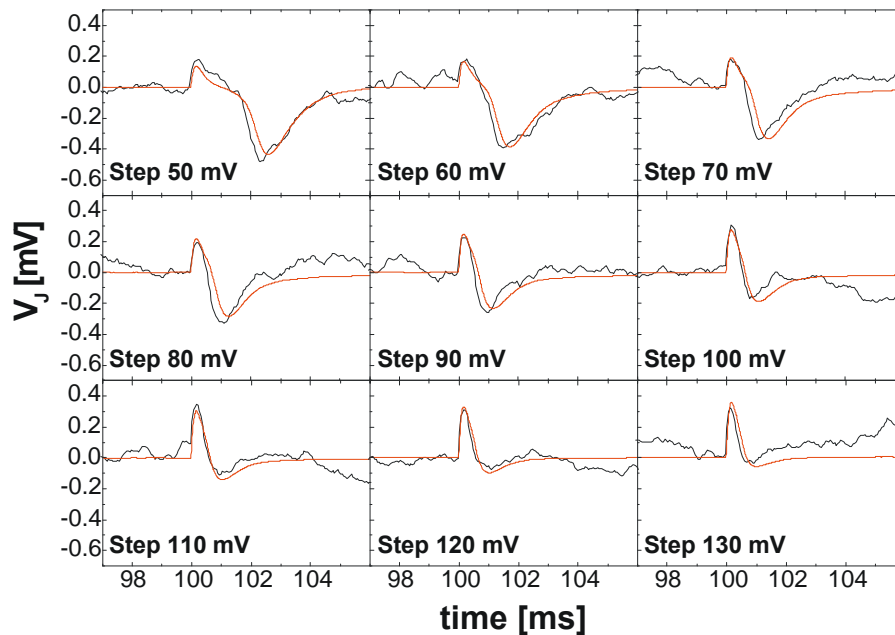


Figure 5-11 Single traces of the coupled sodium signal (signal down) and the coupled capacitive response (signal up) of the cardiac myocyte (un-averaged). The data traces were simulated using PSPICE and the respective fit data can be seen in Table 5.2. The rms-noise level of the single responses was high with about $200 \mu\text{V}$.

<i>Voltage-clamp coupling</i>	Patch-Clamp input	All Steps
Chip: p-channel 584232 ($V_{DS} = -3\text{V}$, $V_{GS} = -1.8\text{V}$) $g_m = 0.33 \text{ mS}$; Gatesize: $3 \times 8 \mu\text{m}^2$ Fibronectin coated	$V_{rest} = -36 \text{ mV}$ $G_L = 2.48 \text{ nS}$ $C_{slow} = 9.02 \text{ pF}$	$V_{step} = 50 - 130 \text{ mV}$ $R_M = 2 \text{ G}\Omega$ $i_M^L = 148.1 \text{ pA}$
Date: 06.01.00 files: Si000601.003 - 005 (averaged 135x)	$R_S = 19.1 \text{ M}\Omega$; $C_{fast} = 7.14 \text{ pF}$	$R_J = 1451600.0 \Omega$
10 % of membrane attached Cell: Cardiac Myocyte (1 DIV)	$A_M = 9.1 \cdot 10^{-10} \text{ m}^2$ $r_{cell} = 8.5 \mu\text{m}$	$g_J = 0.759 \text{ S/cm}^2$

Table 5.2: Values for the simulation of the single responses the voltage-clamp coupling experiment using a cardiac myocyte (1 DIV).

The response reveals a very high noise level, but can also be modelled by the *Point Contact Model*. In Figure 5-11 the fits to the single responses are shown.

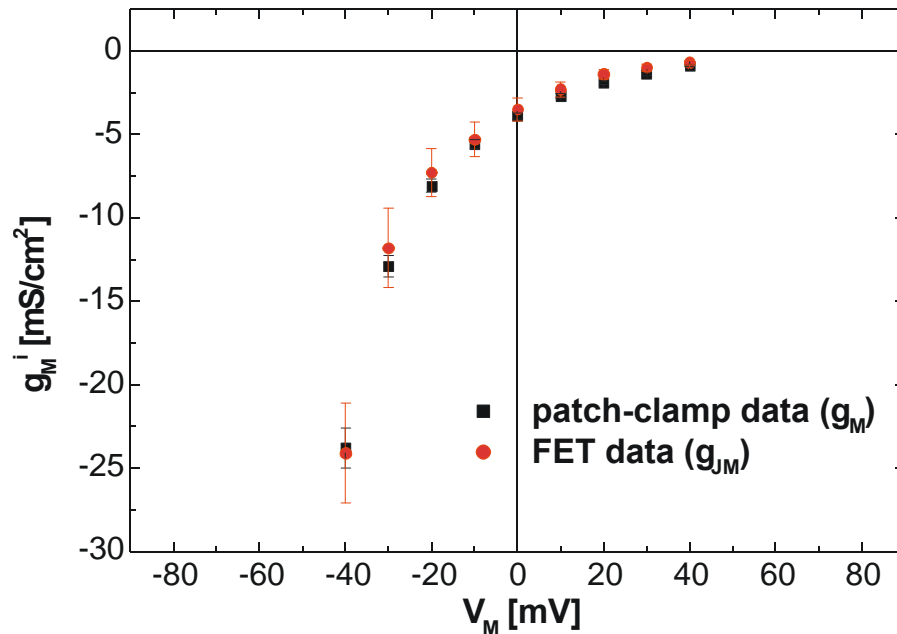


Figure 5-12 Specific ion conductances for sodium ions at the different membrane voltages V_M from the measurement in Figure 5-11. The conductances are calculated using the respective membrane area (junction membrane or whole-cell membrane).

In this measurement it can be seen that the extracellular responses are in good agreement with the simulated traces. The calculated membrane conductances for sodium ions scaled by the respective membrane areas (junction membrane or whole-cell membrane) g_M^i (mS/cm²) are plotted in Figure 5-12. The plot reflects the observation made in the previous simulations. The measured conductances from the patch-clamp data showed good correlation to the FET data. This means that no additional scaling for the current inside of the attached area has to be made. Therefore it was concluded that the simulation for the averaged response (Figure 5-9) was underestimating the seal conductance g_J . This could be caused by the averaging procedure, which may cut off the capacitive coupled part of the signal. By using the un-averaged signal no additional scaling of the cell current in the attached membrane part has to be made for modelling the fast sodium response.

B: Potassium current of a single brainstem neuron coupled to a p-channel FET

In the second signal simulation a very strong potassium current of a single brainstem neuron was used. The transistor surface was pre-treated with laminin and the cell covered the transistor gate completely. In Figure 5-13 the voltage-clamp coupling

experiment (7-step protocol) using a brainstem neuron (11 DIV) on a p-channel FET is shown.

In this experiment the sealing conductance was extremely low $g_J = 0.256 \text{ S/cm}^2$ and the cell showed very high potassium currents of up to 8 nA. Therefore, the FET responses did not require averaging. The responses were simulated using PSPICE. The slow decay of the signal (Trace C: 200-250 ms) could not be explained by the *Point Contact Model*.

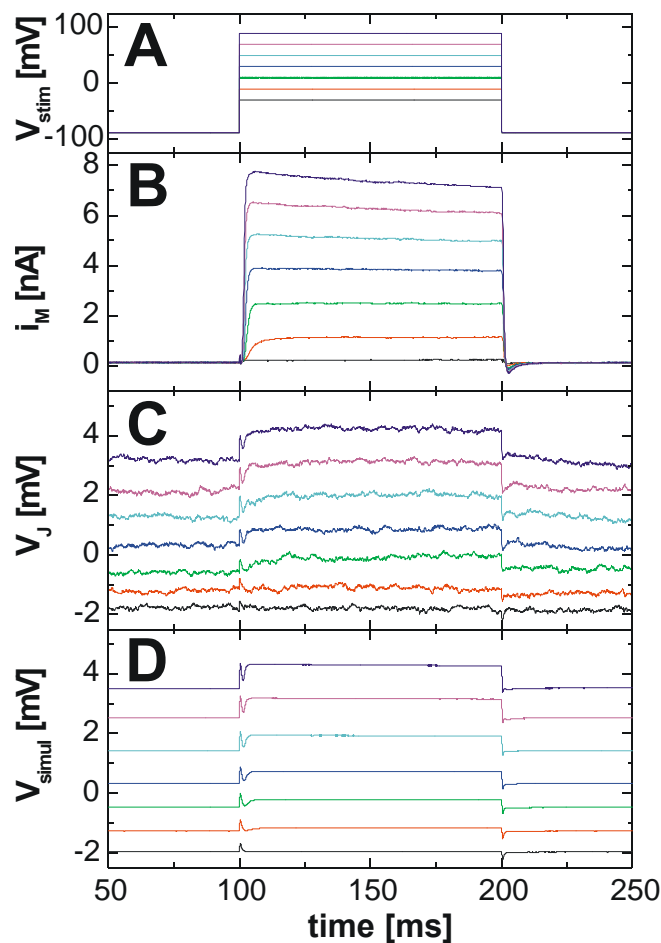


Figure 5-13 Voltage-clamp coupling experiment (7-step protocol) using a brainstem neuron (11 DIV). The sealing conductance was very low and the cell had a very high potassium current up to 8 nA. The slow decay of the higher signals (Trace C: 200-250 ms) could not be explained by the *Point Contact Model*.

For the simulation of the step-to-step measurements the same sealing conductance was used assuming unchanged condition during the measurement. This seemed to be sufficient because the whole step protocol needed less than 3 s measurement time.

A closer view of the fitted data in Figure 5-14 indicates, that the extracellular responses are more and more underestimated with higher stimulation pulses (step 1: -90 mV to -30 mV; step 7: -90 mV to $+90$ mV). For compensating the value of the underestimation the simulated response to the potassium current would have to be scaled by an average factor of $X^i = 1.46 \pm 0.23$.

<i>Voltage-clamp coupling</i>	Patch-Clamp input	All Steps
Chip: p-channel ($V_{DS} = -3V$, $V_{GS} = -2V$) $g_m = 0.35$ mS; Gatesize: $2 \times 8 \mu\text{m}^2$ Laminin coated	$V_{rest} = -50$ mV $G_L = 3.3$ nS $C_{slow} = 39.49$ pF	$V_{step} = 60 - 180$ mV $R_M = 0.856$ G Ω $i_M^L = 135.9$ pA
Date: 07.08.00 File: Si000807.002 (un-averaged)	$R_S = 12.2$ M Ω ; $C_{fast} = 7.05$ pF	$R_J = 1016666.6$ Ω
10 % of membrane attached Cell: Brainstem Neuron (11 DIV)	$A_M = 3.85 \cdot 10^{-9}$ m 2 $r_{cell} = 17.5$ μm	$g_J = 0.256$ S/cm 2

Table 5.3: Values for the simulation of the voltage-clamp coupling experiment (7-step protocol) using a brainstem neuron (11 DIV) (Figure 5-13). The cell had a very high capacitance, which was typical for brainstem neurons.

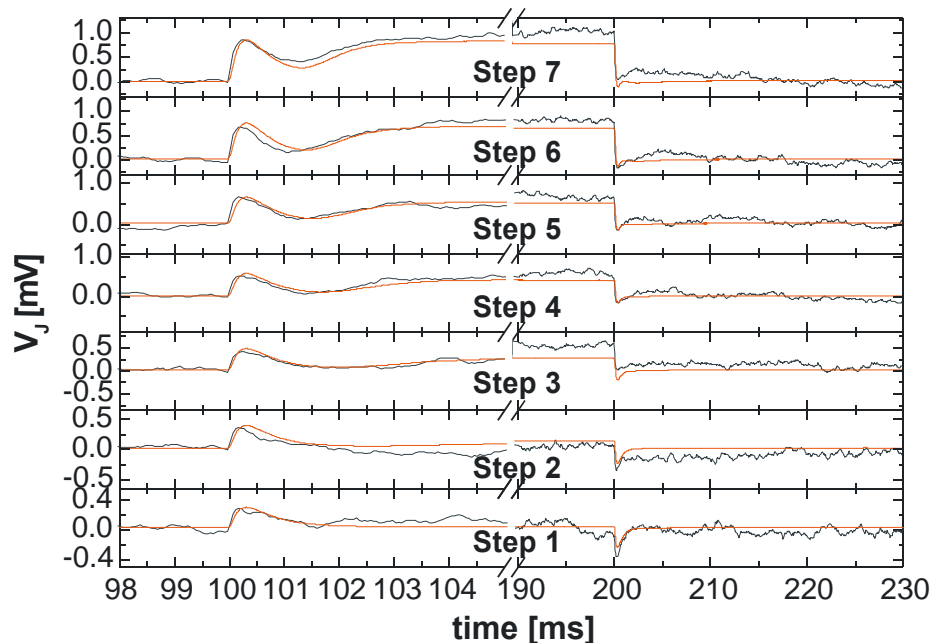


Figure 5-14 Closer view to the simulated data of the voltage-clamp step experiment. The simulation was performed using the values for the cell-transistor assembly shown in Table 5.3. For higher potassium currents (traces at 200 ms) the responses are underestimated by a factor of $X^i = 1.46 \pm 0.23$.

In Figure 5-15 the specific ionconductances obtained with the patch-clamp amplifier and with the FET are compared. The traces are again reflecting the former observation. The FET is overestimating the membrane conductance. This was observed in previous works (Straub et al., 2001; Vassanelli and Fromherz, 1999) and was interpreted as ion-channel accumulation in the attached membrane and hence an increased ion-current in the cleft between cell and transistor. Out of Figure 5-15 it seems that the difference between the patch-clamp data and the FET-data is increasing with higher ion currents, which would be compensated by a constant scaling value of $X^i = 1.46 \pm 0.23$.

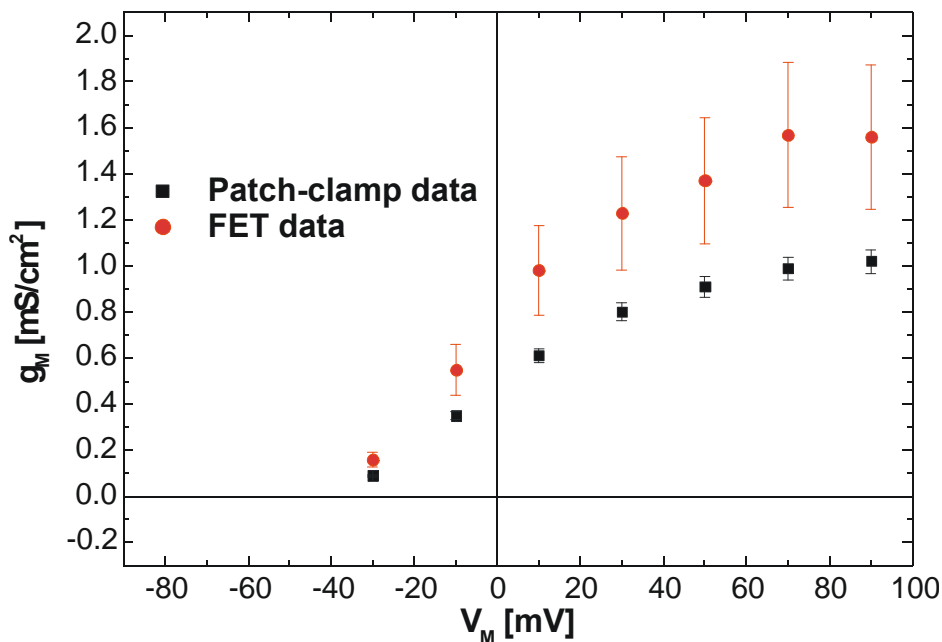


Figure 5-15 Comparison of the specific ionconductances obtained with the patch-clamp amplifier and with the FET. The data are scaled with their respective membrane areas. The FET is overestimating the membrane conductance.

The slow decays of the responses after the stimulation pulse in Figure 5-14 cannot be modelled. To evaluate this fact a second measurement was performed with the same cell by averaging 135 sweeps to the voltage steps of 100 mV, 150 mV, and 200 mV. In Figure 5-16 the results of these averaged responses are shown. For the simulation of the responses the cell-pipette assembly was newly compensated with the values shown in Table 5.4.

A change of the patch-clamp values to lower C_{slow} , higher G_L , and higher R_S values during a measurement was always observed, indicating a stressed cell membrane. When compensating the cell-pipette assembly again, the passive data in the PSPICE modelling had to be adjusted. Because the cell was under stress the sealing conductance g_J went slightly up to a value of $0.277 \text{ S}/\text{cm}^2$ (one averaging measurement lasted about 1 min). It can be explained by a slightly shrinking cell, which would lead to a different C_{slow}

value. In the measurements, where C_{slow} was compensated before each measurement this effect was taken into account by adjusting the cell radius r_{cell} for the simulation using Eq. 5.10. In the experiments with the averaged responses, the slower decay of the active potassium signal in the FET transistor could not be explained by varying all parameters in a wide range.

Voltage-clamp coupling	Patch-Clamp	Step 1	Step 2	Step 3
Chip: p-channel ($V_{DS} = -3V$, $V_{GS} = -2V$) $g_m = 0.35$ mS; Gatesize: $2 \times 8 \mu\text{m}^2$ Laminin coated	$V_{rest} = -59$ mV $G_L = 4.85$ nS $C_{slow} = 34.42$ pF	$V_{step} = 200$ mV $R_M =$ 3.5 G Ω $i_M^L =$ 285.3 pA	$V_{step} = 150$ mV $R_M =$ 4.6 G Ω $i_M^L =$ 330.5 pA	$V_{step} = 100$ mV $R_M =$ 0.96 G Ω $i_M^L =$ 367.5 pA
Date: 07.08.00 Files: Si000807.005 / 7 / 9 (un-averaged)	$R_S = 28.8$ M Ω ; $C_{fast} = 7.05$ pF	$R_J =$ 1056000.0 Ω	$R_J =$ 1056000.0 Ω	$R_J =$ 1056000.0 Ω
10 % of membrane attached Cell: Brainstem Neuron (11 DIV)	$A_M = 3.4 \cdot 10^{-9}$ m ² $r_{cell} = 16.5$ μm	$g_J =$ 0.277 S/cm²	$g_J =$ 0.277 S/cm²	$g_J =$ 0.277 S/cm²

Table 5.4: Values for averaged response to the voltage-clamp coupling experiment (3-step protocol) using the same brainstem neuron as before (Figure 5-16). The cell was new compensated with higher R_S and G_L , but lower C_{slow} values, which may indicate a slightly shrinking cell.

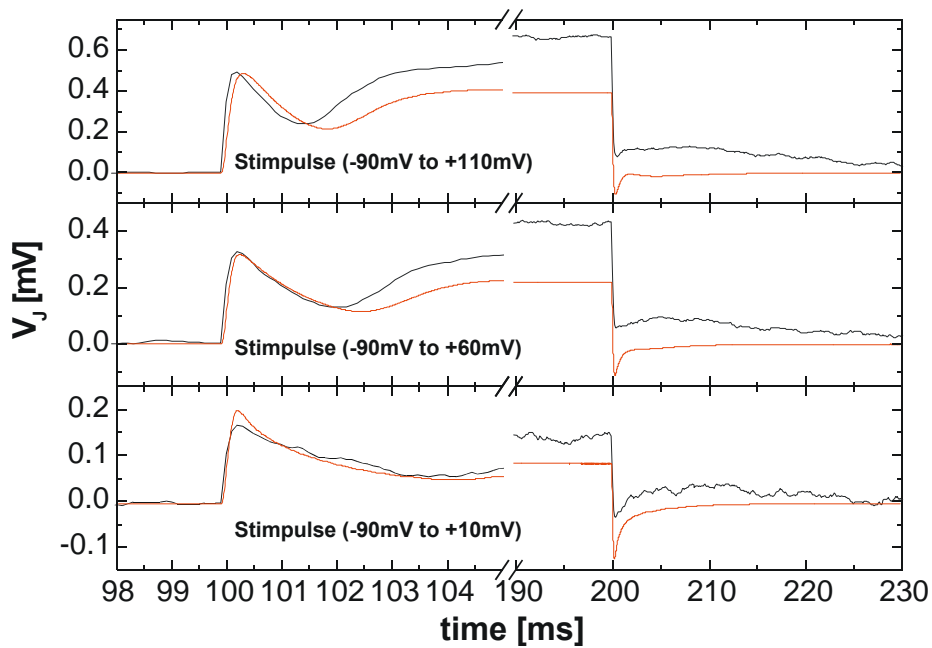


Figure 5-16 Averaged responses of the cell-transistor coupling experiment with the brainstem neuron (11 DIV). The slow decay (200-230 ms) cannot be modelled. The sealing conductance g_J was modelled to be 0.277 S/cm^2 .

In Figure 5-16 it can be seen that at the beginning of the response the difference of the fitted data was not as high as at the end of the response (after 100 ms potassium current). Distorted ion-channel gating in the attached area was assumed in previous works by (Fromherz, 1997) and interpreted with '*self-gating of ion-channel in the attached membrane*'. This has to be assumed in addition, because a constant current scaling for the responses in Figure 5-16 would not explain the higher difference between the beginning and the end of the response.

C: Potassium current of a single hippocampal neuron coupled to an n-channel FET

In the third signal simulation a single hippocampal neuron (1 DIV) was coupled to the gate of an n-channel FET. The transistor surface was again pre-treated with laminin and the cell seemed to be drawn into the gate structure forming an extremely closed contact with the gate oxide. The sealing conductance was relatively high and the signals were 40 times averaged in order to obtain a better signal-to-noise ratio.

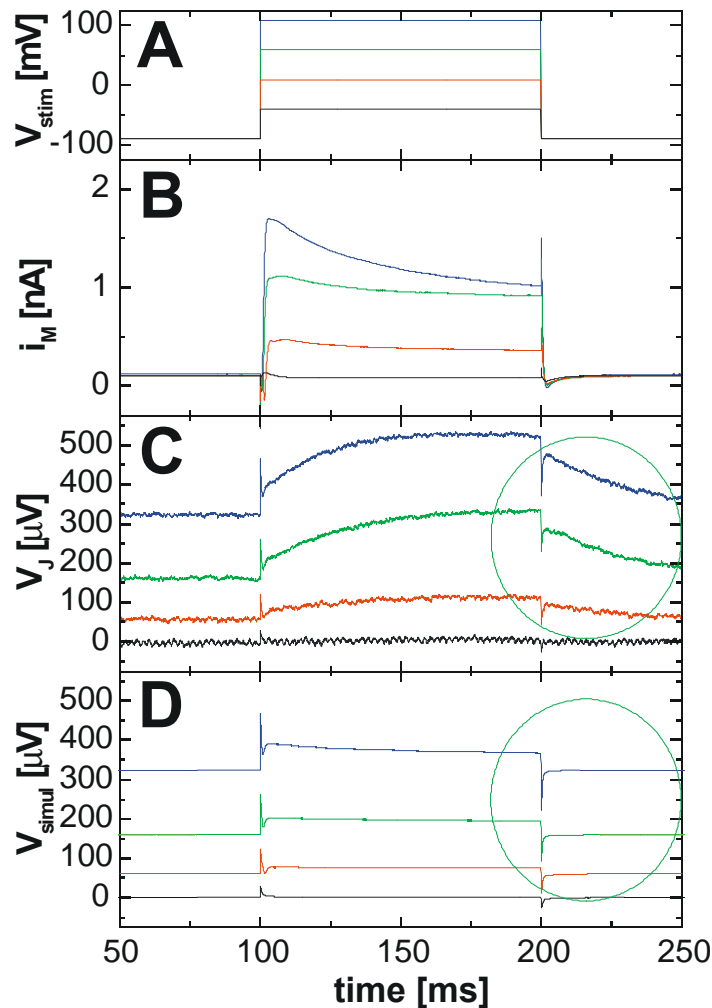


Figure 5-17 Four step voltage-clamp experiment with a single hippocampal neuron (1 DIV) coupled to the gate of a n-channel FET device. Trace A shows the 4 stimulation pulses of different height from the initial holding potential of $V_{hold} = -90$ mV. In trace B the active potassium current of the cell can be seen, corresponding to the relevant stimulation step. The extracellular signal shape in trace C cannot be modelled with the *Point Contact Model* using PSPICE (trace C/D; cycled areas). The signals were averaged 40 times.

In this measurement the slow decay of the potassium signal, which was observed many times in the voltage-clamp experiments with strong potassium currents, was very

pronounced. In the highest stimulation step, the cell showed a very strong potassium A-type current (paragraph 5.2) with an overshoot of about 50 % of the total potassium current (Figure 5-17 Trace B). Four individual experiments were performed. The stimulation pulses were from the holding potential of $V_{hold} = -90$ mV to -40 , 10 , 60 , and 110 mV respectively (Figure 5-17 Trace A).

A very high potassium efflux of the cell dominates the corresponding whole-cell current. The second stimulation step showed only a weak sodium signal (Figure 5-17 Trace B, at the beginning of the second high response) of 0.3 nA. The most interesting thing in this measurement was the very strong potassium A-type overshoot in the highest stimulation. It is apparent that the extracellular signal is not at all reflecting the shape of the active cell current. This was observed in previous works (Vassanelli and Fromherz, 1999) and was explained by different accumulation-properties of the potassium A-type channels with respect to the potassium K-type channels in the attached area of the cell.

If one compares the shapes of the extracellular signals in Figure 5-17, trace C, with the modelled signal shapes in trace D - especially in the circled areas - a strong difference in signal amplitude and decay can be observed. In Table 5.5 the values used for the fitted data are shown.

<i>Voltage-clamp coupling</i>	Patch-Clamp	Step 200 mV	Step 150 mV	Step 100 mV	Step 50 mV
Chip: n-channel ($V_{DS} = 3V$, $V_{GS} = 1.8V$) $g_m = 1.15$ mS; Gatesize: $2 \times 16 \mu\text{m}^2$ Laminin coated	$V_{rest} =$ -36 mV $G_L = 2.1$ nS	$C_{slow} =$ 13.2 pF $R_M =$ 1.8 G Ω $i_M^L =$ 117.7 pA	$C_{slow} =$ 12.8 pF $R_M =$ 2.97 G Ω $i_M^L =$ 112 pA	$C_{slow} =$ 12.9 pF $R_M =$ 2.17 G Ω $i_M^L =$ 103.7 pA	$C_{slow} =$ 12.3 pF $R_M =$ 1.88 G Ω $i_M^L =$ 106.4 pA
Date: 25.05.00 Files: Si000525.008 / 10 / 12 / 14 (averaged 40 x)	$C_{fast} =$ 7.05 pF	$R_J =$ 340200 Ω $R_S = 32.4$ M Ω	$R_J =$ 340200 Ω $R_S = 34.9$ M Ω	$R_J =$ 340200 Ω $R_S = 37.9$ M Ω	$R_J =$ 340200 Ω $R_S = 42.8$ M Ω
10 % attached Cell: Hippocampal Neuron (1 DIV)	$A_M =$ $1.3 \cdot 10^{-9}$ m 2 $r_{cell} = 10$ μm	$g_J = 2.34$ S/cm 2	$g_J = 2.34$ S/cm 2	$g_J = 2.34$ S/cm 2	$g_J = 2.34$ S/cm 2

Table 5.5: Values for the simulation the voltage-clamp coupling experiment (4-step protocol) using a hippocampal neuron (1 DIV) (Figure 5-17). The cell-pipette assembly was compensated before each measurement.

A closer examination at the fitted data in Figure 5-18 reveals that the shapes of the capacitive responses to the stimulation pulses at the beginning of the signals (100 ms) are exactly modelled. This means that the size of the seal conductance $g_J = 2.34 \text{ S/cm}^2$ was estimated very precisely.

The responses to the cell current and especially slow decay of the extracellular signal after the stimulation step cannot be modelled with the standard *Point Contact Model*. For obtaining the right amplitude of the extracellular response, the cell current of step 2 to 4 would have to be scaled by factors of 6.1, 6.2, and 6.4 respectively.

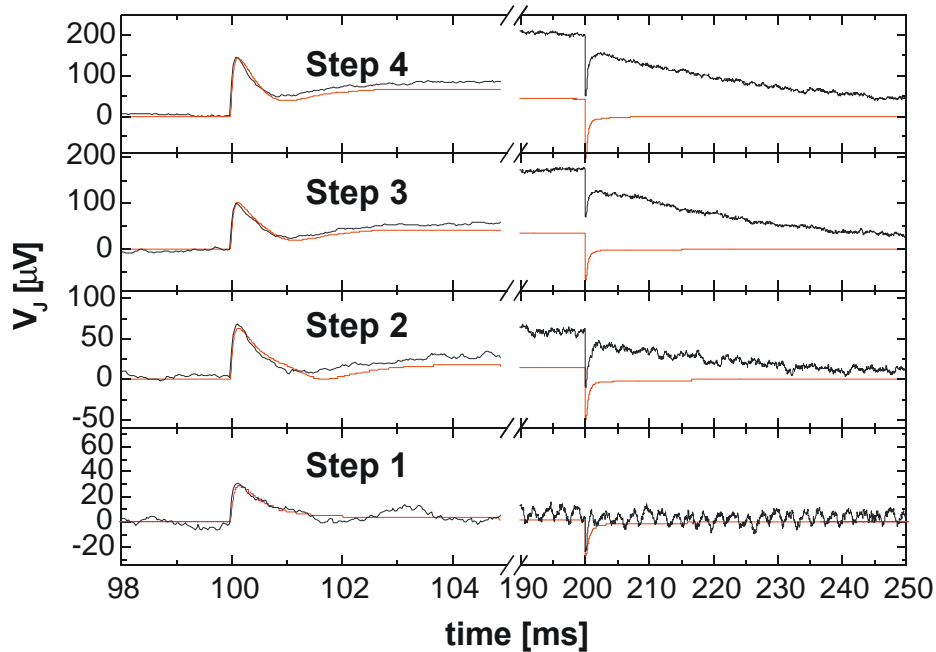


Figure 5-18 Closer look at the fitted data of the extracellular responses. The capacitive responses to the stimulation pulses are exactly modelled (left side). This means that the size of the seal conductance $g_J = 2.34 \text{ S/cm}^2$ was estimated very precisely. The response to the cell current at the end of the traces and the slow decay of the extracellular signal after the stimulation step was finished, cannot be modelled. For obtaining the right amplitude of the extracellular response, the cell current of step 2 to 4 would have to be scaled by factors of 6.1, 6.2, and 6.4 respectively.

For further examination of the extracellular signal part, which cannot be modelled with the Point Contact Model, the fitted responses were subtracted from the extracellular responses. The rising and decay times of the remaining signal parts were fitted with:

Rise time:

$$V_J = V_J^{\max} \cdot \left(1 - \exp \left(- \left(\frac{t - t^{\text{start}}}{t} \right) \right) \right) \quad (5.18)$$

Decay time:

$$V_J = V_J^{\max} \cdot \exp\left(-\left(\frac{t - t^{\text{start}}}{t}\right)\right) \quad (5.19)$$

In the Eqs. 5.18 and 5.19 V_J^{\max} is the maximum value of the extracellular response and t^{start} is the starting time for the rise or the decay respectively. In the following the rising and decay time indicated by t are compared. In Figure 5-19 the fitted data are shown.

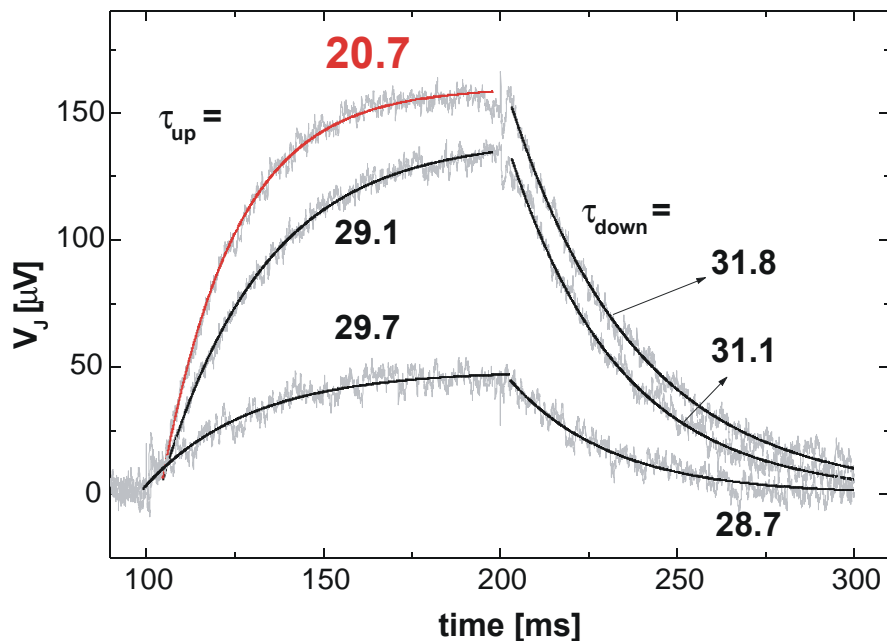


Figure 5-19 Fits for the rise or decay of the extracellular signals after subtracting the simulated data out of the PSPICE simulation from the FET signals (stimulation pulses 100, 150, and 200 mV). The remaining so far unknown part of the extracellular response shows a rise and decay with time constants of about $t = 30$ ms. Only the rise time of the highest response shows a much quicker time constant of $t = 21$ ms. The quicker rising of this signal seems to be caused by the potassium A-type overshoot of the potassium efflux.

The fits to the rise and decay of the remaining so far unknown part of the extracellular response shows time constants of about $t = 30$ ms. Only the rise time of the highest response shows a much quicker time constant of $t = 21$ ms. The quicker rising of this signal seems to be caused by the potassium A-type overshoot of the potassium efflux. Therefore, it is concluded that, although the coupled signal does not reflect the signal shape of the cells membrane current, the potassium A-type signal is coupled to the FET sensor as opposed to previously made observations (Vassanelli and Fromherz, 1999). In the next paragraph a possible explanation will be given.

5.4 Ionsensitivity of the BioFETs

5.4.1 Concentration Changes in the Cell-Transistor Cleft

The remaining signal shape after subtraction of the simulated traces Figure 5-19 is very similar to the responses of standard ion sensitive FETs (ISFETs) to pH-changes. For an estimation of the ion concentration changes in the cleft between cell and transistor during a strong potassium signal the following dimensions are playing a major role (Figure 5-20).

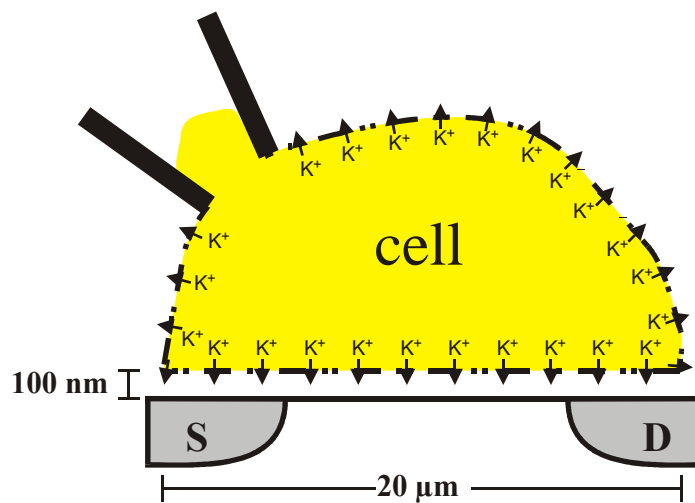


Figure 5-20 Sketch for the estimation of the liquid volume between cell and transistor. The distance of the cell is known to be up to 100 nm. The radius of the cell is estimated to 10 μm , which is a fairly high value for neurons but also valid for cardiac myocytes.

For simplification, the distance of the cell to the substrate should be 100 nm, which even overestimates the reported distance (35-70 nm were determined by fluorescence interference contrast microscopy (Braun and Fromherz, 1998)). The cell's radius is 10 μm and a bowl membrane surface is assumed. This leads to an attached membrane area (10 % of the total membrane) of $A = 1.26 \cdot 10^{-10} \text{ m}^2$ (10% of the total membrane surface $S = 4\pi r^2$) and hence a liquid volume between cell and substrate of $V = 1.26 \cdot 10^{-17} \text{ m}^3 = 12.6 \text{ fl}$. In our extracellular solution, a potassium concentration of $(\text{K}^+) = 5 \text{ mM}$ was used (paragraph 4.3.4). With Avogadro's constant of $6.023 \cdot 10^{23} \text{ 1/l}$ a total number of $n(\text{K}^+) = 3.012 \cdot 10^{21}$ ions per litre extracellular solution can be calculated. With the cleft-volume V this leads to an initial number of potassium ions in the cleft of $n_{\text{cleft}}(\text{K}^+) = 3.8 \cdot 10^7$.

For the current signal response to a stimulation pulse of 150 mV (Figure 5-17) is nearly rectangular with a height of 1 nA and a duration of 100 ms. This leads with the

current $I = dQ/dt$ to a total charge exchanged over the whole membrane of $Q = 1 \cdot 10^{-10} \text{C}$. One single ion carries a charge of $e = 1.602 \cdot 10^{-19} \text{C}$ which leads to the total number of potassium ions $n_{\text{flow}}(\text{K}^+) = 6.24 \cdot 10^8$ flowing over the membrane. In the attached area 10% of this number adds to the initial number of ions from above.

By assuming that all ions are trapped in the small volume (which is certainly not the case) would lead to a concentration of 13.2 mM at the end of the signal. It corresponds to a pK^+ -change (analogue definition to the pH value of a solution) from $\text{pK}^+(\text{extracellular sol.}) = 2.3$ to $\text{pK}^+(\text{after pulse}) = 1.88$. The values of the estimation are reflecting the upper range, as normally the neurons are even smaller in size and closer attached (below 100 nm). This lead to an even smaller volume, hence higher concentration changes.

5.4.2 Calibration Curve: Ionsensitivity of the BioFETs

For the calibration of the ion sensitive BioFETs to concentration changes of the three different ion types K^+ , Na^+ , and Ca^{2+} from their respective initial concentration in the extracellular solution, a stock solution was made up. The 2l-stock contained less sodium- (110 mM) and less calcium chloride (0.25 mM), but the same amount of potassium chloride than the extracellular solution (5 mM). The pH-value of the stock-solution was adjusted to $\text{pH} = 7.41$ with 1 N NaOH solution.

1. Extracellular Sol.	2. (K^+)- Solution	3. (Na^+) ⁻ Solution	4. (Ca^{2+}) ⁻ Solution
KCl: 5 mM pK = 2.301	KCl: 15.85 mM pK = 1.8	KCl: 5 mM pK = 2.3	KCl: 5 mM pK = 2.3
NaCl: 150 mM pNa = 0.824	NaCl: 150 mM pNa = 0.824	NaCl: 110 mM pNa = 0.959	NaCl: 150 mM pNa = 0.824
CaCl ₂ : 2.5 mM pCa = 2.602	CaCl ₂ : 2.5 mM pCa = 2.602	CaCl ₂ : 2.5 mM pCa = 2.602	CaCl ₂ : 0.25 mM pCa = 3.602
MgCl ₂ : 1 mM	MgCl ₂ : 1 mM	MgCl ₂ : 1 mM	MgCl ₂ : 1 mM
HEPES: 10 mM	HEPES: 10 mM	HEPES: 10 mM	HEPES: 10 mM
Glucose: 10 mM	Glucose: 10 mM	Glucose: 10 mM	Glucose: 10 mM

Table 5.6: Concentrations of the four different solutions. All solutions were made up from the same stock and had a pH-value of $\text{pH} = 7.41$. For the calibration measurement the concentration of this solutions reflected the maximum examined concentration range. All concentration in between the maximum values were reached by mixing of the respective solution with the extracellular solution.

The final concentration value of sodium in the stock solution was corrected by the amount of added NaOH. After this the stock was divided into 4 solutions having exactly

the same pH-values. It was essential to confirm that the responses of the FET were only caused by the respective ion type and not by artificial pH-changes. The concentrations of the solutions are tabulated in Table 5.6:

By using these solutions, the ion sensitivity for each ion type was examined. The extracellular solution was used as the 'baseline' concentration. In Figure 5-21 the response of a p-channel standard FET array to a series of different sodium concentrations is plotted.

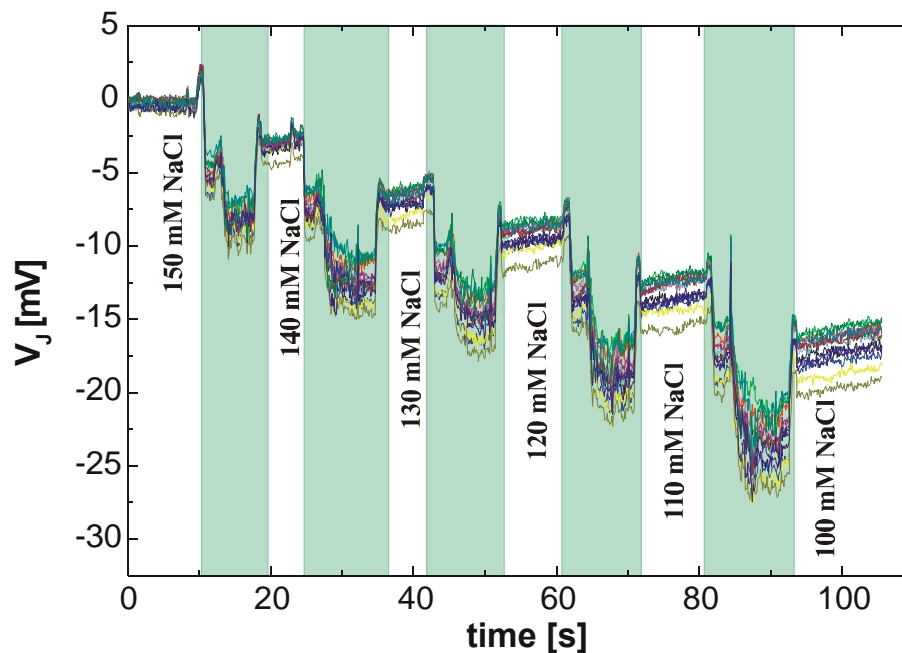


Figure 5-21 Ionsensitivity of a p-channel standard FET-array to different sodium concentrations. The individual channels are scaled with their respective transconductance to equivalent gate potential. The un-stable baselines (boxes) are caused by the solution exchange procedure. The respective sodium concentrations are indicated in the figure.

For all the different solutions measurement series were performed with many different FET-chips from both, p- and n-channel type. It appeared that the p- and n-channel FETs possessed similar sensitivities. All of these ion-effects have the same direction in the gate potential as the active ion-current contribution observed in the voltage-clamp experiments with living cells. Therefore, the effects of the concentration changes would be able to enhance the responses to extracellular signals from cells for all three ion-types.

In Figure 5-22 the responses to the three different ion types are plotted. As error bars for the concentrations and for the gate voltage, the standard estimated deviations (s.e.m) of the responses were used. It was found that the traces have different slopes, which means the chips show different sensitivity for different ion types. The differences of the

two FET types were not significant (the difference was analysed using Student's unpaired t-test: $P > 0.03$, not significant). For obtaining the results shown in Figure 5-22, $n = 20$ were analysed.

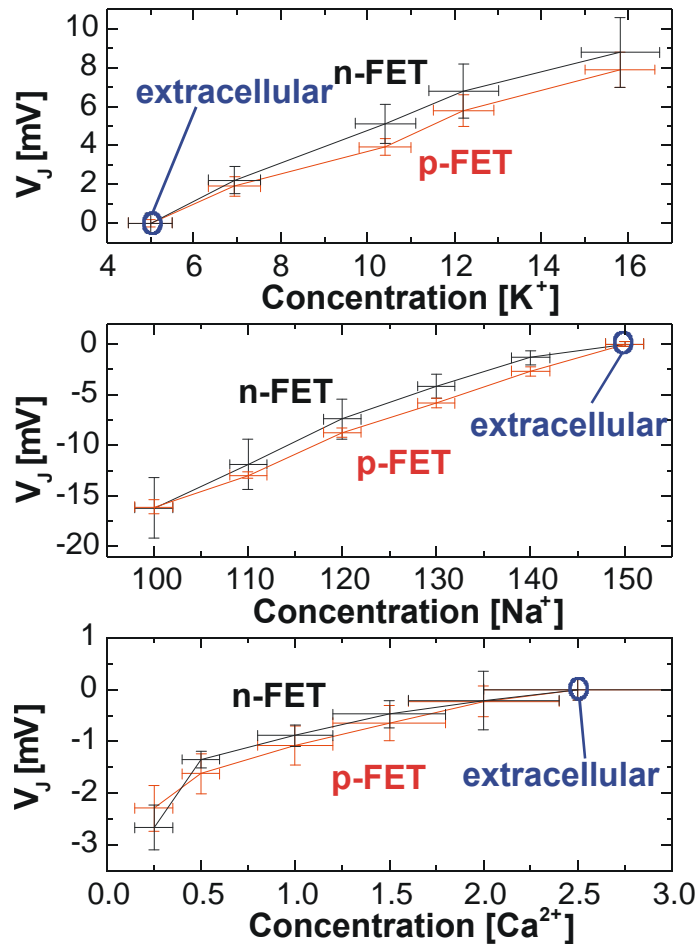


Figure 5-22 Dependence of the gate potential to the concentration of the three ion types in the bath solution. The p- and n-channel FETs show nearly the similar behaviour. The errorbars for the concentration were estimated from the mixing procedure, whereas for the gate voltage the standard deviations of the responses were used as error bars ($n = 20$ for each data point).

Superimposing the three different plots can perform further investigations. In Figure 5-23 the responses again are shown. For the Ca^{2+} -ions the available range is very limited, because the extracellular solution contains only 2.5 mM of calcium chloride. In the extracellular volume close to a cell the Ca^{2+} -concentration can only be lowered by an influx into the cell. Therefore, a maximum range of $\Delta c = 2.5$ mM is appropriate. For the explanation of the shapes of the recorded signals from dense cardiac myocyte layers using the FET sensors (chapter 6) and the relevant range is plotted in Figure 5-24. Signals up to amplitude of 5 mV were recorded with the cardiac myocyte layers. Here,

the sealing of the layer may enhance the effect of the ion concentration change in the cleft between cells and sensors.

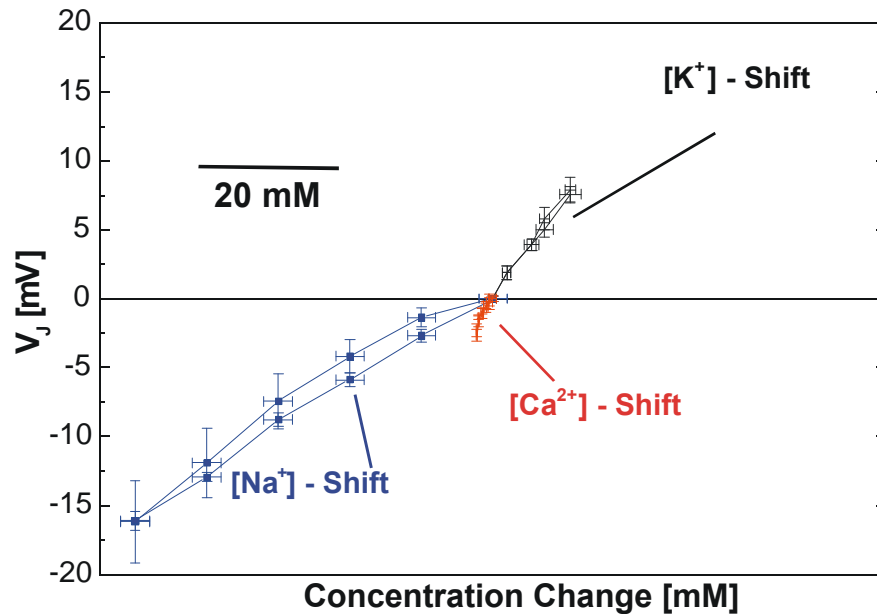


Figure 5-23 Comparison of the slopes. The whole range of the calibration data is plotted.

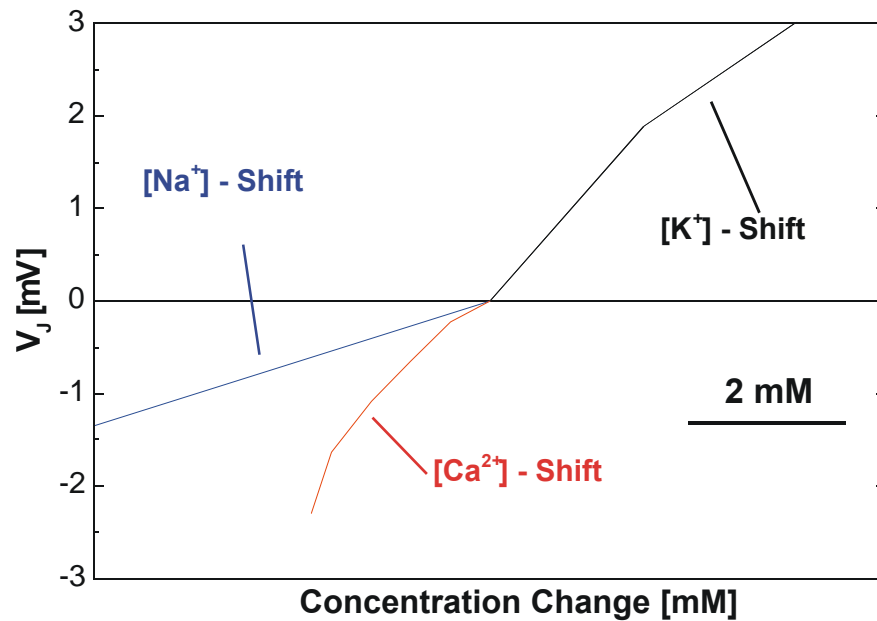


Figure 5-24 Range of the concentration changes relevant for extracellular signals from cardiac myocyte layers.

In Figure 5-25 the relevant range for single cell patch-clamp measurements is shown. The signal amplitude is normally below 1 mV. From the plot, it can be seen that the remaining signal in Figure 5-19 can be explained by a concentration change of

$c(K^+) \approx 0.11$ mM, which reflects only a small amount of the estimation made in paragraph 5.3.1 (Dc was 8.2 mM, by assuming a closed volume).

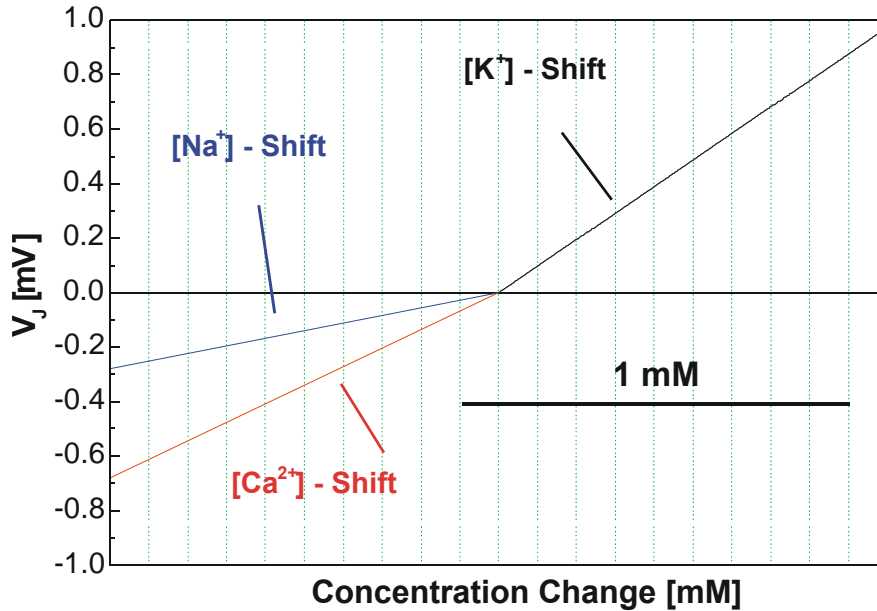


Figure 5-25 Range of the concentration changes relevant for single cell coupling.

In this narrow region, the response of the FET to concentration changes can be treated approximately linear. From this calibration curve the sensitivity to the respective ion species would be:

- $V_{Gate}(Dc(Na^+)) = 0.28$ mV/mM
- $V_{Gate}(Dc(Ca^{2+})) = 0.68$ mV/mM
- $V_{Gate}(Dc(K^+)) = 0.97$ mV/mM

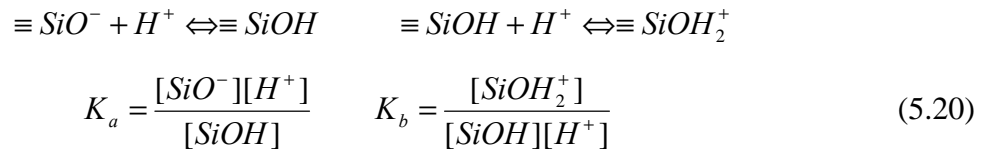
This means the sensitivities to concentration changes are scaling with 1:2.4:3.5 for $Na^+ : Ca^{2+} : K^+$ ion concentration changes. Here, linear responses in the narrow region of the extracellular point are assumed.

5.4.3 Ionsensitivity of Transistors

Although the ion-sensitive field-effect transistors (ISFET) were invented in 1970 (Bergveld, 1970), they are still of current interest in research. Compared to standard ion-sensitive electrodes the ISFET has clear advantages in response time, compact size, and low output resistance. ISFETs with pH-sensitivity (H^+ -ions) are constructed with gate insulator materials like SiO_2 , Si_3N_4 , or Al_2O_3 . The poorest sensitivity and stability of these gate materials has SiO_2 . In addition, it is well known that these materials have sensitivity to changes in potassium K^+ , calcium Ca^{2+} , and sodium Na^+ concentration in

the electrolyte (Elbhiri et al., 2000; Hajji et al., 2000; Liao et al., 1999). The basic theory, which describes the physics behind these effects goes back to the *Site-Binding model* introduced in 1974 (Yates et al., 1974). It was shortly discussed in paragraph 3.2.1 and will now be further investigated.

In the *Site-Binding model* the charge and potential distribution in the electrolyte-insulator system depends on the dissociation constants of the surface groups and on the space charge layers of the electrode-electrolyte interface (paragraph 3.2.7)(Yates et al., 1974; Siu and Cobbold, 1979). A pH change in the electrolyte varies the charge of the gateoxide surface and is influencing the potential drop Ψ_E in the electrolyte interface layer. This is affecting the flatband voltage of the transistor (Eq. 3.25). The flatband voltage V_{FB}^E is influencing the transistor by shifting the threshold voltage V_{th} (paragraph 3.2.1). This leads in the working point of the transistor to a change in the drain source current I_{DS} . The charge at the oxide surface is defined by the equilibrium reaction of the silanol groups with the protons (or positive ions) in the electrolyte and by the dissociation constants K_a and K_b of SiOH:



By comparing the flatband voltages of a transistor with metallised gate (Eqs. 3.1, 3.2) and the flatband voltage of an EOSFET structure (Eq. 3.25), following difference between the two devices can be extracted:

$$V_{Fb}(MOSFET) = \Phi_{MS} - \frac{Q_I}{C_I} = \frac{\Phi_M - \Phi_{SC}}{q} - \frac{Q_I}{C_I} \quad (5.21)$$

$$V_{Fb}^E(EOSFET) = V_{ref} - \frac{\Phi_{SC}}{q} - \Psi_E - \frac{Q_I}{C_I} + \mathbf{c}^E + \mathbf{dc} \quad (5.22)$$

The value for the surface potential \mathbf{dc} is close to zero and can be ignored (paragraph 3.2.1). Subtracting Eq. 5.21 from Eq. 5.22 leads to following difference:

$$Diff. = V_{ref} - \frac{\Phi_M}{q} + \mathbf{c}^E - \Psi_E \quad (5.23)$$

The potential drop Ψ_E in the electrolyte interface layer is in the *Site Binding model* coupled to the pH-value of the solution as follows:

$$2.303(pH_{pzc} - pH) = \frac{\Psi_E}{V_{th}} + \sinh^{-1} \left(\frac{\Psi_E}{V_{th}} \frac{1}{\mathbf{b}} \right) \quad \text{with } \mathbf{b} = 2 \frac{qN_s}{C_d V_{th}} \sqrt{K_a K_b} \quad (5.24)$$

The sensitivity factor \mathbf{b} of the sensor is dependent on the density of the surface binding sites N_s , on the capacitance of the double layers $C_d^{-1} = C_D^{-1} + C_H^{-1}$, and on the

equilibrium constants K_a and K_b of SiOH (Eq. 5.20). This value was introduced in the *Site-Binding model* to take sensitivity deviations from the theoretical value into account. The higher the sensitivity, which means higher reactivity of the surface, the lower is the influence of the \sinh^{-1} term in Eq. 5.24. Then the equation fully reflects the nernstian response and the gate potential is linear to the pH-value of the solution.

For pH-values close to the *Point of Zero Charge value* ($\text{pH}_{\text{pzc}}(\text{SiO}_2) = 2.3 \pm 0.2$, (Bousse, 1982)) the \sinh^{-1} -function is linear. The Eq. 5.24 can then be approximated with (Liao et al., 1999):

$$\Psi_E = 2.303 \frac{kT}{q} \frac{b}{b+1} (\text{pH}_{\text{pzc}} - \text{pH}) \quad (5.25)$$

In most cases, the sensitivity factor b turns out to be large (e.g. 58.6 reported by Liao et al. (1999)) and the term $b/b + 1$ can be ignored. The potential drop Ψ_E in the electrolyte interface layer is then linearly coupled to the negative pH value. With the definition of the pH-value ($\text{pH} = -\log(\text{H}^+)$) it is then linearly coupled to the logarithm of the concentration of protons in the solution. The flatband voltage difference of MOSFET and EOSFET (Eq. 5.23) is then only dependent on Ψ_E as the other values remain constant ($V_{\text{ref}} - F_{\text{SC}}/q - c^E = 0.705 \pm 0.05$ V, for an Ag/AgCl reference electrode (Liao et al., 1999)).

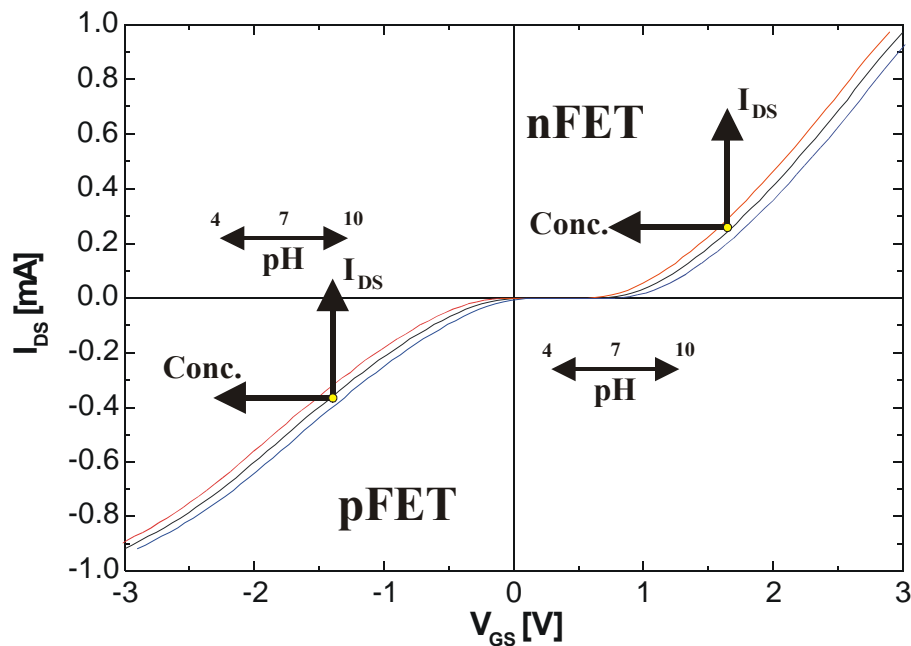


Figure 5-26 Direction of the shift in the drain source current I_{DS} to changes in (H^+) ion concentration. For both transistor types a higher concentration of (H^+) ions leads to a more positive signal in the transistor current. The traces for pH 7 are the responses of standard FET arrays (chapter 3). The respective traces for pH 4 and pH 10 are calculated with $Y_E = 34 \pm 2$ mV/pH reported by Sprössler (1997).

Higher proton concentration values, which mean lower pH values, are leading with Eq. 5.25 to higher potential drops Y_E in the electrolyte interface layer. This result in a lower value for the flatband voltage V_{FB}^E and the transfer characteristics of the transistor is shifted to lower values of V_{GS} as indicated in Figure 5-26. This effect is for both transistor types (p-channel or n-channel) towards the same direction and we are measuring more positive I_{DS} values. In Figure 5-26 the respective pH-shift to changes in pH is indicated.

For the classical pH-electrode a value of $Y_E = 59 \text{ mV/pH}$ can be calculated using Eq. 5.24. For electrolyte-SiO₂-systems pH-sensitivities in the range of 20...40 mV/pH are reported (Abe et al., 1979; Madou et al., 1988). In previous work a pH-sensitivity of $Y_E = 34 \pm 2 \text{ mV/pH}$ for our BioFET gateoxides was determined by Sprössler (1997).

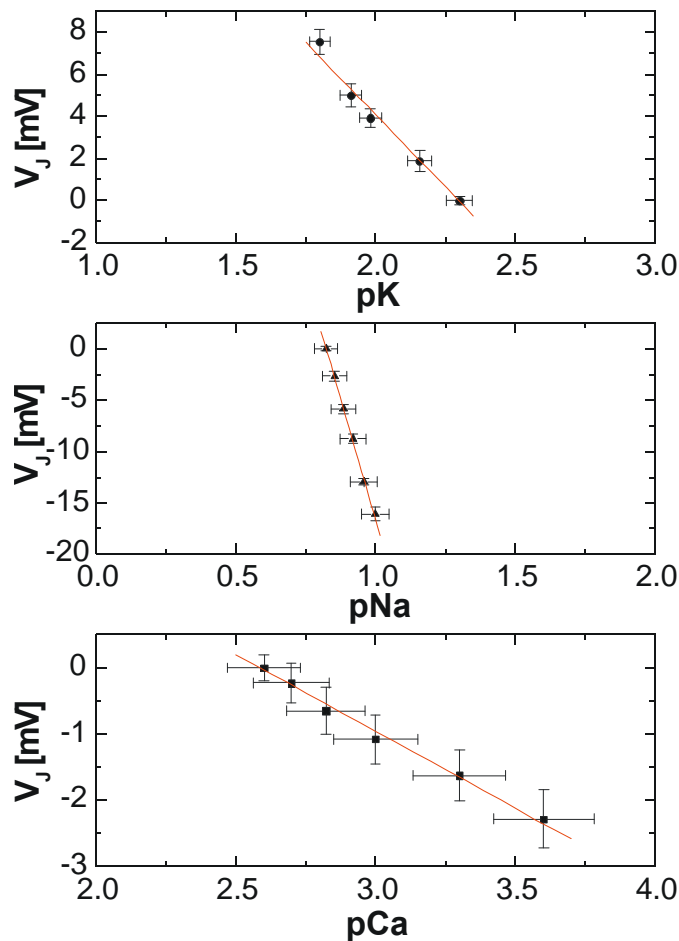


Figure 5-27 Linear fits to the p(ion) responses with similar scaling of the p(ion) axis. From the slopes sensitivities of $V_{gate} = 2.3 \text{ mV/pCa}$, $V_{gate} = 13.7 \text{ mV/pK}$, and $V_{gate} = 94 \text{ mV/pNa}$ can be extracted.

The detection properties of ISFET chemical sensors were investigated by Hajji et al. (2000). It was found out that the sensitivity to the different ionic species is highly

dependent on each other. At a physiological pH-value of the electrolyte ($6 \leq \text{pH} \leq 8$), a linear response to pK and pNa values of the solution have been found. Here, the definition of a pNa and pK value is the same as that of the classical pH-value:

$$p[\text{ion}] = -\log(c[\text{ion}]) \quad (5.26)$$

It was also stated that the concentrations of the salts should not be too high to give linear nernstrian responses. For the lowest concentrations ($\text{pK} > 4$ or $\text{pNa} > 3$), no detection properties have been obtained. The theoretical description of the effects is adapted to the formalism for sensitivity to pH-changes from above with Na^+ , Ca^{2+} , or K^+ as positive ion type interacting with the surface.

By having a closer look at the calibration measurements in Figure 5-23 and Figure 5-24 it can be seen that the response curves are bent. In Figure 5-27 the negative logarithms of the single responses (Figure 5-22) are plotted and linearly fitted.

From the slopes of the linear fits, sensitivities of $V_{gate} = 2.3 \text{ mV/pCa}$, $V_{gate} = 13.7 \text{ mV/pK}$, and $V_{gate} = 94 \text{ mV/pNa}$ can be extracted. These values are fully comparable to the results in the literature (Elbhiri et al., 2000; Hajji et al., 2000). They stated that pNa values lower than 1 reveals non-nernstrian responses, because not only the potential drop Y_E in the electrolyte interface layer but also the Ag/AgCl reference electrode is affected. For the lowest concentrations above $p(\text{ion}) > 3$ almost no detection properties have been obtained. This would be the case for the calcium ions (Figure 5-27 lower trace: $V_{gate} = 2.3 \text{ mV/pCa}$). For the response of the potassium concentration, an almost identical response was found ($V_{gate} = 14 \text{ mV/pK}$, (Hajji et al., 2000)). In the following, the ions sensitivity effects are adapted to the classical *Point Contact Model* for the cell-transistor coupling (paragraph 5.1).

5.5 Extended Point Contact Model

In the following, the ion sensitivity of the BioFET surface was integrated into the *Point Contact Model* for further description of the signal shapes. The previous discussion demonstrated that the ionic responses are linearly coupled to the gate potential V_j . The estimation made in paragraph 5.3.1 is highly coupled to the initial ion concentration in the extracellular solution. It was apparent that the estimation of a closed volume doesn't lead to the appropriate description of the concentration change. For the recorded potassium signal in Figure 5-19 the estimation of a concentration change of $Dc = 0.11 \text{ mM}$ would explain the additional recorded signal. By assuming the same rectangular signal of a whole cell current of 1 nA for a period of 100 ms and by using the scaling factors from the last paragraph, the total signal amplitude would be

different for different ion species (the assumption of such signal shapes for Ca- and Na-currents is certainly not valid, but for comparison reasons practical):

$$V_J(\text{conc.}) = S_{ion} \log\left(\frac{\Delta c_{ion} + c_0}{c_0}\right) \quad (5.27)$$

with the sensitivity values S_{ion} ($S_{Ca} = 2.3$ mV/pCa, $S_K = 13.7$ mV/pK, and $S_{Na} = 94$ mV/pNa) and the initial ion concentration c_0 of the respective ion species in the extracellular solution ($c_0(\text{Ca}^{2+}) = 2.5$ mM, $c_0(\text{K}^+) = 5$ mM, and $c_0(\text{Na}^+) = 150$ mM). By assuming the same signal shape and a rectangular 1 nA current pulse of the cell current the charge $z = 2$ of the calcium ion has to be kept in mind. With this a concentration change $\mathbf{Dc} = 0.11$ mM for K^+ and Na^+ (value of the measurement in Figure 5-17) and a $\mathbf{Dc} = 0.055$ mM for Ca^{2+} occurs in the cleft between gate and transistor. This leads with Eq. 5.27 to the following signal amplitudes in the extracellular voltage V_J .

- $V_J(\mathbf{Dc}(\text{K}^+) = +0.11 \text{ mM}) = +130 \mu\text{V}$ (as observed above in Figure 5-19)
- $V_J(\mathbf{Dc}(\text{Na}^+) = -0.11 \text{ mM}) = -30 \mu\text{V}$
- $V_J(\mathbf{Dc}(\text{Ca}^{2+}) = -0.11 \text{ mM}) = -22 \mu\text{V}$

As a result of this estimation it can be seen that for the same cellular signal by assuming the same cell-transistor dimensions the amplitudes of the ion-effects are different with $V_J(\text{Ca}^{2+}) < V_J(\text{Na}^+) < V_J(\text{K}^+)$ and are scaling with **1:1.4:5.9**.

Such scaling factors have been previously used in our group for the explanation of the signal shapes recorded from cardiac myocyte layers (Krause, 2000; Sprössler et al., 1999). Here, the cell current was scaled directly (Eq. 5.4) and justified by an ‘*accumulation of ion-channels in the attached membrane area*’ (Straub et al., 2001; Vassanelli and Fromherz, 1999). This explained only the right signal amplitudes but a second effect of ‘*different gating properties of ion-channels in the attached membrane area*’ would be needed to explain the different time courses. The response to the overshooting A-type potassium current of a neuronal cell was not recognised. This fact was attributed to a *depletion* of this type of ion-channels in the attached membrane area.

As it can be seen, the effects of the ion sensitivity are playing a major role in the coupling behaviour of cells to field-effect transistors. The assumption of unchanged reversal voltages E_0^i , requiring unchanged ion concentrations with respect to the bulk electrolyte in the cell transistor cleft, is not valid for strong ionic currents. Even for small ionic concentration changes, where the assumption of unchanged reversal voltages is still valid, a major signal part caused by the ion sensitivity contribution of the transistor may contribute to the total signal shape. A modification of the *Point Contact Model* has to take the empirical values obtained by the calibration measurement into account:

$$V_J = \frac{1}{g_J} \left(c_M \frac{dV_M}{dt} + \sum_i i_M^i \right) + \sum_i S_{ion}^i \log \left(\frac{\Delta c_{ion}^i + c_0^i}{c_0^i} \right) \quad (5.28)$$

The respective sealing conductance g_J can be derived from the procedure described in paragraph 5.1. It scales the capacitive response and the response to the electrical current flowing over the seal resistance from the cleft to the electrolyte. The sensitivity factors S_{ion}^i for the respective ion species are strongly dependent on the initial p(ion) value in the used extracellular solution. These values will certainly vary if other ion-sensitive gate materials (e.g. Si_3N_4 , Al_2O_3 , Ta_2O_5 ...) are in use. The concentration change Δc_{ion}^i in the cleft between cell and transistor reflects the dynamic behaviour of the ionic response. It is dependent on the ion fluxes in the cleft and the dimensions of the cell-transistor assembly. In ionic solutions, very high diffusion coefficients are reported in the literature (Vanýsek, 1995):

Ionic conductivity and diffusion at infinite dilution

The molar (equivalent) conductivity I for common ions at infinite dilution and the diffusion coefficient D_i of the ion in dilute aqueous solution are related with following equation:

$$D_i = \frac{RT}{F^2} \cdot \frac{I}{|z|} \quad (5.29)$$

with the molar gas constant ($R = 8.314 \text{ JK}^{-1}\text{mol}^{-1}$), T the absolute temperature, F the Faraday constant ($F = 9.649 \cdot 10^4 \text{ Cmol}^{-1}$), and z the charge of the ion. The variation with temperature is fairly sharp; for typical ions, I and D_i increase by 2 to 3% per degree, respectively, as the temperature increases from 25°C. For the treated ion species following values at 25°C are stated (Vanýsek, 1995):

$$\text{Calcium: } I = 59.47 \cdot 10^{-4} \text{ m}^2\text{Smol}^{-1}; D = 0.792 \cdot 10^{-5} \text{ cm}^2\text{s}^{-1}$$

$$\text{Sodium: } I = 73.48 \cdot 10^{-4} \text{ m}^2\text{Smol}^{-1}; D = 1.957 \cdot 10^{-5} \text{ cm}^2\text{s}^{-1}$$

$$\text{Potassium: } I = 50.08 \cdot 10^{-4} \text{ m}^2\text{Smol}^{-1}; D = 1.334 \cdot 10^{-5} \text{ cm}^2\text{s}^{-1}$$

The diffusion coefficient for a salt, D_{salt} , may be calculated from the D_+ and D_- values of the constituent ions by the relation:

$$D_{salt} = \frac{(z_+ + |z_-|)D_+D_-}{z_+D_+ + |z_-|D_-} \quad (5.30)$$

The different diffusion constants may also influence the time course of the ionic contribution of the respective ion species.

For the above discussed potassium signal (Figure 5-17) we assumed a concentration change of $Dc(K^+) = 0.11 \text{ mM}$ at the end of the signal ($V_J = 130 \mu\text{V}$). It is decaying in 50 ms down to an amplitude of $V_J = 25 \mu\text{V}$. For potassium ions with the above stated value, diffusion occurs in a time range of 50 ms to an area of $A_{diff} = 6.67 \cdot 10^{-11} \text{ m}^2$. With the estimated attached membrane area of the neuron bigger than $1.26 \cdot 10^{-10} \text{ m}^2$ (see paragraph 5.4.1) thermal diffusion is not sufficient to lower the concentration of the potassium accumulated in the cleft quickly enough. May be the concentration decay is accelerated by the strong current efflux.

The dynamic responses of ISFET sensors are still a topic of current research (Hara et al., 1996; Oelßner et al., 1995). Response times in the range of 250-300 ms ($t_{5-95\%}$) for pH changes of 2.5 have been reported. This means that the signal shapes we observed were strongly influenced by non-linear response dynamics of the sensor. In particular, the response of the potassium and calcium contribution to the signal shape in extracellular recorded cardiac myocyte signals is delayed by 50-150 ms (Krause, 2000; Sprössler, 1999).

The sealing properties of the dense cell layers may even enhance the ionic effects and may slow down the diffusion of the ions accumulated during a cell signal (chapter 6). The introduced extended *Point-Contact Model* is able to explain the higher signal amplitudes of the extracellular signals only by chemical and physical effects. Diffusion processes of the ions in the cleft between cell and transistor may even explain the slower time response. A qualitative estimation of the dynamic responses turns out to be very complicated. The observed dynamic effects are varying in a range of 30-150 ms.

The explanation of the observed effects by an ion-sensitivity effect seemed to be more conclusive than an explanation by a distorted ion-channel function caused by the ion changes in the cleft ('*self-gating of ion-channels*' in (Fromherz, 1997)). For the full explanation of the signal amplitude of $130 \mu\text{V}$, which would be attributed to a scaling factor of 6 for the active cell current scaling in the standard *Point Contact Model*, a minute concentration change of $Dc(K^+) = 0.11 \text{ mM}$ would be enough. Therefore this interpretation seemed to be more plausible than a distorted ion-channel function or an accumulation of ion-channels in the cleft. For the ion-channels it should make no difference if the K^+ ion-concentration is 5 mM or 5.11 mM in the surrounding volume of the cell.

Chapter 6

Cell-Transistor Coupling Measurements

In this chapter the cell transistor coupling experiments with living cells cultured on extracellular sensors are described.

The single cell coupling experiment utilised *cell lines* and *primary cultures* obtained from:

- Dissociated neurones from rat hippocampus
- Dissociated neurones from rat neocortex
- Rat cardiac myocyte
- Rat brainstem neurons (explant cultures)

All primary cultures were prepared from embryonic rats between embryonic 15 to 19 days old (E15-E19). The pregnant rats were purchased from the animal facilities of the

group of Prof. Maelike⁽¹⁾ or from Charles River company⁽²⁾. Relative few experiments were performed using cortical cultures. Majority of the data was obtained using the hippocampus neurons as they has been established for several years in our group (Krause, 2000; Scholl et al., 2000; Sprössler, 1997; Sprössler et al., 2001). In the present study, migrated neurons from an explant culture were introduced. The slices of the brainstem were prepared and plated on the laminin treated sensor surface. After adherence, and a few days of culturing in the incubator, single cells started to migrate out of the slice onto the sensor surface. These cells exhibited very high electrical activity and, once they adhered on the gates of the chip, very strong cell-transistor couplings have been observed.

As second cell type for the single cell-transistor coupling measurements two different *cell lines* were used:

- Human neuronal cell line SH-SY5Y
- Neuroblastoma cell line TR14

In contrast to the primary cultured cells, the *cell lines* are from carcinogenic tissue or from artificially induced abnormal cell evolution. The advantage of these cells is that they can divide a number of times in culture and yet maintain their electrophysiological characteristics. In contrast to the primary cultured neurons the properties of these cells are not completely determined and can be influenced by genetic modification. The SH-SY5Y cells from the two cell lines are not able to form synapses. However, they exhibit voltage-gated ion channels and are able to elicit action potentials (Ginsborg et al., 1991; Toselli et al., 1991; Toselli et al., 1996; Tosetti et al., 1998). For the TR14 cells no electrophysiological characterisation has been reported.

In the second part of this chapter cardiac myocyte layers cultured on the sensor surfaces will be discussed. First the signal shapes will be explained using the previous introduced extended *Point Contact Model* (see Chapter 5). With these cultures additional upside-down measurements were performed, where the cells were cultured on small glass and polystyrol pieces. For the recording the pieces were placed upside-down on the sensor, which provided interesting results for the coupling model.

In the last part of this chapter the potentialities of this cardiac myocyte-transistor hybrid system in terms of pharmaceutical application is shown. As a mimetic of ‘model heart’, the cell-transistor chip showed all typical responses to well-established heart stimulants and relaxants and the propagation velocity across the whole cell monolayer

⁽¹⁾ Institute of Physiological Chemistry and Pathobiochemistry, University of Mainz, Duesbergweg 6, D-55099 Mainz, Germany

⁽²⁾ CD-rats, Chales River GmbH, Sulzfeld.

can be determined. The hybrid-chip does not only provide the changes in beat frequency but also the changes of signal shapes in the present of pharmacological agents.

6.1 Sensor Preparation for Cell Cultures

Before the culturing of living cells on the sensor surfaces the EGE and FET arrays have to be cleaned and primed with biocompatible protein layers.

Cleaning of the sensors

The encapsulated sensors are very robust and can be used several times (> 20x) for culturing of cells. Mechanical cleaning of dead cell material is possible, but always cotton buds should be used for this procedure. Then the single cleaning steps were:

- Rinsing of the sensors with normal water
- Rinsing of the sensors with de-ionised (DE) water
- Ultrasonification for 10 min in 2 % detergent (Hellmanex II, Helma GmbH & Co. KG, Mühlheim, Germany)
- Rinsing with de-ionised (DE) water
- Rinsing with Milli-Q water
- Ultrasonification for 10 min in Milli-Q water
- Blow-drying of the sensors with dry N₂-gas flow
- Boiling of the cell culture containers with 20 % H₂SO₄ acid for 30 min at 80°C
- Rinsing with Milli-Q water
- Immersing the clean sensor arrays in 70 % Ethanol solution can do storage.

An intensive cleaning procedure for the sensors appeared to be crucial to having good cell culture conditions. It is very important that the main cleaning materials, the detergent solution and the H₂SO₄ acid, are completely washed off before the subsequent steps.

Surface modification of the extracellular sensor surfaces

The clean sensor surfaces were primed with different materials. The function of the materials is to make the SiO₂ surface biocompatible and to promote a close adherence of the cells on the surface. The closer the cells get to the sensor spot the lower sealing conductance g_J (Chapter 5) and a higher signal amplitude is thus possible. The different materials used for surface modification were:

- Fibronectin
- Laminin
- Nitro-Cellulose
- Poly-L-Lysin

Fibronectin, Laminin and Poly-L-Lysin are proteins from the extracellular matrix of cells. The proteins were all physisorbed on the surface. This was a much easier process than the chemical modification by functionalisation with aminosilane and further crosslinking of peptides described by Scholl (1999). During this work the physisorption was found to be sufficient for the cell experiments. The fundamental rule for the physisorption of these materials was 'as little as possible'. If a high concentration of these proteins is used, the cell development is good but thick layers of proteins are shielding the sensor spots of the devices and no recording can be achieved. The careful selection of the concentration used is thus important.

All steps for priming the sensors with the different materials were performed in a sterile box. The sensors were removed from the storage ethanol and rinsed two times with autoclaved Milli-Q water. The third rinsing step was done in PBS-Buffer (Dulbecco, GibcoBRL). The processing steps for each protein matrix were different:

Fibronectin:

The sensitive areas of the chips were plated with 20 μl (standard FET), 40 μl (backside FET), 80 μl (EGE) of 5 $\mu\text{g/ml}$ fibronectin solution. The sensors were then incubated for 60 min at 37°C in an atmosphere enriched with 5% CO₂. Following this incubation period, the fibronectin solution was removed and the surfaces were gently rinsed three times with PBS.

Laminin:

Laminin was used in different concentrations (5, 10, 15, 25 $\mu\text{g/ml}$) and plated in the same procedure as fibronectin. For the culturing of hippocampal neurons following procedure appeared to yield the best results (Scholl, 1999):

Laminin was reconstituted in PBS buffer at a concentration of 7.5 $\mu\text{g/ml}$. The sensors were incubated for more than 3 h once the whole culture containers of the sensors were filled. Afterwards the surfaces were rinsed three times with PBS buffer.

Poly-L-Lysin:

Poly-L-Lysin was the least used in this study. A concentration of 25 $\mu\text{g/ml}$ was chosen for use and it had similar results as those obtained from fibronectin treated surfaces.

Nitro-Cellulose:

The use of Nitro-Cellulose as un-specific cellular ‘adhesive agent’ is widespread in slice recordings on microelectrode sensors (MED64, 2000). The Nitro-Cellulose was dissolved in methanol at different concentrations (0.1, 0.25, 1, 2.5 mg/ml). The lowest concentration showed the best results. The priming procedure was easier than that of protein plating. The sensors were air dried in N₂-flow and plated with 20 µl (FETs) and 40 µl (EGE) of methanol/Nitro-Cellulose solution. After a few minutes, the methanol evaporated and thin cellulose coatings at the surface remained. The cellulose plating was exclusively used in cardiac myocyte cultures but gave the best results in terms of external signal amplitude.

6.2 Experiments with Single Neurons

The different cell types used in this work are discussed in terms of culturing, electrophysiological characterisation and cell-transistor coupling behaviour. In most of the coupling measurements the *voltage-clamp mode* was used. With some cell types external recordings in *current-clamp mode* were more successful.

Based on the results of previous works (Krause, 2000; Sprössler et al., 1999), further investigation into the specific ion conductivity of voltage-gated ion channels in the attached membrane of the cell was performed. The *voltage-clamp mode* is the best procedure to distinguish the influence of different ion channel types (Na⁺, K⁺, Ca²⁺) in the extracellular signal. With controlled stimulation of the cell from the basic holding potential of -90 mV to a distinctly higher membrane potential, it is possible to switch during an experiment between calcium, sodium or potassium activity.

6.2.1 Cell Lines

In this work the observation of the coupling behaviour of neuronal cell lines to external sensors was continued from some previously attempted cell lines. Initial work was performed using endothelial cells (EA.hy-926) and kidney cells (HEK) (Krause, 2000). It was subsequently switched to the neuroblastoma cell line SH-SY5Y (Krause, 2000), which were also used in the starting period of the experimental phase in the present study. Another neuroblastoma cell line TR14 was used, which showed higher voltage-gated ion currents over the membrane, but was more difficult in achieving usable culturing.

Both SH-SY5Y and TR14 cell lines showed ‘neuronal-like’ electrophysiological properties acting via voltage-gated K⁺- and Na⁺ channels. The strength of the ionic conductivities was about 2-3 times lower than that of primary cultured neuronal cells.

Morphologically, these cells have larger membrane diameters, which made them easier to attach the patch-clamp tips. In addition, the sealing properties within the transistor gates were enhanced as the cells had a higher probability of covering the whole gate structure.

6.2.1.1 Neuroblastoma Cell Line SH-SY5Y

The human neuronal cell line, SH-SY5Y⁽¹⁾, is a subclone dissected from carcinogen tissue of the un-cloned neuroblastoma line SK-N-SH in 1970 (Biedler et al., 1978). They exhibit the morphological and biochemical features of cells from the neural crest. Electrophysiological characterisations of the SH-SY5Y cells have been described (Ginsborg et al., 1991; Toselli et al., 1991; Toselli et al., 1996; Tosetti et al., 1998). The activities of the Na⁺-, K⁺- and Ca²⁺-channels and the ability of these cells to generate action potentials have been demonstrated (Johansson, 1994).

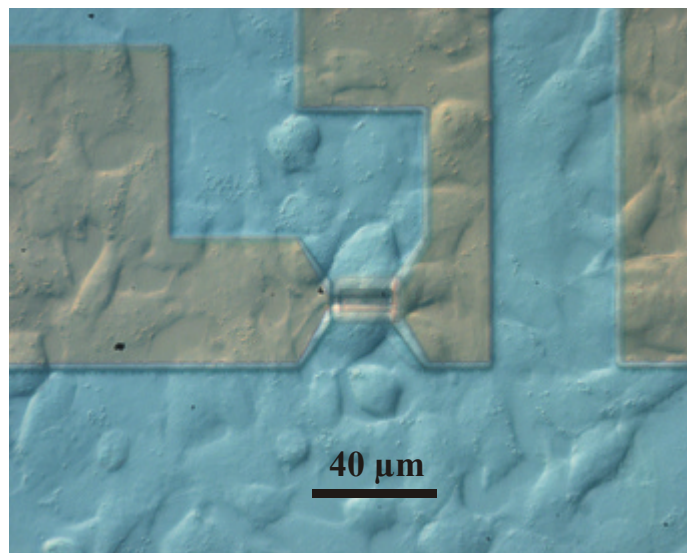


Figure 6-1 SH-SY5Y cells (3 DIV) on a FET surface. The scale bar indicates the size of the cells. In the middle part a single cell was closely attached to the gate of the device.

Cell culture⁽²⁾

The cells were grown as monolayers in cell-culturing flasks. The used culture medium DMEM/ HAMS F12 (GibcoBRL) contained in addition 200 mM Glutamax

⁽¹⁾ The SH-SY5Y cell line was a gift from the group of Prof. Maelike, Institute of Physiological Chemistry and Pathobiochemistry, University of Mainz, Duesbergweg 6, D-55099 Mainz, Germany.

⁽²⁾ The main culture steps were done by Manuela Hemmerlein and Anisa Kosan in the group of Prof. Maelike.

(GibcoBRL), 1 % penicillin/streptomycin solution (GibcoBRL), and 12.5 % foetal calf serum (FCS, GibcoBRL). For the culturing of the cells on the extracellular sensors the medium is sucked out of the flasks. The remaining cells in the flasks were washed with 0.02 % EDTA (GibcoBRL) containing PBS-buffer (Dulbeco, GibcoBRL). The cells were incubated (37°C / 5 % CO₂) in 0.25 % Trypsin Type III (Sigma) and 0.025 % EDTA containing PBS-buffer for 1-3 min. Adding standard culture medium stopped the trypsinisation and the cells were centrifuged at 370 rpm for 5 min. The resulting cell suspension was adjusted accordingly. Approximately 4,000-30,000 (FET) or 80,000-100,000 (EGE) cells were plated onto the precleaned and primed sensor surfaces (see Appendix C)).

Electrophysiological characterisation of the cells

The SH-SY5Y cells did not form a confluent layer. No functional synapses have been found in these cultures but the main advantage was that they were larger in size than primary cultured neurons (Figure 6-1).

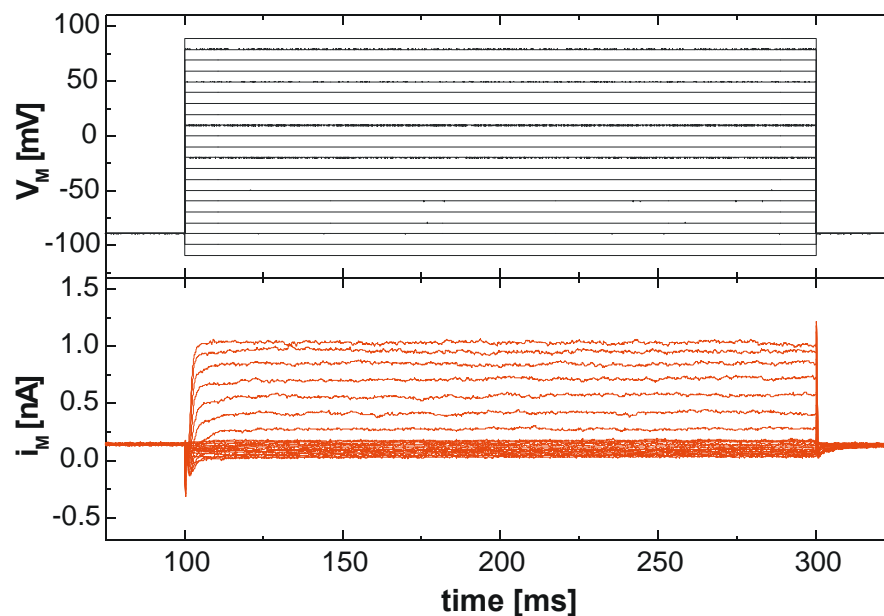


Figure 6-2 Voltage-clamp experiment with a SH-SY5Y cell (6 DIV, $V_{rest} = -30$ mV) on a laminin coated FET array. The cell showed a potassium current of 1 nA and a very weak sodium current of 0.16 nA.

In Figure 6-2 a voltage-clamp experiment with a SH-SY5Y cell is shown. It can be seen that the sodium current *is* much weaker than the potassium current, which *is* a typical characteristic of this cell-line (Krause, 2000; Toselli et al., 1996). A maximum sodium current of 1 nA has been reported. By scaling the whole-cell current with the calculated membrane surface (Eq. 5.10 and the C_{slow} value of the experiment) the

specific ion conductivity can be calculated. In Figure 6-3 a closer view to the initial period of the stimulation pulse and the respective membrane conductance for Na^+ and K^+ as functions the membrane voltage V_M is shown. Typical for this cell-line is the delayed sodium current, which normally starts in neuronal cells at membrane potentials higher than -30 mV.

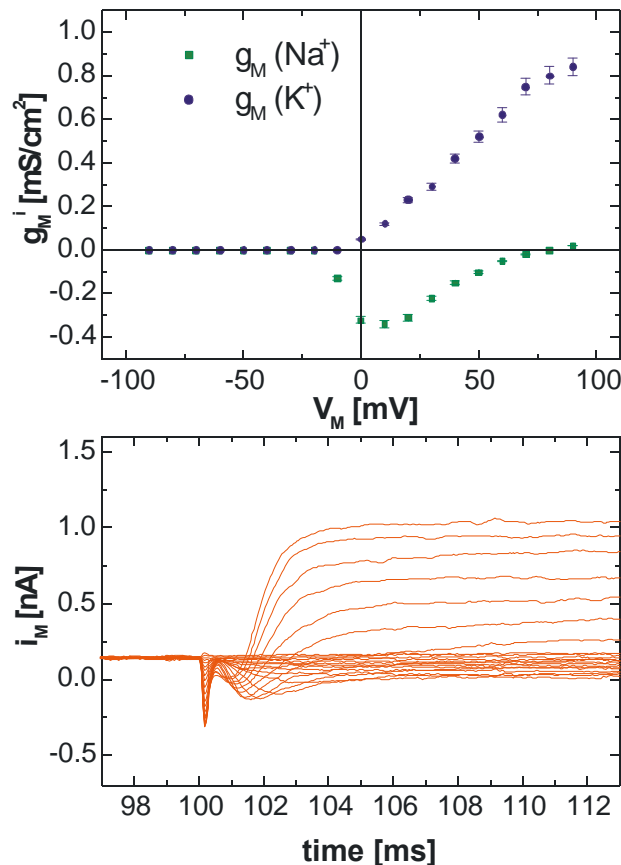


Figure 6-3 Closer view to the initial period of the stimulation pulse (lower plot) and the respective membrane conductance for Na^+ and K^+ as function of V_M .

In Figure 6-4 an action potential of a SH-SY5Y cell is shown. The fast uprising of the action potential (indicated by a steeper rising flank than that of the capacitive loading curve caused by the current stimulation pulse), which is a result of the opening of the sodium channels, is at $V_M = -10$ mV. However, in this case, the sodium channel activities are slow and somewhat delayed.

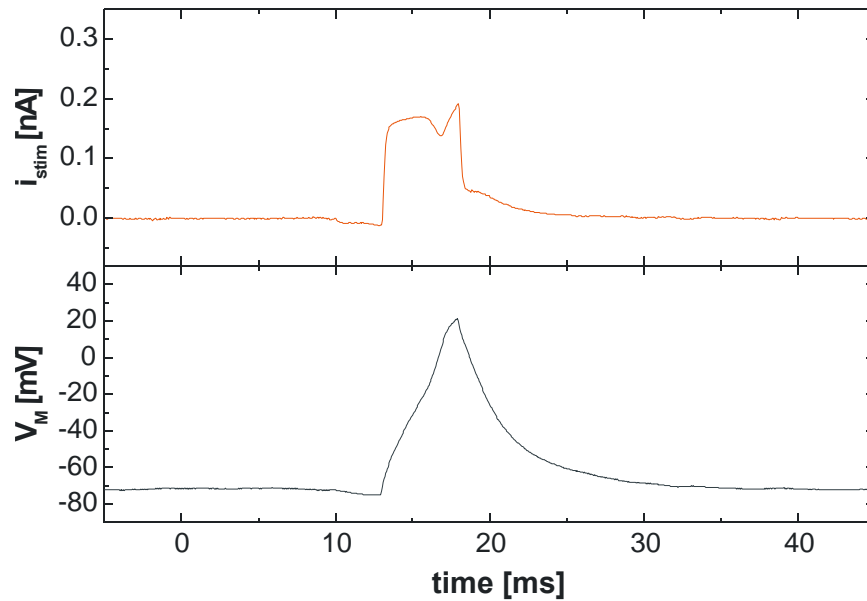


Figure 6-4 Action potential of a SH-SY5Y cell (2 DIV). The cell was clamped in *current-clamp mode* to -70 mV. A current pulse of 0.15 nA stimulates an action potential.

Voltage-clamp coupling experiments

The characterisation of the SH-SY5Y cell using a voltage-clamp coupling measurement is shown in Figure 6-3. The cell was stimulated from an initial holding potential of -90 mV to -30 , $+10$, $+40$, and $+80$ mV, respectively. The cell-pipette assembly was compensated before each measurement and the extracellular response obtained was the result of 135 averages. In Figure 6-5 it can be seen that the values from the PSPICE fits are matching perfectly with the capacitive response at the beginning of the stimulation pulse, whereas the total potassium current is underestimated.

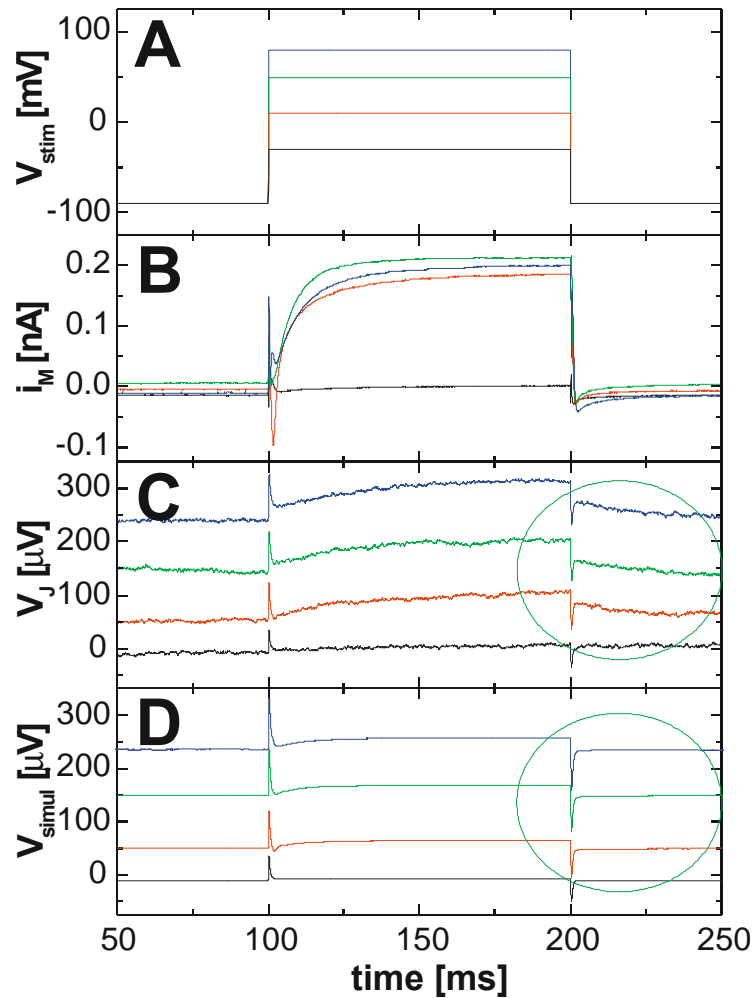


Figure 6-5 Four step voltage-clamp coupling experiment with the SH-SY5Y cell characterised in Figure 6-3. At the end of the traces (circled area) the simulated PSPICE data (plot D) are not matching the extracellular response (plot C).

In the coupling experiment in Figure 6-5 it can be seen that the cell was highly stressed during the measurements. Especially the current response to the highest stimulus pulse showed a weaker whole-cell current than the stimulation experiment. Although the cell was dying slowly, the capacitive extracellular response was simulated perfectly. In Figure 6-6 a detailed view of the fitted data is shown.

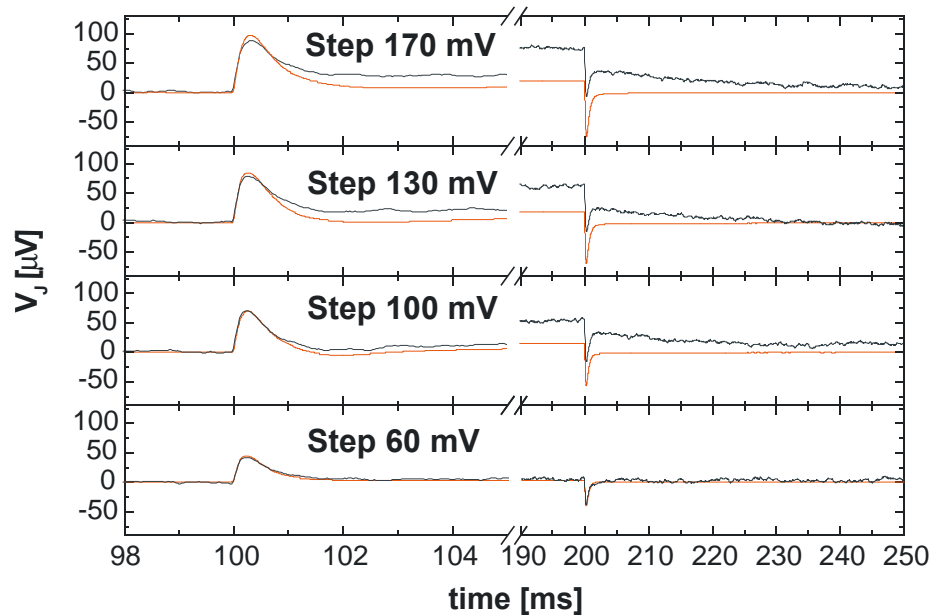


Figure 6-6 Closer look to the fitted PSPICE data. The respective capacitive response at the beginning of the stimulation pulses was modelled nicely, whereas the slow decays at the end of the responses are not matching.

<i>Voltage-clamp coupling</i>	Patch-Clamp	Step 60 mV	Step 100 mV	Step 130 mV	Step 170 mV
Chip: n-channel ($V_{DS} = 3V$, $V_{GS} = 1.8V$) $g_m = 1.15$ mS; Gatesize: $2 \times 16 \mu\text{m}^2$ Fibronectin coated	$V_{rest} =$ -22 mV	$C_{slow} =$ 6.8 pF $R_M =$ 2.5 G Ω $i_M^L =$ 51.5 pA $G_L = 1.2$ nS	$C_{slow} =$ 6.2 pF $R_M =$ 5.9 G Ω $i_M^L =$ 27.7 pA $G_L = 1.2$ nS	$C_{slow} =$ 5.4 pF $R_M =$ 60.7 G Ω $i_M^L =$ 51.3 pA $G_L = 1.9$ nS	$C_{slow} =$ 5 pF $R_M =$ 11.8 G Ω $i_M^L =$ 22.5 pA $G_L = 1.5$ nS
Date: 25.05.00 Files: Si991207.011 / 13 15 / 17 (averaged 135 x)	$C_{fast} =$ 6.75 pF	$R_J =$ 673333 Ω $R_S = 40.4$ M Ω	$R_J =$ 731422 Ω $R_S = 51.4$ M Ω	$R_J =$ 846434 Ω $R_S = 70.5$ M Ω	$R_J =$ 900164 Ω $R_S = 94.2$ M Ω
10 % attached Cell: SH-SY5Y (6 DIV)		$g_J = 2.16$ S/cm ² $A_M =$ $6.88 \cdot 10^{-10}$ m ² $r_{cell} = 7.4$ μm	$g_J = 2.16$ S/cm ² $A_M =$ $6.34 \cdot 10^{-10}$ m ² $r_{cell} = 7.1$ μm	$g_J = 2.16$ S/cm ² $A_M =$ $5.47 \cdot 10^{-10}$ m ² $r_{cell} = 6.6$ μm	$g_J = 2.16$ S/cm ² $A_M =$ $5.15 \cdot 10^{-10}$ m ² $r_{cell} = 6.4$ μm

Table 6.1: Values for the simulation the voltage-clamp coupling experiment (4-step protocol) using a SH-SY5Y cell (Figure 6-5). The cell-pipette assembly was compensated before each measurement.

6.2.1.2 Neuroblastoma Cell Line TR14

The neuronal cell line TR14⁽¹⁾ exhibits the morphological and biochemical features of cells from the neural crest. Electrophysiological characterisations have not been reported to date. The existence of voltage-gated Na⁺-, and K⁺-channels were shown. These cells were also able to elicit action potentials.

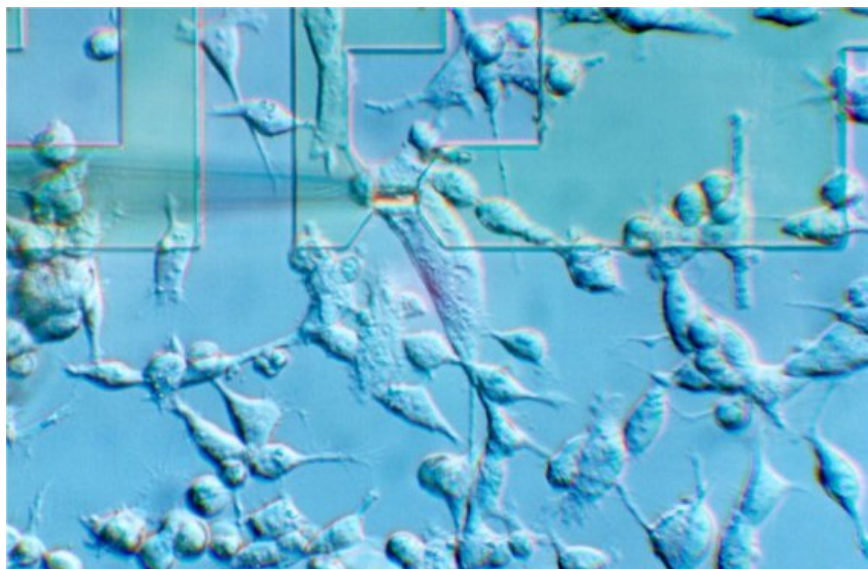


Figure 6-7 TR14 cells (4 DIV) on a FET surface. The cells exhibit the morphology of neurons with a slightly elongated structure. For the axon-like structures no synaptic formations have been reported in literature. In the middle part a single cell was closely attached to the gate of the device. The shadow from the left side is caused by a patch-pipette closely maneuvered on top of the cells.

Cell culture⁽²⁾

The cells were grown as monolayers in cell-culturing flasks. The procedures were very similar to those used in culturing SH-SY5Y cells. The culture medium contained: DMEM/ HAMS F12 (GibcoBRL), 200 mM Glutamax (GibcoBRL), 1 % penicillin/streptomycin solution (GibcoBRL), and 16 % foetal calf serum (, GibcoBRL) Approximately 4,000-20,000 (FET) or 60,000-80,000 (EGE) cells were plated onto the precleaned and primed sensor surfaces (see Appendix C)).

⁽¹⁾ The TR14 cell line was a gift from the group of Prof. Maelike, Institute of Physiological Chemistry and Pathobiochemistry, University of Mainz, Duesbergweg 6, D-55099 Mainz, Germany

⁽²⁾ The main culture steps were done by Anisa Kosan in of the group of Prof. Maelike.

Electrophysiological characterisation of the cells

The TR14 cells did not form a confluent layer. They were not able to form synapses, although there are outwardly growing axonal-like structures, which are forming contacts with each other. The cells were slightly larger in size than the primary cultured neurons (Figure 6-7), which made attachment in the patch-clamp experiments. Mainly cells that were not attached to sensitive spots of the sensor were chosen for characterisations. In Figure 6-8 a voltage-clamp experiment with a TR14 cell (2 DIV) is shown. At the beginning of the potassium responses an A-Type potassium-like overshoot of the current signal can be seen.

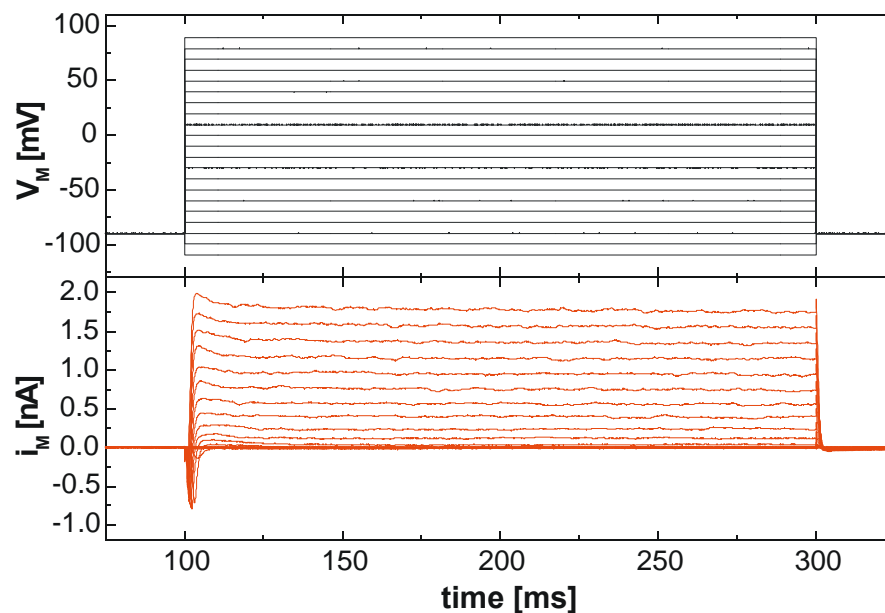


Figure 6-8 Voltage-clamp experiment with a TR14 cell (2 DIV, $V_{rest} = -38$ mV) on a fibronectin coated FET array.

The cell was able to elicit an action potential, which is shown in Figure 6-9. It was clamped at a holding potential of $V_{hold} = -80$ mV.

A stimulation pulse of $i_{stim} = 0.15$ nA depolarised the cell. The action potential is slower than the action potentials observed with hippocampal and brainstem slice neurons (see below). The repolarisation needs more than 30 ms. The TR14 cells were characterised electrophysiologically between 2 DIV and 8 DIV. In Figure 6-10 the statistical data can be seen. Between 4 DIV and 5 DIV the cell revealed the highest sodium currents and the lowest resting potentials. The strongest potassium currents were observed at 5 DIV with the strongest A-Type-like overshoot.

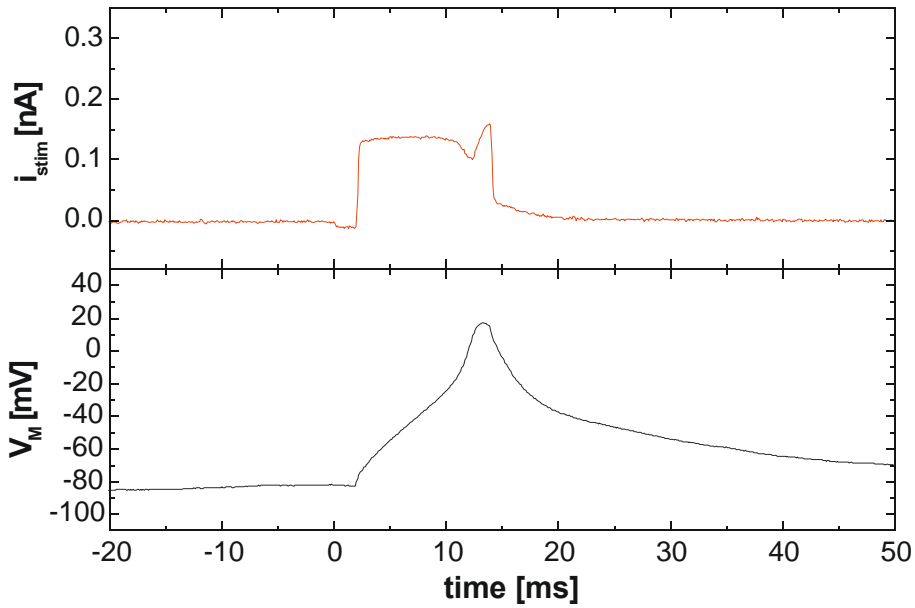


Figure 6-9 Action potential of the TR14 cell characterised in Figure 6-8.

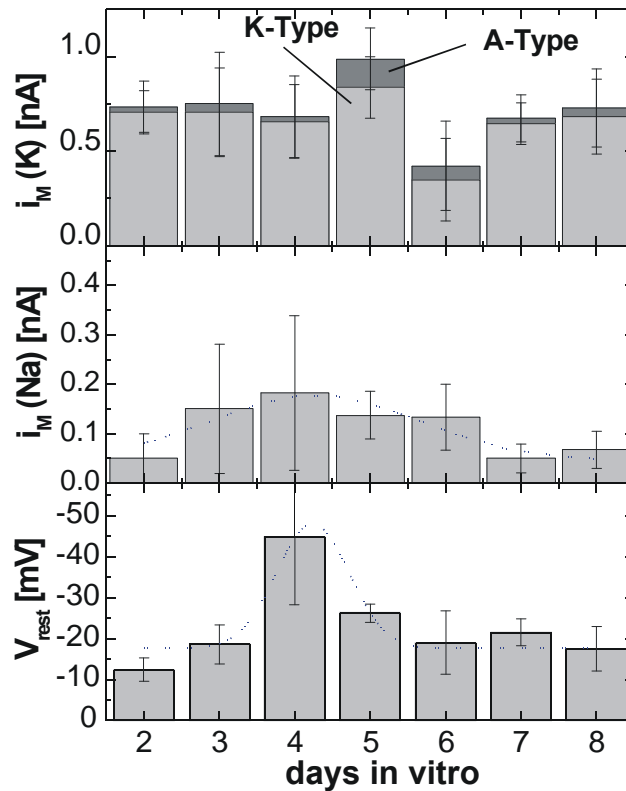


Figure 6-10 Statistical data of the TR14 culture. In the lower plot the resting potential is shown. In the middle plot the strenght of the sodium current is plotted and in the upper plot the potassium current with the potassium A-Type current on top can be seen. For this plot $n = 38$ cells were electrophysiologically characterised.

Therefore, on days 4 and 5 the coupling experiments were performed (see below). In Figure 6-11 the ion-conductances calculated are plotted with a closer view to the initial period of the stimulation pulse and the respective membrane conductance for Na^+ and K^+ as function of the membrane voltage V_M . The radius of the cell was calculated with Eq. 5.10 to $r = 11.3 \mu\text{m}$.

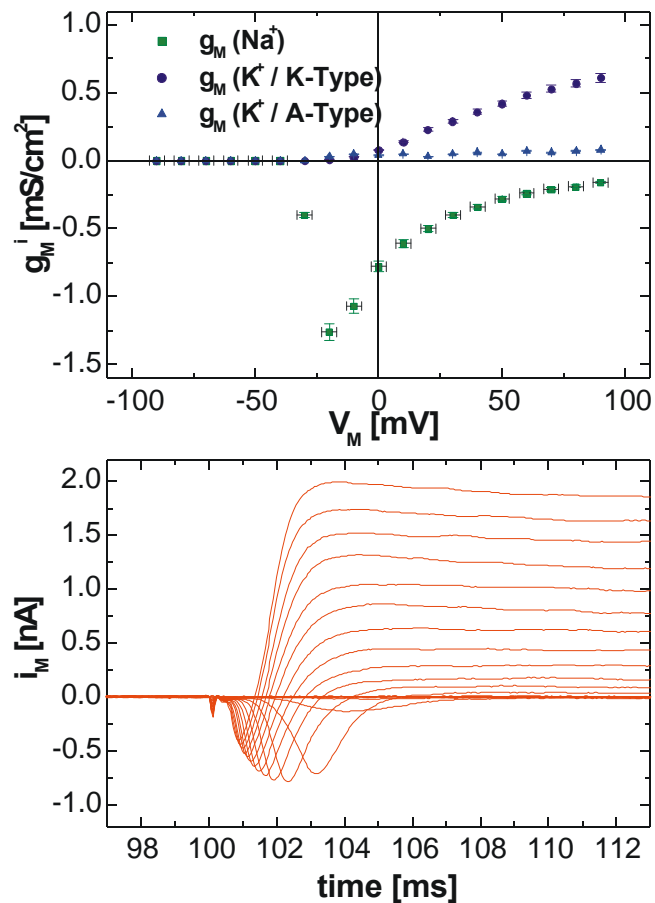


Figure 6-11 Ion conductances of the TR14 cell (2 DIV) characterised in Figure 6-8.

It can be seen that the sodium conductance is not crossing the zero line, which would mean that the sodium influx is converted into a sodium efflux. This effect is normally observed for primary cultured neurons at $V_M = +60 \text{ mV}$.

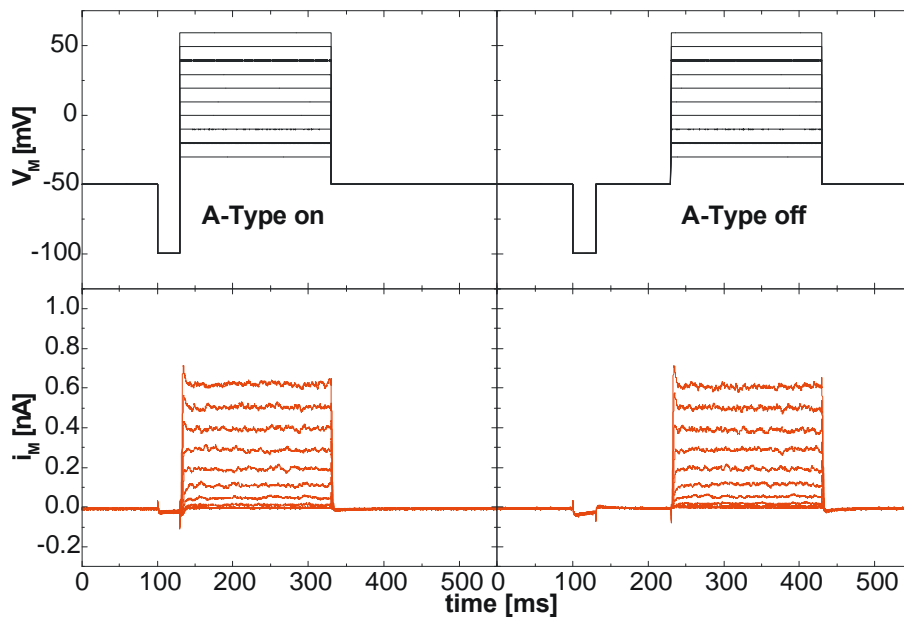


Figure 6-12 Electrophysiological protocol for the on- and off-switch of the potassium A-type current (Storm, 1990).

In Figure 6-12 a special electrophysiological protocol for the further investigation of the A-type-like potassium overshoot of the TR14 cells was adapted. The negative prepulse should be able to switch the A-type channels off, only if a break of 100 ms lies between the prepulse and the stimulation steps (Storm, 1990). This indicates that the TR14 cell line has some major differences in their electrical characteristics to typical primary cultured neurons (see below). The differences are not only a weaker current strength over the membrane (about a factor of 4) but also sodium channels, which are not behaving like sodium channels in primary cultured neurons.

Voltage-clamp coupling experiments

With the TR14 cells many voltage-clamp coupling measurement were performed. The recorded signals were categorised in three main types, called A-, B-, or C-Type coupling (Krause, 2000). In the first two categories only the passive components of the cell-transistor circuitry are contributing to the extracellular signal. The C-Type is a high channel conductance coupling, where active currents caused by the cell, are recorded extracellularly. The A-Type was the case, when only the capacitive peaks were monitored, and the B-Type reflected the signal shape of the rectangular stimulation pulse. In most cases, both of the passive types are mixed, which was called AB-Type.

AB-Type:

During the simulation with PSICE it appeared that the two passive types are both caused by the rectangular stimulation pulse. They are strongly dependent on the R_{JM}

resistor in the attached membrane. If it is very large, only the capacitive transients are influencing the voltage at the transistor gate.

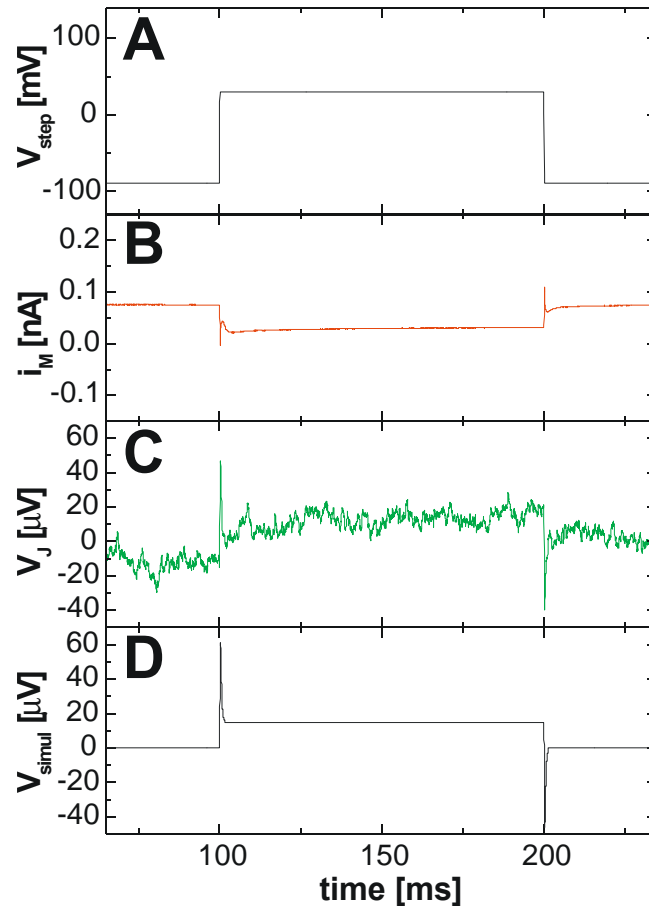


Figure 6-13 AB-Type coupling with a TR14 cell. The cell was partly destroyed during the patch-clamp experiment (indicated by a small C_{slow} and a high G_L value). The cell-pipette assembly was good compensated as nearly no effective current signal was monitored by the patch-clamp amplifier (trace B). The extracellular signal (trace C) reflects an ohmic and capacitive response to the rectangular stimulation pulse (trace A).

If the resistance is smaller, a certain current is flowing into the point contact. The voltage drop caused by this current over the junction resistance R_J is then monitored by the FET as rectangular voltage pulse.

In Figure 6-13 a so-called AB-Type coupling with a TR14 cell is shown. The cell membrane was partly ruptured during the patch-clamp experiment. The simulation data are given in Table 6.2.

Upon further analysis of the simulated PSPICE data in Figure 6-14 it can be seen that the extracellular response is accurately modelled. The respective capacitive response and the ohmic part of the stimulation pulse are producing the extracellular signal shape.

<i>Voltage-clamp coupling</i>	Patch-Clamp	Step 120 mV
Chip: n-channel 025321 ($V_{DS} = 3V$, $V_{GS} = 0V$) $g_m = 0.5$ mS; Gatesize: $2 \times 16 \mu\text{m}^2$ Fibronectin coated	$V_{rest} = -3$ mV $C_{slow} = 2.21$ pF $G_L = 8.06$ nS	$R_M = 1.01$ G Ω $i_M^L = -37.81$ pA $R_S = 112.1$ M Ω
Date: 14.01.00 File: Si00011415 (averaged 135 x)	$C_{fast} = 6.97$ pF	$R_J = 1307833.3$ Ω $g_J = 3.45$ S/cm 2
10 % attached Cell: TR14 (5 DIV)	$r_{cell} = 4.2$ μm	$A_M = 2.22 \cdot 10^{-10}$ m 2

Table 6.2: Values for the simulation of the AB-Type voltage-clamp coupling experiment using a TR14 cell (Figure 6-13).

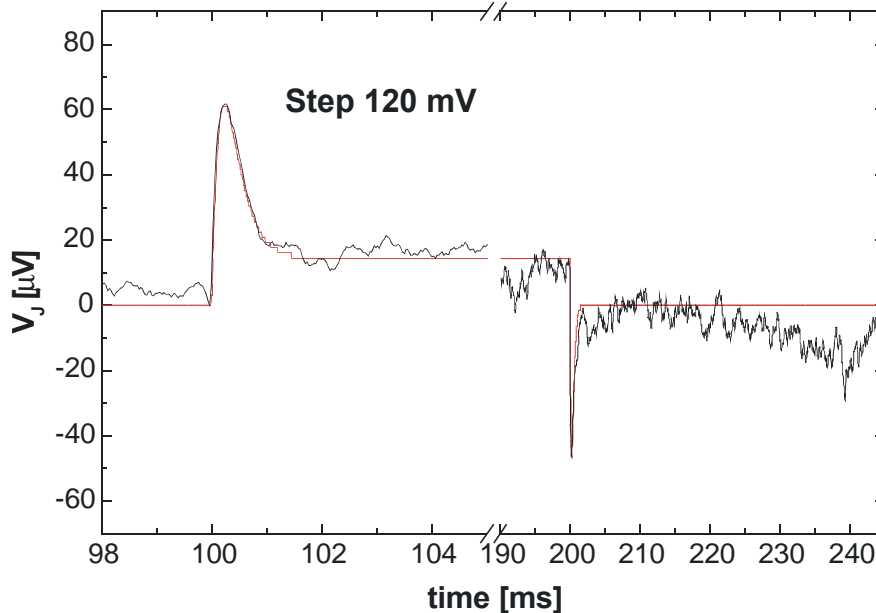


Figure 6-14 Closer look to the fitted PSPICE data of the AB-type coupling. The respective capacitive response and the ohmic part of the stimulation pulse was modelled nicely.

The B-type reflects the case when the amplitude of the voltage step caused by the ohmic part of the AB-Type signal is larger than the tip height of the capacitive responses.

B-Type:

In the called B-Type coupling when the extracellular signal is composed mainly of the ohmic coupling of the stimulation pulse. In Figure 6-15 a TR14 cell was attached to the gate of an n-channel transistor. The values used for the simulation of the extracellular signal are shown in Table 6.3.

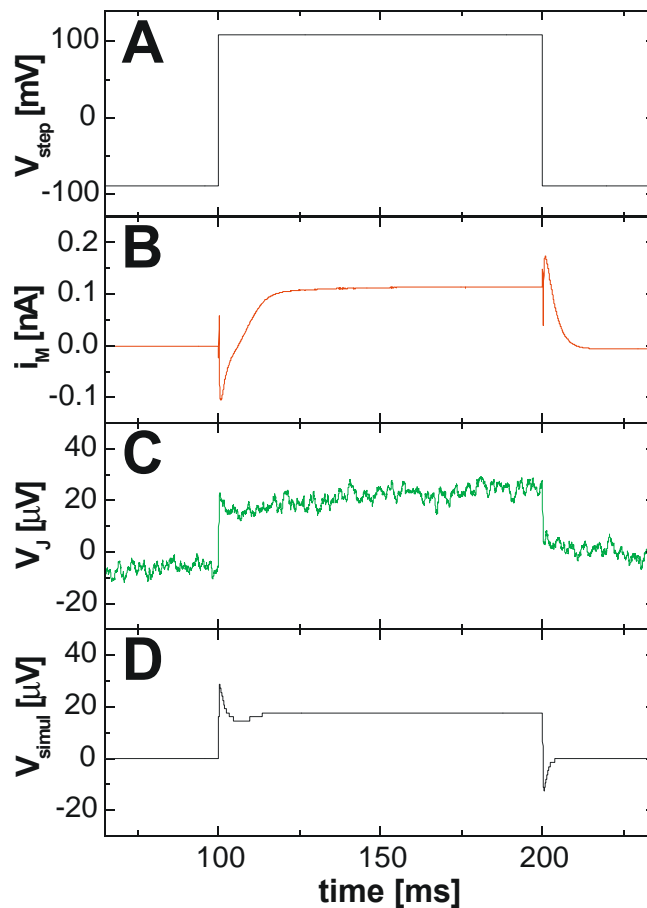


Figure 6-15 B-Type coupling with a TR14 cell.

The patch-clamp amplifier monitors a potassium signal (trace B), whereas the extracellular signal shape reflects a voltage drop of the ohmic current over R_{JM} caused by the stimulation pulse. A closer view to the coupled signal shows that the shape of the capacitive part is precisely modelled, but the ohmic part was slightly underestimated.

<i>Voltage-clamp coupling</i>	Patch-Clamp	Step 200 mV
Chip: n-channel 116321 ($V_{DS} = 3V$, $V_{GS} = 1.5V$) $g_m = 1.05$ mS; Gatesize: $2 \times 16 \mu\text{m}^2$ Laminin coated	$V_{rest} = -22$ mV $C_{slow} = 7.76$ pF $G_L = 5.5$ nS	$R_M = 1.94$ G Ω $i_M^L = 98.46$ pA $R_S = 319$ M Ω
Date: 03.03.00 File: Si00030306 (averaged 135 x)	$C_{fast} = 6.96$ pF	$R_J = 446600$ Ω $g_J = 2.86$ S/cm²
10 % attached Cell: TR14 (4 DIV)	$r_{cell} = 7.9$ μm	$A_M = 7.84 \cdot 10^{-10}$ m ²

Table 6.3: Values for the simulation of the B-Type voltage-clamp coupling experiment using a TR14 cell (Figure 6-15).

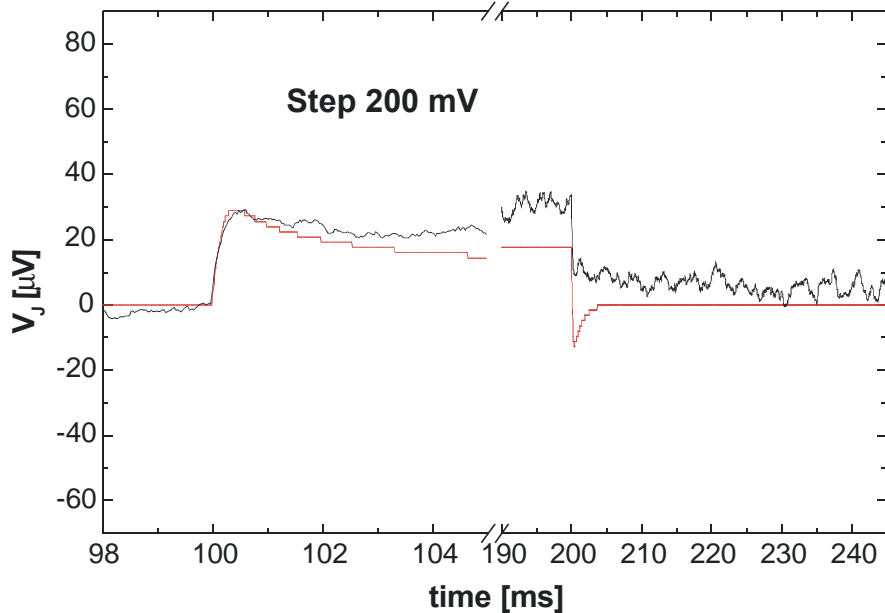


Figure 6-16. Closer view to the simulated extracellular signal simulated with PSPICE.

C-Type:

In the third category, the stimulation pulse and the passive elements of the electrical circuit do not only produce the extracellular signal shape. The active current of the cells is causing a voltage drop at the seal resistor R_J and contributing to the total signal shape monitored by the transistor. In the first part, a weak sodium current of a TR14 cell was recorded in a voltage-clamp coupling experiment.

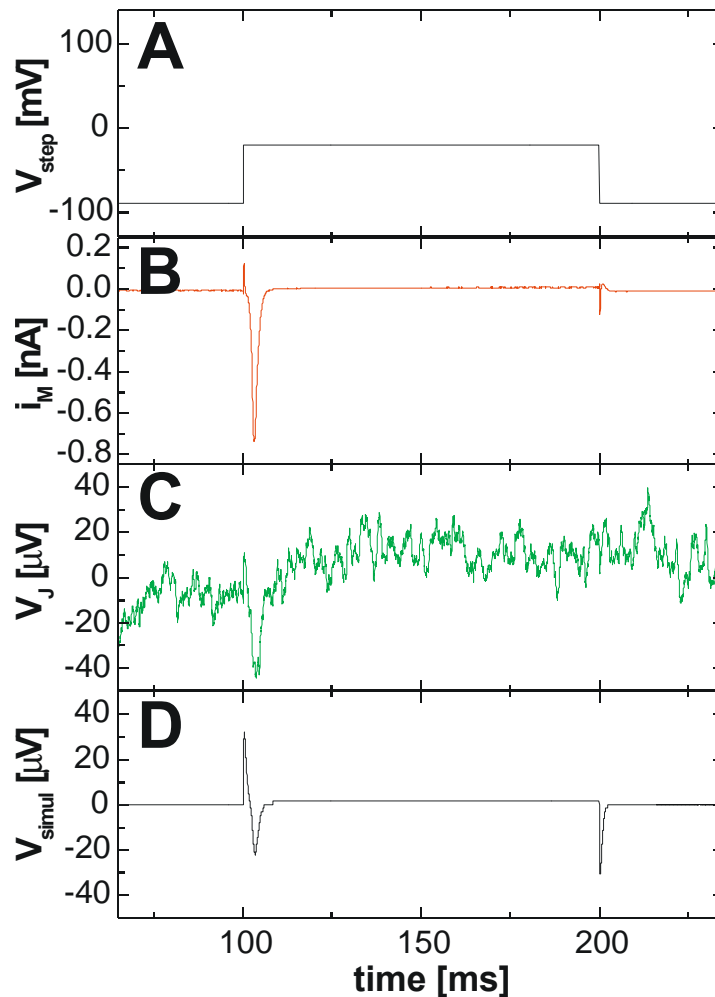


Figure 6-17 C-Type coupling of a sodium current caused by a TR14 cell.

A stimulation step of $V_{step} = 70$ mV caused a relative high sodium current of 0.75 nA. The simulation data used for these measurements are given in Table 6.4. The fitted data in Figure 6-18 shows that the capacitive transients caused by the stimulation pulse are vanishing in the relatively high noise level of 30 μ V.

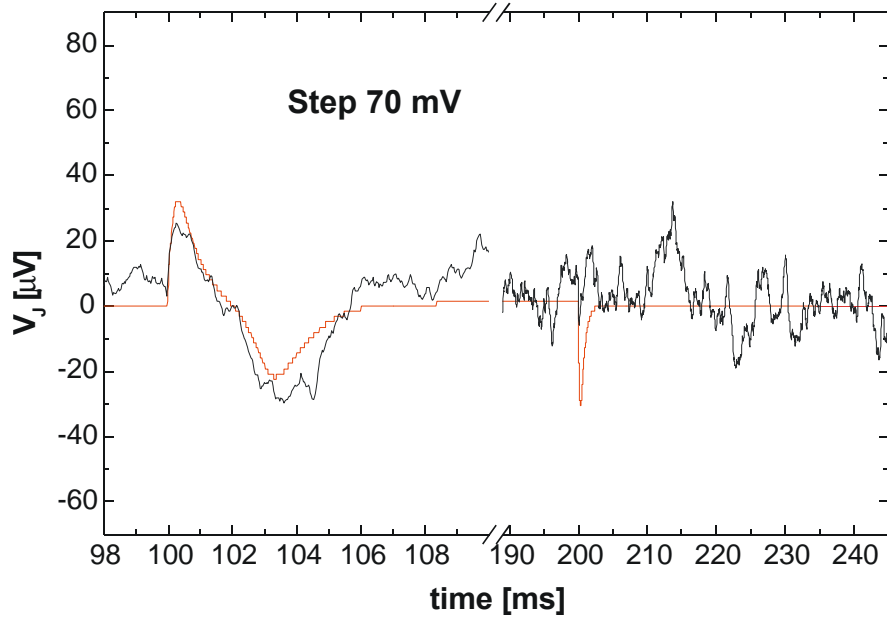


Figure 6-18 Closer look to the simulated data of the C-Type signal in Figure 6-17. The capacitive transients are vanishing inside of the relatively high noise level.

<i>Voltage-clamp coupling</i>	Patch-Clamp	Step 70 mV
Chip: p-channel 544221 ($V_{DS} = -3V$, $V_{GS} = -2V$) $g_m = 0.55$ mS; Gatesize: $2 \times 16 \mu\text{m}^2$ Fibronectin coated	$V_{rest} = -65$ mV $C_{slow} = 13.44$ pF $G_L = 0.13$ nS	$R_M = 12.34$ G Ω $i_M^L = -5$ pA $R_S = 47.3$ M Ω
Date: 02.03.00 File: Si00030201 (averaged 135 x)	$C_{fast} = 6.75$ pF	$R_J = 337857.1$ Ω $g_J = 2.18$ S/cm²
10 % attached Cell: TR14 (4 DIV)	$r_{cell} = 10.4$ μm	$A_M = 1.36 \cdot 10^{-9}$ m ²

Table 6.4: Values for the simulation of the B-Type voltage-clamp coupling experiment using a TR14 cell (Figure 6-15).

In the next part, a series of potassium currents were extracellularly recorded. Again, the slow decay at the end of the stimulation pulses cannot be simulated in the standard *Point Contact Model*. The responses to the stimulation pulses of 50 and 100 mV are well modelled. The potassium currents in the cell transistor cleft of the higher responses to 150 and 200 mV would have to be scaled by factors of 2.6 and 4, respectively.

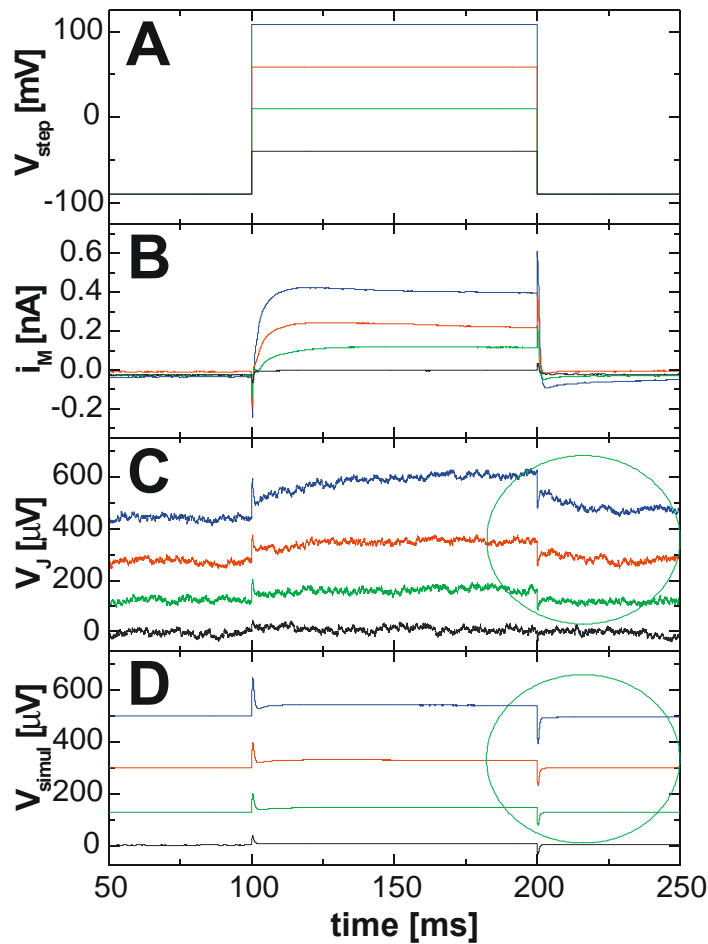


Figure 6-19 Voltage-clamp coupling experiment with a TR14 cell (8 DIV).

In Table 6.5 the simulation values for this coupling measurement are given.

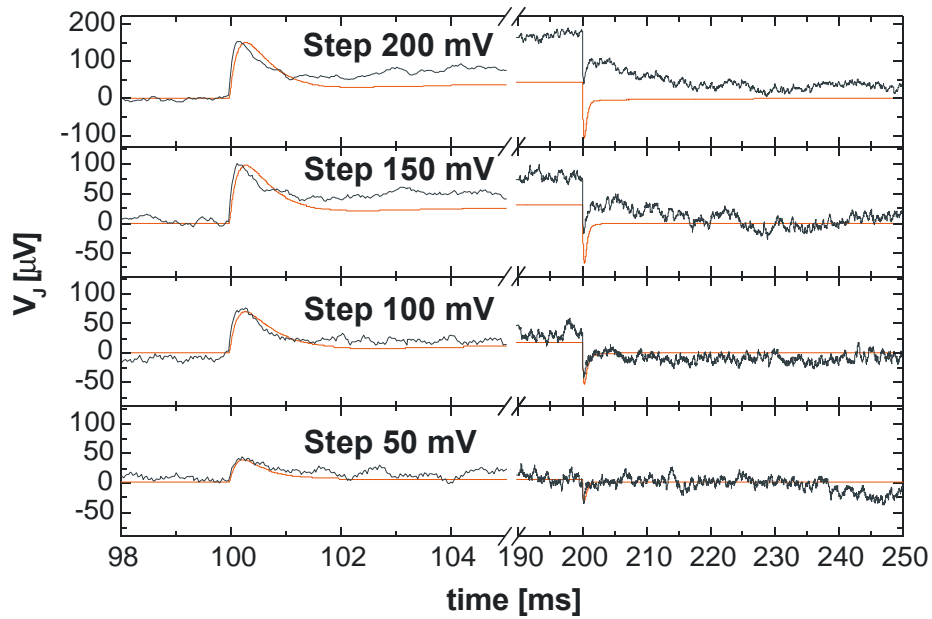


Figure 6-20 Closer view to the fitted data out of the coupling experiment in Figure 6-19.

Voltage-clamp coupling	Patch-Clamp	Step 50 mV	Step 100 mV	Step 150 mV	Step 200 mV
Chip: p-channel ($V_{DS} = -3V$, $V_{GS} = -2.5V$) $g_m = 0.45$ mS; Gatesize: $2 \times 16 \mu\text{m}^2$ Laminin coated	$V_{rest} =$ -40 mV	$C_{slow} =$ 8.542 pF $R_M =$ 2.82 G Ω $i_M^L =$ 8.97 pA $G_L = 3.13$ nS	$C_{slow} =$ 8.542 pF $R_M =$ 0.624 G Ω $i_M^L =$ -72 pA $G_L = 3.13$ nS	$C_{slow} =$ 8.781 pF $R_M =$ 0.607 G Ω $i_M^L =$ -18.26 pA $G_L = 2.68$ nS	$C_{slow} =$ 4.739 pF $R_M =$ 1.11 G Ω $i_M^L =$ -44.86 pA $G_L = 7.15$ nS
Date: 23.03.00 Files: Si000323.024 / 26 28 / 30 (averaged 135 x)	$C_{fast} =$ 6.61 pF	$R_J =$ 800800 Ω $R_S = 57.2$ M Ω	$R_J =$ 800800 Ω $R_S = 57.2$ M Ω	$R_J =$ 701578 Ω $R_S = 56.1$ M Ω	$R_J =$ 1407504 Ω $R_S = 85.2$ M Ω
10 % attached Cell: SH-SY5Y (8 DIV)		$g_J = 1.47$ S/cm 2 $A_M =$ $8.66 \cdot 10^{-10}$ m 2 $r_{cell} = 8.3$ μm	$g_J = 1.47$ S/cm 2 $A_M =$ $8.66 \cdot 10^{-10}$ m 2 $r_{cell} = 8.3$ μm	$g_J = 1.47$ S/cm 2 $A_M =$ $8.66 \cdot 10^{-10}$ m 2 $r_{cell} = 8.3$ μm	$g_J = 1.47$ S/cm 2 $A_M =$ $4.83 \cdot 10^{-10}$ m 2 $r_{cell} = 6.2$ μm

Table 6.5: Values for the simulation the voltage-clamp coupling experiment (4-step protocol) using a SH-SY5Y cell (Figure 6-19). The cell-pipette assembly was compensated before each measurement.

Current-clamp coupling experiments

A cell-transistor coupling in the current-clamp mode was found to be much more complicated than the voltage-clamp coupling (see paragraph 5.2). Here a similar categorisation than in the voltage-clamp coupling is usual. The A-Type extracellular signal reflects the first derivative of the action potential and the B-Type signal an ohmic coupling. This extracellular signal has the same shape than the action potential itself. In the C-Type, coupling different ion currents (K^+ and Na^+ for neurons) are influencing the signal shape. With the TR14 cell several coupling measurements in current-clamp mode were successful, all reflecting the ohmic B-Type coupling. In Figure 6-21 such a coupled action potential is shown.

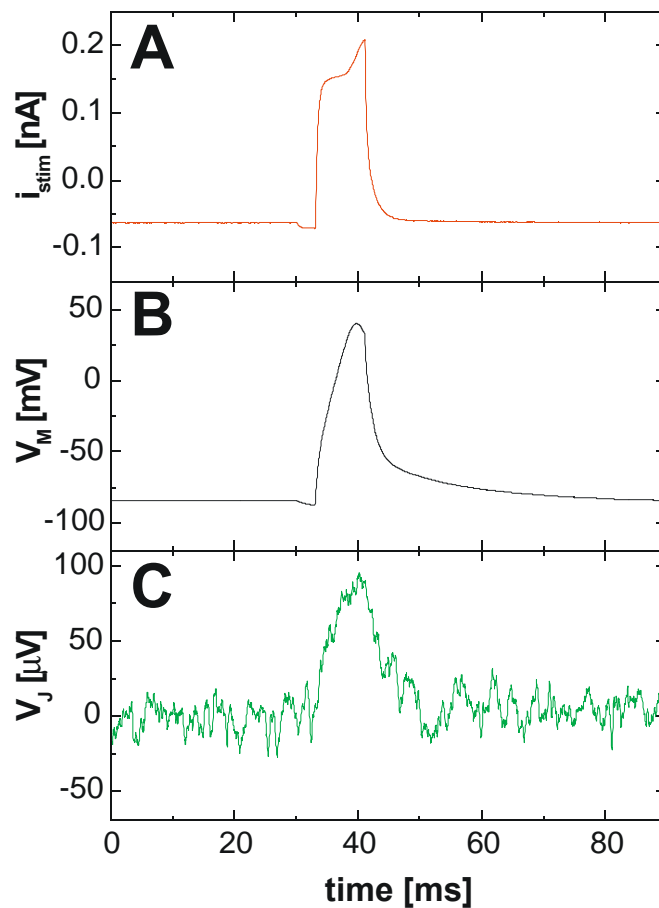


Figure 6-21 Action potential of a TR14 cell extracellularly recorded in the Current-clamp mode. The signal (trace C) was averaged 40 times.

6.2.2 Primary Cultured Neurons

The main advantage of primary cultured cells is that they are completely differentiated, which means that they are fully expressed (in most cases) and are already fulfilling their normal physiological functions. After they are cultured on the extracellular sensors, they continue their activity in this artificial surrounding like signal processing. In addition the observed ionic currents over the cell membrane were 2-5 times higher than in the cell-line cultures.

6.2.2.1 Dissociated Neurons of the Neocortex

The dissociated cortical neuronal culture was the most un-specific one, but had the best yield. One culture alone (approximately 5-8 embryonic, E15-19, rat brains) can provide enough cells to plate several hundred FET devices.

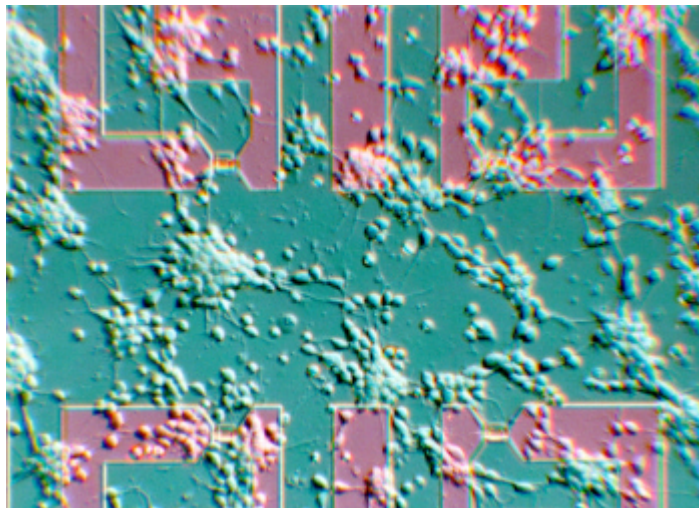


Figure 6-22 Dissociated cortical neurones cultured on the surface of a FET sensor.

Cell culture^[1]

Embryonic rat brains were removed and placed in ice-cold sterile HBSS. These tissues were placed in 0.25 % trypsin and incubated at 37°C / 5 % CO₂ enriched atmosphere for 8 minutes. The tissues were then transferred to a 15 ml centrifuge tube containing 2 ml neurobasal medium (supplemented with 2 % B27). The trypsinisation was halted by washing the cells with 2 ml of neurobasal medium 5 times at 5 min intervals and was then mechanically broken up to cell suspension by gentle trituration.

^[1] The cell culture of the cortical neurons was done by Dr. Chi-Kong Yeung.

The resulting cell suspension was counted and adjusted to $1 \cdot 10^6$ cells/ml. The total number of cells plated on the devices was 10-20,000 (FETs) and 20-40,000 (EGEs), respectively.

Electrophysiological characterisation of the cells

With the cortical neuron culture only a few experiments were done. In Figure 6-23 a voltage-clamp characterisation experiment with a cortical neuron is shown.

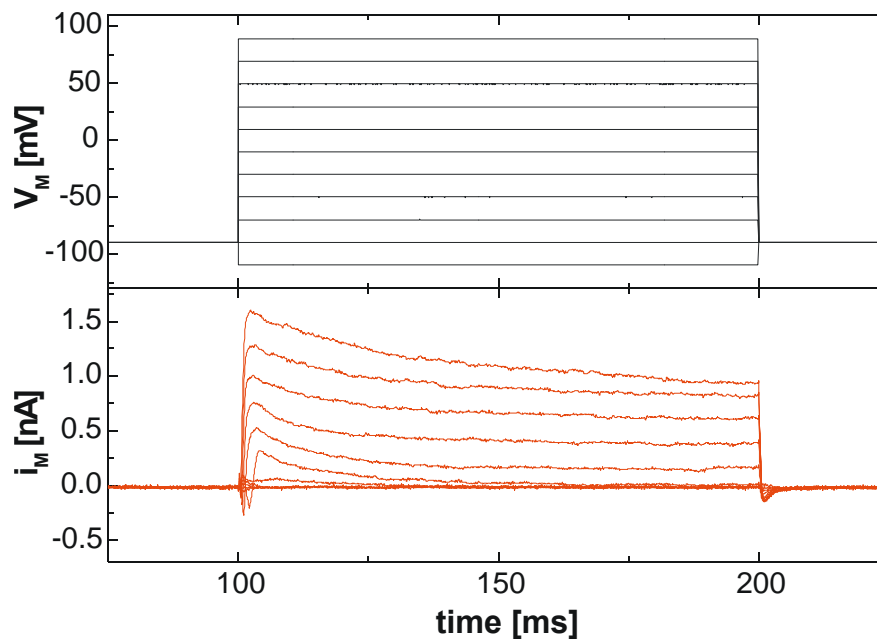


Figure 6-23 Voltage-clamp experiment with a neuronal cell from the neocortex (2 DIV). The potassium A-Type current was very pronounced in this cell experiment.

Here the potassium A-Type current is very pronounced. An action potential (Figure 6-24) of such a neuron is much faster than an action potential of cells from cell lines. The values for this patch-clamp experiment were $R_S = 48.3 \text{ M}\Omega$, $G_L = 0.17 \text{ nS}$ and $C_{slow} = 5.35 \text{ pF}$. With this capacitance value the radius of the cell was calculated to $r_{cell} = 6.6 \text{ }\mu\text{m}$, which leads to a membrane surface of $A_M = 5.39 \cdot 10^{-10} \text{ m}^2$.

With this membrane surface the specific ion conductances of the neuron can be calculated (Figure 6-25). The A-Type conductance is plotted as overshoot current $i_{over} = i_{K-A-type} - i_{K-K-type}$.

With the cortical neurons only a few voltage-clamp coupling experiments were done. All responses were passive (B-Type, see above) and are not shown here.

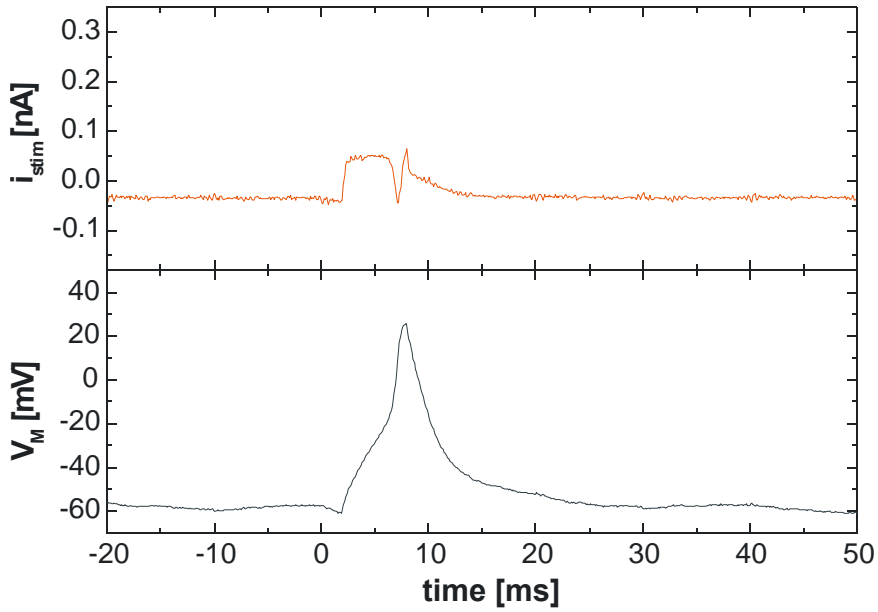


Figure 6-24 Action potential of a cortical neuron stimulated by $i_{stim} = 0.1$ nA.

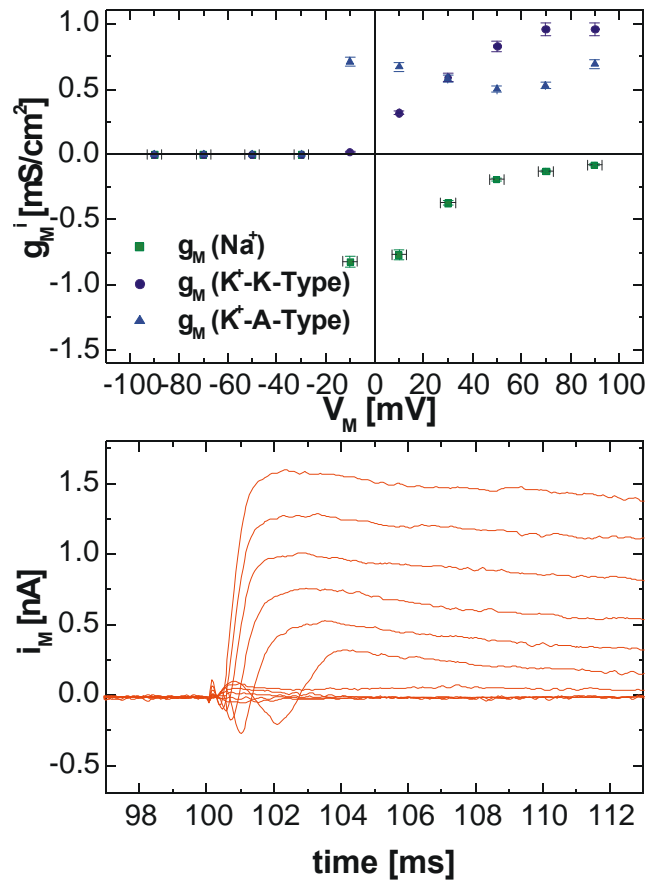


Figure 6-25 Specific ion conductances for a cortical neuron (2 DIV).

6.2.2.2 Dissociated Hippocampal Neurons

The hippocampal neurons were intensively used in this work. A hippocampus culture has the lowest yield of all neuronal cultures used in this work. The main advantage of the hippocampal neurons is the much higher ion currents (1-2 nA Na⁺-current and 2-3 nA K⁺-current) compared to the neuroblastoma cell from the cell lines. The overall goal for the use of primary cultured neurons is the construction of neuronal networks on the sensor surfaces (Lauer, 2001; Offenhäusser et al., 1995; Scholl et al., 2000; Sprössler et al., 2001; Yeung et al., 2001 a). The main focus in the recent work was the coupling behaviour of single neurons to the extracellular sensors.

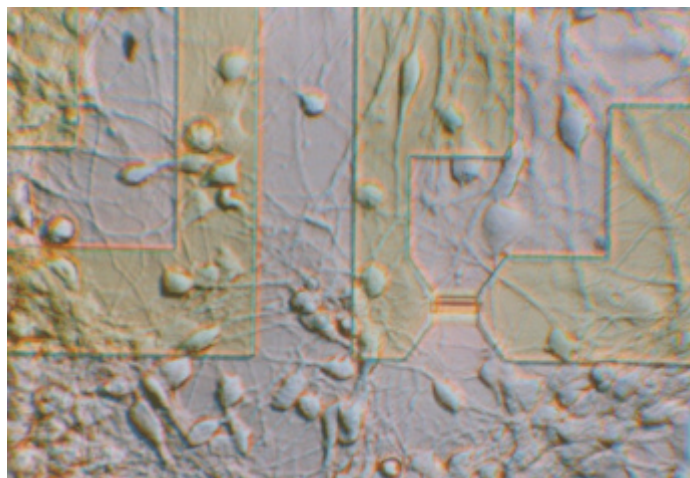


Figure 6-26 Hippocampus neurons (3 DIV) on a laminin primed FET surface. On the right side a rectangular transistor gate can be seen. The neurons have the typical pyramidal shape and are highly connected to each other in a neuronal network.

Cell culture^[1]

After extraction of the whole embryonic 18 days old Sprague-Dawley rat brains, they were washed in sterile HBSS solution. Using a stereo magnifying glass, the hippocampi were dissected, collected in 0.25 % Trypsin in HBSS solution and then placed in an incubator at 37°C and in a 5 % CO₂ enriched atmosphere for 8 minutes. The tissue were then taken with a 5 ml graduate pipette into a 15 ml centrifuge tube filled with 2 ml culture medium (neurobasal medium supplemented with 2 % B27). The trypsin was then washed 5 times with 2 ml medium per step and 5 min breaks in between. The cells

^[1] The cell culture of the hippocampal neurons was done by Dr. Martin Scholl in the group of Prof. Maelike, Institute of Physiological Chemistry and Pathobiochemistry, University of Mainz, Duesbergweg 6, D-55099 Mainz, Germany

were mechanically separated by using a fire-polished glass Pasteur pipette. The cells were then counted. Approximately $5 \cdot 10^5$ cells per hippocampus could be obtained. The cell solution (density in the solution was $1-1.5 \cdot 10^6$ cells/ml) were plated onto the surface (20 μ l onto the FETs and 40 μ l onto the EGEs). This leads to a total number of cells of 20,000-30,000 cells on the FET- and 40,000-60,000 cells on the EGE-sensors.

Electrophysiological characterisation of the cells

The hippocampal neurons were characterised electrophysiologically between 1 DIV and 8 DIV. The statistical data are shown in Figure 6-27.

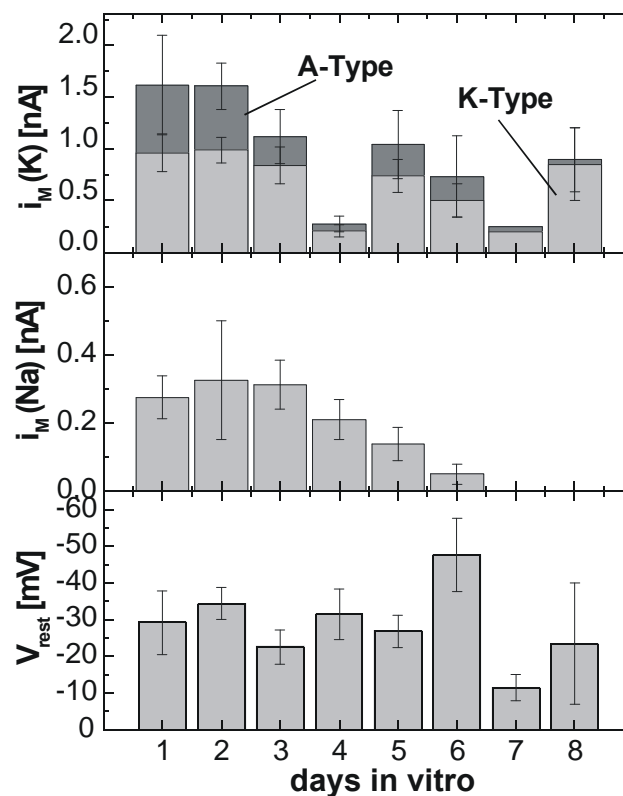


Figure 6-27 Statistical data of the hippocampal neuron culture. In the lower plot the resting potential is shown. In the middle plot the strength of the sodium current is plotted and in the upper plot the potassium current with the potassium A-Type current on top can be seen. For this plot $n = 52$ cells were electrophysiologically characterised.

The hippocampal neuron culture was different from the culture of the TR14 cells (Figure 6-10). The sodium channels in the membrane may be damaged by the trypsinisation treatment and need 1 day for recovery. The highest potassium A-Type overshoot can be measured at the first three days in culture. The sodium current cannot be observed after 6 DIV, indicating a progressive cell death on the sensor surfaces.

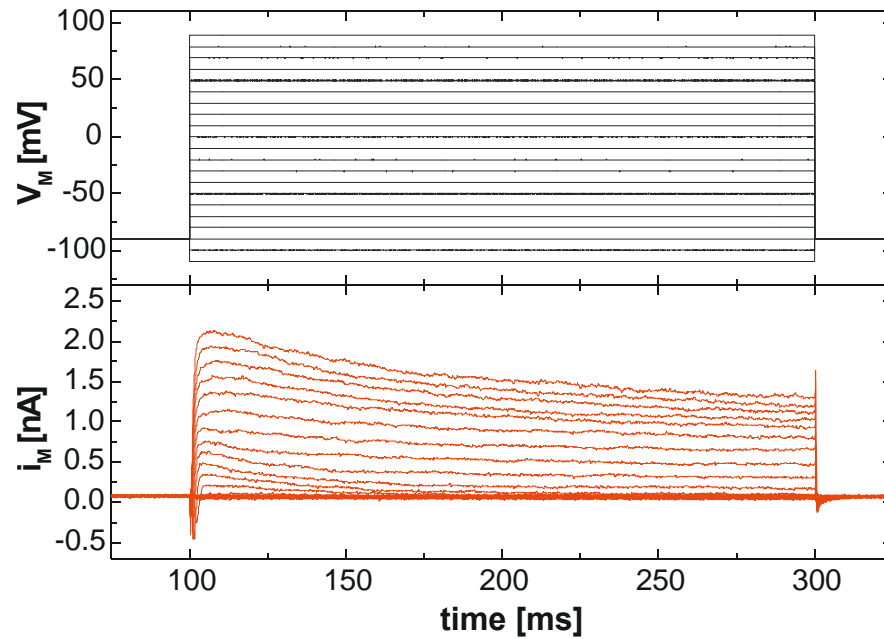


Figure 6-28 Voltage-clamp experiment with a hippocampal neuron (3 DIV) on a Laminin coated FET surface. The cell showed a very pronounced potassium A-Type current.

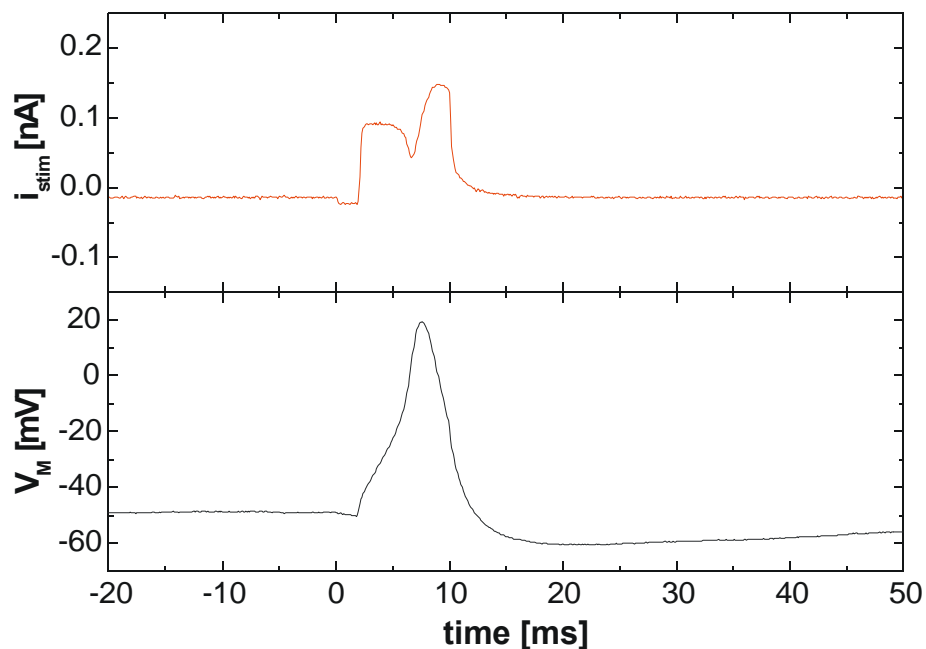


Figure 6-29 Action potential of a hippocampal neuron measured in current-clamp mode. The depolarisation of the cell was caused by a stimulation pulse of $i_{stim} = 0.1$ nA. The cell was clamped from its resting potential of -23 mV to a holding potential of $V_{hold} = -50$ mV. The over-repolarisation (after 10 ms) was typical for hippocampal neurons.

For the construction of neuronal networks of hippocampal neurons the stability of the culture has to be further improved, as the cells are known to form synapses after 12 DIV. In Figure 6-28 a voltage-clamp experiment is shown.

The ion conductances of the cell in the voltage-clamp experiment (Figure 6-28) were calculated using the following values:

$$R_S = 22.1 \text{ M}\Omega, G_L = 1.21 \text{ nS}, C_{slow} = 7.89 \text{ pF}, r_{cell} = 7.95 \text{ }\mu\text{m}, A_M = 7.94 \cdot 10^{-10} \text{ m}^2$$

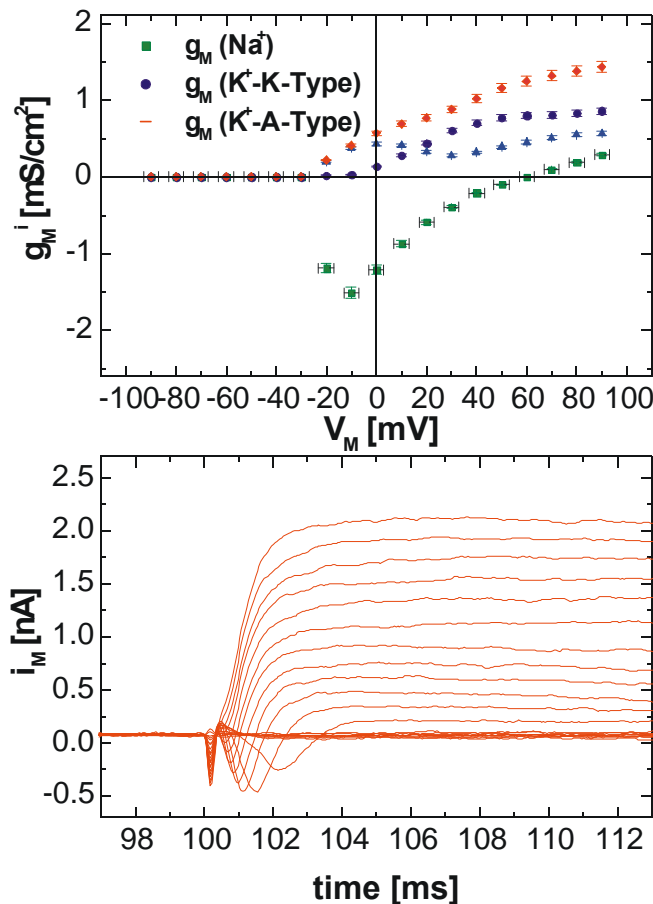


Figure 6-30 Ion conductances of the hippocampal neuron characterised in Figure 6-28. The sodium conductance is crossing the zero line at +60 mV. The conductance of the potassium overshoot (upper trace) is nearly parallel to the sodium conductance.

With the hippocampal neurons a lot of voltage-clamp coupling experiments were successful. In all active C-Type couplings, the strong potassium current of the cells was extracellularly monitored. The highest response of the potassium with a coupled A-Type current was shown above (chapter 5).

6.2.2.3 Brainstem Slice Neurons

The brainstem slice neuron culture was found to be the most stable culture for construction of neuronal cell networks on the extracellular sensor surfaces. After a few days of culturing, the neurons started to migrate out of the slice and tend to stick on the sensor surface. This procedure was very successful for the development of laminin patterned artificial structures on polystyrene dishes (Yeung et al., 2001 a).

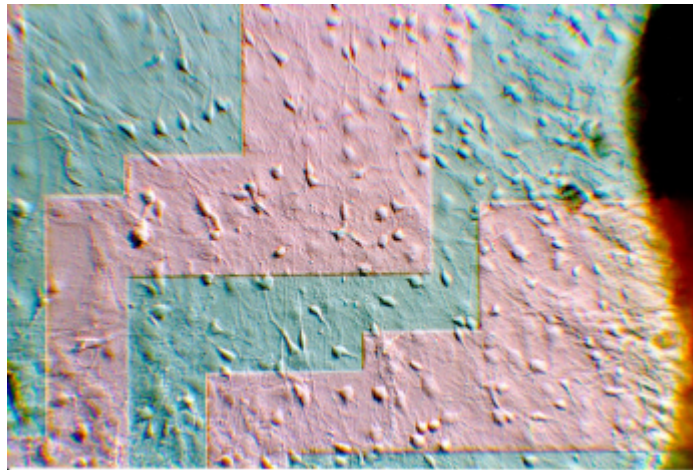


Figure 6-31 Brainstem slice neurons on a FET surface (6 DIV). On the right side the brainstem tissue can be seen. The neurons crawled out of the brainstem slice (from right to left). The glia cells are forming a carpet, which acts as support for the neurons.

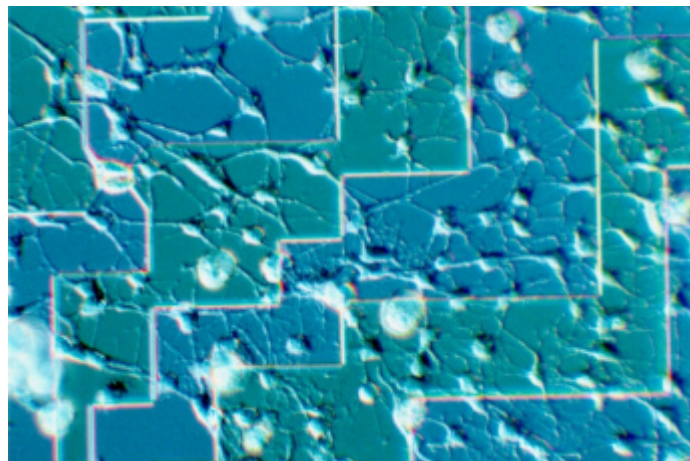


Figure 6-32 Brainstem slice culture on a FET surface (6 DIV). The use of Ara-C on day 4 to 5 in the culture medium blocked the glia cell cleavage and resulted in a clean neuronal network.

The neurons from this culture showed very high voltage-gated ion currents. This could be due to the fact that the culture still contains the necessary supporting cells.

This co-culture was found to be a disadvantage for the cell-transistor coupling, because the glia supporter cells formed a dense layer on the surface, which blocked the sensitive spot from the electrical active cells (Figure 6-31). The use of the anti-mitotic agent Ara-C (β -D-arabinofuranoside) between day 4 and day 5, which blocks the cleavage of the supporter cells, increased the neuron-supporter cell ratio and resulted in more defined neuron networks on the sensor surfaces (Figure 6-32).

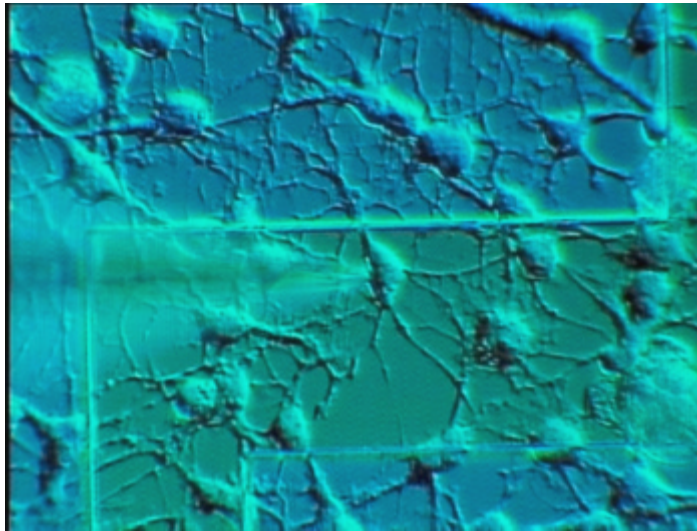


Figure 6-33 The brainstem slice culture was relatively un-specific. Here a DIC image is shown where the patch pipette attaches a Purkinje neuron with its pyramidal structure. Right below a motor neuron with its roundshaped dendritic area can be seen.

Cell culture^[1]

Upon extraction of the whole embryonic rat brains, coronal sections of brainstem slices were harvested in sterile conditions in chilled brain slice culture medium (BSM, pH 7.4). The thus prepared slices were placed in an incubator at 37°C and a 5% CO₂ enriched atmosphere for 4-5 hours minimum prior to plating onto the laminin patterned or non-patterned FETs. Unlike the method described by Gähwiler (Gähwiler, 1981), plasma clot or collagen was not used in immobilising the slices. In all culture dishes, a critical amount of BSM was added to all devices such that they would not be dried up overnight. In some cases anti-mitotic agent, cytosine β -D-arabinofuranoside (ARA-C) was added on day 4 or 5 to inhibit non-neuronal cells proliferation. If ARA-C was used, the culture medium was reverted back to ARA-C-free after 5-7 days. BSM was made from HAMS F10 supplemented with 20-25% foetal bovine serum and 4 mM glutamine (Yeung et al., 2001 a).

^[1] The cell culture of the brainstem slices was done by Dr. Chi-Kong Yeung.

Electrophysiological characterisation of the cells

The brainstem slice culture was relatively unspecific as different regions of the brainstem contain different neurons (Figure 6-33). Therefore, a lot of different characteristics were measured in the patch-clamp experiments. The neurons in this culture appeared to be very active. This could be due to the fact that some of them were motoneurons (see chapter 3) and were spontaneously active (Figure 6-37). The high connection density in the culture seemed to produce some ‘echoes’ from the applied stimulation pulses, which indicated the possible existence of functional synapses. During the voltage-clamp characterisation experiments some cells revealed very high currents up to 10 nA potassium and up to 7 nA sodium current. Therefore, this cell system was shown to be ideal for the investigation of the neuron-transistor coupling.

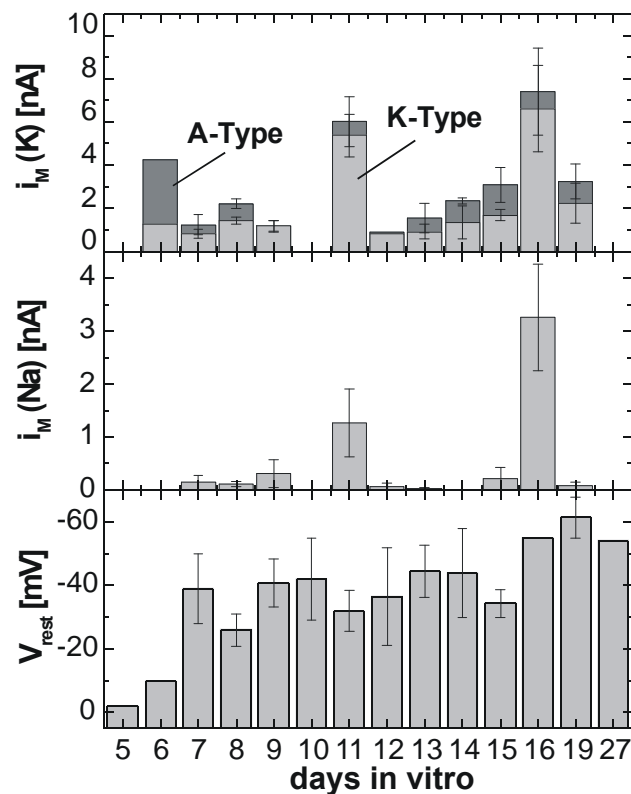


Figure 6-34 Statistical data of the brainstem slice culture. The patch-clamp experiment were possible after 6 DIV, because the neurons need at least this length of time to spread away from the slice. Most of the experiments were done after 2 weeks of culturing, but the cells could survive for more than 4 weeks on the extracellular sensor surfaces. The resting potentials after 1 week were stable between -40 and -50 mV. The current data are dominated by two very good cultures, which were characterised on day 11 and day 16. For this plot $n = 51$ cells were electrophysiologically characterised.

In Figure 6-34 the statistical data of the brainstem slice culture are shown. The optimum period to perform the coupling experiments with these cells was found to be between 11 DIV and 16 DIV. The highest ion currents measured in voltage-clamp mode are shown in Figure 6-35.

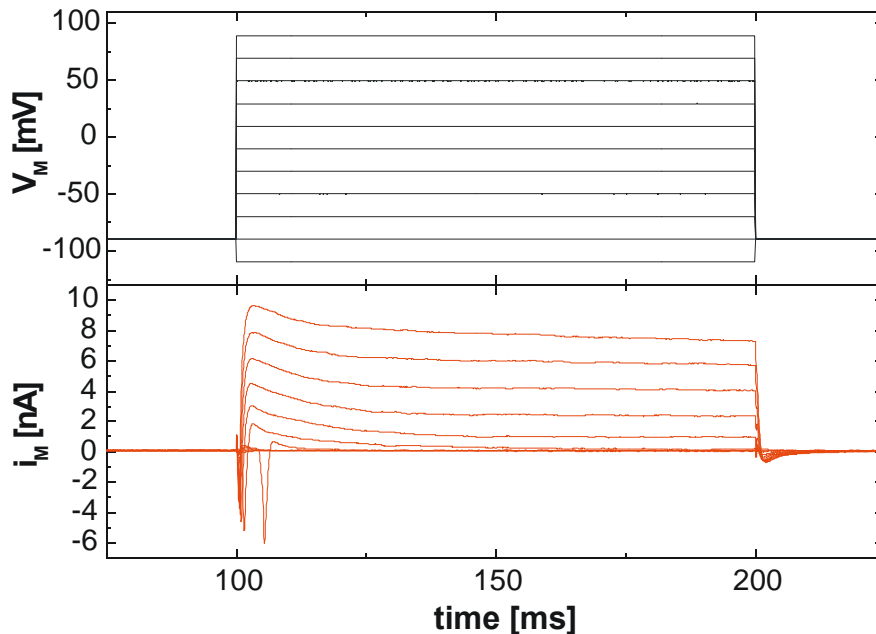


Figure 6-35 Voltage-clamp experiment with a brainstem neuron (16 DIV). The potassium current (10 nA) and the sodium current (6 nA) were the highest measured in all cell cultures.

Neurons from the brainstem cultures usually had very large capacitance values (up to $C_{slow} = 45$ pF). By using this value and the specific capacitance $c_M = 1 \mu\text{F}/\text{cm}^2$ for bilayer membranes, very large cell diameters were calculated (Eq. 5.10). In Figure 6-35 a very strong sodium current and a very strong potassium A-Type current dominate the extracellular signal. In most of the voltage-clamp experiments these A-Type currents were observed, but some cells showed pure potassium K-Type signal.

The ion conductances of the cell in the voltage-clamp experiment (Figure 6-35) were calculated using the following values:

$$R_S = 11.7 \text{ M}\Omega, G_L = 2.87 \text{ nS}, C_{slow} = 38.76 \text{ pF}, r_{cell} = 17.6 \mu\text{m}, A_M = 3.89 \cdot 10^{-9} \text{ m}^2$$

The cell radius seemed to be overestimated in this experiment by comparing this value with the microscope observation. Although the specific ion conductance for sodium was calculated to $g_M(\text{Na}^+) = 6.1 \text{ mS}/\text{cm}^2$, which was a very high value for the brainstem neurons. The specific ion conductances are plotted in Figure 6-36.

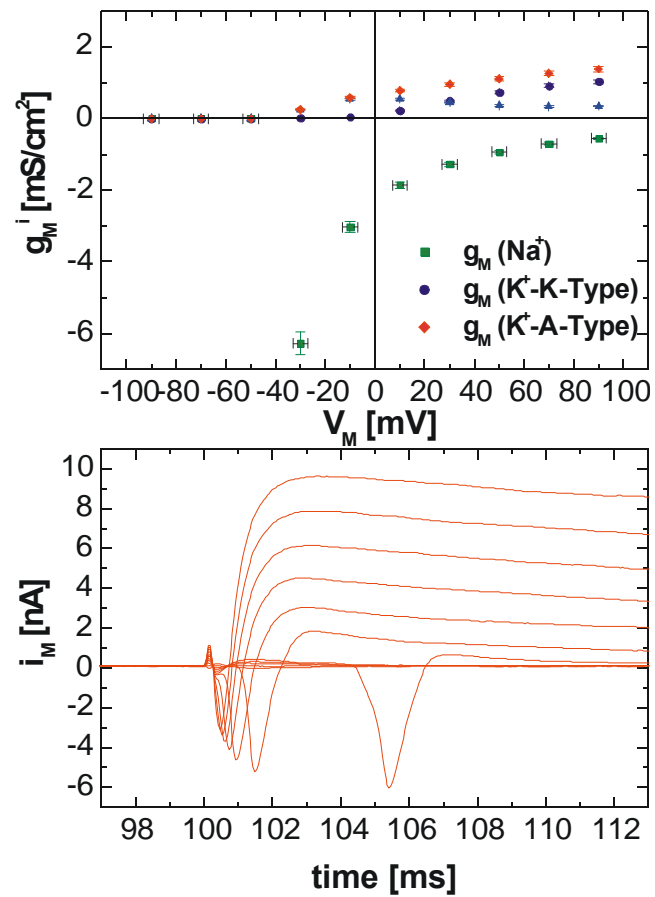


Figure 6-36 Specific ion conductance values for the brainstem neuron characterized in Figure 6-35. The sodium ion conductance was very high.

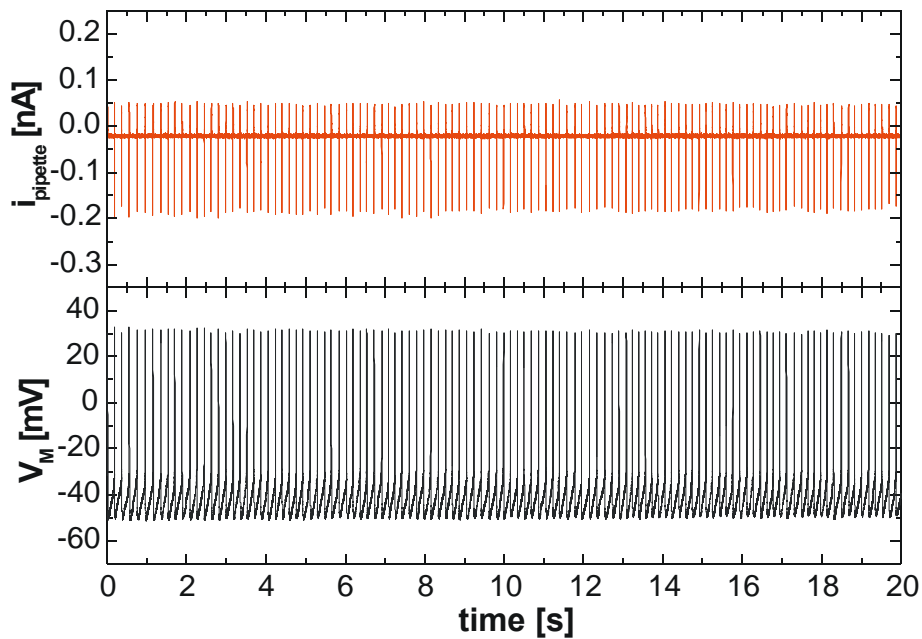


Figure 6-37 Spontaneous action potentials monitored without stimulation in CC-mode.

By switching to the current-clamp mode using the same brainstem neuron as before, it appeared that the cell was a motoneuron. It was firing spontaneous action potential with a very constant rate of 5.3 Hz (Figure 6-37).

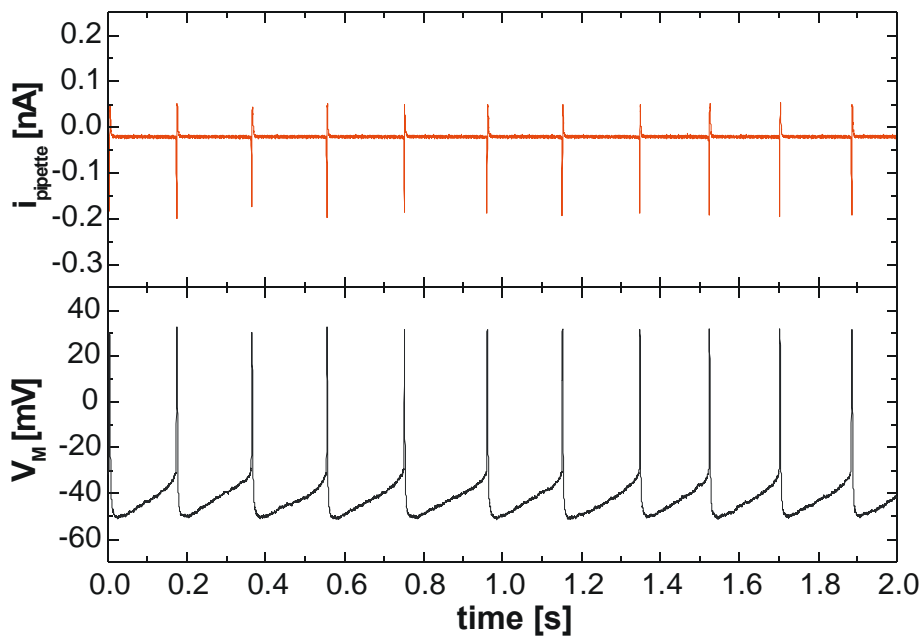


Figure 6-38 Closer look to the spontaneous action potentials. The cell had a resting potential of -50 mV. By reaching $V_M = -30$ mV a action potential is fired.

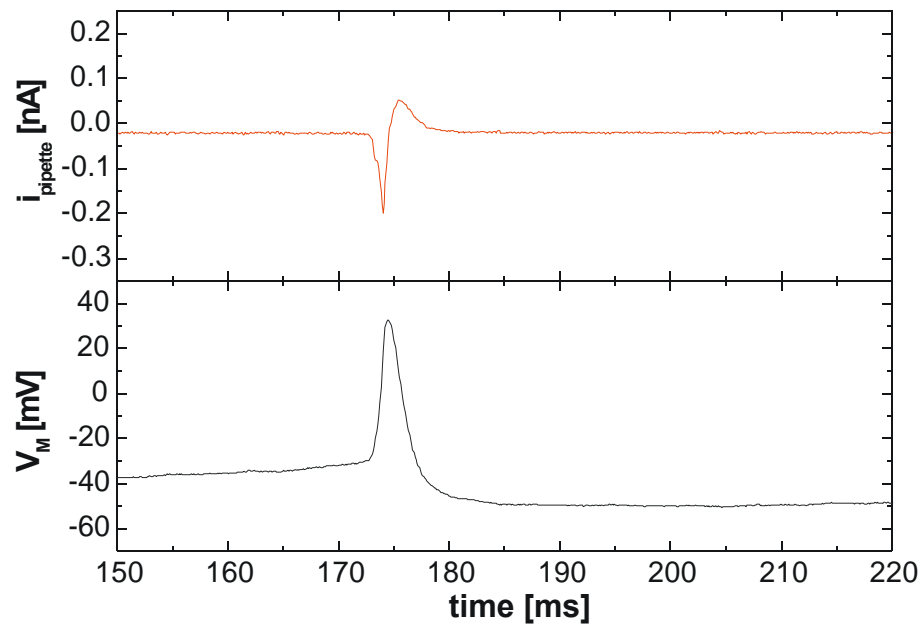


Figure 6-39 Single action potential of the motorneuron. The total duration of the firing is below 5 ms. In the upper trace the ionic signal, which is monitored by the patch-pipette is shown. This current normally disturbs the rectangular stimulation pulse in current-clamp mode (see above).

The signal in Figure 6-39 reflects an ideal case of a spontaneous action potential of neurons.

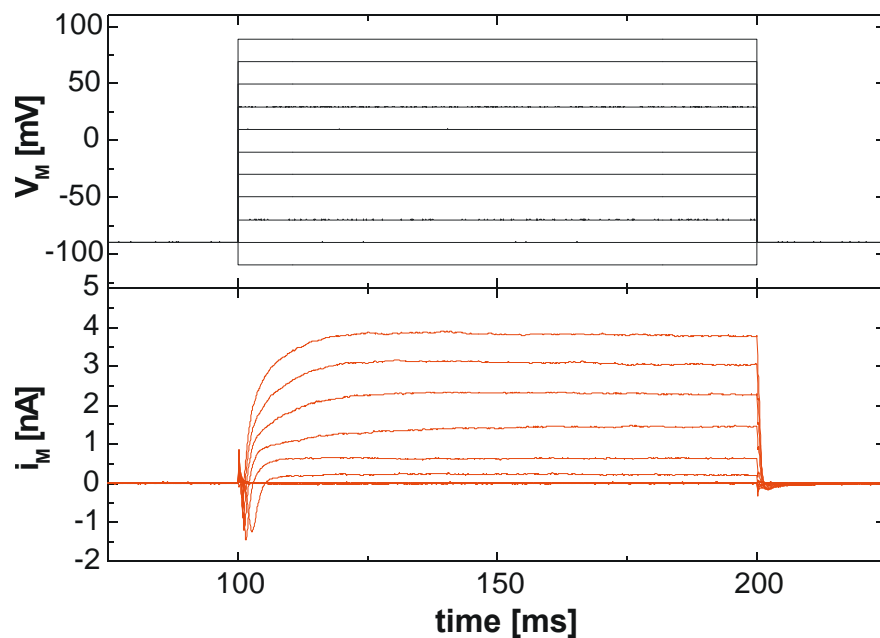


Figure 6-40 Brainstem neuron (15 DIV, on Laminin coated FET surface) with no portion of A-Type current in its potassium signal.

With the brainstem neurons also current signals with no A-Type portion in the potassium current were observed (Figure 6-40). Without these quick-acting current efflux the repolarisation during an action potential is much slower (Figure 6-41).

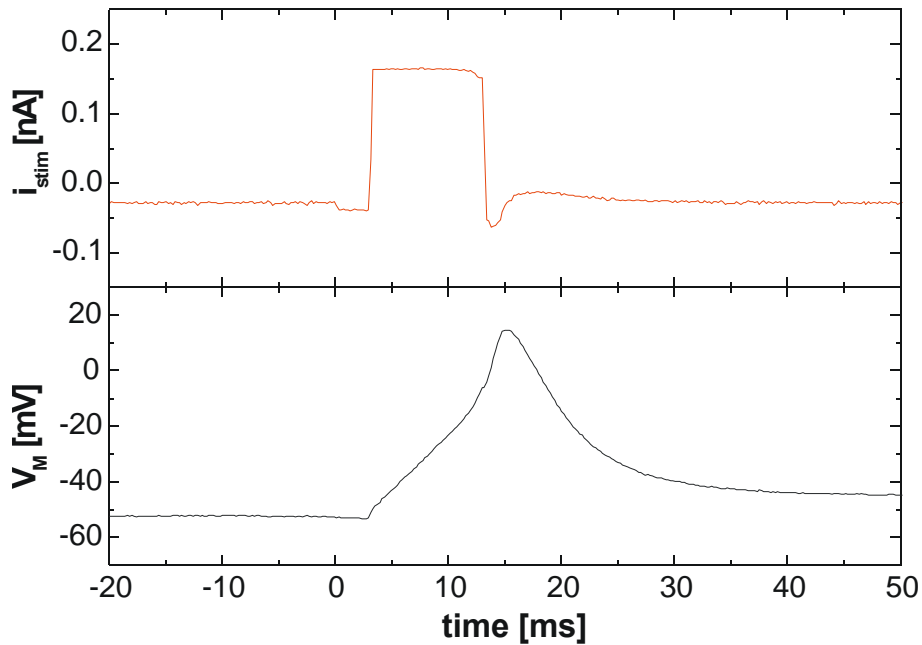


Figure 6-41 Without the quick-acting potassium A-type channel the repolarisation during an action potential is slowed down.

The neuron characterised in Figure 6-40 had a resting potential of -30 mV and a very high membrane capacitance ($C_{slow} = 42.37$ pF).

The voltage overshoot in the potassium current signal was partly caused by voltage-gated A-type potassium channels. It is possible to switch off this type of ion-channel with a delayed prepulse protocol (Storm, 1990) as shown in Figure 6-42. The A-Type channels were not fully deactivated by this protocol.

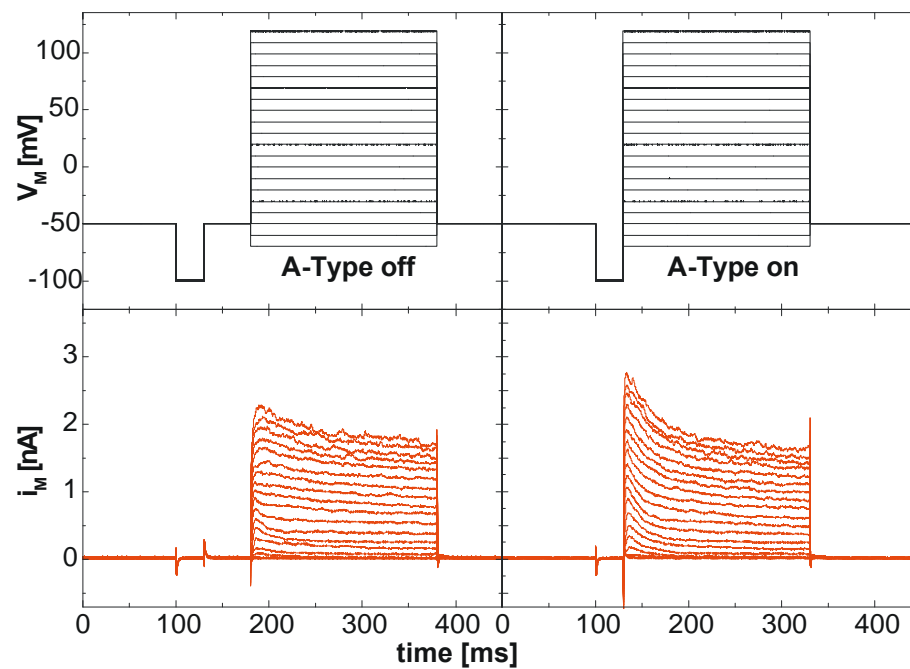


Figure 6-42 The A-Type potassium channels are partly switched off with the delayed prepulse protocol (Storm, 1990). (cell: BS-neuron 15 DIV on Laminin coated FET sensor)

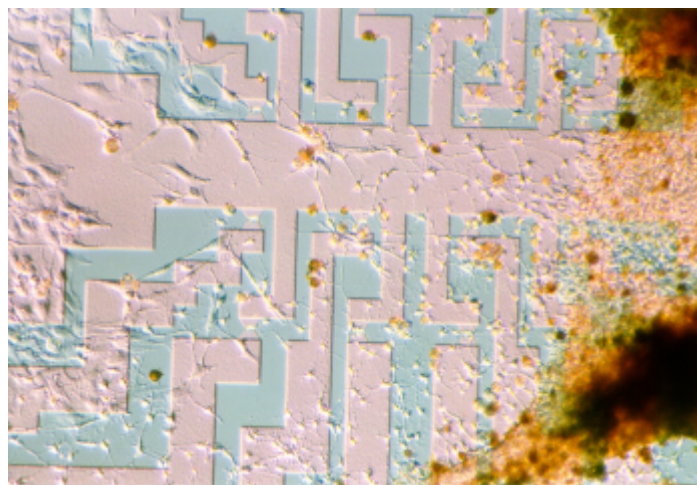


Figure 6-43 The outspread brainstem neurons may have still intact connection to the original slice.

Indications for a communicating neuronal network on the chip were sometimes recorded as ‘echoes’ within the dense cell networks. This could be possible due to new synaptical contacts that had been established by the migrating neurons, or - more likely - the intact connections of the brainstem slice (Figure 6-43).

In Figure 6-44 a single echo measured in current-clamp mode is shown. In Figure 6-45 a double echo was monitored in voltage-clamp mode and in current-clamp mode (Figure 6-46).

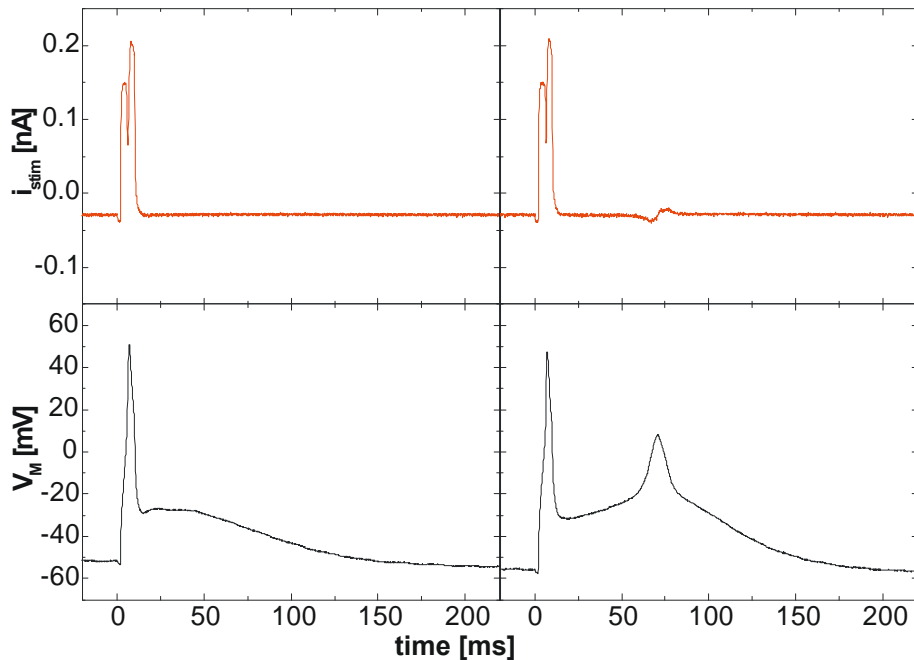


Figure 6-44 Action potential of a brainstem neuron with a very slow repolarisation (left side) and 'echo' signal to the next stimulated action potential (12 DIV, Laminin).

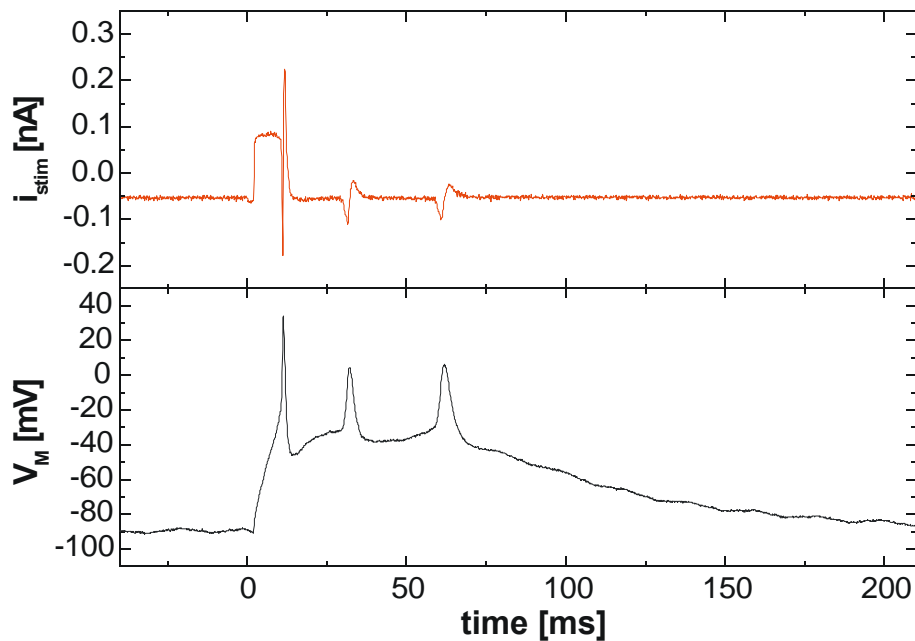


Figure 6-45 Double echo to the first sodium channel monitored in VC-mode. The neuron was cultured on a laminin FET surface (9 DIV).

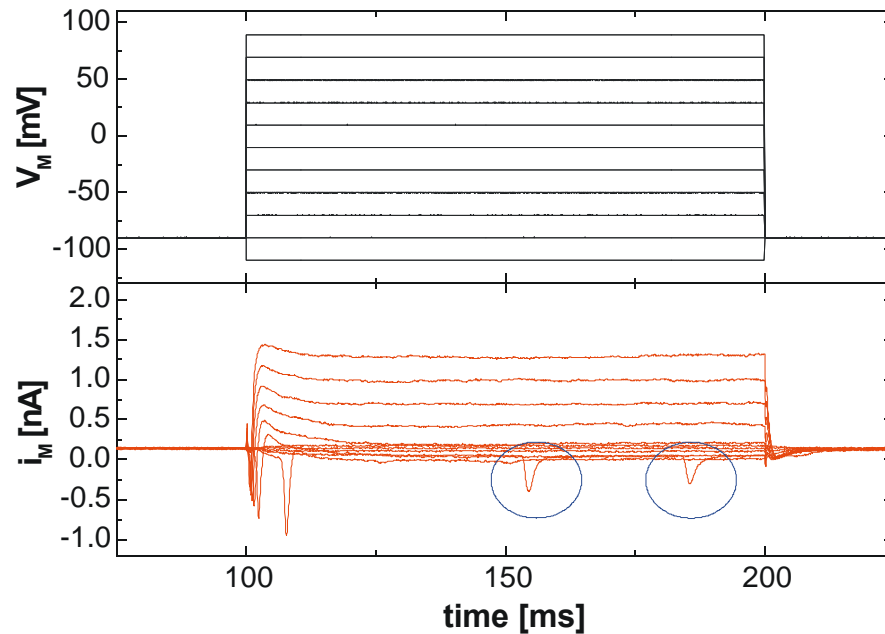


Figure 6-46 The double echo was also monitored in CC-mode.

Voltage-clamp coupling experiments

In the following some coupling experiments with brainstem neurons cultured on backside contacted FET arrays are shown. The gate structures of the backside chips are much larger than the gate structures of the standard FET arrays to compensate the series resistances of the backside contacts (chapter 3).

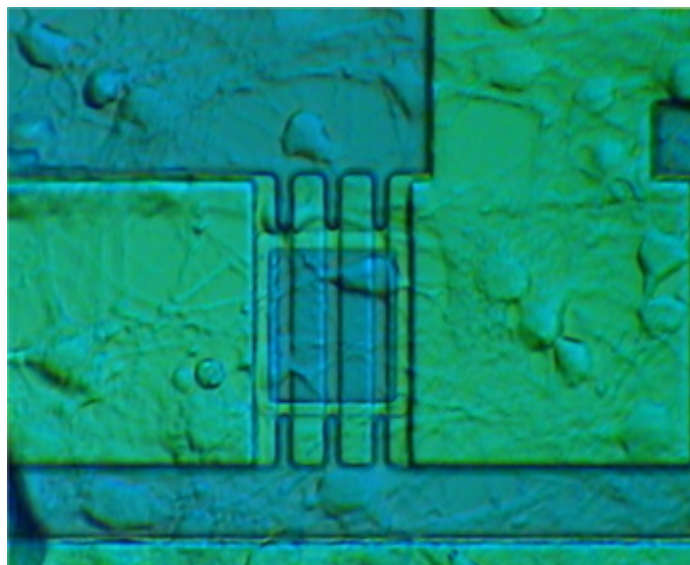


Figure 6-47 Brainstem neuron (7 DIV) cultured on a laminin coated $32 \times 38 \mu\text{m}^2$ triple-gate structure. The next coupling experiment was using this neuron.

Although the single neuronal cells are not able to cover a gate structure completely (brainstem neuron on a $32 \times 38 \mu\text{m}^2$ triple gate structure in Figure 6-47) it was possible to couple active cell signals in voltage-clamp experiments. This would offer the possibility of constructing a large multi-gate structure to increase the probability of randomly seeded cells to localise onto the sensitive spots in future.

<i>Voltage-clamp coupling</i>	Patch-Clamp	Step 200 mV
Chip: backside FET 27DD32x38 ($V_{DS} = -3\text{V}$, $V_{GS} = -2\text{V}$) $g_m = 0.4 \text{ mS}$; Gatesize: $32 \times 38 \mu\text{m}^2$ Laminin coated	$V_{rest} = -20 \text{ mV}$ $C_{slow} = 10.59 \text{ pF}$ $G_L = 5.47 \text{ nS}$	$R_M = 2.6 \text{ G}\Omega$ $i_M^L = 354.88 \text{ pA}$ $R_S = 26.9 \text{ M}\Omega$
Date: 26.07.00 File: Si00072619 (averaged 100 x)	$C_{fast} = 8.09 \text{ pF}$	$R_J = 112980 \Omega$ $g_J^* = 8.32 \text{ S/cm}^2$
10 % attached Cell: BS neuron (4 DIV)	$r_{cell} = 9.2 \mu\text{m}$	$A_M = 1.06 \cdot 10^{-9} \text{ m}^2$

Table 6.6: Values for the simulation of the C-Type voltage-clamp coupling experiment using a brainstem neuron (Figure 6-48). *The origin of the higher value for g_J is explained in the text.

As it can be seen in Figure 6-47 the neuron was not at all covering the gate structure. However, it was possible to monitor the capacitive and the active cell current in this experiment.

The very high seal conductance value $g_J = 8.32 \text{ S/cm}^2$ can be explained with the following suggestions. For calculating the effective gate voltage from the transconductance value g_m of the FET device, a complete coverage of the gate structure is assumed. This is certainly not the case for this measurement where the cell was covering about 8 % (1/4 of a single channel line) of the sensitive triple-gate structure. This means the effective gate voltage change would be about 12 times higher, which would lead to capacitive peaks of about $500 \mu\text{V}$. Therefore, the sealing conductance would have to be scaled down to the normal values of $1\text{-}3 \text{ S/cm}^2$.

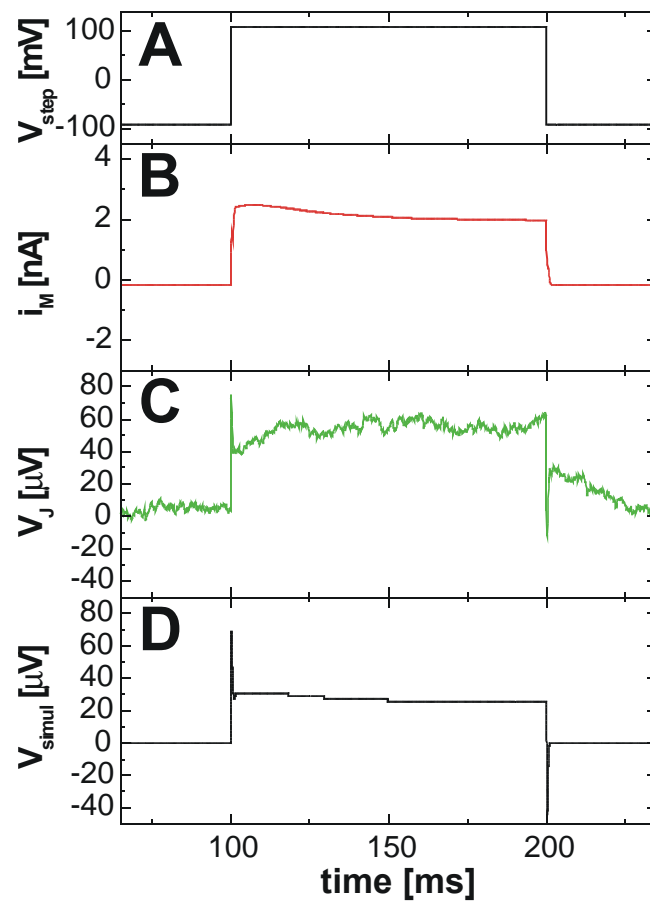


Figure 6-48 Voltage-clamp coupling using a brainstem neuron (7 DIV) on a laminin coated backside-contacted FET with big triple gate structure (32x38 μm^2).

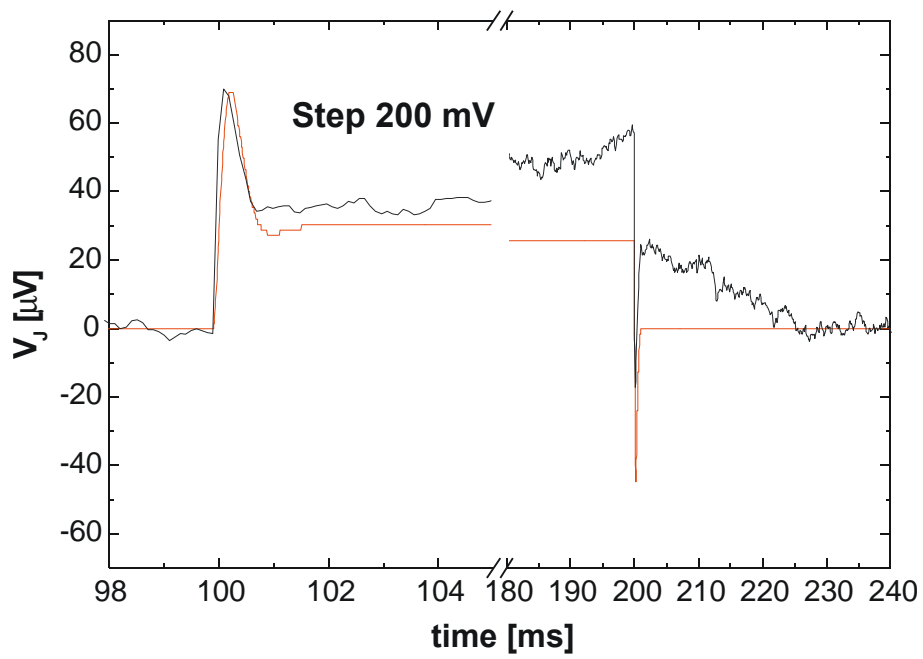


Figure 6-49 Closer view to the simulated data shown in Figure 6-48.

In the next voltage-clamp coupling experiment the potassium signal of a brainstem neuron was extracellularly monitored with a backside-contacted FET device (doublegate: gatesize $18 \times 20 \mu\text{m}^2$).

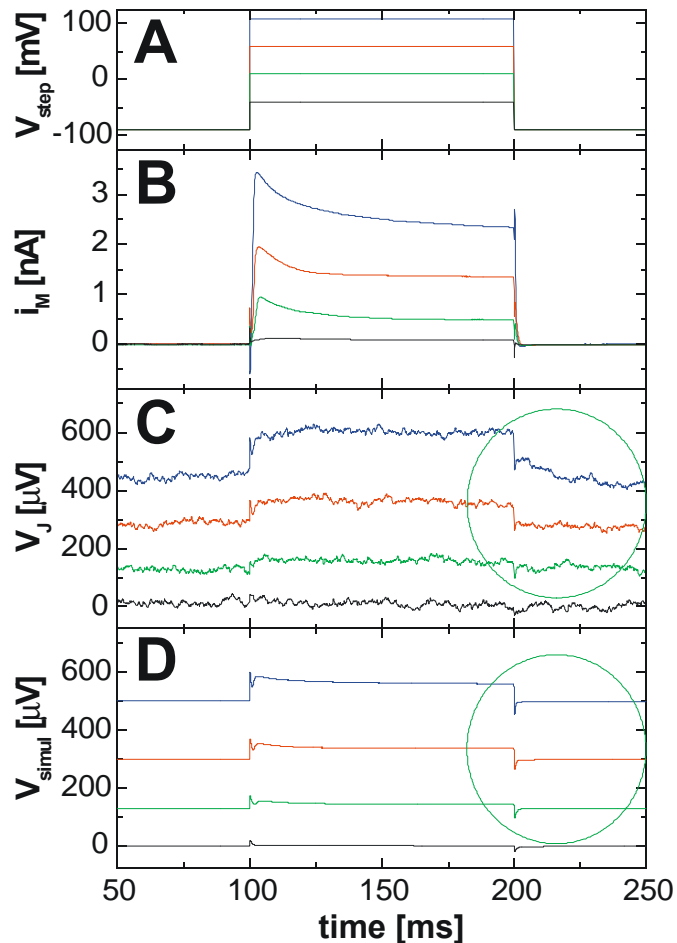


Figure 6-50 Voltage-clamp coupling experiment with a brainstem neuron (7 DIV) on a laminin coated backside contacted FET sensor (doublegate: gatesize $18 \times 20 \mu\text{m}^2$). The cell had a relatively high potassium A-Type conductance. Again the higher responses at the end of the stimulation pulses are underestimated in the standard PSPICE circuit.

A closer view to the fitted data in Figure 6-51 shows that the extracellular responses are accurately modelled. With this cell it was possible to monitor a weak signal in a current-clamp mode coupling experiment (see below). The data used for the signal modelling in PSPICE are shown in Table 6.7.

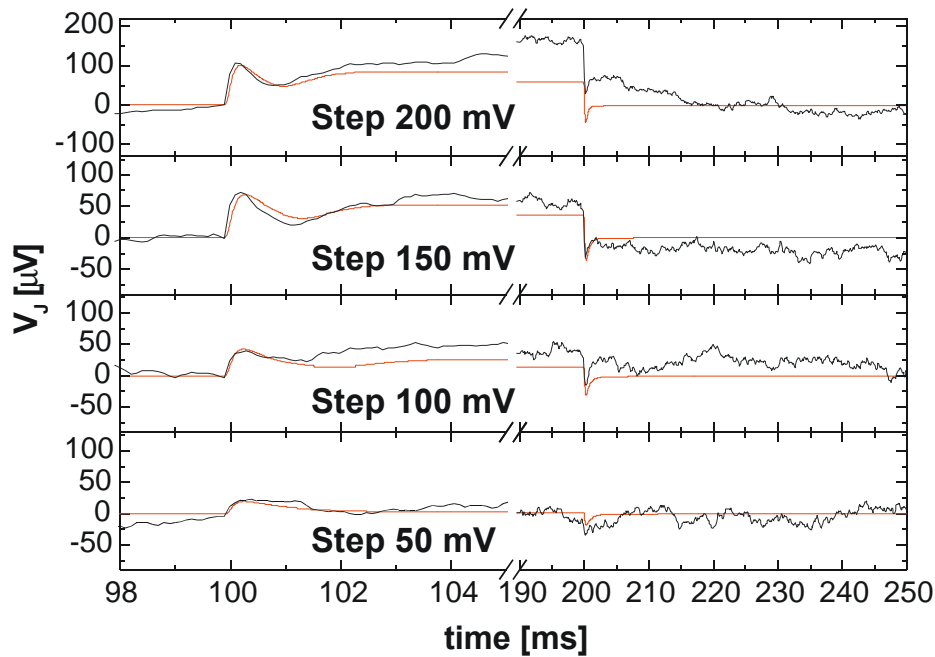


Figure 6-51 Closer view to the fitted data for the voltage-clamp coupling experiment shown in Figure 6-50. The current signal of the highest response is clearly underestimated.

<i>Voltage-clamp coupling</i>	Patch-Clamp	Step 200 mV	Step 150 mV	Step 100 mV	Step 50 mV
Chip: Backside FET 27D18x20 ($V_{DS} = -3V$, $V_{GS} = -2V$) $g_m = 0.18$ mS; Gatesize: $18 \times 20 \mu\text{m}^2$ Laminin coated	$V_{rest} =$ -23 mV	$C_{slow} =$ 18.56 pF $R_M =$ 1.18 G Ω $i_M^L =$ 123.8 pA $G_L = 2.34$ nS	$C_{slow} =$ 16.87 pF $R_M =$ 2.06 G Ω $i_M^L =$ 134.1 pA $G_L = 2.34$ nS	$C_{slow} =$ 16.87 pF $R_M =$ 2.01 G Ω $i_M^L =$ 133.9 pA $G_L = 2.34$ nS	$C_{slow} =$ 16.11 pF $R_M =$ 1.65 G Ω $i_M^L =$ 108.6 pA $G_L = 2.13$ nS
Date: 27.07.00 Files: Si000727.003 / 05 07 / 09 (averaged 100 x)	$C_{fast} =$ 8.49 pF	$R_J =$ 241000 Ω $R_S = 24.1$ M Ω	$R_J =$ 266576.5 Ω $R_S = 41$ M Ω	$R_J =$ 266577.9 Ω $R_S = 41$ M Ω	$R_J =$ 280917.8 Ω $R_S = 53.5$ M Ω
10 % attached Cell: Brainstem neuron (7 DIV)		$g_J = 2.219$ S/cm ² $A_M =$ $1.87 \cdot 10^{-9}$ m ² $r_{cell} = 12.2 \mu\text{m}$	$g_J = 2.219$ S/cm ² $A_M =$ $1.69 \cdot 10^{-9}$ m ² $r_{cell} = 11.6 \mu\text{m}$	$g_J = 2.219$ S/cm ² $A_M =$ $1.69 \cdot 10^{-9}$ m ² $r_{cell} = 11.6 \mu\text{m}$	$g_J = 2.219$ S/cm ² $A_M =$ $1.61 \cdot 10^{-9}$ m ² $r_{cell} = 11.3 \mu\text{m}$

Table 6.7: Values for the simulation the voltage-clamp coupling experiment (4-step protocol) using a brainstem neuron (Figure 6-50). The cell-pipette assembly was compensated before each measurement.

6.3 Primary Cultured Cardiac Myocytes

Primary cardiac myocyte cultures are a very good cell system for the cell-transistor coupling. They show voltage-gated ion currents up to 3 nA (chapter 5) and the yield from one culture was relatively high as whole organs were used. However, this culture was also very unspecific in that different regions of the heart contain cells of slightly different origins (e.g. myocytes, pacemaker cells, fibroblasts). In the cell culture, the cell-cell bonds were broken using trypsin as in the neuronal cultures. The plating of the cells on the sensor were done using the eventual cell suspension. The big advantage of cardiac myocytes compared to neurons is the spontaneous activity. After a few days *in vitro* (2-4 DIV) the cardiac myocytes formed a confluent layer on the sensor connected to each other via electrical synapses called the gap junctions (chapter 3). In this stage, the cells are mimicking the organ tissue, where the entire syncytium is beating spontaneously on the sensor surface much the heart inside our body. This cell-transistor chip can be treated as a model heart and the first drug testing experiments was done with this kind of biochip (paragraph 6.4). In the first part, the signal shapes of such coupled action potentials were investigated by using single cells in cell-transistor coupling experiments.

Cell Culture^[1]

Hearts of embryonic day 15 to 18 Sprague Dawley (Charles River, Sulzbach, Germany) rats were used. The hearts were removed, minced and placed into ice cold Ca/Mg-free Hanks balanced salt solution (HBSS). The chopped hearts (usually about 8 to 12) were then pooled in a 10 ml centrifuge tube and washed gently for 3 to 4 times to remove traces of blood and other non-heart tissues. Most importantly is to rid of any proteolytic enzymes and endotoxins that might be present as a result of mechanical damage of the cells during preparation. After washing, the HBSS was replaced with 4 ml of crude 0.05 % trypsin and after 8 min incubation at 37°C, the supernatant was discarded. The dissociation cycle then began with 2 ml of 0.05 % crude trypsin for 8 min preceded by the addition of 100 µl DNase type II solution (10,000 units per ml) for 1 to 2 min. The resulting supernatant was collected and added into the stop solution (to block trypsinisation) of HAM F10 solution containing 36 % foetal calf serum (FCS), 0.5 % insulin, transferrin, selenite, (ITS) solution, 6 mM of L-glutamine and 2 ml of penicillin/streptomycin mixture (5000 units/5 mg/ml) for every 100 ml of F10. This cell suspension was then centrifuged at 1500 rpm for 5 min. The pellet was resuspended using HAMS F10 containing 10 % FCS, 0.5 % ITS and 6 mM glutamine and 2 ml of

[1] The cell culture was done by Maria Theresa Siepchen, MPI for Polymer Research Mainz, Germany.

antibiotic mixtures. The above dissociation was repeated 4 to 5 times or until all the heart tissue had been dissociated. All the procedures were carried out under sterile conditions.

The subsequently yielded cell suspensions were pooled in a 25 cm² tissue culture flask and incubated for 1.5 to 2 hours at 37°C. This incubation allowed cell debris and fibroblasts to adhere to the flask surface preferentially over cardiac myocytes leaving a higher myocytes to fibroblasts ratio. The final cell suspension was counted and adjusted accordingly. About 20 µl of 1 to 2 million cells per ml suspension was used plated onto pre-cleaned and extracellular matrix primed FETs or EGEs. As one culture could yield approximately 1 to 2 ml of 1 million cells per ml of cell suspension, 50 to 100 FETs could potentially be prepared with a single culture.

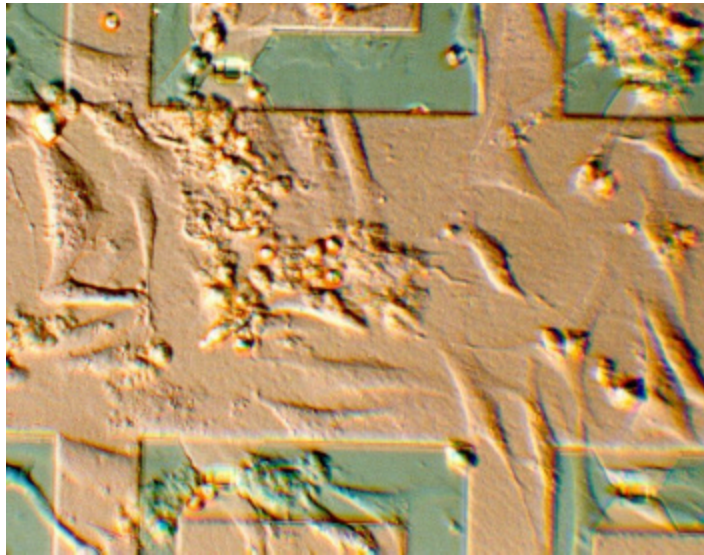


Figure 6-52 Single cardiac myocyte cells (1 DIV) cultured on a fibronectin coated FET surface. A very low density of cells (~ 6,000 cells per FET and ~ 12,000 cells per EGE) was plated onto the devices.

6.3.1 Single Cell Experiments with Cardiac Myocytes

For the single cell experiments a very low density of cells (~ 6,000 cells per FET and ~ 12,000 cells per EGE) was plated onto the devices (Figure 6-52). The experiments were usually carried on day 1 and day 2 after the cultures because the cell density became too high as the fibroblasts continued to divide and forming a thick cell layer. Patch-clamp experiments with single cardiac myocyte cells were found to be very difficult as the cells once they are stimulated, either in voltage-clamp or current-clamp mode, tend to contract and break the pipette-cell connection. In the previous chapter, a voltage-clamp coupling experiment with a single cardiac myocyte, where a strong

sodium current was influencing the extracellular signal, was shown. In other experiments only passive coupling types – mainly AB-Type – were monitored.

Coupling experiments

From many different coupling experiments only one AB-Type signal will be discussed.

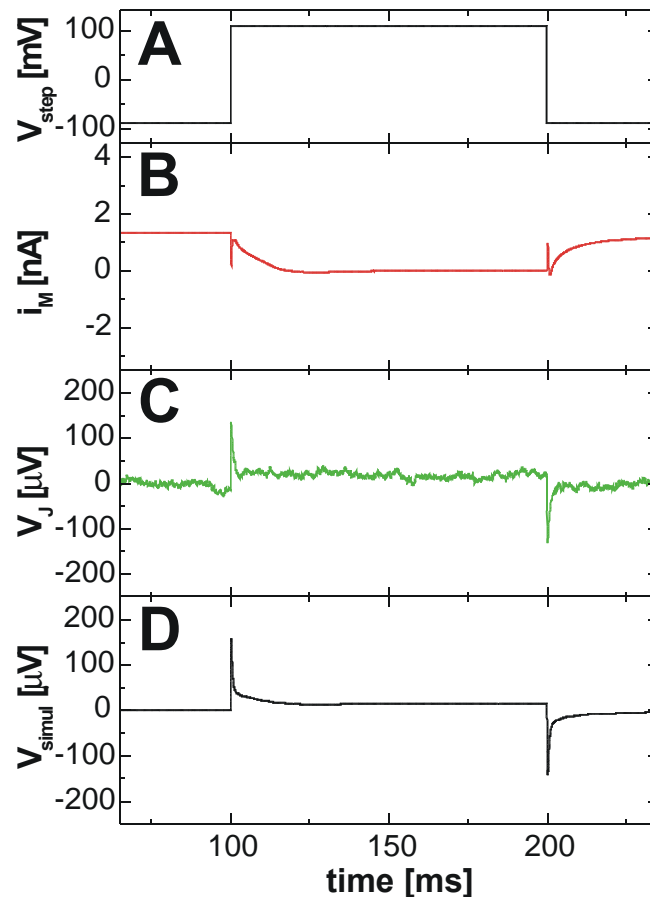


Figure 6-53 Passive extracellular recording (AB-Type) using a cardiac myocyte cell (2 DIV). The cell membrane was very leaky. Therefore the patch current signal (trace B) is not compensated to zero.

In this extracellular signal only the capacitive and ohmic components of the stimulation pulse are extracellularly monitored. The cell membrane was very leaky ($G_L = 24$ nS), which was not compensated completely in the patch-clamp output current.

A closer view to the simulated data in Figure 6-54 shows that the capacitive tips are well modelled

<i>Voltage-clamp coupling</i>	Patch-Clamp	Step 200 mV
Chip: p-channel FET 563412 ($V_{DS} = -3V$, $V_{GS} = -2V$) $g_m = 0.3$ mS; Gatesize: $2 \times 2 \times 16 \mu\text{m}^2$ Fibronectin coated	$V_{rest} = -21$ mV $C_{slow} = 8.81$ pF $G_L = 24$ nS	$R_M = 1.13$ G Ω $i_M^L = 1327.1$ pA $R_S = 28.4$ M Ω
Date: 29.04.00 File: Si00042905 (averaged 60 x)	$C_{fast} = 7.05$ pF	$R_J = 486600 \Omega$ $g_J = 2.407$ S/cm²
10 % attached Cell: Cardiac myocyte (2 DIV)	$r_{cell} = 8.4 \mu\text{m}$	$A_M = 8.87 \cdot 10^{-10}$ m ²

Table 6.8: Values for the simulation of the AB-Type voltage-clamp coupling experiment using a single cardiac myocyte cell (Figure 6-53).

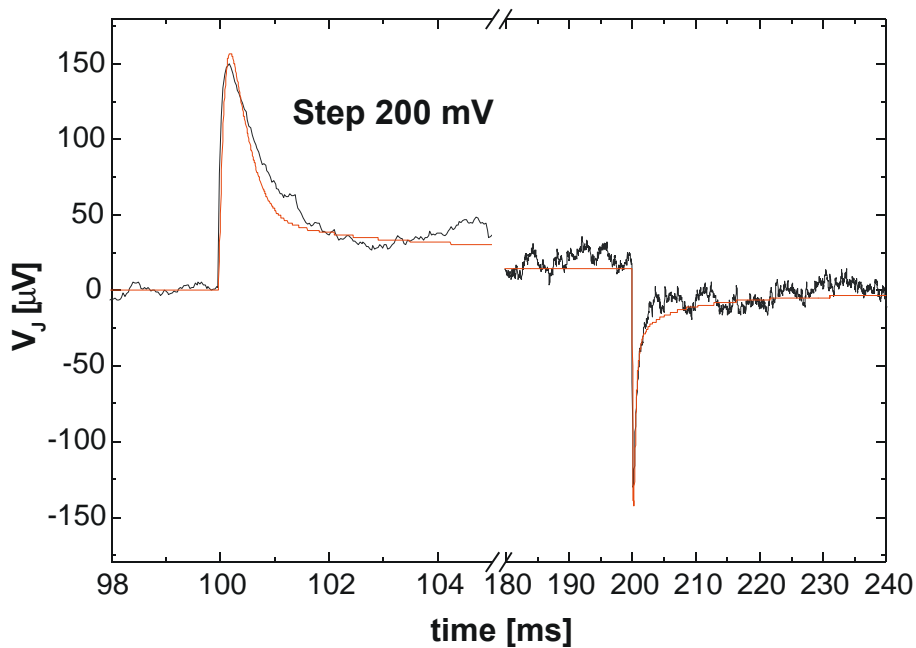


Figure 6-54 Closer view to the simulated data of the AB-Type signal of a single cardiac myocyte cell.

6.3.2 Cardiac Myocyte Layers

For the culturing of cardiac myocyte, cell layers at higher cell density (20,000 – 30,000 per FET- and 40,000 – 60,000 cells per EGE-device) of cells is plated onto the devices. After 3-4 DIV the cardiac myocytes tended to form dense cell layers (Figure 6-55). In most of the cases, a rhythmic contraction was then developed. Sometimes when the cells didn't contract at very high lateral amplitude, patch-clamp experiments were

possible. In the following a voltage-clamp experiment using a non-contracting cell on a cell layer on top of a transistor gate was performed.

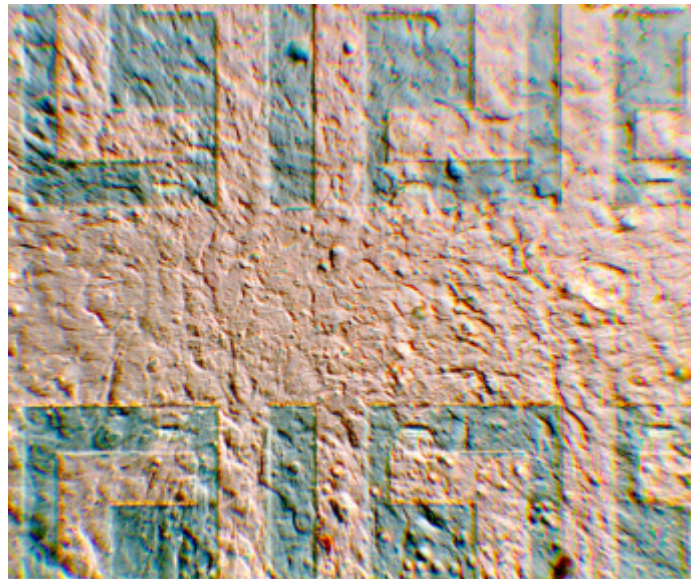


Figure 6-55 Cardiac myocyte cell layer (4 DIV) on a fibronectin coated FET surface.

<i>VC coupling</i>	Patch-Clamp	200 mV	150 mV	100 mV	60 mV	50 mV
Chip: n-channel FET 038141 $V_{DS} = 3V$ $V_{GS} = 1.5V$ $g_m = 0.5 \text{ mS}$; Gatesize: $4 \times 16 \mu\text{m}^2$ Fibronectin coated	$V_{rest} =$ -50 mV $C_{slow} =$ 7.95 pF $G_L =$ 13.24 nS	$R_M =$ 0.4313 G Ω $i_M^L =$ 722 pA	$R_M =$ 0.625 G Ω $i_M^L =$ 625 pA	$R_M =$ 0.239 G Ω $i_M^L =$ 633 pA	$R_M =$ 0.571 G Ω $i_M^L =$ 571 pA	$R_M =$ 0.221 G Ω $i_M^L =$ 473 pA
Date: 12.05.00 Files: Si000512.006 08 / 10 / 12 / 14 (averaged 60 x)	$C_{fast} =$ 6.99 pF $R_S =$ 63.5 M Ω	$R_J =$ 1111250 Ω	$R_J =$ 973666.7 Ω	$R_J =$ 889000 Ω	$R_J =$ 762000 Ω	$R_J =$ 762000 Ω
10 % attached Cell: (2 DIV) Cardiac cell layer	$A_M =$ $8.04 \cdot 10^{-10} \text{ m}^2$ $r_{cell} = 8 \mu\text{m}$	$g_J =$ 1.119 S/cm 2	$g_J =$ 1.277 S/cm 2	$g_J =$ 1.399 S/cm 2	$g_J =$ 1.632 S/cm 2	$g_J =$ 1.632 S/cm 2

Table 6.9: Values for the simulation the voltage-clamp coupling experiment (5-step protocol) using a cardiac myocyte cell layer (Figure 6-56).

It can be seen that the extracellular responses cannot be modelled using the standard PSPICE circuitry. The signal is formed from the whole cell sheet and cannot be reduced to the response of a single cell. The capacitive responses are not linear to the height of the simulation pulses as in all other experiments with single cells. The interpretation of this can be done by assuming that part of the stimulation pulse is transferred over the gap junctions (see chapter 3) into the whole cell layer (Figure 6-58). This may weaken the flank of the stimulation pulse inside of the attached cell and hence weaken the capacitive response monitored by the extracellular device.

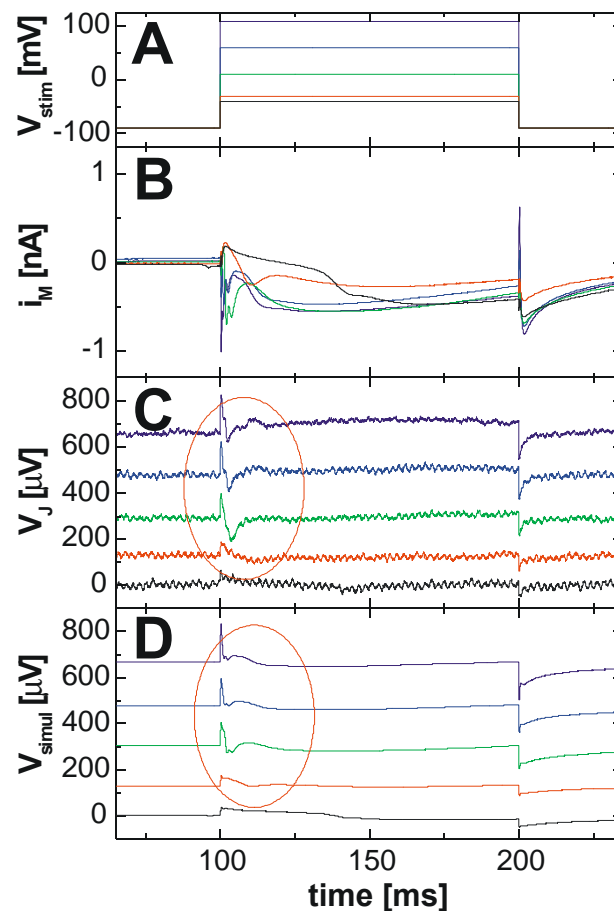


Figure 6-56 Voltage-clamp coupling experiment using a cell from a non-contracting cell layer (2 DIV). The responses in the circled area cannot be simulated in the PSPICE circuit.

In Table 6.9 the data for the PSPICE simulation are shown. The seal resistance has to be scaled to reflect the capacitive responses. Scaling g_J can be explained by scaled capacitive responses V_J^0 . A closer view to the fitted data in Figure 6-57 shows that the initial 20 ms of the extracellular response are not fitted. Here a contribution of the neighbouring cells is influencing the extracellular response.

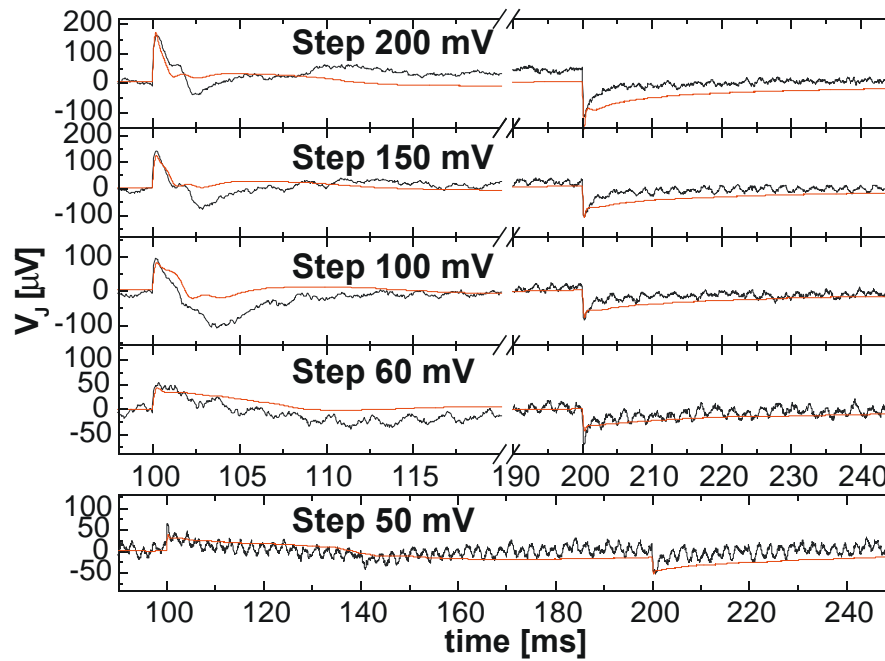


Figure 6-57 Closer view to the fitted data of the voltage-clamp experiment in Figure 6-56. The initial phase of the extracellular responses cannot be modelled. This may be a result of the not included influence by neighbouring cells.

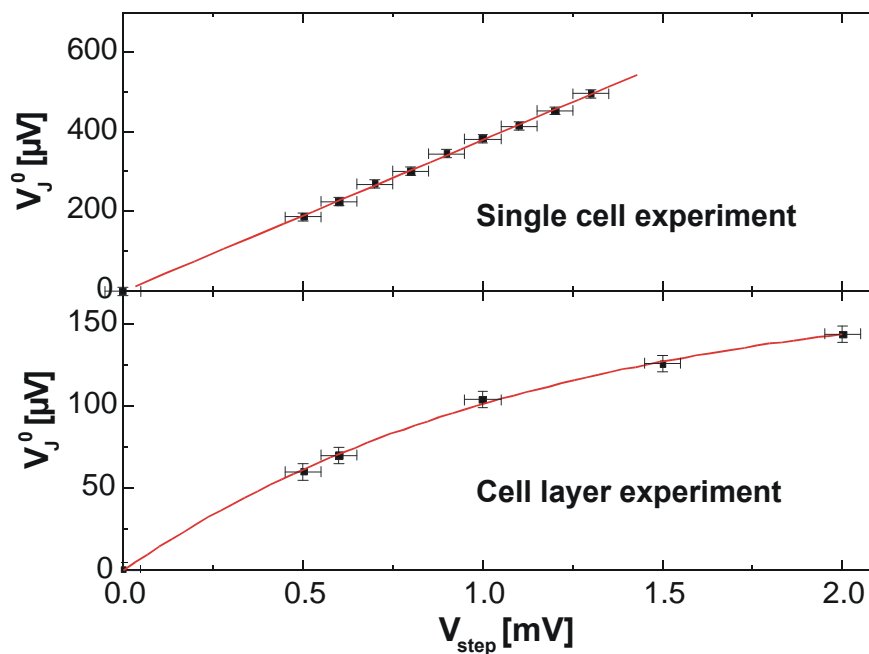


Figure 6-58 Comparison of the extracellular recorded tip height V_J^0 of a single cell experiment using a cardiac myocyte cell and of the cell layer experiment (Figure 6-56).

When the extracellular monitored capacitive tip heights are plotted against the height of the stimulation pulses the non-proportionality can be seen (Figure 6-58).

In comparison to the data of the voltage-clamp experiment using a cell layer the capacitive transients of a single cell are directly proportional to the height of the stimulation pulses. The sealing conductance values g_J of the cell layer experiment are relatively low.

6.3.3 Signal Shapes of Extracellular Recorded Action Potentials from Cardiac Myocyte Layers

The extracellular signals of spontaneous action potentials of cardiac myocyte cell layers are varying in a wide range and have been categorised into 4 different types D1-D4 (Krause, 2000; Sprössler et al., 1999). In Figure 6-59 a simultaneous recording of a cardiac myocyte cell layer using a patch-pipette and a FET sensor is shown.

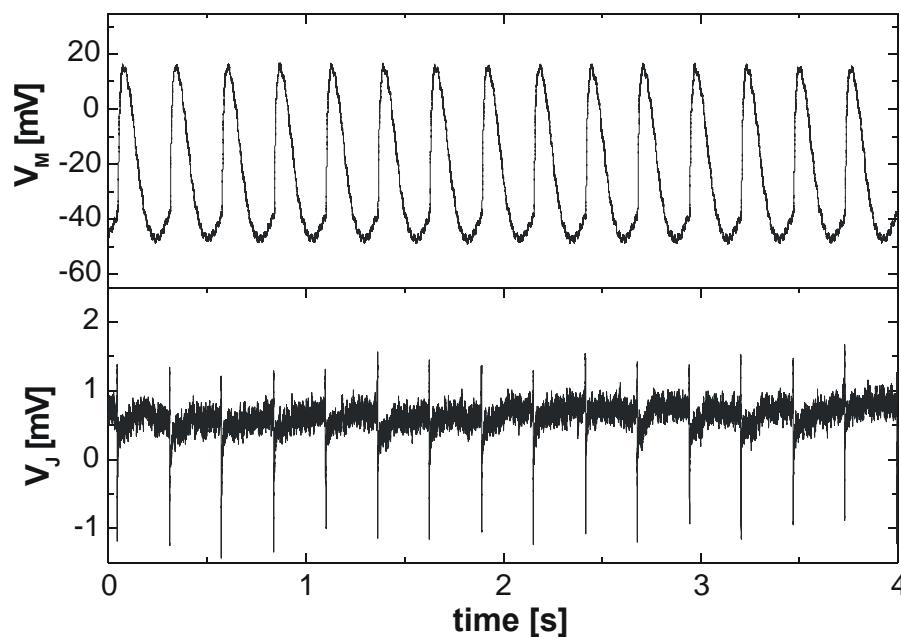


Figure 6-59 Simultaneous recording from a spontaneous beating cardiac myocyte cell layer (7 DIV) on a cellulose coated FET sensor. The upper trace shows an intracellular recording with a patch pipette and the lower trace the extracellular recording of the FET sensor.

As in all previous experiments shown is the extracellular response V_J a composition of capacitive, ohmic, ionic current and concentration-change components. In a cell layer many of these components are not known for the simulation of the responses:

- The capacitive component is dependent on the cell transistor distance (as the sealing conductance g_J scales strongly with the distance) and on the steepness of the rising and falling flanks of the intracellular voltage V_M .
- The ohmic contribution is dependent on the leakage conductance of the cell membrane. This part is neglected and intact cell membranes are assumed.
- The ion currents are not known and will be different for different cell types from the different regions of the heart.
- The responses to the ion concentration change are dependent on the structure of the cell transistor assembly (also strongly dependent on the cell transistor distance). They may enhance the responses to the ion currents and prolong them because of slower diffusion processes.

As in the previous signal simulation (Krause, 2000; Sprössler et al., 1999) the simulation software Oxsoft HEART ver. 4.8 (DiFrancesco and Noble, 1985) is used to model the membrane potential $V_M(t)$ and the specific ion conductances for Na^+ , K^+ and Ca^{2+} during an action potential. For the simulation, the model of a ventricle cell is used (Earm and Noble, 1990). For the maximum specific ion conductances g_M^i of the cell membrane following values are assumed:

- $g_M(\text{Na}^+) = 18.75 \text{ mS/cm}^2$ (see chapter 5)
- $g_M(\text{K}^+) = 7.5 \text{ mS/cm}^2$
- $g_M(\text{Ca}^{2+}) = 8 \text{ mS/cm}^2$

With these values the, simulation software calculates the action potential and the different ion currents over the membrane as shown in Figure 6-60.

For the simulation of the extracellular signal in PSPICE an attached area of 10 % is assumed. For the simulation in HEART a membrane capacitance of $C_M = 200 \text{ pF}$ was used. The same value will be used for the simulation in PSPICE and a membrane resistance R_M of $5 \text{ G}\Omega$. The seal conductance g_J is estimated to 1 S/cm^2 using the simulation of the patch-clamp experiment in Figure 6-56. The membrane voltage $V_M(t)$ is provided as voltage source inside the cell and the currents are independently provided as 10 % of the total values over the attached membrane into the contact area.

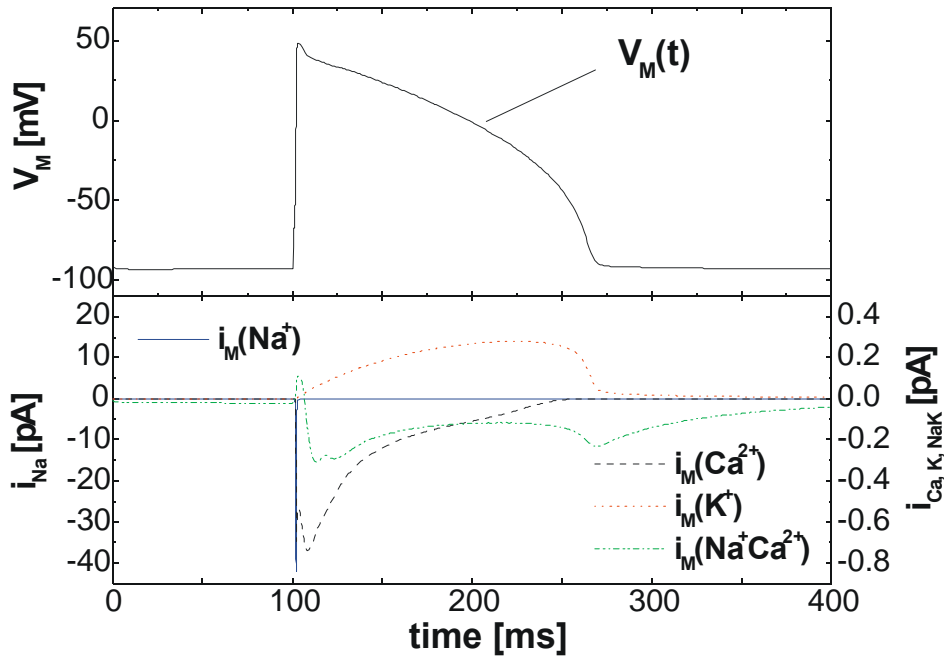


Figure 6-60 Action potential of a ventricle model cell and the ion currents flowing over the membrane during this action potential. The signal was simulated with the Oxsoft HEART simulation software ver. 4.8 (DiFrancesco and Noble, 1985; Earm and Noble, 1990). In the following these data are used as input data for the simulation of the point contact model using PSPICE.

The signal shapes of the extracellular responses to action potentials from cardiac myocyte layers are varying in a wide range. The different shapes are the results of scaling the current contributions of the different ion species with:

$$g_J V_J = c_M \frac{dV_M}{dt} + \sum_{i=Na^+, K^+, Ca^{2+}} X^i i^i \quad (6.1)$$

This has been done in previous works (Sprössler et al., 1999), (Krause, 2000) and the different signal shapes are called D1-D4 types. In Figure 6-61 the four different types were simulated using PSPICE.

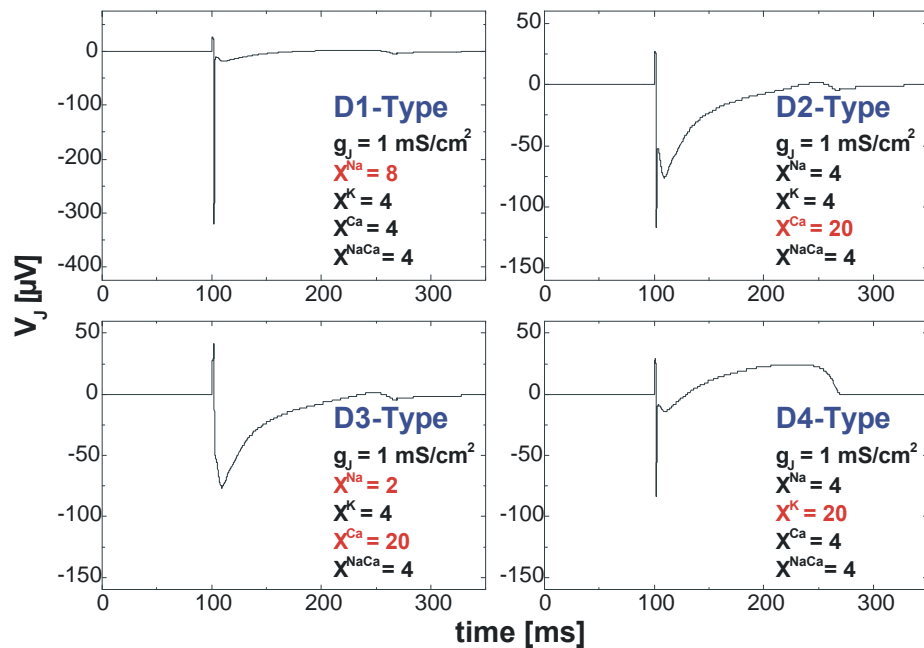


Figure 6-61 Four different signal types with their respective scaling values for the ion currents.

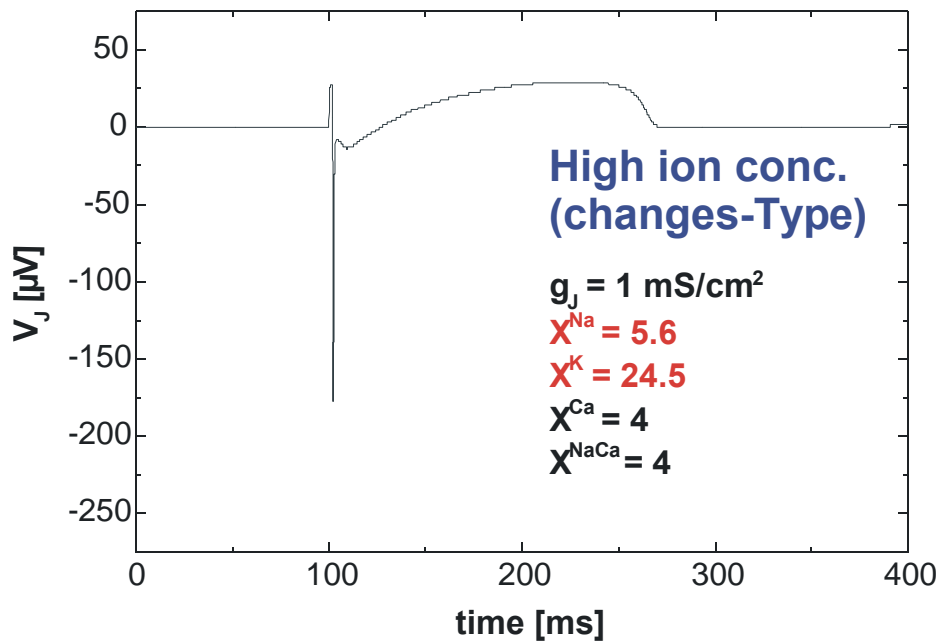


Figure 6-62 The D4 type may be caused by a high ion concentration change in the contact area. For the simulation of this signal type the scaling between the different ion species is similar to the sensitivity of the FET sensors to ion concentration changes (chapter 5), with $X^{\text{Ca}}:X^{\text{Na}}:X^{\text{K}}$ is 1:1.4:5.9.

The D1 type is caused by higher sodium current into the contact area. The D2 and D3 types are very similar, as the calcium current part is scaled 5 times bigger. In type D3, the sodium current is decreased and the quick downward peak is absent. The D4 type is resulting from higher potassium current into the contact area. Using the scaling values for the different sensitivity to ion concentration changes from the previous chapter always results in a D4 signal shape (Figure 6-62), with $X^{\text{Ca}}:X^{\text{Na}}:X^{\text{K}} / 1:1.4:5.9$ (see chapter 5). A fifth main signal shape is called A-Type signal. Here the ion current for all species of ions are decreased and the signal is only caused by the capacitive response to the rising flank of $V_M(t)$ (Figure 6-63).

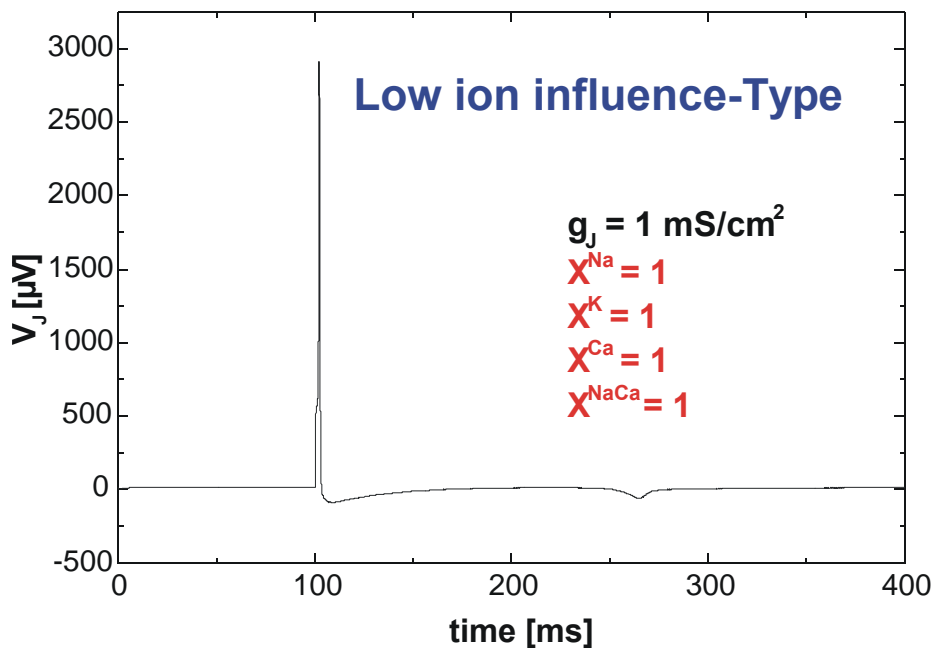


Figure 6-63 If the extracellular signal is weakly influenced by the ion currents the signal only reflects the capacitive response to $V_M(t)$. This type is called A-Type.

The need for scaling the ion currents to simulate the extracellular signal shapes may have the following reasons:

- The ion currents are reflecting the case for a ventricular cell. The culture contains many different kinds of heart muscle cells like Purkinje fibres, pacemaker cells, ventricle cells, fibroblasts... The ion currents and the $V_M(t)$ during an action potential of these cells are different.
- The influence of the ion concentration change to the extracellular signal shape is enhancing the responses of different ion types. Scaling the ion currents with the sensitivity factors from the previous chapter will result in a D4 shape for a ventricular cell.

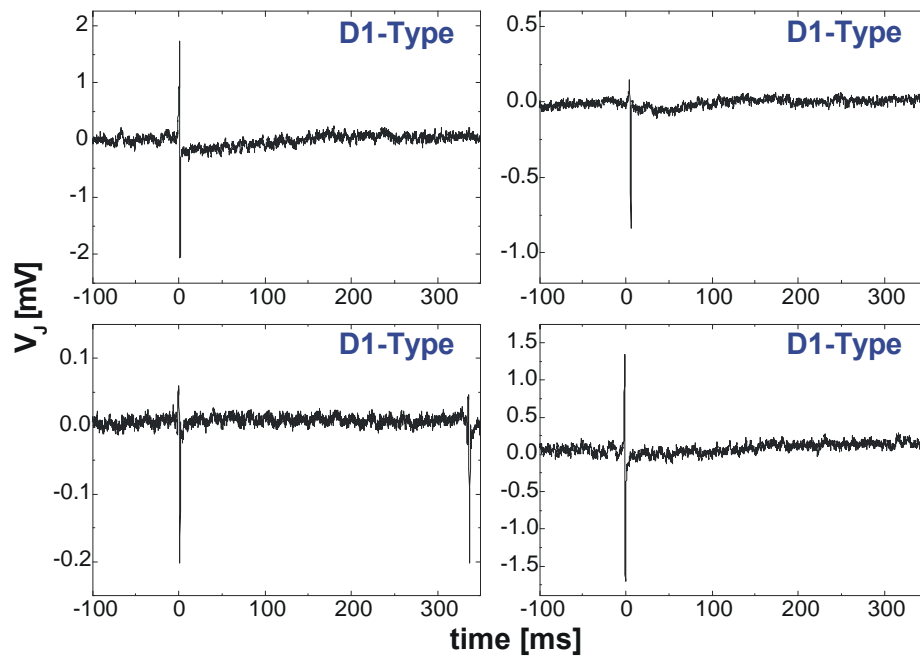


Figure 6-64 D1-Type signal shapes. The ratio between the capacitive part (uprising peak) and the sodium part (down peak) is varying. The lower left signal was obtained with an EGE device, where the observed signal amplitudes are about ten times lower than recorded with FET sensors.

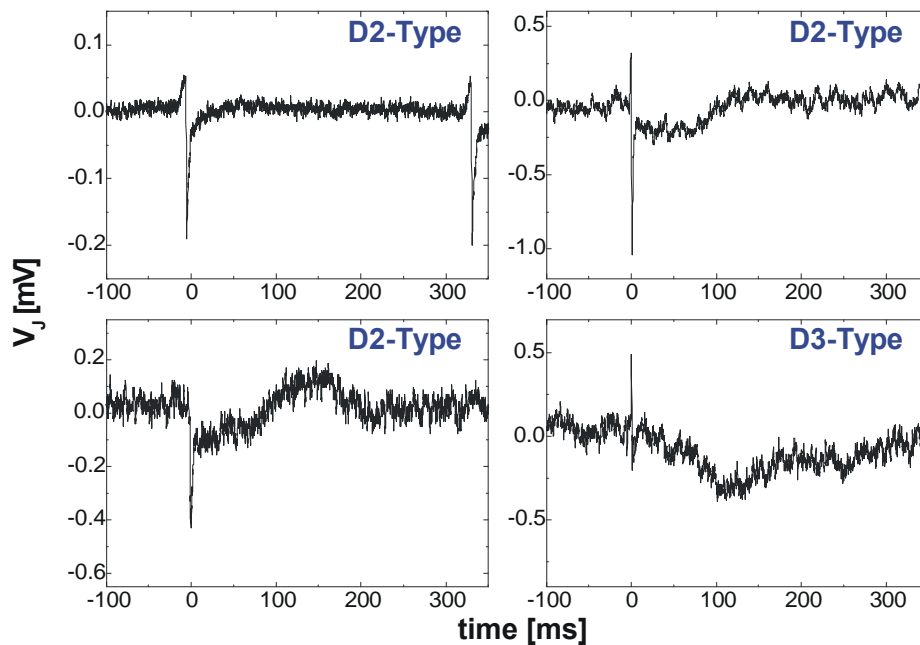


Figure 6-65 D2- and D3-Type signals. The upper left signal is obtained with an EGE device. The D3-Type is a special case of the D2-Type with less sodium activity. Sometimes the capacitive part of the signal is not visible like in the lower left signal.

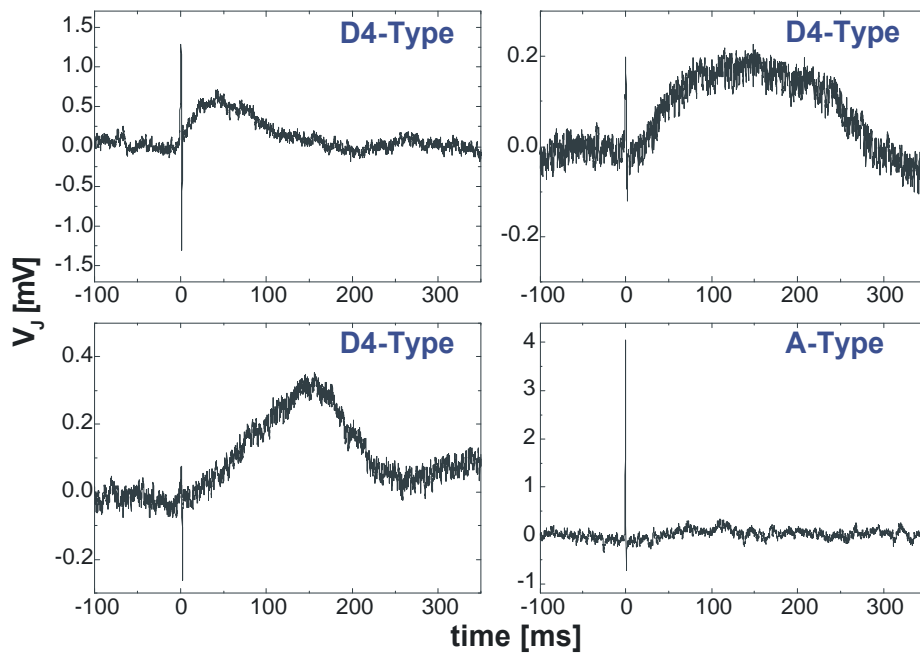


Figure 6-66. D4-Type signal shapes with high potassium activity. The A-Type in the lower left trace is also very often observed.

The most common signal shape was the D1-Type. The passive A-Type was also frequently observed. In all types of signal shapes the total amplitude is strongly influenced by the sealing conductance g_J .

Another indication of the strong influence of the extracellular signals will be explained below. On day 2 to day 3, the cell layer is not completely connected over the whole chip and may be two or more pacemaker centres are counteracting. In some cases the interaction was such that the beat frequency was accelerated by this effect to the maximum frequency of around 250 bpm. The maximum beat frequency is limited by the duration of the single action potential, as the cell must undergo the absolute refractory period before the next action potential can occur. This is of course the mechanism of the cardiac myocyte to safeguard any possibility of a summation action potential (like that occurs in normal skeletal muscle fibre). When the cells got to the point of maximum beat frequency, the beat was stopped completely. After 5-20 s, the beating started again. During the strong acceleration phase, the total baseline of the extracellular signal was shifted to more positive values (Figure 6-67). The positive direction is the direction of the concentration effect for accumulated potassium (Chapter 5). Maybe the signal shift is caused by an accumulation of positive charges in the cleft between the cell layer and the device surface.

In Figure 6-68 the signal shape change during the acceleration period can be seen. The signal shape is shifted from D2-Type (high calcium activity) to D4-Type (high

potassium activity), which indicates a strong dependency of the extracellular signal shape to ionic changes in the cleft between cell layer and transistor surface.

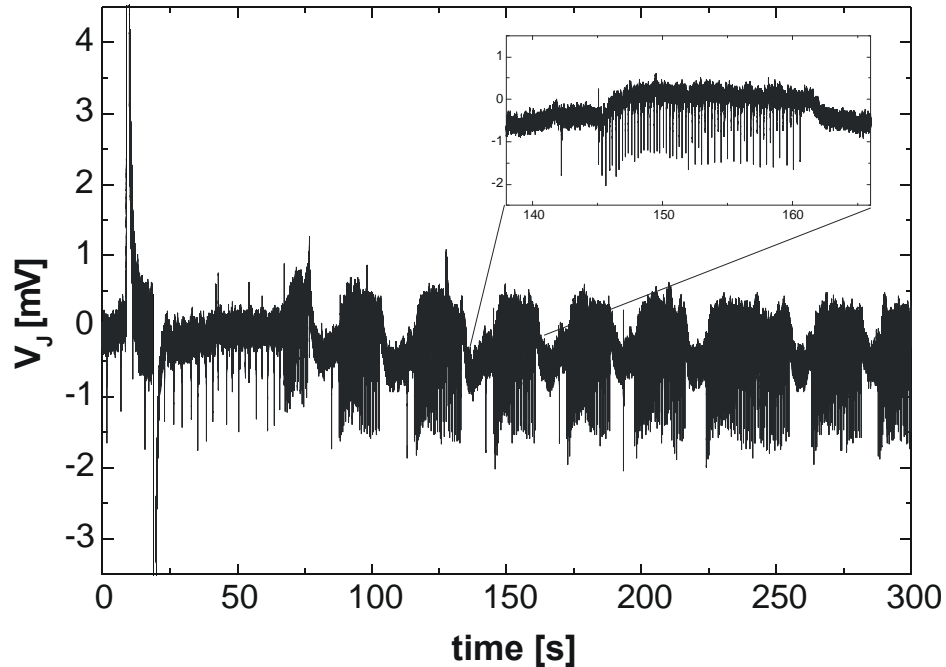


Figure 6-67 Extracellular signal of a cardiac myocyte cell layer (3 DIV) on a cellulose coated n-channel FET sensor. Two pacemaker regions are counteracting and the beating is accelerated to the maximum possible frequency of 250 bpm. During the acceleration phase the baseline of the signal is shifted to more positive values.

The total shift of the baseline is about 0.7 mV, which could be related to an increase in positive ion concentration 0.7 mM (for potassium ions) in the cleft between cells and transistor (Figure 5-25).

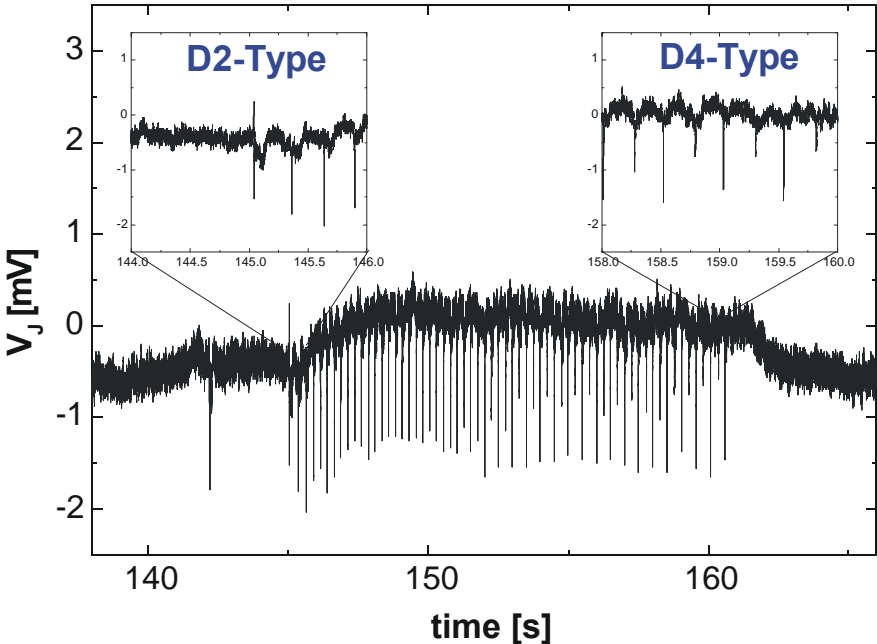


Figure 6-68 At the end of the acceleration phase the signal shape has shifted from D2-Type to D4-Type. In the upper right inset the two different signals caused by the two independent pacemaker regions can be seen.

6.3.4 Upside-Down Measurements

To further investigate the relationship between the extracellular signal amplitude and the distance between the cells and the sensor, an upside-down measurement was performed. The cells were cultured for 4 days on fibronectin coated 2 mm diameter glass substrates. The glass substrates were removed from the incubator and placed the cell surface down onto the FET devices (Figure 6-69).

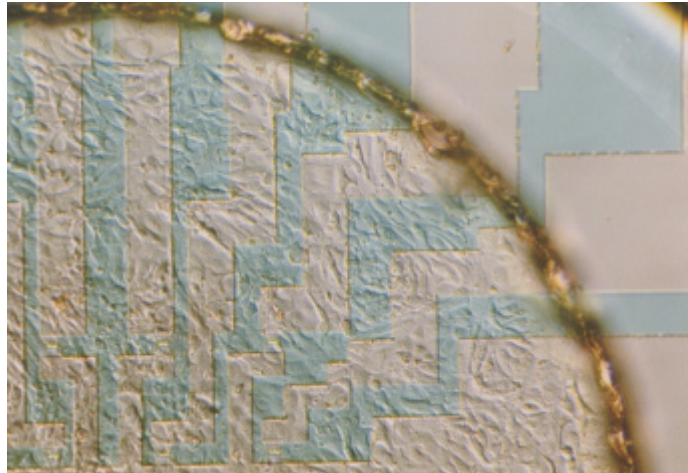


Figure 6-69 Cardiac myocyte cells (4 DIV) were cultured on glass substrates with 2 mm diameter. The glass supports were then placed upside-down onto the sensor surfaces. The image shows the edge of the glass substrate on the transistor structure. The cells are sandwiched between the two glass surfaces.



Figure 6-70 With two glass pipettes of the double patch-clamp set-up (Figure 6-71) gentle pressure was given to the backside of the glass substrate. This decreased the cell-transistor distance and extracellular signals with amplitudes up to 12 mV were recorded.

The double patch-clamp set-up offered the possibility for *in vitro* positioning of the substrate with two glass pipettes (Figure 6-71). Very fine, microscopic movements in x- and y-directions were possible. The substrate could even be rotated and the cell-containing substrate was placed over the FET gates.

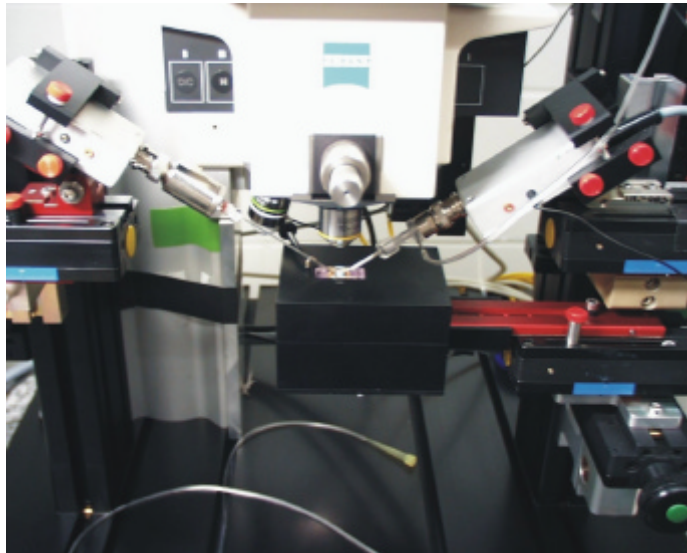


Figure 6-71 With the micromotors and the two patch-clamp heads very fine pressure was applied on the backside of the glass substrates.

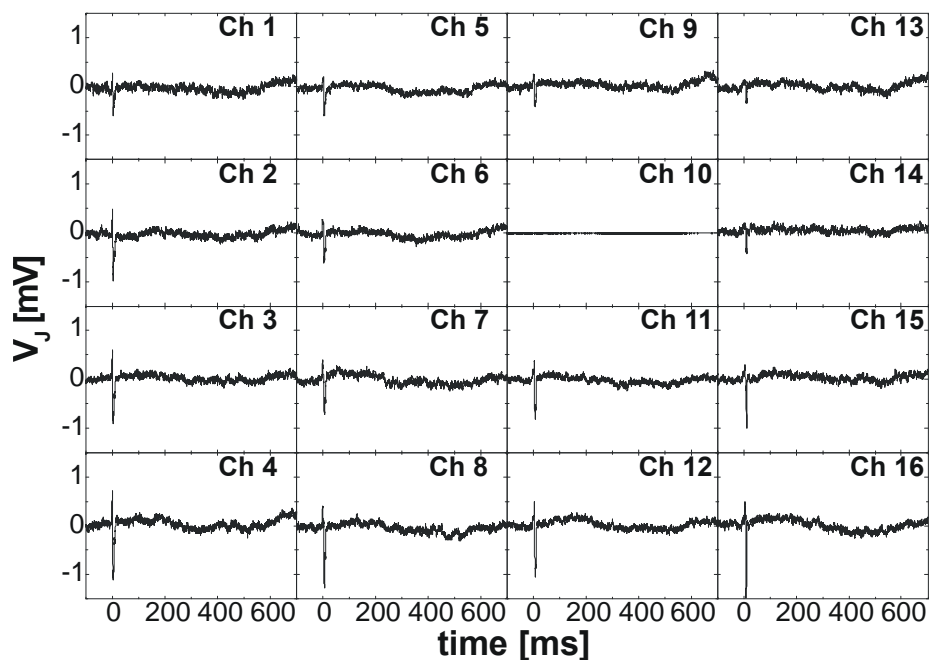


Figure 6-72 Signal shapes without pressure. 15 out of 16 channels are recording a signal from the cardiac myocyte layer. The largest signal amplitudes are about 2 mV, which is a standard value for the normal cultures.

With a very slight movement in the z-direction, it was possible to apply some pressure at the backside of the substrate and push the cell layer further onto the sensor device. In Figure 6-72 it can be seen that the positioning of the substrate was very successful as 15 out of 16 channels showed an extracellular recording. The arrangement of the channels in the figure is compatible to the positions of the gates on the sensor. The highest amplitude shows channel 16 with about 2 mV.

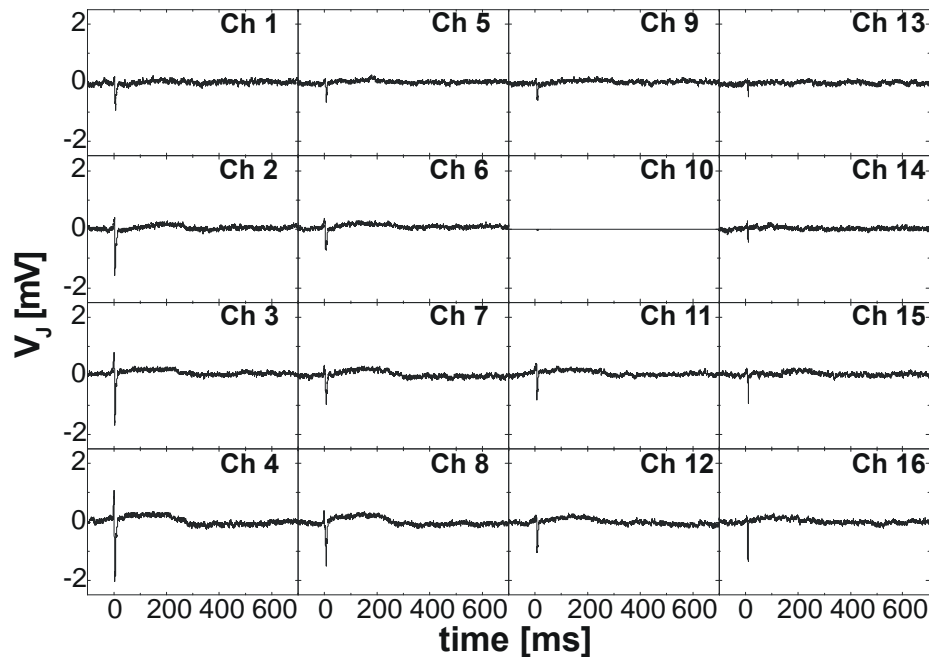


Figure 6-73 Signal shapes with very gentle pressure applied. The signal amplitude in the lower channels is brought up to 3 mV and a slow part of the signals (D4-type) becomes visible.

Applying very gentle pressure on the backside of the substrate (Figure 6-73) increased the amplitude of the extracellular signals. Here channel 4 shows the highest amplitude of about 3 mV. It can be seen that the amplitude increase was higher at the lower channels (ch. 2, 3, 4, 7, 8, 12, 16), which indicates that the pressure was not applied in the middle of the substrate.

Further increase of the pressure resulted in maximum amplitudes of 5 mV in channel 4 (Figure 6-74). The signal shape of the lower channels has shifted from D1-Type to D4-Type, which may indicate a strong dependency to ion concentration changes between the cells and sensors (Figure 6-62). The total concentration change should increase as the volume of the cleft gets smaller.

With the maximum pressure applied, the signal amplitude of channel 4 went up to 12 mV, which was the highest extracellular signal recorded in the present study.

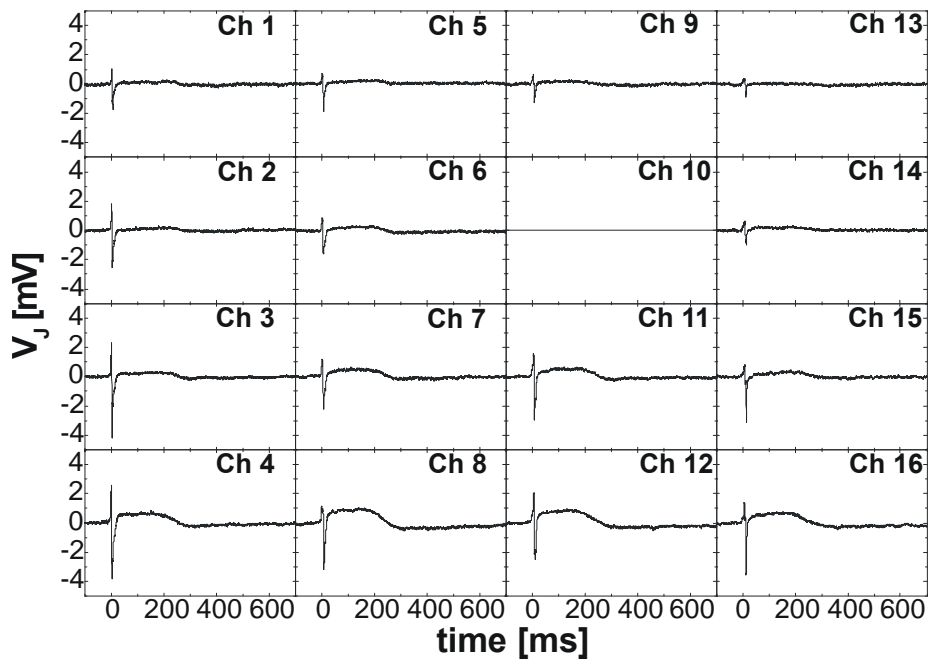


Figure 6-74 Higher pressure at the cells. The signal amplitude in the lower channels is higher, because the pipettes were not exactly placed in the middle of the substrate. The signal amplitude went up to 5 mV and a clear slow part of the signals becomes visible in nearly all channels.

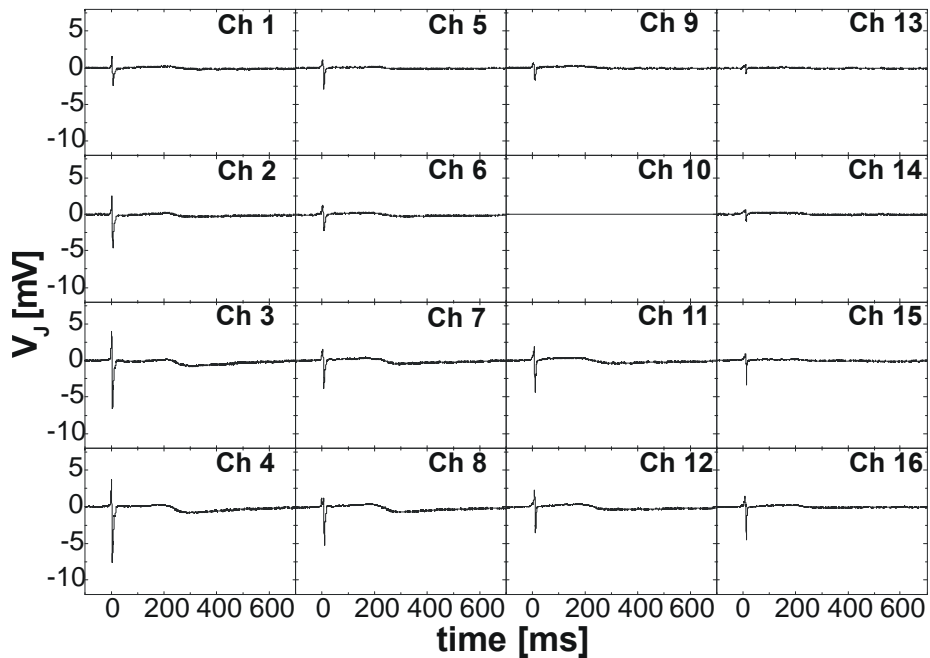


Figure 6-75 Highest pressure on the cells. Channel 4 shows a signal amplitude of 12 mV, which is the highest signal monitored in this work.

A closer look at the signal of channel 16 in Figure 6-74 shows that the signal shape of the higher responses totally correspond to the situation for a high dependency of the signal shape to ion concentration changes (Figure 6-62). By comparing the signal with the PSPICE simulation in Figure 6-62 it was found that the extracellular response to the potassium signal is delayed. The time constant for the decay after the maximum potassium signal was reached (Figure 6-76) corresponded to the observed signal decay time in the voltage-clamp experiment with the single neuronal cell in chapter 5 (Figure 5-19).

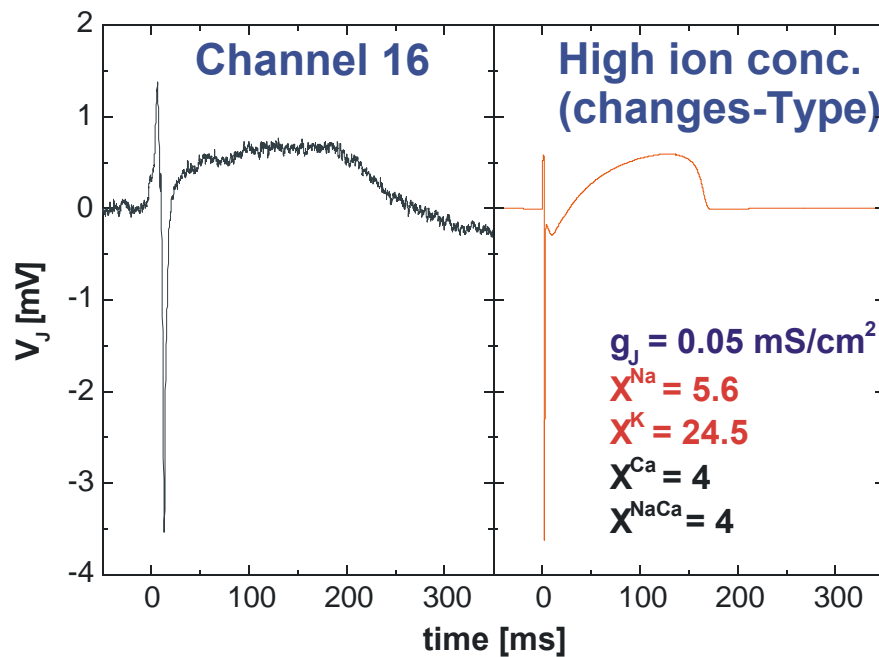


Figure 6-76 Comparison of the signal of channel 16 in Figure 6-74 with the simulation of the high ion concentration change dependency in Figure 6-62. The signal amplitude can be modelled by assuming a very low seal conductance of $g_j = 0.05 \text{ S/cm}^2$. The potassium response has a much longer decay time as the simulated signal. The time constant for this decay corresponds to the time constants fitted to the single-cell responses in Figure 5-19.

The slowed signal recovery to the baseline may be caused by the accumulation of extracellular potassium ions. However the interpretation of the signal shapes is very uncertain for this particular experiment. The cells were highly stressed between the two glass substrates. Cardiac myocytes are known to have stretch-activated ion-channels in their membrane. Maybe an additional influence of these channel types has to be taken into account for the upside-down measurements.

6.4 The Cell-Transistor Chip for Pharmacological Screening

^[1]Many pharmacological bioassays rely heavily on the appropriate use of *in vitro* techniques to acquire data of drug profiles before these drugs can proceed to further stages of evaluations. Most of these methods are invariably short-term and are not suitable for long-term monitoring of drug actions or cellular recovery upon drug intervention. The use of bioelectronic interfaces, such as our FET- and EGE-chips could provide us with a system that is sensitive enough to detect changes of the extracellular electrochemical gradients; durable enough to be re-used for many times and capable of recording for many hours in the absence of an operator. The surfaces of the chips (silicon oxide), were treated with various adhesion proteins such as laminin and poly-lysine, with fibronectin as cellular glue and with nitro-cellulose for unspecific cell adhesion (see paragraph 6.1). The cultured dissociated cardiac myocytes were spontaneously active within 24 to 48 hours after initial plating. Recordings of beating myocytes syncytium were generally taken on post day 3 of culture to avoid the periodicity effects of different pacemaker regions (Figure 6-67).

All known cardiac stimulants (isoproterenol, norepinephrine) and relaxants (verapamil, carbamylcholine, SDZ PCO400) showed their characteristic effects on the heart cells in terms of the changes of beat frequencies in the absence or presence of corresponding agents. If the myocytes are in a complete syncytium on each chip it is possible to detect ionic changes (paragraph 6.3). The system also offers an opportunity to study the interconnections and communications between different cells. Furthermore, the changes of signal shapes in the presence of different agents could also be detected. This paragraph demonstrates how versatile and sensitive this recording system is in discrimination of different ionic signal shapes. The cell-transistor hybrid system will possibly have the potential to replace some currently employed *in vitro* methods and it certainly offers an alternative, which can substantially reduce animal use in pharmacological experiments.

For many decades, the evaluations of the effects of pharmacologically active agents have been based on a variety of functional *in vitro* bioassays. These could be in a form of a tissue-organ bath to monitor mechanical and pressure changes (e.g. Langendorff preparations) or electrophysiological techniques (e.g. patch-clamp recordings). However, all the currently available methods can only be used for short-term recordings (8 to 10 hours at most) and, in most cases, the tissues or cells are irretrievably damaged.

^[1] Parts of this chapter are published in: (Yeung et al., 2001 b), (Ingebrandt et al., 2001)

Furthermore, all the drug studies that utilise electrophysiological techniques are extremely time consuming. A reliable long-term recording system, which is non-invasive, efficient, reproducible and durable (>24 hours to days), would be useful, when the recovery of cellular functions upon interventions are important to the investigation. The recent use of bio-microelectronic interfaces may provide the answer. Not only do these devices provide a mean of long-term recording for the monitoring and assessment of cellular functions but they also reduce the use of animal tissues significantly as only about 20 thousand or fewer cells are needed on each device.

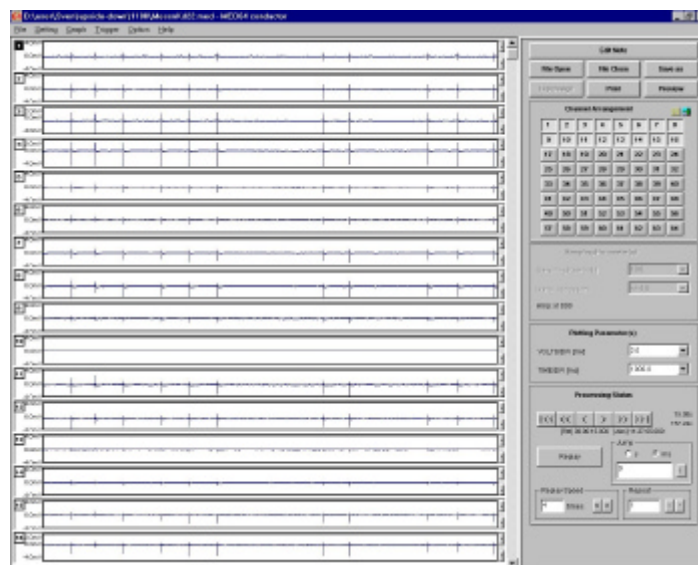


Figure 6-77 With the fast data acquisition card (NI 6110, National Instruments, Germany) and the recording software Med64 conductor (MED64cond., Panasonic, Japan) it is currently possible to perform an on-line sampling of 16 channels.

The use of *field effect transistors* (FET) as bio-electronic interfaces, as well as multielectrode arrays, with life cells recordings in recent years has been well documented (Krause et al., 2000; Offenhäusser et al., 1997; Sprössler et al., 1998; Sprössler et al., 1999). Despite of many attempts to demonstrate the use of these microelectronic devices in the past few years, none have shown any real promise as to their reliability in *in vitro* functional study applications. Furthermore, the signal strength is often only in the range of tens to hundreds of microvolts, coupled with low signal-to-noise ratios, often no identifiable signal shapes can be recognised. By using a fast data acquisition card (NI 6110, National Instruments, Germany) and the recording software Med64 conductor (MED64cond., Panasonic, Japan) it is currently possible to perform an on-line sampling of 16 channels (with the potential of recording up to 64 simultaneously) (Figure 6-77). Further reduction of the noise level was achieved with the introduction of a new modified power supply (chapter 3).

This paragraph presents the steps that have been taken to increase the reliability of the system and shows high amplitude extracellular recordings of dissociated cardiac myocytes on FETs with excellent signal-to-noise ratios.

6.4.1 Pharmacology

To validate the applicability of FETs in pharmacological bioassays, some well-established cardio-stimulants (isoproterenol, ISO and arterenol bitartrate (norepinephrine), NA) and relaxants (verapamil, VP; carbamylcholine, CARB; SDZ PCO400, SDZ) were used. Atropine (ATROP, 10 μ M) was used to antagonise the response of CARB in drug combination experiments. The appropriate concentrations of the pharmacological agents used were prepared using the external solution. A simple drug-cycle paradigm was employed. A basal beat frequency of cultured myocytes on a particular FET or EGE was recorded for 60 s. This is followed by completely replacing the external solution with one that containing either ISO (10 nM, 100 nM, 1 μ M) or NA (10 nM, 100 nM, 1 μ M). After recordings in the presence of drugs for 60 s have been obtained, the cell layer was washed gently 5 times at 1 min intervals. Same procedures were carried out with the relaxants. In drug combination experiments, different agents were administered on the cell layer in each corresponding group (A to D) in the following order as indicated below.

- A: NA vs CARB vs ATROP (0.1, 1, 10 μ M)
- B: VP vs NA (1, 10 μ M)
- C: VP vs ISO (1, 10 μ M)
- D: NA vs CARB (0.1, 10 μ M).

Solutions and Reagents

Cell culture reagents were obtained from Sigma: F10 HAMS (N1387), HBSS (H6648), FCS (F7524), pen-strep mixture (P0906), L-glutamine (G7513), trypsin-EDTA (T4049), DNase II (D8764). ITS (51300-036) was obtained from Gibco.

The different concentrations of all the pharmacological agents used in this study were made up using the external solution. The stock solutions of all the agents were made up using appropriate vehicles (in bracket): Isoproterenol bitartrate (1/10N HCl), arterenol bitartrate (1/100N HCl), verapamil hydrochloride (water), carbamylcholine chloride (water), and atropine sulphate (water). They were all purchased from SIGMA.

6.4.2 Dose-response Curves for Stimulants and Relaxants

The stimulatory effects of isoproterenol and norepinephrine on myocytes

Administration of ISO and NA caused the beat frequency of the cells to increase. Figure 6-78 shows the response of one channel to the administration of 1 μM ISO.

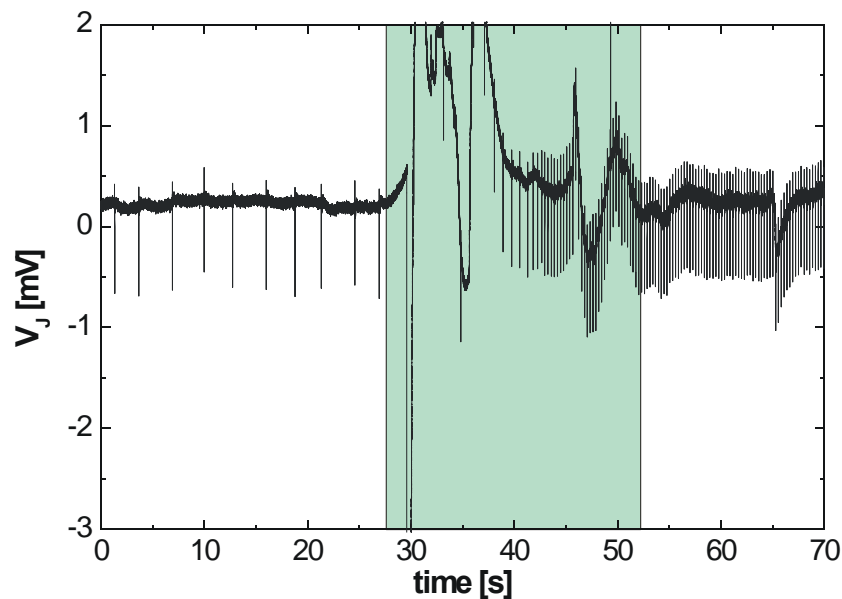


Figure 6-78 Response of the cardiac myocyte cell layer to the administration of 1 μM ISO. The drug adding was done between 28 and 52 s by complete exchange of the extracellular medium with drug containing medium.

The partial concentration-response curves for both drugs are shown in Figure 6-79. The results are expressed as changes in beat frequency (C vs T), $\text{bpm} \pm \text{s.e.m}$ in percent normalised to the end frequency of each experiment. Therefore, 100 % implied that no further increase of heartbeat was observed as the concentration was further increased. The difference was analysed using Student's unpaired t-test. ISO gave a slightly higher stimulatory effect ($P > 0.05$, not significant). In Figure 6-80 the recorded signal showed a marked change of the shape after the drug was administered. The slow signal after the first quick down peak is related to an elevated Ca^{2+} channel activity in the presence of 0.01 μM NA (D2-Type).

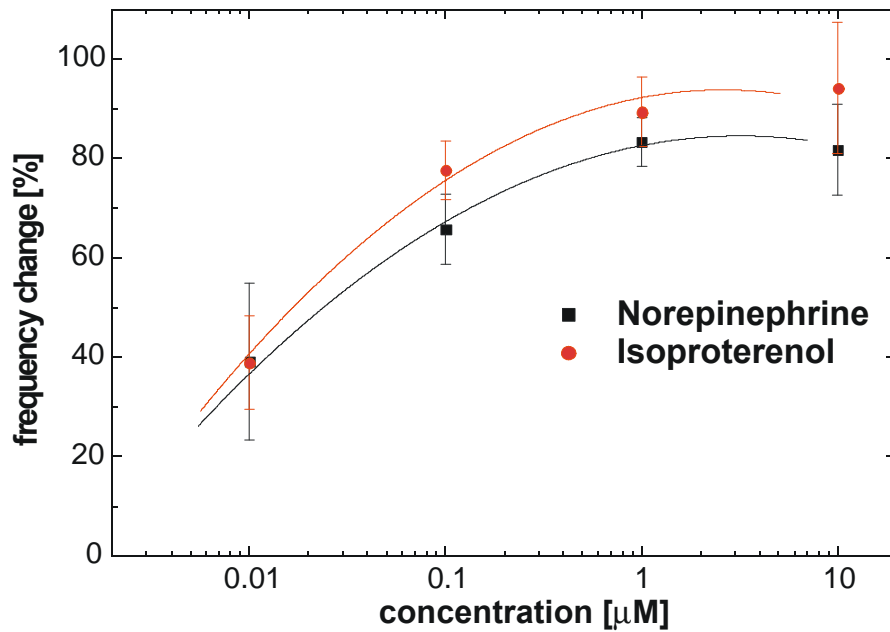


Figure 6-79 Stimulatory effects of isoproterenol and norepinephrine on cardiac myocytes cell layers on extracellular sensors. The results are expressed as changes in beat frequency (C vs T), bpm \pm s.e.m in percent normalised to the end frequency of each experiment.

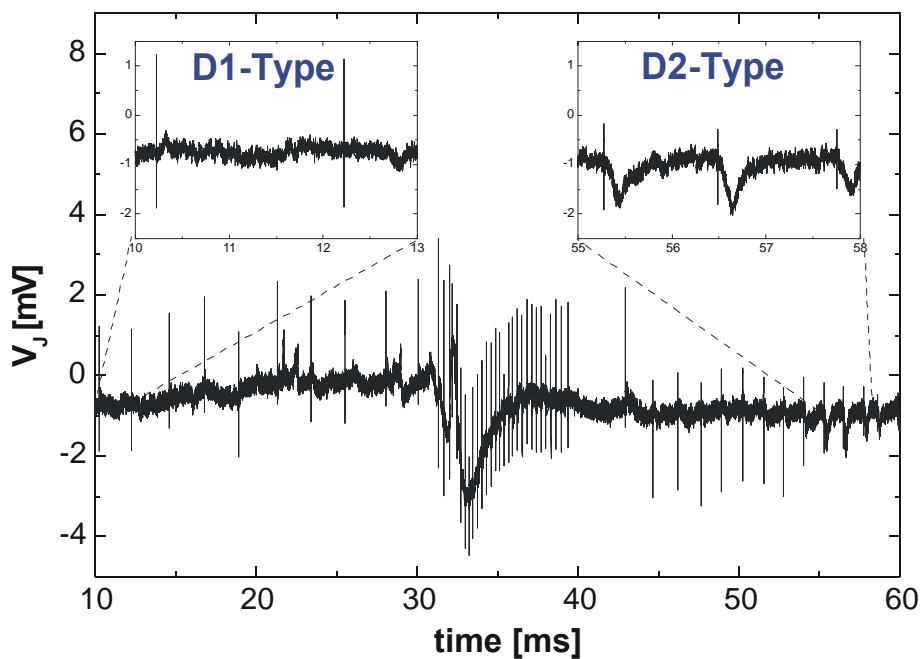


Figure 6-80 Signal shape change as response to the administration of $0.01 \mu\text{M}$ NA (between 30 and 40 s) to the cardiac myocyte cells. The signal shape changed from D1-Type to D2-Type, which is attributed with higher calcium activity caused by the cardio-stimulant.

The inhibitory effects of carbamylcholine, verapamil, and SDZ PCO400 on myocytes:

Administration of these relaxants caused the beat frequency of the cells to decrease. The partial concentration-response curves for the three drugs are shown in Figure 6-81.

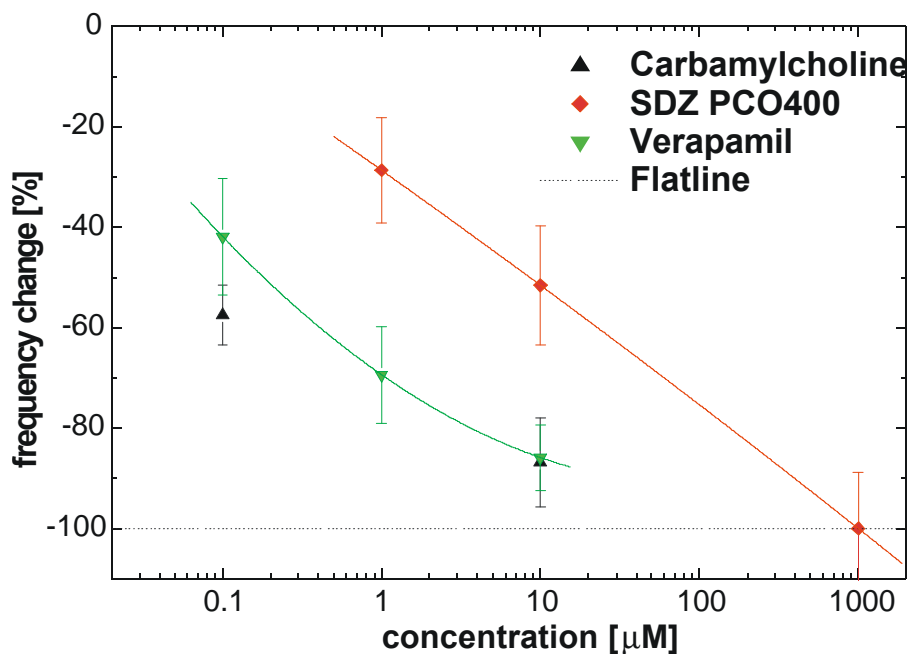


Figure 6-81 Inhibitory effects of carbamylcholine, verapamil, and SDZ PCO400 on myocytes.

The results are expressed as changes in beat frequency (C vs T), bpm \pm s.e.m in percent normalised to the start frequency of each experiment and 100 % implied the complete cessation of beat (ie, flatline). CARB was the most potent with relative potency of CARB>VP>SDZ in this preparation.

The effects of sequential administration of isoproterenol, carbamylcholine, atropine, SDZ PCO400, and verapamil on myocytes

In four independent experiments (A to D), we investigated if the cells could undergo rapid sensing to the changes of the environment and the stability in long term experiments.

A) NA, CARB, ATROP (0.1, 1, 10 µM):

After the administration of NA (0.1 µM) the heart rate elevated from 16 ± 2 (n = 9) to 235 ± 12 bpm (n = 9) (P<0.001). The heartbeat went down to 7 ± 1 bpm (n = 9) by complete exchange of the cell media with medium containing 1 µM CARB. The

inhibitory effect of CARB was reversed to 150 ± 14 bpm ($n = 9$) when $10 \mu\text{M}$ ATROP was administered.

B) VP, NA (1, 10 μM):

Verapamil ($1 \mu\text{M}$) reduced the initial beat frequency from 250 ± 20 bpm ($n = 11$) to 8 ± 1 bpm ($n = 11$). The heart rate was partially restored (110 ± 10 bpm ($n = 11$)) when $10 \mu\text{M}$ NA was subsequently administered.

C) VP, ISO (10, 10 μM):

The adding of a high concentration of VP ($10 \mu\text{M}$) caused a complete cessation of the basal beat frequency of 105 ± 8 bpm ($n = 6$). After 3 min flatline, albeit very slowly, some activity of the cell layer was restored by adding ISO ($10 \mu\text{M}$) (17 ± 3 bpm ($n = 6$)).

D) NA, CARB (0.1, 10 μM):

With the administration of $0.1 \mu\text{M}$ NA the beating of 14 ± 3 bpm was elevated to 96 ± 8 bpm ($n = 5$). This effect of NA was reversed by CARB ($10 \mu\text{M}$) to 7 ± 2 bpm ($n = 5$).

The responses to the drugs administered showed that the sensor could detect rapid cellular physiological changes. The cells were stable over several hours and in some cases the cells completely recovered after a washing procedure and a couple of hours in the incubator. In principle, it would be possible to keep the cells on the chip and execute a long-term experiment over several days.

6.4.3 Signal Shape Changes induced by Drugs^[1]

In order to obtain different extracellular signal shapes, the respective ion currents for sodium, potassium and calcium $i^{Na, K, Ca}$ have to be scaled with factors $X^{Na, K, Ca}$ (Eq. 6.1 in paragraph 6.3). With the knowledge of the coupling mechanism and how the signal shapes of the extracellular recordings are related to different ion currents, it is possible to distinguish the corresponding current activity. Once a certain drug is administered, the activity of the ion-channels in the membrane is either hindered or stimulated. It is possible to detect the signal shape changes as result of the drug response by comparing the signal shapes before and after drug administration (Figure 6-80).

In the following only some examples for shape changes are shown. In total the number of shape changes for the different drugs were:

^[1] Parts of the results shown in this paragraph are published in: (Ingebrandt et al., 2001)

- ISO: 58 channels recorded; 16 channels changed shape 27.6 %
- NA: 90 channels recorded; 20 channels changed shape 22.2 %
- VP: 90 channels recorded; 27 channels changed shape 30.0 %
- NA: 39 channels recorded; 20 channels changed shape 51.3 %

It can be seen that the changes of the signal shapes are not reliable enough for the detection and screening of drug responses. In many cases the signal-to-noise ratio was too low to detect any changes of the signal shapes reliably. If a signal shape change was recorded it was always in the right direction (e.g. if a channel blocker blocked the calcium activity, the signal shape caused by calcium current was diminished). With a better signal-to-noise ratio or the use of only the very clear signal shapes the reliability of the shape change effects would be much higher.

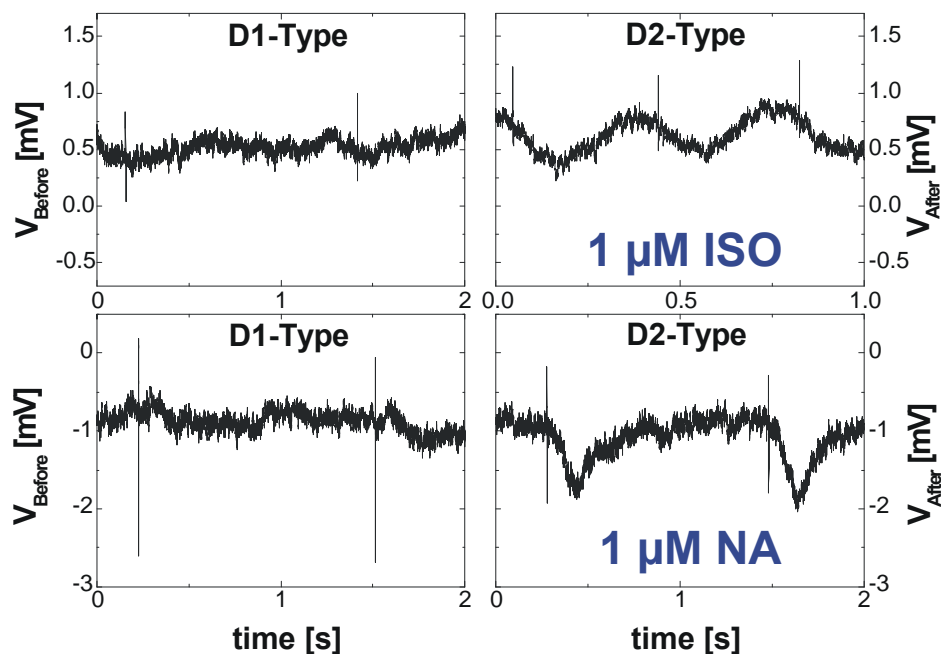


Figure 6-82 Shape change of the extracellular signal caused by administration of ISO and NA. In both cases a shift of D1-Type to D2-Type was observed, which corresponds to an increased Ca^{2+} activity.

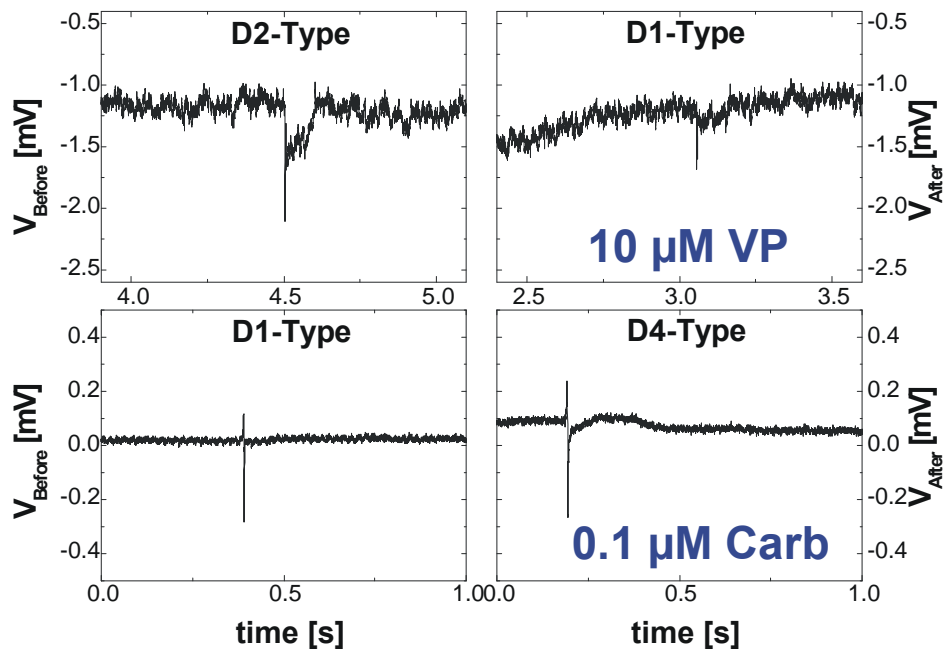


Figure 6-83 Shape change of the extracellular signal caused by administration of VP and CARB. VP blocks the calcium entry into cells, whereas CARB opens potassium channels.

In Figure 6-82 the effects of the two stimulants ISO and NA are shown. The results showed that ISO and NA caused an increased in Ca^{2+} signal, as they are known to open Ca^{2+} channels of the membrane. Both signal shapes shifted from D1-Type to D2-Type. In Figure 6-83 the inhibitory effects of VP and CARB are shown. VP diminished the Ca^{2+} signal whereas CARB increased the K^{+} signal shape.

6.4.4 Signal Velocity in the Cell Layer

The signal velocity within a syncytium of cardiac myocytes can be calculated. After 4 DIV the cell layer is beating as a whole ‘model organ’, where 1 region of the layer predominates the speed of contraction. From this region, the signal is transmitted over the gap junctions throughout the whole layer. The signal spreads in a circular manner, from the central pacemaker region, over the whole layer. The distribution of the sensitive spots in a 4x4 array (with distances of 100 or 200 μm) detected a delayed in signal recording. If many channels are recording a signal, the position of the pacemaker cell and the signal velocity in the cell layer can be determined.

In the following discussion a cellular signal with arrhythmic behaviour was observed. The beating rate of the cell layer (2 DIV) was not stable. As reason for this effect it was assumed that several pacemaker regions are counteracting. Once the beating rate accelerated the signal became slower in the syncytium. In Figure 6-84 the

signals of a cardiac myocyte layer (2 DIV) on a Nitro-Cellulose coated n-channel FET array are shown.

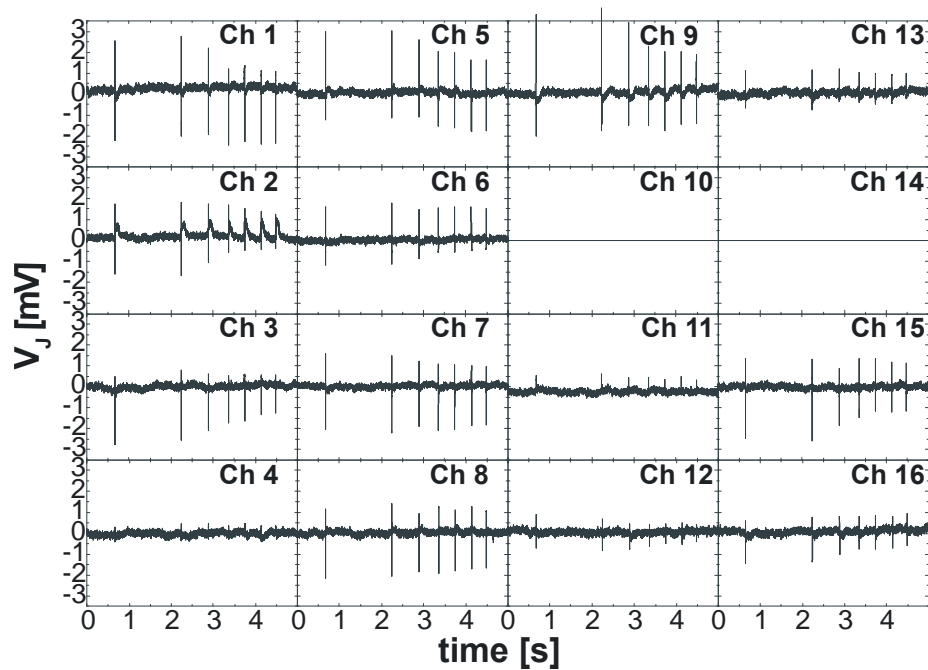


Figure 6-84 Unstable beating rate of a relatively young cell layer (2 DIV) on a Nitro-Cellulose coated FET array.

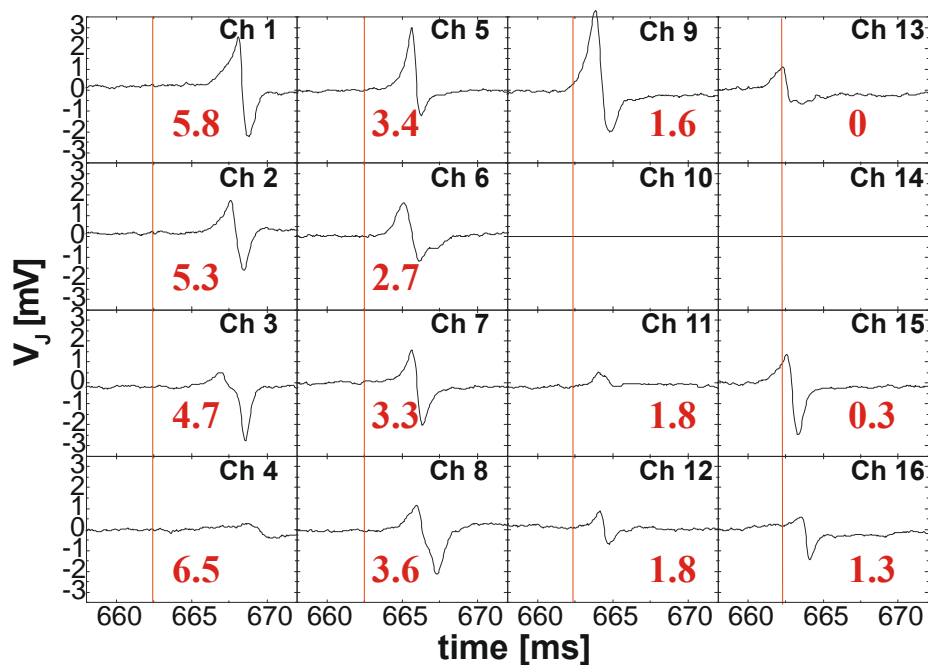


Figure 6-85 Time delays (in ms) of the first signal shown in Figure 6-84. The signal was propagating from the upper right corner (0 ms) to the lower left corner (6.5 ms) of the array. The signal velocity was: $v \sim 0.17$ m/s.

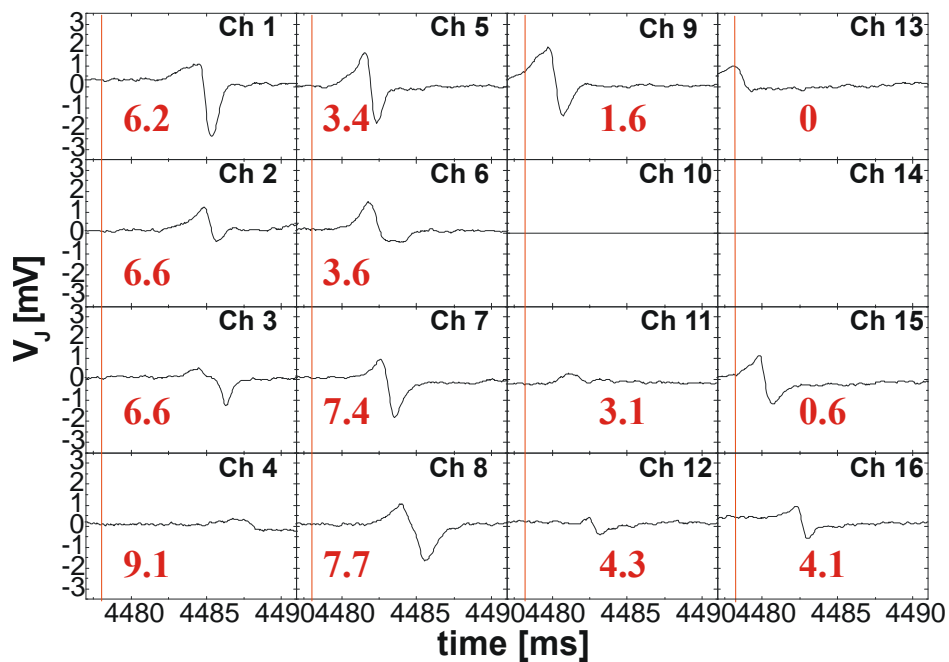


Figure 6-86 The last signal of the trace shown in Figure 6-84 propagated slower and the signal amplitudes were weaker. Calculated out of the higher time delays the velocity of this signal was $v \sim 0.12$ m/s.

With cell layers cultured for a longer period (> 3 DIV) this periodical effect was not observed. In Figure 6-87 a stable signal of a cardiac myocyte layer (5 DIV) cultured on a Nitro-Cellulose coated p-channel FET is shown.

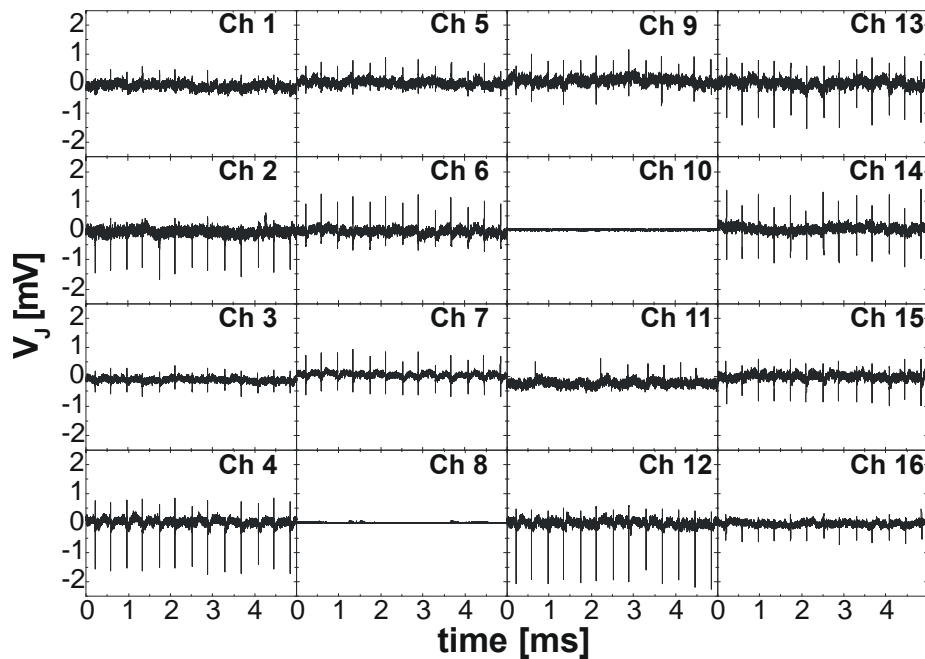


Figure 6-87 Stable signal of a cell layer (5 DIV) on a p-channel FET (156 ± 5 bpm).

In the next plot the first, the fifth and the seventh signal (shown in Figure 6-87) were overlaid by shifting in time and the signal velocity was calculated.

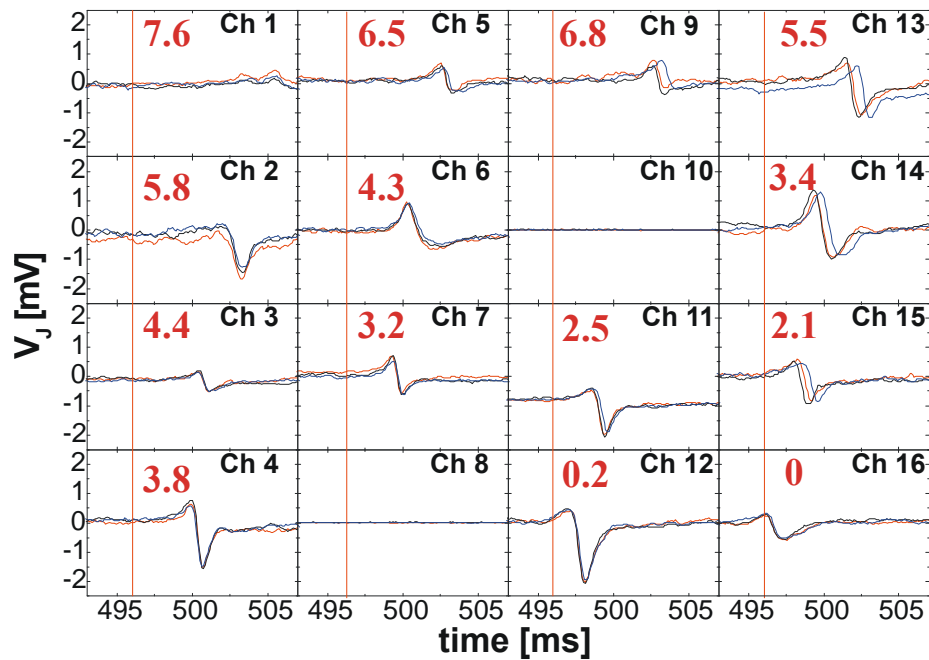


Figure 6-88 Three overlaid responses from the cell layer shown in Figure 6-87. The signal was propagating from the low right corner to the upper left corner, as indicated by the time delays. The velocity was calculated to $v \sim 0.15$ m/s. The propagation of the third signal to the upper right corner was slightly delayed but the error in velocity was below 0.005 m/s.

The system has shown its capability for tracking the signal velocity inside of the syncytium. For a qualitative examination of drug induced signal velocity changes a software routine would be desirable. It was shown that the signal velocity for stable signals could be measured with a good reliability using this system.

Chapter 7

Conclusion and Outlook

Three different goals have been addressed in this thesis:

- A further improvement of the existing set-up and a further development in chip design for extracellular recordings
- A deeper understanding of the mechanisms in cell-transistor coupling and an extension of the existing Point Contact Model
- The applicability of the cardiac myocyte-transistor hybrid system in pharmacological bioassays

Technical Improvements:

A new type of FET device for extracellular recordings having backside contacts etched through the chips has been developed. With this new design, a larger free area on the transistor surface is available. The chip design of the backside contacts was adapted to the contact board of a special ceramic chip carrier. With the use of the flip-chip

technique previously introduced by Krause (Krause, 2000), it was possible to encapsulate the chip without using the standard wire-bonding concept. The former used funnel for the covering of the bondwires was no longer needed and the sensor offers a flat encapsulated surface for culturing of whole tissue slices and for the adaptation of microflow systems (Thiébaud et al., 2001).

The set-up for extracellular recording was further improved by using a battery power supply. This completely disconnected the whole system from the main voltage supply, which significantly decreased the amount of interspersed noise.

A new concept of signal transduction with metal microelectrode devices was introduced. In this case, metal electrodes are directly connected to the gates of standard low-noise junction field effect transistors (JFETs). The JFETs are operating in the low frequency range, where the biological signal transduction occurs (0.1-5000 Hz), with a much lower amount of intrinsic noise than the MOSFETs. The use of these devices in the input stage of the electrode devices has two major advantages:

- The noise level of these devices was much lower than in signal amplification configuration of the standard microelectrode set-ups described in the literature.
- No surface modification of the electrode surfaces was necessary in order to decrease the input impedance. A major decrease of the input impedance normally results in a change in time-resolution of the standard microelectrode measurement circuits. With the use of JFETs in the input stage, very similar signal shapes of the extracellular responses from the EGE system compared to the responses monitored by the FET sensors were observed.

The EGE microelectrode system developed by Krause et al. (Krause et al., 2000) was extended. With a new rapid data acquisition card and new recording software it is currently possible to perform an online sampling of 64 channels. A new main amplifier for the 16- and the 64-channel system was developed, which automatically compensates the DC-current parts of the FET devices at the input. This concept makes the recording system much easier to operate.

Single Cell-Transistor Coupling Experiments:

In the cell-transistor coupling measurements, many different electrically active cellular systems were investigated for the use in whole-cell based biosensors. It was possible to detect cellular responses of SH-SY5Y and TR14 cells lines, cultured neurones, cardiac myocyte cells, and cells from brainstem slice cultures.

Brainstem slice cultures showed the best results amongst all cell cultures. After 3 to 5 DIV, the neuronal growth started to spread outwardly from the slice and began building a random network of neurons on the sensor surfaces. With the use of the anti-

mitotic agent, cytosine β -D-arabinofuranoside (ARA-C), which inhibits non-neuronal cell proliferation, it was possible to have clearer networks of neurons on the sensor surfaces. The cells from the brainstem cultures showed very high membrane voltage-gated currents of up to 10 nA potassium- and 6 nA sodium-current. In the coupling measurements the active currents of these cells were such high that in some cases no signal averaging was required.

Extension of the Point Contact Model:

The extracellular signals from the single cell-transistor coupling experiments were simulated using the *Point Contact Model* circuitry implemented in the simulation program PSPICE. With the knowledge of the compensation circuitry used by the EPC-9 patch clamp amplifier it was recognised that the rising and falling flanks of the rectangular stimulation pulse in voltage-clamp mode were weakened by an exponential law with the time constant $\tau = R_S \cdot C_{slow}$. This result in a much smaller value for the derivative of the membrane voltage dV_M/dt during the stimulation pulse, which is directly proportional to the observed amplitude of the extracellular-recorded capacitive transient V_J^0 . With this knowledge, the calculated seal conductances g_J were found to be much lower than reported before ($g_J = 5\text{-}100 \text{ S/cm}^2$; (Krause, 2000)). The values from the signal simulations of $g_J = 1\text{-}3 \text{ S/cm}^2$ were found to be similar to the values reported in literature ($g_J = 1 \text{ S/cm}^2$ for a hippocampal neuron measured with frequency-dependent impedance analysis (Fromherz et al., 1993)).

In the literature, a higher ion-conductance monitored in the cleft between cell and transistor during coupling experiments has been reported (Vassanelli and Fromherz, 1999), (Straub et al., 2001). This effect was interpreted by the '*accumulation of ion-channels in the attached membrane*' model. In addition, it was observed that extracellular sensors could not monitor the contribution of the quick A-type potassium current. This was explained by a complete '*depletion of this ion-channel type in the attached part of the membrane*' (Vassanelli and Fromherz, 1999). It was also observed that the time response of the extracellular signal was being delayed and this effect was explained by the '*self-gating of ion-channels in the attached part of the membrane*' (Fromherz, 1997).

From the PSPICE simulations in recent work, it was found that a major signal fraction observed in the extracellular response could not be modelled by the standard *Point Contact Model* circuitry. The remaining part of the signal after subtraction of the simulated signal appeared to be very similar to the standard pH-response curves of ion-sensitive field-effect transistors. By overlaying the rise and decay times of the responses, it could be seen that the quicker rising time was mainly caused by the quick A-Type potassium current. This was the first time that the extracellular recording of a potassium A-Type current had been observed.

A possible explanation of the observed effects was given by calibrating our standard FET devices to ion concentration changes in the electrolyte. Very strong responses with different sensitivities to Na^+ , K^+ and Ca^{2+} ion concentration changes have been found. The differences in sensitivity are caused by the different initial ion concentrations in the standard extracellular medium. All effects at the gate potential caused by ion concentration changes during a cellular signal may enhance the active current signals. It was shown that the direction in gate potential change is adding to the active cellular signals for all ion types. With the empirical values from the calibration measurements, a new *Extended Point Contact Model* was introduced, which took the effects of ion concentration changes in the cleft between attached part of the membrane and transistor into account. A rough estimation of the ionic changes in the cleft during a standard potassium signal of a neuronal cell showed that this effect would be large enough to have a major influence in the extracellular response.

- With this new concept all observations in the cell transistor coupling may be explained. The higher recorded ion currents could be explained by this additional effect, which increases the amplitude of the extracellular signal.
- The different gating properties may be explained by a slower response of the sensor to these ion concentration changes. The dynamic quantification of the responses is very complicated and cannot be explained by thermal diffusion processes. The observed dynamics are within the range of the time limit for the dynamic responses of ion-sensitive field effect transistor reported in literature.
- The quicker response to the potassium A-type signal suggests that this type of ion-channel be not depleted in the contact area. The response to this current is completely overlaid by the response to the ion concentration change, which are about 6 times higher in the observed signal. The response curve itself has a quicker rising time if the A-type ion-channels are active.

The Cardiac Myocyte - Transistor Hybrid System in Pharmacological Bioassays:

The steps that have been taken to increase the reliability of the cardiac myocyte cell layer-transistor hybrid system were presented. High amplitude extracellular recordings of dissociated cardiac myocytes on FETs with excellent signal-to-noise ratios were achieved. It was shown, for the first time, that quantitative and reproducible recordings of the effects of drugs on myocytes being cultured on the FETs could be obtained. The responses to all well-established cardio-stimulants (isoproterenol, and arterenol bitartrate (norepinephrine)) and relaxants (verapamil, carbamylcholine, SDZ PCO400) were conclusive and reliable. The present study demonstrated the versatility and applicability of the FET system in pharmacological bioassays. Furthermore, the cultured whole-cell integrated biosensor system can be viewed as a 'miniature/model biological

system', albeit a much simplified version, and can be used in a more in-depth physiological functional analysis.

In some cases (about 30 % of all responses) changes in the shape of the extracellular responses were observed, which could also be explained by the response to the drugs used. In many cases, the signal-to-noise ratio of the extracellular response was still too low to observe these shape changes in all the recordings. The later use of Nitro-Cellulose as unspecific cellular glue on the sensor surfaces showed some remarkable results.

It was also shown that the sensor array has the potential to record the signal propagation velocity within the cell layer and to track the pacemaker centre of the syncytium.

With the cardiac myocyte system, it was shown that upside-down measurements on the sensors were also possible. By applying a gentle pressure on the backside of the substrates, a positive influence on the *cell-transistor distance* to the *signal amplitude* was shown. In this experiment very high extracellular signal amplitudes of up to 12 mV with a strong influence of the active ion currents were recorded. However the interpretation of the signal shapes is very uncertain for this particular experiment, because the cells were highly stressed between the two glass substrates. Cardiac myocytes are known to have stretch-activated ion-channels in their membrane. Perhaps an additional influence of these channel types has to be taken into account for the upside-down measurements.

Outlook

The backside-contacted FET arrays provide a low-labour intensive system for use in a variety of biological studies. It also offers a possibility to adapt the microflow systems. With the use of cultured cardiac myocyte monolayer, it would be possible to establish a whole-cell biosensor system for rapid pharmaceutical screenings. Furthermore, in theory, many different cell types could be used in a similar manner.

On the other hand, the backside-contacted sensor could offer the possibility to develop an upside-down encapsulation, which can be manoeuvred directly onto cells that have been cultured elsewhere (i.e tissue culture dishes or different substrates)

For a further increase of the signal-to-noise ratio of the extracellular devices following developments may be recommended:

The lanes of the EGE devices were found to act as antennas and had a major contribution to the total noise of the set-up. Smaller chips and/or a shielded backside of the chip by evaporation of a grounded metal layer may lower the antenna effect. In future, chip generations may be advantageous if the electrodes and JFET structures are

integrated on one chip. The much lower intrinsic noise of the JFETs in the observed frequency range may be a justification to build BioFET chips with EOSFET structures as a recording device with the second amplification stage of JFET structures on one chip.

With the 64-channel EGE system, the limit of independently addressable channels arranged in a squared array on one chip is reached. A further increase of the channel number could be controlled by a multiplexer system in order to keep a clear arrangement.

A further improvement of the EOSFET structures should bear following criteria in mind:

- An entirely different gate material, which is known to be more sensitive to ionic changes in the electrolyte like Si_3N_4 , or Al_2O_3 .
- With the concept of the multigate structures, a larger effective gate area-to-free area ratio can be achieved, which dramatically increases the probability of cultured cells being localised on the sensitive spots of the sensor.
- For lower noise of the FET devices, a very clean and stable fabrication process for the gate oxide are necessary, because the major noise source, the $1/f$ generation recombination noise, is strongly dependent on the semiconductor/gateoxide interface region. New annealing protocols or nitride loading of the oxide, similar to the standard industrial process, may enhance the transistor performance.
- The noise and the transconductance values may be improved by the use of different gate materials with higher relative dielectric constants like $(\text{Ba}, \text{Sr})\text{TiO}_3$ or ZrO_2 .

An upside-down process may be successful in the design of artificial networks of neuronal cells on the sensor surfaces. It has been demonstrated that artificial networks of brainstem neurons grown on laminin patterns can be released from the substrate surface (Yeung et al., 2001a). These nearly perfect networks can be transferred to the extracellular sensors. After adherence and a few days of growth to re-establish cellular contacts with the substrate, recording can then begin.

8 Appendix

A Fabrication of the backside-contacted p-channel FETs

In this paragraph the exact fabrication process for the backside contacted field-effect transistor devices is described. On the wafer layout (Figure 8-1) in total 254 chips are located on a 5'-Wafer with size of $6 \times 6 \text{ mm}^2$ each. One wafer contains 44 chips with a gate area of 2 lines (8 gates in line) with spacing of $20 \mu\text{m}$ and a distance of $100 \mu\text{m}$ of the lines. The lower bigger area of the wafer contains 140 chips with a 4×4 FET array of $200 \mu\text{m}$ spacing and in the middle part 70 chips with a 4×4 FET array with $100 \mu\text{m}$ spacing are located. On the left and on the right side the test marks and the marks for aligning the wafers during the process can be seen.

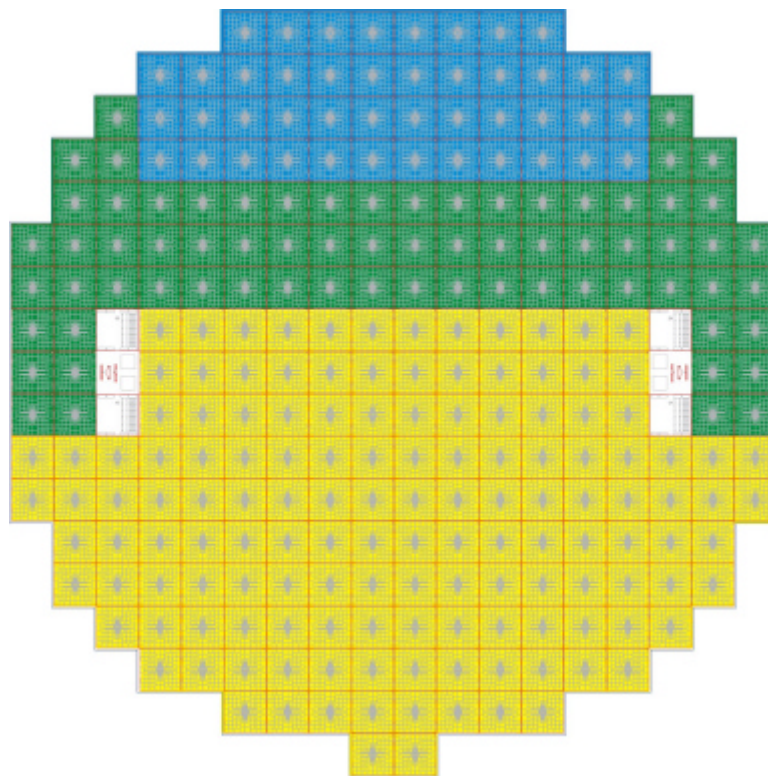


Figure 8-1 Wafer layout for the backside contacted FET-arrays (5'-Wafer). In the top area 44 chips with a gate area of 2 FET lines (8 gates in line) with spacing of 20 μm and a distance of 100 μm of the lines (blue area). The lower big part contains 140 chips with a 4x4 FET array of 200 μm spacing (yellow area) and in the middle part 70 chips with a 4x4 FET array with 100 μm spacing are located (green area). On the left and on the right side the test marks and the marks for aligning the wafers during the process can be seen. In total 254 chips with 6x6 mm^2 size are designed on the wafer.

In the first steps of the chip production process the initial material of n-doped silicon (doped with phosphor $1 \times 10^{15} / \text{cm}^3$; $R_{\text{y}} = 8.5\text{-}11.5 \Omega\text{cm}$) polished from both sides was wet oxidised. The oxide thickness was adjusted to 1 μm . In the first photolithographic step the lane contacts on the frontside were implanted with a boron dose of $D = 8 \times 10^{15} / \text{cm}^2$ (Figure 8-2).

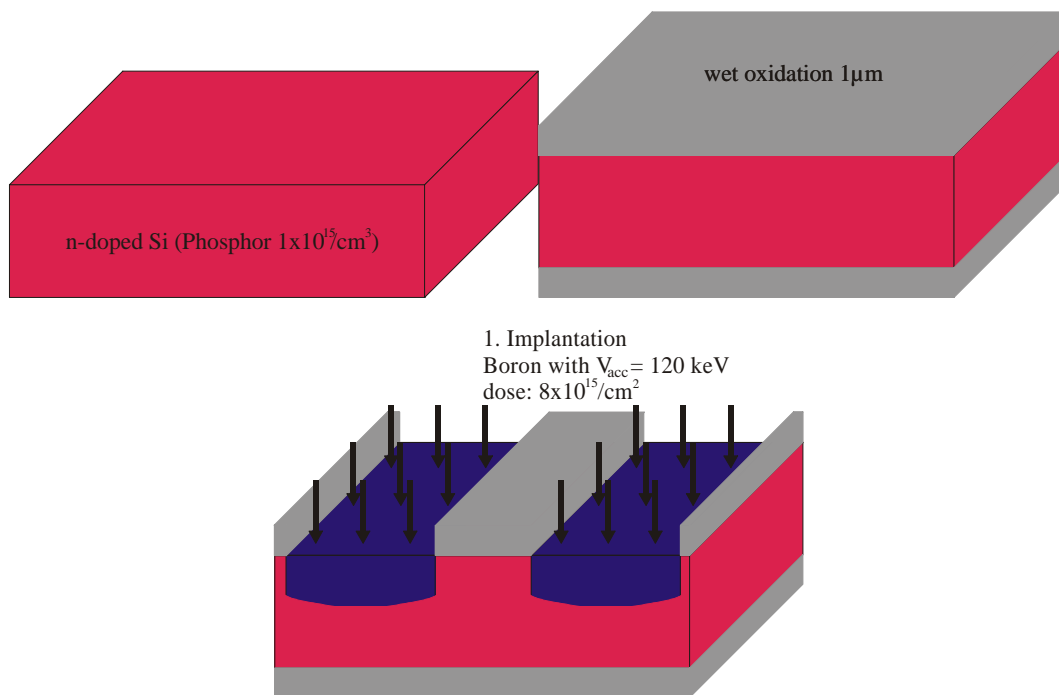


Figure 8-2 First steps of the chip production process. The initial material of n-doped silicon (doped with phosphor $1 \times 10^{15} / \text{cm}^3$; $R_y = 8.5\text{-}11.5 \text{ Wcm}$) polished from both sides is wet-oxidised. The oxide thickness was adjusted to $1 \mu\text{m}$. In the first photolithographic step the lane contacts on the frontside were implanted with a boron dose of $D = 8 \times 10^{15} / \text{cm}^2$.

After this implantation a diffusion and wet-oxidation process followed. Here the depth of the implanted areas (conducting lanes) was adjusted to about $4 \mu\text{m}$. After 16 h diffusion @ 1000°C the lanes had a square resistance of $R_y = 13.2 \Omega$. The oxide thickness was adjusted to 1000 nm on the lanes (990 nm measured by FTP) for the first layer of the membranes and etching stop for the advanced silicon plasma etching (ASE) process (Figure 8-3). Then the second implantation step followed by the second photolithographic step, where the gate dimensions were defined and the outer lane areas, where the membranes of the backside contacts will be produced, were covered.

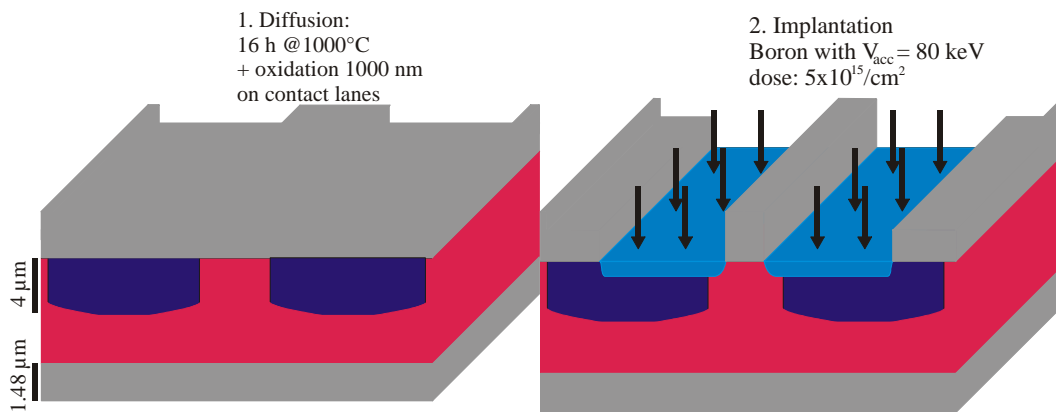


Figure 8-3 Second photolithographic step with implantation of the source and drain contacts in the gate region. The outer lane areas, where the backside membranes will be produced remain covered by resist. The second implantation was performed with a lower acceleration voltage and dose ($D = 8 \times 10^{15} / \text{cm}^2$, $V_{acc} = 80$ keV).

The drain source distance on the mask was $6 \mu\text{m}$. For a layer thickness of $1.5 \mu\text{m}$ underetching of $1.5 \mu\text{m}$ from each side had to be taken into account. With a lateral diffusion of about $0.5 \mu\text{m}$ (simulated with Mathematica 3.0) the drain source distance was adjusted to about $2 \mu\text{m}$ for all chips types. The second diffusion step was carried out @1000°C for 53 min combined with a wet oxidation of 250 nm thickness (Figure 8-4).

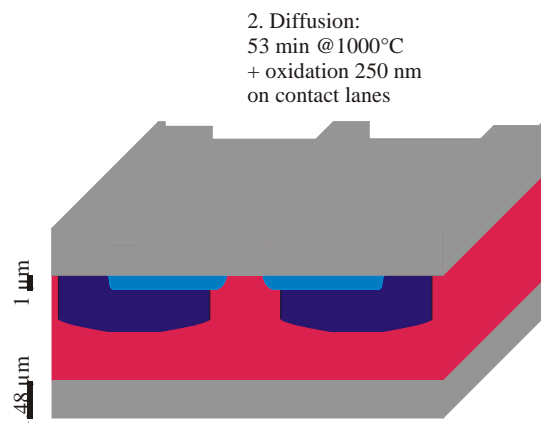


Figure 8-4 Second diffusion step @1000°C combined with a wet oxidation of 250 nm thickness for the contact lanes. The diffusion was adjusted to a depth of about $0.8 \mu\text{m}$. The drain source distance was adjusted to about $2 \mu\text{m}$.

Then the third photolithography followed. First the gate areas were opened by wet etching, then a thin (70 nm) oxide was deposited for etchstop in the gate area. After this the LPCVD-nitride (low-pressure chemical vapour deposition) was deposited on the whole wafer. The oxide thickness on the areas, where the remaining membranes should remain, was measured to be 1060 nm. A thin oxide layer has a pressure stress of

400 MPa and a thin nitride layer a drawing pressure of 1100 MPa. Therefore, the needed thickness for the silicon nitride was calculated to be 380 nm and deposited in a LPCVD DSC-process @790°C on the whole wafer (Figure 8-5).

After this the design of the wafer backside started. In the fourth photolithographic step the outer lane area on the backside was opened through the nitride layer in a reactive ion etching process (RIE) using fluor gas. The remaining 1.55 μm thick oxide layer was opened in a wet etching process.

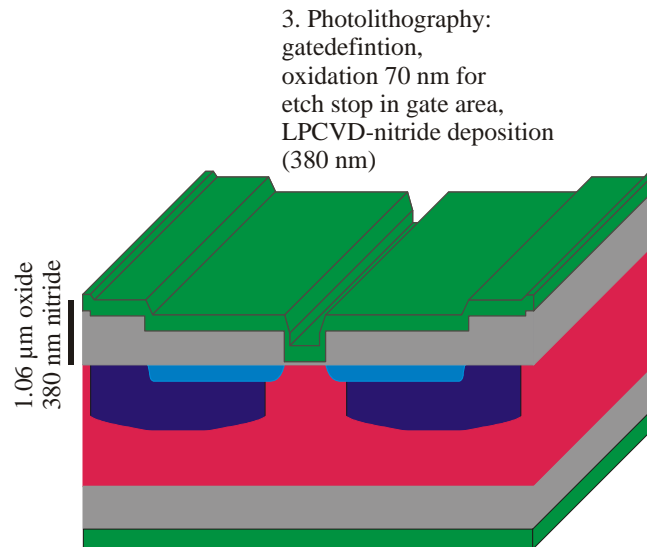


Figure 8-5 In the third photolithographic step the gate areas were opened by wet etching and a thin (70 nm) oxide was deposited for etch stop in the gate area. After this 380 nm nitride was deposited on the whole wafer in a LPCVD DSC-process @790°C.

After this the fifth photolithography step followed where the roundshaped holes ($d = 100 / 150 \mu\text{m}$) on the backside were designed. The photoresist on the backside was used as mask layer for the inductive coupled plasma etching process for the production of the holes through the wafers. This advanced silicon etching process was a two step cycle process (duty 10 s) with reactive etching and deposition of passivation material on the walls. The etchstop for this process was the oxide layer on the frontside. In this step it was crucial to avoid underetching in order not to de-stabilise the membranes. From this step on the wafers had to handle with extreme care, because the remaining membranes had a thickness of only 1060 nm oxide plus 380 nm nitride but a diameter of about 150 μm (Figure 8-6).

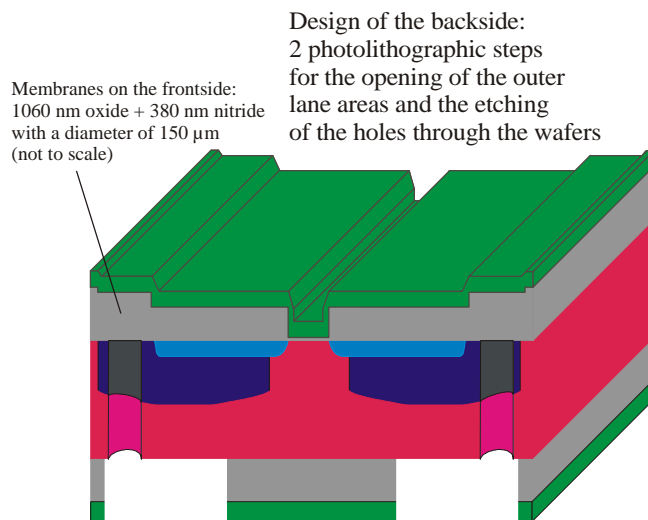


Figure 8-6 For the design of the backside 2 photolithographic steps were needed. First the outer lane area had to be opened through the nitride (380 nm) and the oxide layer (1550 nm). In the next step the holes were produced by a two step duty (10 s) etching process, with reactive ion etching and deposition of passivation material at the walls. The wafer was mask by photoresist on the frontside and partly shielded (after photolithography) on the backside. The etching process stopped at the oxide layer on the frontside. Underetching had to be minimised in order not to aggravate the stability of the membranes.

After this the most complicated steps in this flowchart followed. The holes had to be implanted in a gas phase doping process in order to get contact from the backside to the frontside.

This was done using BN-Wafers in sandwich configuration with the wafers in the diffusion oven @950°C. In order to get rid of the borsilicate glass forming at the silicon surface (isolation layer) the wafers were first wet-oxidised for 20 s getting a shielding layer of 20 nm oxide on the backside contacts. After the BN-diffusion (20 min @950°C in N₂ gas) this shielding layer was wet etched in two steps after a second wetoxidation. This resulted in a layer resistance of $R_{\gamma} = 100 \Omega$ on the backside contacts. The resistance from the backside to the frontside of the wafers was measured to 200-250 Ω per hole. After this step the final design of the frontside could start. First a PECVD-layer (plasma enhanced chemical vapour deposition) of 100 nm thick silicon oxide was deposited as passivation and modification layer during the cell culturing.

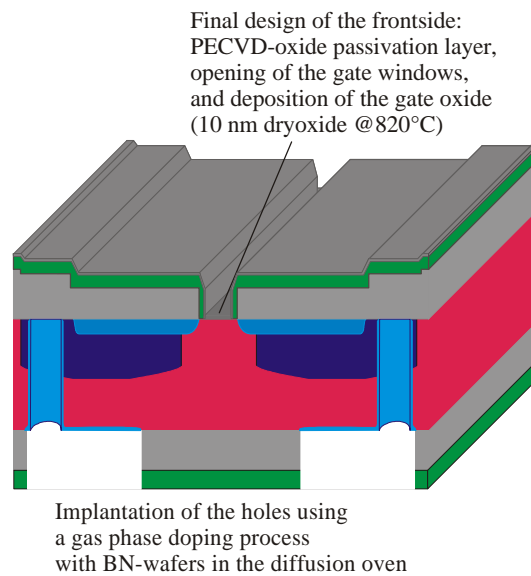
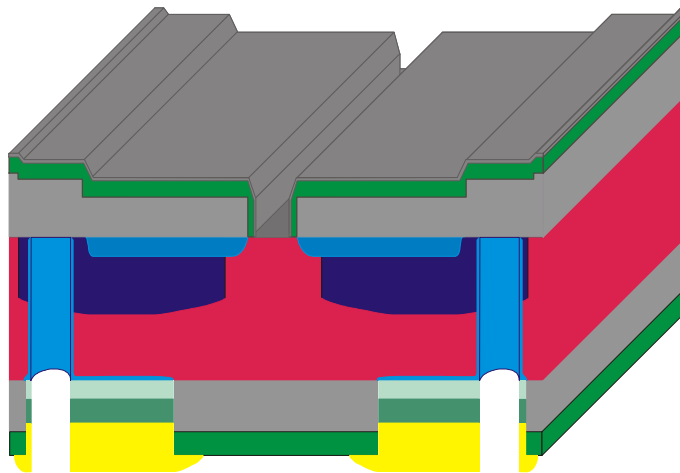


Figure 8-7 In this step the holes through the wafers were implanted using a gas phase diffusion process (BN-Wafers @950°C in the diffusion oven). First the design of the frontside was finished with deposition of a PECVD-oxide layer (100 nm) for passivation and final design of the gate windows using 10 nm dry oxide (@820°C with anneal @850°C in N₂).

After this the gate windows were opened in the sixth photolithographic step for the second time through the three isolation layers (100 nm PECVD-oxide, 380 nm LPCVD-nitride, 70 nm wet-oxide). Then the gate oxide was deposited in a dry-oxide process ($d_{oxide} = 10$ nm; $T = 820^{\circ}\text{C}$; 80 min with 20 min anneal @850°C in N₂ gas) (Figure 8-7).

In the last steps the backside contacts had to be produced. For the use of the dyes in a flip-chip process it was found that gold contacts are essential for obtaining good contact resistances in the mΩ range. First the metallic contacts to the p-doped silicon were produced by sputtering aluminium with 1% Si with a thickness of 1 μm. Then the front side was shielded with a polyimide layer and the aluminium was pre-etched for the preparation of electroless metal deposition.



Design of the backside metal contacts:
sputtering of Al(1% Si), zincatation,
and electroless deposition of Ni and
Au contacts.

Figure 8-8 The metallic backside contacts had to be made of gold for the use of the chips in a flip-chip encapsulation process. The contacts were produced with an electroless galvanic deposition process using sputtered Al (1% Si) for contacting the p-doped silicon lanes. For the use of this deposition methode first nucleation centres had to be produced by zincatation. Then the galvanic processes for deposition of nickel and gold followed.

After this a precursor of zincate solution (NaOH, ZnO, HNa-Tartrate, KNO₃, FeCl₃) produced nucleation centres on the aluminium surface. Then the electroless deposition of nickel and gold was done. After removing the polyimide from the frontside the wafers were sawed and the chips were ready for encapsulation (Figure 8-8).

B Source Code for the Simulation of the Point Contact Model using OrCADs PSpice 9.1

In this paragraph the full source code for the simulation of the Point Contact Model using OrCADs PSpice ver. 9.1 is shown. The cell transistor measurements are all simulated using these routines.

Simulation of the point contact model using a voltage-clamp experiment with a hippocampal neuron and a simulated n-channel BioFET

```

*****
* File: HCVC_200ISFETLP.cir
* Date: 16.03.2001
* Version: 1.1
* Author: Sven Ingebrandt
* MPIP for Polymer Research Mainz
* Ackermannweg 10
* 55128 Mainz
* email: sven@ingebrandt.de
*****
* The circuit describes the point contact of a single cell coupled to a transistors gate.
* For the systemelectrode-cell-junction with the stimulation pulse from the voltage-clamp
* experiment (voltage source V1 (Tida-data) at node 1) and an active cell-current as
* current source I1 (Tida-data - 10% of the whole cell current into the contact area)
* the BioFET is monitoring the resulting signal at the point contact.
* The voltage step inside of the cell at node 2 (V2) is delayed as result of the membrane
* loading with the time constant  $t=C_{slow} \cdot R_s$  (both provided from the patch-clamp amplifier).
* The resulting signal amplitude scales strongly with the seal resistance R4 ( $g_j \cdot 10\%$ 
* membrane area) of the junction. The BioFET (gate at node 3, source and bulk at node 4 with
* source voltage from node 4 to ground, drain at node 5 with drain voltage from node 5 to 6) is
* driven in the working point of  $V_{DS}=2.4V$  ;  $V_{GS}=2V$  ;  $g_m=0.51786mS$ . The resulting voltage drop
* at the drain resistor R5 is low pass filtered by the amplifier electronics  $t=R6 \cdot C4=0.333ms$  and the
* resulting simulation signal corresponds to the voltage at node 7 (to be scaled with the transistors
* characteristics!)
*
* Network:
* Point contact model
*****
* Library of the components:
* -----
.LIB eval.lib
* Lists of the voltage- and current sources:
* -----
*****

* Voltage source:

V1 1 0 PWL(0.00ms -89.6932m 0.03ms -89.6828m ...
+ ... 299.91ms -89.6646m 299.94ms -89.6625m)

*****
* Current source: 10% of the whole-cell current over the membrane !

```

```
I1 2 3 PWL(0.00ms 0.0000n 0.03ms 0.0000n ...
+ ... 0.0000n 299.91ms 0.0000n 299.94ms 0.0000n)
```

```
*****
```

```
* Point contact network:
```

```
*****
```

```
* Resistors:
```

```
* -----
```

```
R1 1 2 {_R1} ; Cell attach resistance  $R_s$ 
.Param _R1=22800000
R2 2 0 {_R2} ; membrane resistance of the free membrane
* 90% of the total membrane resistance provided by the patch-clamp amplifier
.Param _R2=2088888889
R3 2 3 {_R3} ; membrane resistance of the attached membrane
* 10% of the total membrane resistance provided by the patch-clamp amplifier
.Param _R3=18800000000
R4 3 0 {_R4} ; seal-resistance of the junction (to be scaled !)
.Param _R4=1340200.0
R5 6 0 {_R5} ; drain resistor
.Param _R5=10000
R6 6 7 {_R6} ; resistor of the low pass
.Param _R6=10000000000
```

```
* Capacitors:
```

```
* -----
```

```
C1 1 0 {_C1} ; pipette capacitance  $C_{fast}$ 
.Param _C1=0.00000000000699
C2 2 0 {_C2} ; membrane capacitance of the free membrane
* 90% of  $C_{slow}$  provided by the patch-clamp amplifier
.Param _C2=0.000000000011094
C3 2 3 {_C3} ; membrane capacitance of the attached membrane
* 10% of  $C_{slow}$  provided by the patch-clamp amplifier
.Param _C3=0.000000000001233
C4 7 0 {_C4} ; capacitance of the low pass:  $f=3\text{kHz} \rightarrow$ 
.Param _C4=0.000000000000333333
```

```
*****
```

```
* Design of the BioFET:
```

```
*****
```

```
.MODEL BIOFET NMOS LEVEL=2
+ VTO=0.75 LAMBDA =0.003 RSH=2.5E+01 TOX=10E-9
+ UO=6E+02 TPG=0 KP=1.5E-5
+ UEXP=8E-02 NSUB=3.5E+15 NFS=1E+10
+ NEFF=1 VMAX=5E+04 Delta=2 LD=1.45E-06
+ UCRIT=8E+04 XJ=6E-09 CJ=4.5E-4 IS=1E-11
+ CJSW=5E-10 PHI=5.5E-01 GAMMA=1
+ MJ=0.4 MJSW=0.33 PB=0.6
```

```
*****
```

```
* BioFET in the point contact network:
```

```
*****
```

```
M1 5 3 4 4 BIOFET L=2u W=16u NRS=20 NRD=40
* Drain resistance  $R_D = \text{NRD} * \text{RSH}$  (1000 Ohms)
* Source resistance  $R_S = \text{NRS} * \text{RSH}$  (500 Ohms)
* Transistor in working point:  $V_{DS}=2.4\text{V}$  ;  $V_{GS}=2\text{V}$  ;  $g_m=0.51786\text{mS}$  !!!
```

```

*****
* Voltage supplies for the BioFET
*****
Vdrain 4 0 DC {_Vd1} ; Characteristics (AP-voltage =  $-V_{GS}$ )
.Param _Vd1=-2
Vsource 5 6 DC {_Vs1} ; Characteristics (FET-voltage =  $-V_{GS} + V_{DS}$ )
.Param _Vs1=0.4
*****
* Analysis:
* -----
*****
.tran 0.01ms 0.3s 0s 0.01ms ; analysis over 0.3s with 0.01 ms steps
*****
* Probe-Kommandos
* -----
*****
.Probe

```

C Patch-Clamp equipment

Instruments and materials for the Patch-Clamp measurements:

Patch-Amplifier	Whole Cell / Patch-Clamp Amplifier, model: EPC-9/2, Software: Tida 4.11 HEKA Elektronik, Dr. Schulz GmbH, 67466 Lambrecht/Pfalz
Glassmicroelectrodepuller	Horizontal Puller model: P-97 Sutter Instrument Company, USA
Glasselectrodes	Borosilicat glass capillaries with filament $L = 100\text{mm}$, $d_o = 1.5\text{mm}$, $d_i = 0,87\text{mm}$ $t = 0.315\text{ mm}$ Filament diameter $d_F = 0,315\text{mm}$ No.: 1810016 Hilgenberg, 34323 Maisfeld

D Equipment for Cell-Transistor Coupling Measurements

Microscope	Axitech Vario (45032) DIC Differential Interference Contrast, Objektive: Epiplan 5x (442920), Epiplan 10x (442930), LD Epiplan 20x (442840) Carl Zeiss Jena GmbH, 60335 Frankfurt
Immersion-objective	UMPLFL 20xW/0.50 UIS-Obj AA33 No.: 037588 Olympus Optical Co.(Europe) GmbH, 20097 Hamburg
Micro-manipulators	Micro-manipulators for the microscope and the Patch-Clamp Preamplifier-Headstage, XYZ-direction Luigs&Neumann GmbH, 40880 Ratingen
Oscilloscope	Digital Oscilloscope model: 9400A LeCroy, Switzerland
Sterile Workplace	Sterile Workbench model: Lamin Air HB 2436 Heraeus Instruments GmbH, 63450 Hanau
Incubator	Incubator, with CO ₂ – inlet Modell: BB 6060 Heraeus Instruments GmbH, 63450 Hanau
I/O card	PIO-24 I/O card, BMC Inc., Germany
data aquisition card	data aquisition card model: PCI 6110 National Instruments, USA
testsocket	PLCC 68 T+B IC 51, YAMAICHI Inc., Munich
CCD-camera	Sony XC-333P, Sony International Europe GmbH Stuttgart

Video card	Matrox Meteor II, Matrox Imaging GmbH, Germany
Software	MED64 cond. 2.1, Panasonic Inc., Japan

E FET and EGE Encapsulation

Chipcarriers (standard)	Ceramic Chip-Carriers model: 28 LD S/B Package CS B02880(KD-78368-E) Spectrum Semiconductors Materials Inc., San Jose, USA
Chipcarriers (backside)	Ceramic Chip-Carriers model: 28 LD S/B Package KD-77261-B-JMI Spectrum Semiconductors Materials Inc., San Jose, USA
EGE-PCB	Conducting lanes electroplated with gold 24x24mm, d = 1mm, 64 contacts Schwind-Elektronik, 89081 Ulm-Lehr
LB-PCB	Conducting lanes electroplated with zink 18x30mm, d = 1mm, 12 contacts Schwind-Elektronik, 89081 Ulm-Lehr
H20E-175	EPO-TEK, Epoxy-Glue, 2-Components, Nr.: 12419-016 Polytec GmbH, 76337 Waldbronn
H20E-PFC	Flip-Chip-Glue EPO-TEK, Epoxy- Glue, 2-Components, Polytec GmbH, 76337 Waldbronn
U-300	Liquid underfill encapsulant for flip-chip 2-Components, Polytec GmbH, 76337 Waldbronn
Sylgard 182	Silicon PDMS encapsulant, 2-Components, Dow Corning GmbH, 65201 Wiesbaden
Dow Corning 96-083	Silicon PDMS glue, 2-Components, Dow Corning GmbH, 65201 Wiesbaden

Screen printer	Screen printer model: ESSEMTEC SP-002 ESSEMTEC AG, Switzerland
SMD frame	SMD frame for Screen printer KOENEN, 85521 Ottobrunn
SMD mask	SMD mask (transparent) for Screen printer ELASER, Germany
Fineplacer unit	Placer unit for positioning of the chip during flip-chip process FINEPLACER-145“PICO“ FINETECH electronics, 10247 Berlin
Stereomicroscope	Basis Leica MS5 No.: S/N 5036558 Magnification 4x/52.9mm – 25,2x/8,3 mm, 5 Steps Leica Microscopy Systems Ltd., Switzerland

F Chemicals

Cell culture chemicals:

Glutamax I	Dipeptid L-Alanyl-L-Glutamin, No.: 35050-038 Life Technologies GmbH, 76131 Karlsruhe
ATP	Adenosin 5`-Triphosphate, No.: A8937 Sigma-Aldrich GmbH, 82041 Deisenhofen
DMEM/F12	Dulbecco modified Eagle Medium / Nutrient Mix F12 (1:1)(1x), No.: 21331-012 Life Technologies GmbH, 76131 Karlsruhe
P/S	Penicillin/Streptomycin Solution, No.: 15070-022 Life Technologies GmbH, 76131 Karlsruhe
EDTA	No: G7020 Sigma-Aldrich GmbH, 82041 Deisenhofen
EGTA	No: G7E3889 Sigma-Aldrich GmbH, 82041 Deisenhofen

PBS	Dulbecco phosphate buffered solution No: 14040-083 Life Technologies GmbH, 76131 Karlsruhe
Trypsin	Trypsin Typ II porcine pancreas, No: T7409 Sigma-Aldrich GmbH, 82041 Deisenhofen
M199	Modified Earle Salts, No: 31153-018 Life Technologies GmbH, 76131 Karlsruhe
HBSS	Hank´s buffered salt solution, No.: 14185-045 Life Technologies GmbH, 76131 Karlsruhe
B27	Supplement serumfree, No.: 17504-44 Life Technologies GmbH, 76131 Karlsruhe
Neurobasal	Neurobasal TM -Medium, No.: 21103-49 Life Technologies GmbH, 76131 Karlsruhe
Laminin	No.: L6246 Sigma-Aldrich GmbH, 82041 Deisenhofen
Fibronectin	Fibronectin from bouine plasma, No.: F1141 Sigma-Aldrich GmbH, 82041 Deisenhofen
DNAse II	40.000 units, No.: D4527 Sigma-Aldrich GmbH, 82041 Deisenhofen
HEPES	HEPES Buffer, No.: H9136 Sigma-Aldrich GmbH, 82041 Deisenhofen
F10	Nutrient Mixture Ham´s F-10, No.: 21955-026 Life Technologies GmbH, 76131 Karlsruhe
ITS	Insulin-Transferrin-Selenium Supplement, No.: 1884 Sigma-Aldrich GmbH, 82041 Deisenhofen
FCS	Foetal calf serum, No.: 10119-154 Life Technologies GmbH, 76131 Karlsruhe
TEA	Tetraethylammonium-Chlorid (TEA) Sigma-Aldrich GmbH, 82041 Deisenhofen

Culture media:

Culture medium for SHSY-5Y	DMEM Ham's F12 200 mM 1% P/S 12 % FCS	Dulbecco modified Eagle Medium Nutrient Mix F12(1:1), Glutamax I, Penicillin/Streptomycin, Foetal calf serum
Culture medium for primary cultured Neurons	2 %	B27 Supplement dissolved in Neurobasal Medium
Culture medium for Cardiac myocytes	20 ml 1 ml 180 ml 20 ml 5 ml 1 ml	F10 Nutrient Solution Na ₂ CO ₂ Sodiumbicarbonate HEPES FCS Antibiotica ITS Lösung
Versene Buffer	140 mM 5 mM 5 mM 10 mM 0.5 mM	Sodiumchloride Potassiumchloride Glucose HEPES EDTA adjusted to pH 5 with 5 M NaOH

Literature

- (Abe et al., 1979) H. Abe, M. Esashi, T. Matsuo, **1979**,
ISFET's Using Inorganic Gate Thin Films,
IEEE Trans. Electron. Devices, **ED-26**, 1939-1944.
- (Alberts et al., 1995) B. Alberts, B. Dennis, J. Lewis, M. Raff,
K. Roberts, J.D. Watson, **1995**,
Molekularbiologie der Zelle,
L. Jaenicke, 3rd ed.
VCH Verlagsgesellschaft, Weinheim.
- (Antognetti et al.,
1987) P. Antognetti, G. Massobrio, C. Fasce, E. Meda,
E. Profumo, **1987**,
Semiconductor Device Modeling with SPICE,
McGraw-Hill Book Company.
- (Barry and Lynch,
1991) P.H. Barry and J.W. Lynch, **1991**,
*Liquid junction potentials and small cell effects in
patch-clamp analysis*,
J. Memb. Biol., **121**, 101-117.
- (Bard and Faulkner,
1980) A.J. Bard and L.R. Faulkner, **1980**,
Electrochemical Methods,
Wiley, New York.

- (Baturitsky et al., 1996) M.A. Baturitsky, O.V. Dvornikov, S.I. Reutovich, N.F. Solomashenko, **1996**, *Multichannel Monolithic FrontEnd System Design .2. Microwave BipolarJeeet Process For LowNoise ChargeSensitive Preamplifiers*, Nuclear Instruments & Methods in Physics Research Section A Accelerators Spectrometers Detectors & Associated Equipment, **378**(3), 570-576.
- (Baumgart, 2001) T. Baumgart, **2001**, *Preparation and Physicochemical Characterisation of Solid Supported Model Membrane Systems*, Dissertation, University of Mainz.
- (Bergveld, 1970) P. Bergveld, **1970**, *Development of an ion-sensitive solid-state device for neurophysiological measurements*, IEEE Trans. Biomed. Eng., **BME-17**, 70-71.
- (Bergveld et al., 1976) P. Bergveld, J. Wiersma, H. Meertens, **1976**, *Extracellular potential recordings by means of a field effect transistor without gate metal, called OSFET*, IEEE Trans. Biomed. Eng., **23** (2), S. 136-144.
- (Biedler et al., 1978) J.L. Biedler, S. Rofflertarlov, M. Schachner, L.S. Freedman, **1978**, *Multiple neurotransmitter synthesis by human neuroblastoma cell lines and clones*, Cancer Research, 38, 11, 3751-3757.
- (Bousse, 1982) L. Bousse, **1982**, *Single electrode potentials related to flatband voltage measurements on EOS and MOS structures*, J. Chem. Phys., **76** (10), 5128-5133.
- (Bousse et al., 1983) L. Bousse, N.F. De Rooji, P. Bergveld, **1983**, *Operation of Chemically Sensitive Field-Effect Sensors As a Function of the Insulator-Electrolyte Interface*, IEEE Trans. Electron Devices, **ED-30** (10), 1263-1270.
- (Braun and Fromherz, 1998) D. Braun and P. Fromherz, **1998**, *Fluorescence interferometry of neuronal cell adhesion on microstructured silicon*, Physical Review Letters, **81** 23, 5241-5244.

- (Calusaru, 1979) A. Calusaru, **1979**,
Electrodeposition of metal powder,
Elsevier, Amsterdam.
- (Cho et al., 1998) W.J. Cho, E.S. Kim, J.J. Kang, K.G. Rah, H.S. Kim, **1998**,
Annealing Effects of Polycrystalline Silicon Gate On Electrical Properties of Thin Gate Oxide,
Solid-State Electronics, **42**(4), 557-566.
- (Cho et al., 1999) W.J. Cho, Y.C. Kim, E.S. Kim, H.S. Kim, **1999**,
Effects of oxidation ambient and low temperature post oxidation anneal on the silicon/oxide interface structure and the electrical properties of the thin gate oxide,
Japanese Journal of Applied Physics Part 1-Regular Papers Short Notes & Review Papers, **38**(1A), 12-16.
- (Das, 1972) M. B. Das, **1972**,
FET Noise sources and their effects on amplifier performance at low frequencies,
IEEE Transactions on Electron Devices, **19** (3), 338-348.
- (Demange et al., 1994) P. Demange, D. Voges, J. Benz, S. Liemann, P.Gottig, R. Berendes, A. Burger and R. Huber, **1994**,
Annexin-V - the key to understanding ion selectivity and voltage regulation,
Trends in Biochemical Sciences, **19**(7), 272-276.
- (DiFrancesco and Noble, 1985) D. DiFrancesco and D. Noble, **1985**,
A Model of cardiac electrical activity incorporating ionic pumps and concentration changes,
Philos. Trans. R. Soc. London, Ser. B, **B307**, 353-398.
- (Earm and Noble, 1990) Y.E. Earm and D. Noble, **1990**
A Model of the single atrial cell: relation between calcium current and calcium release,
Proc. R. Soc., **240**, S. 83-96
D. Noble, OXSOFT HEART Manual, version 4.8
(Oxsoft Ltd., Oxford, 1997).
- (Elbhiri et al., 2000) Z. Elbhiri, Y. Chevalier, J.M. Chovelon, N. Jaffrezic-Renault, **2000**,
Grafting of phosphonate groups on the silica surface for the elaboration of ion-sensitive field-effect transistors,
Talanta, **52**(3), 495-507.

- (EPC-9, 1999) User manual,
EPC-9 double patch-clamp amplifier,
HEKA, Germany, **1999**.
- (Fazzi and Rehak,
1996 a) A. Fazzi and P. Rehak, **1996**,
*A Double-Gate Double-Feedback Jfet Charge-Sensitive
Preamplifier*
Nuclear Instruments & Methods in Physics Research Section A
Accelerators Spectrometers Detectors & Associated Equipment
380(12), 346-349.
- (Fazzi and Rehak,
1996 b) A. Fazzi and P. Rehak, **1996**,
*Gate-to-Gate Bjt Obtained From the Double-Gate Input Jfet to
Reset Charge Preamplifiers*,
Nuclear Instruments & Methods in Physics Research Section A
Accelerators Spectrometers Detectors & Associated Equipment,
377(2-3), 453-458.
- (Ficker and
Heinemann, 1992) E. Ficker and U. Heinemann, **1992**,
*Slow and fast transient potassium currents in cultured
rat hippocampal cells*,
J. Physiol (Lond.), **445**, 431-455.
- (Fromherz et al.,
1991) P. Fromherz, A. Offenhäusser, T. Vetter, J. Weis, **1991**,
*A Neuron-Silicon Junction: a Retzius cell of the leech
on an insulated-gate field-effect transistor*,
Science, **252**, 1290-1293.
- (Fromherz et al.,
1993) P. Fromherz, C. O. Müller, R. Weis, **1993**,
*Neuron Transistor: Electrical Transfer Function
Measured by the Patch-Clamp Technique*,
Phys. Rev. Lett., **71** (24), S. 4079-4082.
- (Fromherz and Stett,
1995) P. Fromherz and A. Stett, **1995**,
*Silicon-Neuron Junction: Capacitive Stimulation
of an Individual Neuron on a Silicon Chip*,
Phys. Rev. Lett., **75**, 1670-1673.
- (Fromherz, 1997) P. Fromherz, **1997**,
Selfgating of ion channels in cell adhesion,
Phys. Rev. Lett., **78**, 21, 4131-4134.
- (Fromherz, 1999) P. Fromherz, **1999**,
*Extracellular recording with transistors and the
distribution of ionic conductances in a cell membrane*,
Eur. Biophys. J., **28**, 254-258.

- (Frueh and Felker, 1976) B.R. Frueh, G.V. Felker, **1976**,
Baseball implant. A method of secondary insertion of an intraorbital implant,
Archives of Ophthalmology, **94** (3), 429-30.
- (Frumkin et al., 1974) A. Frumkin, B. Damaskin, I. Bagotskaya, N. Grigoeyev, **1974**,
Potentials of zero charge, interaction of metals with water and adsorption of organic substances II. Potentials of zero charge and the work function,
Electrochim. Acta, **19**, 75-81.
- (Ginsborg et al., 1991) B.L. Ginsborg, R.J. Martin, L. Patmore, **1991**,
On the sodium and potassium currents of a human neuroblastoma cell line,
J. Physiol. (Lond.), **434**, 121-149.
- (Gross et al., 1977) G.W. Gross, E. Rieske, G.W. Kreutzberg, A. Meyer, **1977**,
A new fixed-array multi-microelectrode system designed for long-term monitoring of extracellular single unit neuronal activity in vitro,
Neurosci. Lett., **6**, 101-105.
- (Gross et al., 1995) G.W. Gross, B.K. Rhoades, H.M.E. Azzazy, M.-C. Wu, **1995**,
The use of neuronal networks on multielectrode arrays as biosensors,
Biosensors & Bioelectronics, **10**, 553-567.
- (Hajji et al., 2000) B. Hajji, P. Temple-Boyer, J. Launay, T. do Conto, A. Martinez, **2000**,
pH, pK and pNa detection properties of SiO₂/Si₃N₄ ISFET chemical sensors,
Microelectronics & Reliability, 40(4-5), 783-786.
- (Hamill et al., 1981) O.P. Hamill, A. Marty, E. Neher, B. Sackman, F.J. Sigworth, **1981**,
Improved patch-clamp techniques für high-resolution current recording from cells and cell-free membrane patches,
Pflügers Archiv-European J. Physiol. **391**, 2, 85-100.
- (Hämmerle et al., 1994) H. Hämmerle, U. Egert, A. Mohr, W. Nisch, **1994**,
Extracellular recording in neuronal networks with substrate integrated microelectrode arrays,
Biosensors & Bioelectronics, **9**, 691-696.

- (Hara and Ohta, 1996) H. Hara and T. Ohta, **1996**,
Dynamic Response of a Ta₂O₅-Gate PH-Sensitive Field-Effect Transistor,
Sensors & Actuators B-Chemical, **32**(2), 115-119.
- (Hattori et al., 1999) T. Hattori, H. Nohira, K Takahashi, **1999**,
The initial growth steps of ultrathin gate oxides,
Microelectronic Engineering, **48**(14), 17-24.
- (Hille, 1992) B. Hille, **1992**,
Ionic channels of excitable membranes, 2nd ed.
Sinauer Associates, Inc., Sunderland, USA.
- (Hodgkin and Huxley, 1952) A.L. Hodgkin, A.F. Huxley, **1952**
A quantitative description of membrane current and its application to conduction and excitation in nerve,
J. Physiol., **117**, 500-544.
- (Hofmann, 1996) E. Hofmann, **1996**,
Medizinische Biochemie,
UNI-MED Verlag AG, Lorch, Germany.
- (Hofmann et al., 1997) A. Hofmann, J. Benz, S. Liemann, R. Huber, **1997**
Voltage dependent binding of Annexin-V, Annexin-VI and Annexin-VII to acidic phospholipid membranes,
Biochimica et Biophysica Acta - Biomembranes, **1330**(2), 254-264.
- (Ibl, 1962) N. Ibl, **1962**,
Application of mass transfer theory: the formation of powder metal deposits,
Interscience Publishers, New York.
- (Ingebrandt et al., 2001) S. Ingebrandt, C.-K. Yeung, M. Krause and A. Offenhäuser, **2001**,
Cardiomyocyte-transistor-hybrids for sensor application,
Biosensors & Bioelectronics (accepted)
- (Israel et al., 1984) D.A. Israel, W.H. Barry, D.J. Edell, R.G. Mark, **1984**,
An array of microelectrodes to stimulate and record from cardiac cells in culture,
Am. J. Physiol., **247**, H669-H674.
- (Jakobson et al., 1998) C. Jakobson, I. Bloom, Y. Nemirovsky, **1998**,
1/F Noise in Cmos Transistors For Analog Applications From Subthreshold to Saturation,
Solid-State Electronics, **42**(10), 1807-1817.

- (Jakobson and Nemirovsky, 1999) C.G. Jakobson and Y. Nemirovsky, **1999**, *1/f noise in ion sensitive field effect transistors from subthreshold to saturation*, IEEE Transactions on Electron Devices, **46**(1), 259-261.
- (Jakobson et al., 2000) C.G. Jakobson, M. Feinsod, Nemirovsky, **2000**, *Low frequency noise and drift in Ion Sensitive Field Effect Transistors*, Sensors & Actuators B Chemical, **68**(13), 134-139.
- (Jenker and Fromherz, 1997) M. Jenker and P. Fromherz, **1997**, *Bistability of membrane conductance in cell Adhesion observed in a Neuron Transistor*, Phys. Rev. Lett., **79**, 23, 4705-4708.
- (Johansson, 1994) S. Johansson, **1994**, *Graded action potentials generated by differentiated human neuroblastoma cells*, Acta. Physiol. Scand., **151**, 331-341.
- (Jordan and Jordan, 1964) A.G. Jordan and N.A. Jordan, **1964**, *Theory of Noise in Metal Oxide Semiconductor Devices*, IEEE Transactions on Electron Devices, 148-156.
- (Klee et al., 1997) R. Klee, C. Eder, E. Ficker, U. Heinemann, **1997**, *Age-dependent variation in potassium sensitivity of A-currents in rat hippocampal neurons*, Eur. J. Neurosci., **9**, 1970-1976.
- (Kleinig and Sitte, 1999) H. Kleinig and P. Sitte, **1999**, *Zellbiologie*, G. Fischer, Stuttgart, Germany.
- (Krause et al., 2000) M. Krause, S. Ingebrandt, D. Richter, M. Denyer, M. Scholl, C. Sprössler, and A. Offenhäusser, **2000**, *Extended gate electrode arrays for extracellular signal recordings*, Sensors & Actuators B, **70**, 101-107.
- (Krause, 2000) M. Krause, **2000**, *Untersuchungen zur Zell-Transistor Kopplung mittels der Voltage-Clamp Technik*, Dissertation, University of Mainz.
- (Lau, 1995) J.H. Lau, **1995**, *FLIP-CHIP Technologie*, McGraw-Hill, New York, S. 223.

- (Lauer, 2001) L. Lauer, **2001**,
Netzwerke von Nervenzellen auf strukturierten Oberflächen charakterisiert mit optischen und electrophysiologischen Methoden,
Dissertation, University of Mainz.
- (Lauer et al., 2001) L. Lauer, S. Ingebrandt, M. Scholl, A. Offenhäusser, **2001**,
Aligned Microcontact Printing of Biomolecules on Microelectronic Device Surfaces,
IEEE Trans. Biomed. Eng. (in press)
- (Lauritzen, 1965) P.O.Lauritzen, **1965**,
Low-frequency generation noise in junction field effect transistors,
Solid State Electronics, **8**, 41-58.
- (Liao et al., 1999) H.K. Liao, L.L. Chia, J.C. Chou, W.Y. Chung, T.P. Sun S.K. Hsiung, **1999**,
Study on pH(pzc) and surface potential of tin oxide gate ISFET,
Materials Chemistry & Physics, **59**(1), 6-11.
- (Liemann et al., 1996) S. Liemann, J. Bent, D. Voges, A. Hofmann, R.Huber and P.Gottig, **1996**,
Structural and functional characterisation of the voltage sensor in the ion channel human Annexin-V,
Journal of Molecular Biology, **258**(4), 555-561.
- (Lucovsky et al., 1997) G. Lucovsky, A. Banerjee, H. Niimi, K.Koh, B. Hinds, C. Meyer, G. Lüpke, H. Kurz, **1997**,
Elimination of Sub-Oxide Transition Regions At Si-SiO₂ Interfaces By Rapid Thermal Annealing At 900°C,
Applied Surface Science, **117/118**, 202-206.
- (Lund et al., 1996) M.W. Lund, K.W. Decker, R.T. Perkins, J.D. Philips, **1996**,
Low noise JFETs for room temperature xray detectors,
Nuclear Instruments & Methods in Physics Research Section A Accelerators Spectrometers Detectors & Associated Equipment **380**(12), 318-322.
- (Madden et al., 1977) W.G. Madden, R. Gomer, M.J. Mandell, **1977**,
The Effect of Electrolyte on Dipole Layers at Liquid-Air Interface,
J. Phys. Chem., **81**, 2652-2655.

- (Madou et al., 1988) M.J. Madou, K.W. Frese jr., S.R. Morrison, **1980**,
The Silicon/Silica Electrode,
Phys. Stat. Sol. A, **57**, 705-712.
- (Marty and Neher, 1995) A. Marty and E. Neher, **1995**,
Single-Channel Recording,
edited by B. Sackmann and E. Neher
Plenum Press, New York.
- (Masson et al., 1999) P. Masson, P. Morfouli, J.L. Autran, J. Brini, B. Balland
E.M. Vogel, J.J. Wortman, **1999**,
*Electrical properties of oxynitride thin films using noise and
charge pumping measurements*,
Journal of Non-Crystalline Solids, **245**, 54-58.
- (Matsuura and Katsuhiko, 1997) H. Matsuura and K. Nishida, **1998**,
*A New Structure of an N-Channel Junction Field-Effect
Transistor Embedded in a Pin Diode For an X-Ray Detector*,
Japanese Journal of Applied Physics Part 2,
37(2A), L 115-L 118.
- (McWhorter, 1957) A.L. McWhorter, **1957**,
Semiconductor Surface Physics,
edited by R.H. Kingston,
Philadelphia University Press, 169-196, 207.
- (MED64, 2000) Homepage Panasonic MED64 systems, **2000**,
<http://www.med64.com/>
- (Müller, 1987) R. Müller, **1987**,
Bauelemente der Halbleiter-Elektronik,
Halbleiter-Elektronik, **2**, 3. Aufl.,
Springer Verlag, Berlin.
- (Müller, 1990) R. Müller, **1990**,
Rauschen,
Halbleiter-Elektronik, **15**, 2. Aufl.,
Springer Verlag, Berlin.
- (Mueller and Schulz, 1997) H. H. Mueller and M. Schulz, **1998**,
*Random Telegraph Signal - an Atomic Probe of the Local
Current in Field-Effect Transistors*,
Journal of Applied Physics, **83**(3), 1734-1741.

- (Neher and Sakmann, 1976) E. Neher and B. Sakmann, **1976**,
Single channel currents recorded from membrane of denervated frog muscle fibres,
Nature, **260**, 799-802.
- (Neher, 1992) E. Neher, **1992**,
Correction for liquid junction potentials in patch clamp experiments,
In: *Methods in Enzymology*, **207**, 123-131,
Academic Press, New York.
- (Neher, 1995) E. Neher, **1995**,
Chapter 6: Voltage offsets in patch-clamp experiments,
In: *Single-Channel recording*
(B. Sakmann & E. Neher, eds.)
Plenum Press, New York.
- (Nicholls et al., 1995) J.G. Nicholls, A.R. Martin, B.G.E. Wallace, **1995**,
Vom Neuron zum Gehirn,
Gustav Fischer Verlag, Stuttgart, Germany.
- (Nisch et al., 1994) W. Nisch, J. Böck, U. Egert, H. Hämmerle, A. Mohr, **1994**,
A thin film microelectrode array for monitoring extracellular neuronal activity in vitro,
Biosensors & Bioelectronics, **9**, 737-741.
- (Oelßner et al., 1995) W. Oelßner, J. Zosel, F. Berthold, H. Kaden, **1995**,
Investigation of the dynamic response behaviour of ISFET pH sensors by means of laser Doppler velocimetry (LDV),
Sensors & Actuators B-Chemical, **B27** (1-3), 345-348.
- (Offenhäusser et al., 1995) A. Offenhäusser, J. Rühle, W. Knoll, **1995**,
Neuronal cells cultured on modified microelectronic device surfaces,
J. Vac. Sci. Technol. A, **13**, 2606-2612.
- (Offenhäusser et al., 1997) A. Offenhäusser, C. Sprössler, M. Matsuzawa, W. Knoll, **1997**,
Field-Effect Transistor Array for Monitoring Electrical Activity from Mammalian Neurons in Culture,
Biosensors & Bioelectronics, **12**, 8, 819-826.
- (Ottenbacher et al., 1993) D. Ottenbacher, F. Jähnig, W. Göpel, **1993**,
A prototype biosensor based on transport proteins: electrical transducers applied to lactose permease,
Sensors & Actuators B-Chemical, **B13**, 1-3, 173-175.

- (Pancrazio et al., 1999) J.J. Pancrazio, J.P. Whelan, D.A. Borkholder, W. Ma D.A. Stenger, **1999**,
Development and application of cell-based biosensors,
Annals of Biomedical Engineering, **27**(6), 697-711.
- (Parce et al., 1989) J.W. Parce, J.C. Owicki, K.M. Kercso, G.B. Sigal,
H.G. Wada, V.C. Muir, L.J. Bousse, K.L. Ross, B.I. Sikic
and H.M. McConnell, **1989**,
Detection of cell-affecting agents with a silicon biosensor,
Science, **246** (4927), 243-247.
- (Paul, 1994) R. Paul, **1994**,
MOS-Feldeffekttransistoren,
Halbleiter-Elektronik, **21**,
Springer Verlag, Berlin.
- (Pickard, 1979) R.S. Pickard, **1979**,
*A review of printed circuit microelectrodes
and their production*,
J. Neurosci. Meth., **1**, 301-318.
- (Prochazka and Davis, 1992) A. Prochazka, L.A. Davis, **1992**,
*Clinical experience with reinforced, anchored intramuscular
electrodes for functional neuromuscular stimulation*,
Journal of Neuroscience Methods. **42** (3), 175-84.
- (Regehr et al., 1989) W.G. Regehr, J. Pine, C.S. Cohan, M.D Mischke
and D.W. Tank, **1989**,
*Sealing cultured invertebrate neurons to embedded dish
electrodes facilitates long-term stimulation and recording*,
Journal of Neuroscience Methods, **56** (2), 91-106.
- (Ren et al., 1999) L. Ren, S. Okhonin, M. Ilegems, 1999,
Low-frequency noise in electrically stressed n-MOSFETs,
Solid-State Electronics, **43**(5), 849-856.
- (Robinson, 1968) D.A. Robinson, **1968**
The electrical properties of metal microelectrodes,
Proc. IEEE, **56**, 1065-1071.
- (Ruge and Mader, 1991) I. Ruge and H. Mader, **1991**,
Halbleiter-Technologie,
Halbleiter-Elektronik, **4**, 3. Aufl.,
Springer Verlag, Berlin.

- (Sakmann and Neher, 95) B. Sakmann and E. Neher, **1995**, *Single-channel recording*, 2.Aufl., Plenum Press, New York.
- (Santiard and Faccio, 1996) J.C. Santiard and F. Faccio, **1996**, *Noise and Speed Characteristics of Test Transistors and Charge Amplifiers Designed Using a Submicron Cmos Technology*, Nuclear Instruments & Methods in Physics Research Section A Accelerators Spectrometers Detectors & Associated Equipment, **380**(12), 350-352.
- (Schätzthauer and Fromherz, 1998) R. Schätzthauer and P. Fromherz, **1998**, *Neuron-junction with voltage-gated ionic currents*, Eur. J. Neurosci., **10**, 1956-1962.
- (Schechter, 1972) D.C. Schechter, **1972**, *Background of clinical cardiac electrostimulation. 3. Electrical regulation of rapid cardiac dysrhythmias*, New York State Journal of Medicine, **72** (2), 270-84.
- (Schlachetzki, 1990) A. Schlachetzki, **1990**, *Halbleiter-Elektronik: Grundlagen und moderne Entwicklung*, B.G. Teubner, Stuttgart.
- (Scholl, 1999) M. Scholl, **1999**, *Neuronale Netzwerke auf Halbleiteroberflächen*, Dissertation, Cuvillier Verlag, Göttingen.
- (Scholl et al., 2000) M. Scholl, C. Sprössler, M. Denyer, M. Krause, K. Nakajima A. Maelicke, W. Knoll, A. Offenhäusser, **2000**, *Ordered networks of rat hippocampal neurons attached to silicon oxide surfaces*, Journal of Neuroscience Methods, **104**(1), 65-75.
- (Schwan, 1996) C. Schwan, **1996**, *YBa₂Cu₃O_{7-x}/isolator/Au heterostructures: Preparation, characterisation and dielectical properties*, Diploma Thesis, TH Darmstadt, unpublished.
- (Shrier and Clay, 1986) A. Shrier, J.R. Clay, **1986** *Repolarisation currents in embryonic chick atrial heart cell aggregates*, Biophys. J., **50**, 861-874

- (Sigworth et al., 1995) F.J. Sigworth, H. Affolter, E. Neher, **1995**,
Design of the EPC-9, a computer controlled patch-clamp amplifier, 2. Software,
J. Neurosci. Methods, **56**, 203-221.
- (Simon and Reichl, 1990) J. Simon and H. Reichl, **1990**,
Single Chip Bumping for TAB,
Proceedings of 2nd International TAB-Symposium
ITAB '90, San Jose, 4.
- (Siu and Cobbold, 1979) W.M. Siu and R.S.C. Cobbold, **1979**,
*Basic Properties of the Electrolyte-SiO₂-Si System:
Physical and Theoretical Aspects*,
IEEE Trans. Electron. Devices., **ED-26** (11), 1805-1815.
- (Southampton Electrochemistry group, 1985) Southampton Electrochemistry group, **1985**,
Instrumental Methods in Electrochemistry,
E. Horwood Ltd., Chichester.
- (Sprössler, 1997) C. Sprössler, **1997**,
Extrazelluläre Signalleitung durch ein Sensorfeld mit Feldeffekttransistoren,
Dissertation, Cuvillier Verlag, Göttingen.
- (Sprössler et al., 1998) C. Sprössler, D. Richter, M. Denyer, A. Offenhäusser, **1998**,
Long-term recording system based on field-effect transistor arrays for monitoring electrogenic cells in culture,
Biosensors & Bioelectronics, **13**, 613-618.
- (Sprössler et al., 1999) C. Sprössler, M. Denyer, S. Britland, W. Knoll, A. Offenhäusser, **1999**,
Electrical recordings from rat cardiac muscle cells using field-effect transistors,
Physical Review E, **60**, 2, 2171-2176.
- (Sprössler et al., 2001) C. Sprössler, M. Scholl, M.C. Denyer, M. Krause, K. Nakajima, A. Maelike, W. Knoll, A. Offenhäusser, **2001**,
Model network architectures in vitro on extracellular recording systems using microcontact printing,
Synth. Met., **117**(1-3 SI), 281-283.
- (Stett et al., 1997) A. Stett, B. Müller, P. Fromherz, **1997**,
Two-way silicon-neuron interface by electrical induction,
Phys. Rev. E, **55** (2), 1779-1782.

- (Storm, 1990) J.F. Storm, **1990**,
Potassium currents in hippocampal pyramidal cells,
Prog. Brain Research, **83**, 161-187.
- (Straub et al., 2001) B. Straub, E. Meyer, P. Fromherz, **2001**,
*Recombinant maxi-K channels on transistor, a prototype
of iono-electronic interfacing*,
Nature Biotechnology, **19**, 121-124.
- (Thiébaud et al., 1997) P. Thiébaud, N.F. de Rooij, M. Koudelka - Hep,
and L. Stoppini, **1997**,
*Microelectrode arrays for electrophysiological monitoring
of Hippocampal organotypic slice cultures*,
IEEE Trans. BME, **44**, 11, 1159-1163.
- (Thiébaud et al., 2001) P. Thiébaud, L. Lauer, W. Knoll, A. Offenhäusser, **1997**,
*PDMS device for patterned application of microfluids to
neuronal cells arranged by microcontact printing*,
Biosensors & Bioelectronics, accepted.
- (Thomas et al., 1972) C.A. Thomas, P.A. Springer, G.E. Loeb, Y. Berwald-Netter,
L.M. Okun, **1972**,
*A miniature microelectrode array to monitor the bioelectric
activity of cultured cells*,
Exp. Cell Res., **74**, 61-66.
- (Toselli et al., 1991) M. Toselli, S. Masetto, P. Rossi, V. Taglietti, **1991**,
*Characterization of a Voltage-dependent Calcium Current
in the Human Neuroblastoma Cell Line SH-SY5Y
During In Vitro Differentiation*,
Eur. J. Neurosci., **3**, 514-522.
- (Toselli et al., 1996) M. Toselli, P. Tosetti, V. Taglietti, **1996**,
*Functional Changes in Sodium Conductances in the Human
Neuroblastoma Cell Line SH-SY5Y During In Vitro
Differentiation*,
J. Neurophysiol., **76**, 6, 3920-3927.
- (Tosetti et al., 1998) P. Tosetti, V. Taglietti, M. Toselli, **1998**,
*Functional Changes in Potassium Conductances of
human Neuroblastoma Cell Line SH-SY5Y During In
Vitro Differentiation*,
J. Neurophysiol., **79**, 2, S. 648-658.

- (Vanýsek, 1995) P. Vanýsek, **1995**,
Handbook of Chemistry and Physics,
76 th edition, 1995-1996,
McGraw-New York, 5/90-5/98.
- (Vassanelli and Fromherz, 1999) S. Vassanelli and P. Fromherz, **1999**,
*Transistor probes local potassium conductances in the
adhesion region of cultured rat hippocampal neurons*,
J. Neurosci., 19, **16**, 6767-6773
- (Voet and Voet, 1992) D. Voet and J. G. Voet, **1992**,
Biochemie,
Übers. Hrsg. von A. Maelicke, W. Müller-Esterl,
VCH Verlagsgesellschaft, Weinheim.
- (Wedler, 1987) G. Wedler, **1987**,
Lehrbuch der physikalischen Chemie, 3. Aufl.,
VCH Verlagsgesellschaft, Weinheim.
- (Weis and Fromherz, 1997) R. Weis and P. Fromherz, **1997**,
Frequency dependent signal transfer in neuron transistors,
Phys. Rev. E, **55** (1), 877-889.
- (White et al., 1983) R.L. White, L.A. Roberts, O.Kwon and N. Cotter, **1983**,
Thin-film electrodes for an artificial ear,
Journal of Vacuum Science and Technology A -
Vacuum Surfaces and Films, **1**(2), 287-295.
- (Yeung, 2001 a) C.-K. Yeung, L. Lauer, A. Offenhäusser and W. Knoll, **2001**,
*Modulation of the growth and guidance of rat brain stem
neurons using patterned extracellular matrix proteins*,
Neurosci. Lett., **301** (2), 147-150.
- (Yeung, 2001 b) C.-K. Yeung, S. Ingebrandt, M. Krause,
A. Offenhäusser and W. Knoll, **2001**,
*The validation of the potential use of field effect transistors
in pharmacological bioassays*,
J. Pharmacol. Toxicol. Meth. (submitted).
- (Yates et al., 1974) D. E. Yates, S. Levine, T. W. Healy, **1974**,
*Site-binding model of the electrical double layer
at the oxide/water interface*,
J. Chem. Soc. Faraday Trans. I, **70**, 1807-1818.

Abbreviations

Formula signs

in order of chapters

2. Chapter

V_{RP}	: resting potential
E_i	: equilibrium potential for ion species i
$c_i^{interior, exterior}$: ion concentration of ion i inside and outside of cells
T	: absolute Temperature
R	: universal gas constant
z	: number of charges
F	: Faraday constant
V_M	: membrane voltage
P_i	: permeability constant of ion species i
g_i	: specific conductance of ion species i
i_M^i	: ion current density over the membrane for ion species i
c_M	: specific membrane capacitance
g^L	: leakage conductance

3. Chapter

d_{ox}	: gateoxide thickness
F_i	: work function of material i
F_F	: work function of the fermi level
V_g	: gate potential
W_s	: band bending

W_m	: maximum band bending
W_F	: fermi level
W_C	: conduction band
W_V	: valence band
W_i	: intrinsic energy band
V_i	: voltage drop in the intrinsic
W_G	: band gap energy
W_c	: electron affinity
Q_I	: interface charge
C_I	: interface capacitance
V_{FB}	: flatband voltage
W	: channel width of a transistor
L	: channel length of a transistor
a	: channel height for JFETs
V_{GS}	: gate-source voltage
V_{DS}	: drain-source voltage
I_{DS}	: drain-source capacitance
Q	: total electrical charge
q	: electrical charge
c_{ox}	: specific oxide capacitance
ϵ	: relative dielectrical constant of oxide
ϵ_0	: dielectrical constant
Q_B	: charge of the pinned acceptor atoms in the depletion zone
V_{gi}	: gate potential for inversion
$w(x)$: thickness of the depletion zone
Q_n	: charge of the mobile carriers (electrons)
N_D	: doping concentration
N_A	: number of acceptor atoms
μ_n	: mobility of electrons
μ_p	: mobility of holes
V_{th}	: threshold voltage

D	: total thickness of semiconductor region
V_{DS}^P	: pinch-off voltage
E_x	: electrical field perpendicular to the gateoxide
E_y	: electrical field parallel to the gateoxide
m_{eff}^*	: reduced effective electron mobility
m_{eff}	: effective electron mobility
m_0	: ideal electron mobility
q	: surface scattering factor
E_c	: correction field
V_A	: Early voltage
I_{DS}^{max}	: maximum value of IDS
R_S	: source resistance
R_D	: drain resistance
g_m	: transconductance
g_{mb}	: conductance from channel to bulk
g_d	: drain conductance
V_{Si}	: voltage drop in silicon
V_{ox}	: voltage drop in the gate oxide
\mathbf{s}	: channel conductivity
L_d	: thickness of the diffuse layer
\mathbf{Y}_d	: potential drop in the diffuse layer
V_{FB}^E	: flatband voltage for the EOSFET
V_{NHE}	: electrode potential relative to the vacuum level for a normal hydrogen electrode
c_E	: surface potential of the electrolyte
dc	: contact potential
V_{ref}	: reference potential
\mathbf{Y}_E	: potential drop at the electrolyte surface
DV_{FB}	: change in the flatband voltage

C_d	: capacitance of the electrolyte boundary
V_{acc}	: acceleration voltage
C_H	: Helmholtz capacitance
L_D	: Debye length
d_{OHP}	: thickness of the outer Helmholtz plane
C_D	: diffuse layer capacitance
Z, Z', Z''	: impedance, total, real part, imaginary part
ω	: angular frequency
$P(A)$: probability density function
$A(t)$: noise signal
\bar{A}	: average value of the noise signal
s^2	: variance/noise power
$\overline{A^2}$: total noise power
$\overline{A^2}$: DC part of the noise power
c_{12}	: correlation coefficient
$r_{12}(t)$: correlation function
$W(f)$: spectral noise density
$\overline{a^2} \Big _B$: narrow band noise
$r(t)$: autocorrelation function
$w(f)$: spectral noise density
$t(x)$: distribution of the time constants for a tunnelling process
t_{min}	: minimum value for the time constant of a tunnelling process
$\overline{\Delta N^2}$: total number of carriers
$\overline{\Delta n^2}$: carriers per volume unit
$W_N^*(x)$: carrier fluctuations per length
$W(\mathbf{w})$: power spectrum of the fluctuations per volume unit
N_t	: total number of interface traps
\bar{x}	: average tunnelling distance

5. Chapter

R_M	: membrane resistance
i_M^L	: leakage current over the membrane
C_{fast}	: stray capacitance of the patch pipette
G_L	: total leak conductance of the cell
R_S	: access resistance to the cells' interior
C_{slow}	: slow capacitance of the cell-pipette assembly
V_{step}	: commanded step height in <i>voltage-clamp mode</i>
i_{stim}	: current stimulation pulse in <i>current-clamp mode</i>
V_{hold}	: holding potential
i_M^{corr}	: corrected current output of the patch-clamp amplifier
i_M	: membrane current
G_J	: total junction conductance
R_J	: total junction resistance
A_{JM}	: membrane area of the junction membrane
A_{FM}	: membrane area of the free membrane
R_{JM}	: membrane resistance of the junction membrane
R_{FM}	: membrane resistance of the free membrane
C_{JM}	: membrane capacitance of the junction membrane
C_{FM}	: membrane capacitance of the free membrane
r_{cell}	: cell radius
A_M	: total membrane area
g_J	: specific junction conductance
V_J^0	: tip height of the extracellular response
c_i	: concentration of ion species i
c_0	: initial ion concentration in the extracellular medium
pK	: pK-value of the solution with $pK = -\log(c_{K^+})$
pNa	: pNa-value of the solution with $pK = -\log(c_{Na^+})$
pCa	: pCa-value of the solution with $pK = -\log(c_{Ca^{2+}})$

D_i : diffusion coefficient for salt i

I : molar conductivity

6. Chapter

X^i : scaling factor for ion species i

v : signal velocity in the cell layer

Technical Terms

AP : action potential

ASE : advanced silicon etching

CC-Mode : *current-clamp mode*

CV : cyclic voltammetry

DIC : differential interference contrast

DIV : days in vitro

EGE : extended gate electrode

EOSFET : electrolyte oxide semiconductor FET

FET : field-effect transistor

ISFET : ion-sensitive FET

JFET : junction FET

LPCVD : low pressure chemical vapour deposition

PCB : printed circuit board

PECVD : plasma enhanced chemical vapour deposition

RIE : reactive ion etching

SEM : scanning electron microscope

VC-Mode : *voltage-clamp mode*

Thank you / Dankeschön !!!

At the end I like to thank all people, who promoted me during the Ph.D time who contributed to this study and who made this research possible.

I will express my gratitude to the persons in their native language.

Mein Dank gilt...

- ... Prof. Dr. W. Knoll für die Möglichkeit, in seinem Arbeitskreis eine Doktorarbeit mit einer solch spannenden und interdisziplinären Themenstellung durchzuführen. Das internationale Klima in seiner Arbeitsgruppe und die hervorragenden Rahmenbedingungen finanzieller und logistischer Art im Max-Planck Institut haben ganz entscheidend zum Gelingen dieser Arbeit beigetragen. Bei vielen der sogenannten 'events', bei denen die ganze Arbeitsgruppe über mehrere Tage (und Nächte) enger zusammengerückt ist (z.B. Ringberg, Ebernburg,...), war Wolfgang zwar 'einer von uns' aber auch stets Vorbild und 'Vater der Gruppe'. An diese Gelegenheiten werde ich wohl noch lange nach meiner Zeit im MPI gerne zurückdenken.
- ... PD Dr. A. Offenhäuser für seine Unterstützung und sein stetes Interesse an 'neusten Entwicklungen' während meiner Arbeit. Letztendlich war er es, der mich überzeugt hat, dass ein Jahr in Japan mich und meine Frau Corinna persönlich, menschlich und auch fachlich weiterbringen wird.
- ... Prof. Dr. W. Baumann für die Vertretung meiner Arbeit vor dem Fachbereich Chemie und Pharmazie der Universität Mainz und seine spontane Bereitschaft, als Vertretung einzuspringen.
- ... Dr. M. Krause für die schöne gemeinsame Zeit am MPI und die wirklich gute Zusammenarbeit auf dem Gebiet der Zell-Transistor Kopplung.
- ... Dr. C. Sprössler für seine stete Unterstützung und für seine Diskussionsbereitschaft.
- ... Dr. C.-K. Yeung for his enthusiasm in this research area and for the support during all the Ph.D. time. I think we had a great time in Mainz working on this subject and we gained both from our collaboration. Kong, I like to thank you for the spelling correction of my thesis. Now it should be readable even for native english speakers.

- ... Dr. M. Scholl für seine Unterstützung und die Präparation der Hippocampalen Zellkulturen. Martin, eine der zentralen Zell-Transistor Kopplungsexperimente in meiner Arbeit gelang mit der allerletzten von dir präparierten Zellkultur!
- ... W. Staab vom Institut für Mikrotechnik Mainz (IMM) für sein Engagement bei der Herstellung der Transistoren und die Bereitschaft auch viele 'Sonderwünsche' zu erfüllen.
- ... Dr. C. Klein, M. Hemmerlein und A. Kosan aus dem Arbeitskreis von Prof. Maelicke am Institut für Physiologische Chemie und Pathobiochemie der Universität Mainz für die Zell-Linien Kulturen.
- ... T. Baumgart für die Zusammenarbeit im Bereich der Modellmembranen auf Transistoroberflächen.
- ... L. Lauer für die Hilfsbereitschaft und das angenehme Arbeitsklima in unserem kleinen aber feinen Labor.
- ... Je remercie Dr. P. Thiébaud pour son aide et pour les discussions sur le traitement des microlélectrodes.
- ... Herrn D. Richter und Herrn U. Müller vom MPI für Polymerforschung für den Bau und die ständige Weiterentwicklung der Verstärkerelektronik für die Zell-Transistor Messungen.
- ... Herrn Gerstenberg und Herrn Christ für die mechanischen Meisterleistungen beim Bau der Vorverstärkerköpfe.
- ... allen Mitgliedern der Arbeitsgruppe Knoll am MPI für die tolle Zeit und die vielen schönen Stunden im Institut. Für mich und Corinna war es ganz toll, dass so viele Leute aus der Arbeitsgruppe im letzten Jahr den Weg ins Rheinhessische Hügelland zu unserem Polterabend gefunden haben.
- ... meinen Eltern, die meine Ausbildung ermöglicht haben und die gerade in der letzten Zeit der Doktorarbeit oftmals auf meine Anwesenheit verzichten mussten.
- ... und am Ende meiner lieben Frau Corinna, die den ganzen Stress und das ganze Leid am Ende der Arbeit aufgefangen hat. Ich habe die Arbeit ihr und unserer gemeinsamen Zukunft gewidmet. Ich möchte mich auch für deine Abenteuerlust? in bezug auf unsere geplante Japan-Zeit bedanken und hoffe es wird für uns beide eine schöne Erfahrung.

Lebenslauf

Sven Ingebrandt

geboren: 14. August 1971
in Alzey

wohnhaft: Obermühlstrasse 10
55234 Freimersheim

8.1978 - 6.1982 Grundschule

8.1982 - 6. 1991 Gymnasium an der Frankenstrasse Alzey

11.1991 - 7.1998 Studium der Physik
Johannes Gutenberg Universität Mainz

3.1997 - 5.1998 Diplomarbeit in der Arbeitsgruppe Prof. Adrian
Magnetismus und Supraleitung in dünnen Schichten
an der Johannes Gutenberg Universität Mainz

8.1998 - 5.2001 Doktorand im Arbeitskreis Materialwissenschaften
Prof. Knoll am Max-Planck-Institut für
Polymerforschung, Mainz

Hiermit erkläre ich, dass ich die vorliegende Arbeit
selbständig und nur unter Verwendung der angegebenen Hilfsmittel
angefertigt habe.

Ich erkläre ausserdem, dass ich noch keinen Promotionsversuch
unternommen habe.

Mainz im Mai 2001

